Exploring the Diverse Applications of Plasmonic Refractive Index Sensors: Unveiling a New Realm of Possibilities

by

Rummanur Rahad (180021203)
Shadman Shahriar Sharar (180021205)
Mohammad Ashraful Haque (180021229)

A Thesis Submitted in Accordance with the Requirements of the Degree of

BACHELOR OF SCIENCE

IN

ELECTRICAL AND ELECTRONIC ENGINEERING

Islamic University of Technology
Board Bazar, Gazipur-1704, Bangladesh.

Department of Electrical and Electronic Engineering
April, 2023

Exploring the Diverse Applications of Plasmonic Refractive Index Sensors: Unveiling a New Realm of Possibilities

Submitted by

Rummanur Rahad (180021203)
Shadman Shahriar Sharar (180021205)
Mohammad Ashraful Haque (180021229)

has been approved on 15^{th} April, 2023.

Prof. Dr. Rakibul Hasan Sagor
Professor
Department of Electrical and Electronic Engineering
Islamic University of Technology,
Dhaka, Bangladesh

Declaration of Authorship

This is to certify that the work presented in this thesis, titled **"Exploring the Diverse Applications of Plasmonic Refractive Index Sensors: Unveiling a New Realm of Possibilities"**, is the result of diligent research conducted under the guidance of **Prof. Dr. Rakibul Hasan Sagor**. Additionally, it is important to disclose that a portion of this work has been published in the **"Results in Physics"** journal, while two other portions are currently under review in **"Physica E: Low-Dimensional Systems and Nanostructures"** and **"Results in Physics"** journals.

Rummanur Rahad (180021203)

Shadman Shahriar Sharar (180021205)

Mohammad Ashraful Haque (180021229)

Acknowledgement

"In the Name of Allah, the Most Beneficent, the Most Merciful. All the praises and thanks be to Allah, the Lord of the 'Alamin (mankind, jinns and all that exists)."

We are grateful to ALLAH (SWT), the most benevolent and kind to provide us the health strength and ability to research and write this dissertation.

We sincerely thank and express our heartfelt appreciation to our supervisor, **Prof. Dr. Rakibul Hasan Sagor**, for his astounding assistance, meticulous instructions, and guidance. His experience, mentorship, and fruitful contributions were critical to the efficacy of our thesis. We are very grateful for his contributions to the conceptual investigations, pertinent efforts, and overall thesis book drafting.

We express our heartfelt appreciation to our friends and families, specially our parents for their continuous support and dedication towards our life, which has played a pivotal role in our journey towards accomplishing our goals. Their constant encouragement has been instrumental in shaping us into the individuals we are today, and without their steadfast belief in us, our achievements would not have been possible.

Contents

Certification of Approval ii

Declaration of Authorship iii

Acknowledgement iv

List of Figures viii

List of Tables xii

List of Abbreviations xiv

Abstract xv

1 Introduction and Background 1

1.1 Optics and Nanophotonics 2

1.2 Plasmonics 7

1.3 Surface Plasmon Polariton 8

1.4 Plasmonic Waveguide 10

1.4.1 MIM Waveguide 11

1.4.2 IMI Waveguide 13

1.4.3 DLSPP Waveguide 14

1.4.4 Slot Waveguide 16

1.4.5 Nanowire Waveguide 17

1.4.6 Hybrid Waveguide 18

1.5 Present and Future of Plasmonics 19

2 Literature Review 22

3 Methodology 30

3.1 Electromagnetic Wave Theory 30

3.1.1 Maxwell's Fundamental Equations 30

3.1.2 Formulation of Electromagnetic Wave Equations 32

3.1.3 Formulation of Wave Propagation Mode . . . 37
3.1.4 Unveiling the Primary Propagation Mode of Surface Plasmon Polaritons: A TM or TE Conundrum . . . 39
3.2 Material Modeling . . . 43
3.2.1 Lorentz Model . . . 43
3.2.2 Drude Model . . . 47
3.2.3 Lorentz-Drude Model . . . 49
3.3 Formulation of Surface Plasmon Polariton . . . 51
3.3.1 Propagation and Decaying Property of SPP . . . 51
3.3.2 Understanding SPP Propagation at Metal-Insulator Interface . . . 53
3.3.3 Determining the Resonant Wavelength for SPPs . . . 54
3.3.4 Formulation of Dielectric Loss . . . 57
3.4 Simulation Modeling . . . 58
3.4.1 Finite Element Method . . . 58
3.5 Boundary Conditions . . . 67
3.5.1 Scattering Boundary Conditions . . . 67
3.5.2 Port Boundary Conditions . . . 69
3.6 Performance Metrices . . . 71
3.6.1 Transmittance . . . 71
3.6.2 Sensitivity . . . 72
3.6.3 Figure of Merit . . . 74
3.6.4 Quality Factor . . . 75
3.6.5 Sensing Resolution . . . 77
3.6.6 Excitation Ratio . . . 77
3.7 RI Sensor Fabrication Process . . . 79
3.7.1 Nanoimprint Lithography (NIL) . . . 80
3.7.2 Electron Beam Lithography (EBL) . . . 81
3.7.3 Focused Ion Beam Milling (FIB) . . . 83
3.7.4 Reactive Ion Etching (RIE) . . . 84
3.7.5 Atomic Layer Deposition (ALD) . . . 85
3.7.6 Molecular Beam Epitaxy (MBE) . . . 86

4 Advancements in Sensor Technology: Design, Optimization, and Real-world Implementations 88
4.1 Importance of Design and Optimization . . . 88
4.2 Real-world Scope of Plasmonic Refractive Index Sensor . . . 89
4.3 Sensor Design with Modified Rectangular Resonator with Baffles and Nanorod 92
4.3.1 Designing Structure and Methodology . . . 92

4.3.2 Sensing Parameters and Optimization 96
4.3.3 Fabrication Process 109
4.3.4 Applications 109
4.4 Sensor Design with Opposing-Face Semi-Circular Ring Resonators Integrated with Nanorods 117
4.4.1 Structure Model, Methodology and Performance Metrices 117
4.4.2 Results Analysis 119
4.4.3 Optimization of the Design after Adding Nanodots 123
4.4.4 Applications 129
4.5 Sensor Design with Modified Octagonal-shape Resonator with Nanorods . . 136
4.5.1 Sensor Geometry and Theoretical Analysis 136
4.5.2 Sensor Design Optimization 137
4.5.3 Result Analysis 141
4.5.4 Application Scopes of the Proposed Sensor 143

5 Conclusions **149**
5.1 Thesis Summary 149
5.2 Future Prospects of Our Work 149

References **152**

List of Figures

1.1 Propagation of SPP in Metal-Dielectric Interface. 9
1.2 Configuration of MIM waveguide configuration. 12
1.3 Configuration of IMI waveguide. 14
1.4 Isometric view of DLSPP waveguide. 15
1.5 Configuration of slot waveguide. 16

2.1 Different proposed nanosensor designs. (a) Circular Ring Containing a Rectangular Cavity, (b) Hexagonal Ring Cavity, (c). Square Cavity, (d) Rectangular Ring Resonator, (e) U-shaped Resonator, (f) Triangular Resonator, (g) Ring Cavity and Baffles (h) T-shaped Resonator, (i) U-shaped Cavity, (j) Double Square Ring Resonator (k) Rectangular and Circular Ring Resonators, (l) Elliptical Ring Resonator, (m) Square Ring and Triangle Cavity, (n) Racetrack Cavity, (o) V-ring Cavity With Groove. 24

3.1 a. The real part of permittivity b. The imaginary part of permittivity. 46
3.2 Real and Imaginary Part of Drude Model 49
3.3 Propagation property of SPP. 53
3.4 Wave Vector of SPP propagtion in Metal-Insulator Interface. 53
3.5 2D system boundary represented by three triangular finite elements. 61
3.6 A single triangular element with three nodes. 62
3.7 Transmittance of a sensor 72
3.8 Sensitivity 73
3.9 Calculation of FWHM for Symmetrical Curve 74
3.10 Calculation of FWHM for Asymmetrical Curve 75
3.11 High Q-factor 76
3.12 Low Q-factor 77
3.13 Excitation Ratio for Symmetrical Curve 78
3.14 Excitation Ratio for Asymmetrical Curve 78

4.1 Initial structure of the sensor. 92
4.2 Relationship between height (h) and effective refractive index n_{eff} (both real and imaginary parts) for $n = 1$. 93

4.3 Transmittance characteristics for initial structure 96
4.4 Modified structure with baffles. 97
4.5 Transmittance characteristics for modified structure with baffles 97
4.6 Modified structure with single nanorod. 98
4.7 Transmittance characteristics for modified structure with single nanorod . . 98
4.8 Modified structure with multiple nanorods. 99
4.9 Transmittance characteristics for modified structure with multiple nanorods 99
4.10 Electric field distribution (V/m), a. λ = 1594.67 nm, single nanorod b. λ = 1787.32 nm, single nanorod c. λ = 2854.74 nm, single nanorod and d. λ = 1657.18 nm, multiple nanorods e. λ = 1832.07 nm, multiple nanorods f. λ = 3250.92 nm, multiple nanorods. 100
4.11 (a-c) Transmittance characteristics for different values of L and (d-g) shows resonant wavelength relation with refractive index. 100
4.12 (a-b) Transmittance characteristics for different values of w_1 and (c-f) shows resonant wavelength relation with refractive index. 101
4.13 (a-c) Transmittance characteristics for different values of w_2 and (d-g) shows resonant wavelength relation with refractive index. 102
4.14 (a-b) Transmittance characteristics for different values of g_1 and (c-f) shows resonant wavelength relation with refractive index. 102
4.15 (a-c) Transmittance characteristics for different values of H and (d-g) shows resonant wavelength relation with refractive index. 104
4.16 (a-b) Transmittance characteristics for different values of w_3 and (c-f) shows resonant wavelength relation with refractive index. 104
4.17 (a-b) Transmittance characteristics for different values of ‘a’ and (c-f) shows resonant wavelength relation with refractive index. 105
4.18 (a-b) Transmittance characteristics for different values of ‘b’ and (c-f) shows resonant wavelength relation with refractive index. 106
4.19 (a-b) Transmittance characteristics for different values of ‘r’ and (c-f) shows resonant wavelength relation with refractive index. 106
4.20 Transmittance characteristics different values of refractive index for the optimized structure. 107
4.21 Electric field distribution (V/m) for n = 1 a. resonant wavelength = 1614.92 nm b. resonant wavelength = 1816.45 nm c. resonant wavelength = 2897.41 nm and magnetic field distribution, H_z (A/m) for n = 1 d. resonant wavelength = 1614.92 nm e. resonant wavelength = 1816.45 nm f. resonant wavelength = 2897.41 nm. 108
4.22 Fabrication process of the sensor a. Si Substate b. Spin Resin c. Nanoimprint Lithography d. O_2 Plasma Etching e. Electron-beam Evaporation f. Lift-off 109

4.23 a. Transmittance characteristics for different glucose concentration percentages b. Relationship of resonant wavelength with glucose concentration (C%). 110
4.24 a. Transmittance characteristics for different Hemoglobin concentrations b. Relationship of resonant wavelength with Hb concentration. 112
4.25 Comparison of Transmittance Characteristics between Normal and Cancerous Cells in Various Regions (a. Blood (Jurkat), b. Carnival (Hela), c. Breast (MDA-MB-231), d. Adrenal Gland (PC-12), e. Breast (MCF-7), f. Skin (Basal). 113
4.26 Transmittance characteristics for different components of blood. 114
4.27 Transmittance characteristics for different components of brain. 115
4.28 Transmittance characteristics for different components of intracellular components. 116
4.29 Transmittance characteristics for different types of tissues. 117
4.30 Initial structure of the design. 118
4.31 (a) Transmittance characteristic of our initial design for the initial geometric parameter values at different values of n (b) Resonant wavelength shift with a variation in n. 119
4.32 (a) Transmittance characteristic for diverse values of R (b) Sensitivity values for diverse values of R (c) FOM for diverse values of R. 120
4.33 (a) Transmittance characteristic for diverse values of d (b) Sensitivity values for diverse values of d (c) FOM for diverse values of d. 121
4.34 (a) Transmittance characteristic for diverse values of g (b) Sensitivity values for diverse values of g (c) FOM for diverse values of g. 122
4.35 (a) Transmittance characteristic of our initial design for optimized geometric parameter values at different values of n (b) Normalized magnetic field intensity, $|H_z|$ (A/m) for n = 1 at wavelength = 1147.14 nm (c) Normalized magnetic field intensity, $|H_z|$ (A/m) for n = 1 at wavelength = 1408.52 nm (d) Normalized magnetic field intensity, $|H_z|$ (A/m) for n = 1 at wavelength = 2201.39 nm (e) Normalized magnetic field intensity, $|H_z|$ (A/m) for n = 1 at wavelength = 1660 nm. 124
4.36 (a) Structure of the proposed design with added nanodots (b) Transmittance characteristic for initial design with no nanodots and final design with five added nanodots for n = 1. 125
4.37 (a) Transmittance characteristic for diverse values of r (b) Sensitivity values for diverse values of r (c) FOM for diverse values of r. 126
4.38 Transmittance characteristic for diverse values of θ. 127
4.39 Transmittance curve for different chemical pollutants. 129

4.40 Transmittance curve for different concentrations of heavy metal ion solutions (a) Zn^{2+} (b) Pb^{2+} (c) Hg^{2+}. 130
4.41 Transmittance characteristics for different sugar water concentration percentages. 131
4.42 Transmittance characteristics for different NaCl solution concentration percentages. 132
4.43 Transmittance characteristics for alchohol concentration percentages. 133
4.44 Transmittance characteristics for different water concentration percentages in heavy oil. 134
4.45 Transmittance characteristic for different alchohol. 135
4.46 Structure of The Proposed Design. 136
4.47 Transmittance characteristics of the optimized design for different values of the refractive index of the dielectric material. 137
4.48 (a) Transmittance characteristics (b) Resonant wavelength and (c) Sensitivity for different values of length of the arm of octagon L. 138
4.49 (a) Transmittance characteristics (b) Resonant wavelength λ_{res} and (c) Sensitivity for different values of distance between the square and inner octagon cavity t. 139
4.50 (a) Transmittance characteristics (b) Resonant wavelength λ_{res} and (c) Sensitivity for different values of radius of nanodots r. 140
4.51 (a) Transmittance characteristics (b) Resonant wavelength λ_{res} and (c) Sensitivity for different values of width of the slits g_2. 141
4.52 a. Transmittance characteristics of mode 1 for different slit configurations. b. Transmittance characteristics of mode 2 for different slit configurations. c. Magnetic Field Distribution (A/m) for Up and Left slit configuration. d. Magnetic Field Distribution (A/m) for Up and Right slit configuration. e. Magnetic Field Distribution (A/m) for Down and Left slit configuration. f. Magnetic Field Distribution (A/m) for Down and Right slit configuration. . 142
4.53 (a) Transmittance characteristics for different percentages of water, (b) Relationship between resonant wavelength and different percentages of water. . 144
4.54 (a) Transmittance characteristics for different percentages of Lactose, (b) Relationship between resonant wavelength and different percentages of water. 145
4.55 Transmittance characteristics for different percentages of fat in milk. 146
4.56 Transmittance characteristics for different percentages of sucrose. 147
4.57 Transmittance characteristics for different percentages of Glucose. 148

5.1 Optimization of RI sensor using machine learning. 151

List of Tables

2.1 Comparison of Performance Metrics for Recent MIM-Based Plasmonic Refractive Index Sensors . . . 25
2.2 . . . 26
2.3 . . . 27
2.4 . . . 28
2.5 . . . 29

4.1 Geometric properties of the resonator at the initial stage. . . . 92
4.2 Lorentz-Drude parameters for Silver (Ag). . . . 95
4.3 Final geometric parameters of the structure. . . . 107
4.4 Comparison of the sensing performance of the proposed sensor and recent literature. . . . 108
4.5 Primary diagnosis of Diabetes. . . . 111
4.6 Primary classification of Anemia . . . 112
4.7 Detection of cancer affected cell . . . 114
4.8 Various components of blood. . . . 114
4.9 Various components of brain. . . . 115
4.10 Various intracellular components. . . . 115
4.11 Various types of tissues. . . . 116
4.12 Initial values of the geometric parameters. . . . 117
4.13 Optimized values of the geometric parameters. . . . 128
4.14 Comparison with recently proposed sensors . . . 128
4.15 Refractive index and resonant wavelength of different chemical pollutants. . 129
4.16 Refractive index and resonant wavelength of different concentrations of heavy metal ion solutions. . . . 130
4.17 Resonant wavelength for different concentration of sugar water. . . . 131
4.18 Resonant wavelength for different concentration of NaCl solution. . . . 132
4.19 Resonant wavelength for different concentration of alchohol. . . . 133
4.20 Resonant wavelength for different concentration of water in heavy oil. . . . 134
4.21 Refractive index and resonant wavelength of different types of alchohol. . . 135
4.22 Initial parameter values of the 2-D geometric structure . . . 136

4.23 Optimal parameter values of the 2-D geometric structure 143
4.24 Comparison of the sensitivity with previously published MIM structured refractive index sensor designs 143
4.25 Measurement of Water Percentage in Honey Sample 144
4.26 Measurement of Lactose Concentration in Lactose Solution 145
4.27 Measurement of Fat Percentage in Milk. 146
4.28 Measurement of Sucrose Percentage in Solution. 147
4.29 Measurement of Glucose Percentage in Solution. 148

List of Abbreviations

AFM	Atomic Force Microscopy
ALD	Atomic Layer Deposition
DLSPP	Dielectric-Loaded Surface Plasmon Polariton
EBL	Electron Beam Lithography
EM	Electro-Magnetic
ER	Excitation Ratio
FEM	Finite Element Method
FIB	Focused Ion Beam
FOM	Figure of Merit
FWHM	Full Width at Half Maximum
IMI	Insulator-Metal-Insulator
LRSP	Long Range Surface Plasmons
LSPR	Localized Surface Plasmon Resonance
MBE	Molecular Beam Epitaxy
MIM	Metal-Insulator-Metal
NIL	Nano-Imprint Lithography
PDE	Partial Differential Equation
Q-factor	Quality Factor
RBC	Red Blood Cells
RIE	Reactive Ion Etching
RI	Refractive Index
SEM	Scanning Electron Microscopy
SERS	Surface-Enhanced Raman Scattering
SPP	Surface Plasmon Polariton
SR	Sensing Resolution
TEM	Transverse Electromagnetic
TE	Transverse Electric
TMN	Transition Metal Nitrides
TM	Transverse Magnetic

Abstract

This research provides an overview of the design, fabrication, and applications of plasmonic nanosensors, highlighting their unique capabilities in detecting and analyzing molecular interactions at the nanoscale. A plasmonic refractive index nanosensor is a device that utilizes the interaction of light with metallic nanoparticles to detect and quantify changes in the refractive index of the surrounding medium, enabling highly sensitive and label-free detection of various analytes. They use surface plasmon polariton (SPP) and as per light-matter interaction, they provide optical response depending on the quantity to be sensed. In this paper, three plasmonic refractive index sensor designs are proposed. The sensors have been evaluated with the finite element method (FEM) with scattering boundary conditions. The theoretical background of the functionalities and properties of plasmonic materials is explained. A plasmonic refractive index nanosensor with a modified rectangular resonator with baffles and nanorod has been proposed and it exhibits maximum sensitivity of 2963.73 nm/RIU and FOM of 25.1. Another plasmonic nanosensor design with an opposing-face-semi-circular ring resonator integrated with nanorods has been proposed and it exhibits maximum sensitivity of 2975.96 nm/RIU and the recorded maximum FOM is 43.95. Lastly, another novel plasmonic nanosensor design with a modified octagonal resonator embedded with silver nanorods is proposed and as per the numerical investigation, it exhibits maximum sensitivity of 2527.6 nm/RIU with a corresponding FOM value of 16.24. The linear relationship of resonant wavelength with the refractive index has been used in advantage to detect unknown materials. Thus the application of these nanosensor designs in the medical and healthcare sectors e.g. diabetes detection, anemia detection, and classification of cancer cells are investigated. Furthermore, the application of nanosensors in the environment and safety applications are explored by the detection of chemical pollutants and heavy metals in water. The potential application in the food industry has also been explored by testing the capabilities of detecting water adulteration in honey and lactose detection in solutions. The wide range of applications of plasmonic nanosensors and their fabrication process are elaborately discussed.

Chapter 1

Introduction and Background

FROM the early stage of science and innovation, humans have been putting efforts into understanding the laws of nature. The phenomena of nature and attributes of objects or events are great topics of study for humans. In order to comprehend these events through a quantitative study, humans have been developing ways of measuring. It is a commonly practiced way of assigning numerical values to physical quantities in order to understand their dimensions, properties, or even changes. Ever since the use of measurement in studies, it has become an integral part of scientific research, engineering, and commercial activities. It is broadened the way of understanding everything around us.

Measurement plays a crucial role in optics, a branch of physics that deals with the behavior and properties of light. Accurate and precise measurements are essential for understanding and characterizing optical phenomena, designing optical systems, and ensuring their optimal performance. In optics, measurements are used to determine parameters such as wavelength, intensity, polarization, phase, and angle of light waves. These measurements enable the evaluation and calibration of optical instruments, the characterization of optical materials, and the analysis of optical components and systems. With precise measurements, scientists and engineers can design and optimize optical devices, such as lenses, mirrors, cameras, and lasers, to achieve desired outcomes in fields ranging from telecommunications and imaging to astronomy and microscopy. Furthermore, measurement in optics also facilitates the verification of theoretical models, the validation of experimental results, and the advancement of knowledge in this intricate field of study.

In the context of measurement, a sensor is a device that detects and measures physical or environmental changes and converts them into measurable signals. In optics, sensors play a crucial role in capturing and quantifying optical phenomena. Optical sensors are specifically designed to detect parameters such as refractive index, light intensity, wavelength, polarization, and phase. They enable precise measurements and characterization of light waves, aiding in the design, calibration, and optimization of optical systems. By providing accurate

data on optical properties, sensors facilitate advancements in fields like telecommunications, imaging, astronomy, and microscopy. They contribute to the validation of theoretical models, experimental verification, and overall progress in understanding and harnessing light-based technologies.

1.1 Optics and Nanophotonics

Light is an electromagnetic radiation that is composed of photons. The photons carry energy and travel in a periodic pattern. Like other waves, light has wavelength, frequency, and amplitude. Light has a wide range of electromagnetic spectrum which has a visible and invisible spectrum. Optics is a branch of physics that studies the properties and behaviors of light. It also studies the interaction of light with other objects. It investigates the phenomena of reflection, refraction, diffraction, polarization, and other phenomena manifested by lights. Optics also studies the instruments used to observe and measure the phenomena manifested by light.

Nanophotonics is a specialized branch of optics. It studies the properties of light at the nanometer scale. At the nanometer scale, the laws of physics are different and they require more specialized research and investigation. It involves the interaction of light with nanostructures, which are structures with dimensions typically on the order of nanometers (one billionth of a meter). Nanophotonics combines principles from both nanotechnology and optics to explore and control light at these small scales. At the nanoscale, light exhibits several interesting and unique properties due to its interaction with nanostructures. Some of these properties include:

- **Enhanced Light-Matter Interaction**: In the realm of nanoscience and nanotechnology, the interaction between light and nanoscale structures has garnered significant attention due to its remarkable properties and potential applications. When light interacts with structures at the nanoscale, it can be strongly confined, leading to a range of enhanced optical phenomena. One of the key effects observed is enhanced absorption. Nanoscale structures can effectively capture and absorb light across a broad spectrum of wavelengths. This enhanced absorption is attributed to the interaction of light with the nanoscale structure's geometry and material properties, which can manipulate the behavior of light waves. This phenomenon has found applications in various fields, such as solar energy harvesting, where nanoscale structures are employed to increase the efficiency of light absorption and conversion into electricity. In addition to absorption, scattering of light can also be significantly influenced by nanoscale structures. When light encounters these structures, it scatters in a manner that is different from what occurs with larger-scale objects. Nanoscale structures can scatter light in specific directions or manipulate its polarization, enabling precise control over the scattering

properties. This ability to tailor light scattering at the nanoscale has implications for various applications, including optical data storage, imaging, and display technologies. Furthermore, nanoscale structures can also influence the emission of light. In some cases, the confinement of light within nanostructures can enhance the emission of light, resulting in more efficient light-emitting devices. This property is exploited in technologies such as light-emitting diodes (LEDs), where nanoscale structures are used to improve the efficiency and color purity of emitted light. Moreover, the interaction of light with nanoscale structures can also enable novel approaches to manipulate and control the emission characteristics, leading to advancements in areas like quantum optics and nanophotonics. The enhanced interaction of light with nanoscale structures opens up opportunities for efficient energy transfer, sensing, and manipulation of light at the nanoscale. For instance, nanoscale antennas can efficiently couple light into nanoscale devices, facilitating energy transfer processes such as photovoltaics, photocatalysis, and light-driven chemical reactions. Nanosensors can exploit the enhanced interaction to detect and analyze substances with high sensitivity, enabling applications in areas like biomedical diagnostics, environmental monitoring, and food safety. Additionally, by designing and engineering nanoscale structures, researchers can manipulate light at unprecedented scales, leading to advancements in fields such as optical computing, optical data storage, and telecommunications.

- **Localized Surface Plasmon Resonance**: Metallic nanoparticles, when reduced to the nanoscale, possess unique optical properties due to a phenomenon called localized surface plasmon resonance (LSPR). LSPR refers to the collective oscillation of free electrons on the surface of the nanoparticle in response to incident light. This interaction between light and electrons in the nanoparticle leads to fascinating optical effects and enhanced light-matter interactions. LSPR occurs because the collective oscillation of electrons on the surface of the nanoparticle generates a resonant electromagnetic field, known as a plasmon. The plasmon's frequency depends on the size, shape, and composition of the nanoparticle, as well as the dielectric properties of its surrounding medium. This means that by controlling these parameters, it is possible to tune the plasmon resonance to specific wavelengths of light. When the frequency of the incident light matches the plasmon resonance frequency of the nanoparticle, a strong coupling occurs, resulting in enhanced light scattering and absorption. The oscillation of electrons near the surface of the nanoparticle amplifies the electromagnetic field at the nanoparticle's vicinity, thereby enhancing the interaction with light. As a result, the optical properties of the nanoparticle, such as its scattering and absorption coefficients, become significantly enhanced. The ability to control and manipulate LSPR has led to a wide range of applications in various fields. In sensing applications, metallic nanoparticles are often used as nanosensors to detect and quan-

tify specific molecules or analytes. When these nanoparticles are functionalized with specific ligands or receptors, they can selectively bind to target molecules. When the target molecules bind to the nanoparticle surface, it causes a shift in the LSPR wavelength, which can be detected and measured. This enables highly sensitive and specific detection of substances, with applications in fields like medical diagnostics, environmental monitoring, and food safety. In spectroscopy, LSPR enables improved analysis and characterization of materials. By utilizing the enhanced light-matter interactions of metallic nanoparticles, researchers can study the optical properties of various substances with high sensitivity and resolution. This has implications in fields such as chemistry, materials science, and biophysics, where understanding the behavior of materials at the nanoscale is crucial. Optical imaging is another area where LSPR finds utility. Metallic nanoparticles with tunable LSPR properties can act as contrast agents in imaging techniques such as dark-field microscopy, surface-enhanced Raman scattering (SERS), and photoacoustic imaging. These nanoparticles can selectively accumulate in specific regions or target molecules of interest, providing enhanced signal intensity and improved imaging sensitivity.

- **Subwavelength Light Confinement**: Nanostructures refer to materials or devices that have dimensions on the nanoscale, typically ranging from a few nanometers to a few hundred nanometers. They possess unique properties and behaviors that are distinct from their bulk counterparts due to their small size and quantum effects.

  One of the remarkable capabilities of nanostructures is their ability to confine light to dimensions smaller than the wavelength of light. This phenomenon is known as subwavelength confinement. Traditional optical components and devices rely on the manipulation of light using elements with dimensions comparable to the wavelength of light, typically in the range of a few hundred nanometers to several micrometers. However, by utilizing nanostructures, it becomes possible to achieve confinement of light at dimensions smaller than the wavelength.

  Three common types of nanostructures that can enable subwavelength confinement of light are nanowires, nanospheres, and nanoscale waveguides.

  Nanowires: These are nanoscale structures with high aspect ratios, typically elongated in one dimension. Due to their small size, they can effectively guide and confine light along their length. Nanowires made from different materials can exhibit various optical properties, such as enhanced light-matter interactions, strong light confinement, and efficient light propagation.

  Nanospheres: Nanospheres are tiny spherical particles with diameters in the nanometer range. When the size of the nanosphere is comparable to or smaller than the wavelength of light, it can interact with light in unique ways. Nanospheres can scatter and

manipulate light, and they have applications in areas such as sensing, imaging, and optoelectronic devices.

Nanoscale Waveguides: These are waveguides or channels with dimensions at the nanoscale. They are designed to guide and control the flow of light at subwavelength scales. Nanoscale waveguides can be engineered using various materials, including semiconductors, metals, or dielectrics. They enable the confinement and manipulation of light for applications in nanophotonics, such as on-chip optical communication and signal processing.

The ability to confine light at subwavelength scales using nanostructures opens up exciting possibilities for various applications:

- **Miniaturization of Optical Components:** By confining light to dimensions smaller than the wavelength, it becomes possible to create compact and miniaturized optical components. This is particularly useful in the development of integrated photonic circuits, where multiple optical functions can be integrated on a single chip, leading to improved performance and reduced size.
- **High-Resolution Imaging:** Subwavelength confinement of light enables the development of high-resolution imaging techniques. By using nanoscale structures to focus light, it becomes possible to surpass the diffraction limit, which restricts the resolution of traditional optical systems. This allows for detailed imaging of nanostructures, biological samples, and other objects at the nanoscale.
- **Nanophotonic Circuits:** Nanostructures can be combined to create nanophotonic circuits, which are analogous to electronic circuits but operate using light instead of electrons. These circuits can perform functions such as signal modulation, routing, and detection at the nanoscale. Nanophotonic circuits hold promise for applications in optical computing, quantum information processing, and high-speed data communication.

- **Photonic Bandgap Effects**: One fascinating property of nanostructures is their ability to exhibit photonic bandgap effects. In physics, a bandgap refers to a range of energies or wavelengths where certain states or frequencies of a wave are forbidden. In the case of nanostructures, particularly those designed to interact with light, the concept of a photonic bandgap arises. It refers to a range of wavelengths or colors of light that are prohibited from propagating through the structure.

  By carefully engineering the size, shape, and arrangement of nanostructures, researchers can create a periodic arrangement of high and low refractive index regions within a material. This periodicity gives rise to a photonic bandgap, where certain wavelengths of light cannot propagate through the material. This effect is similar to the bandgap found

in electronic materials, where certain energy levels are forbidden for electrons. The existence of photonic bandgaps in nanostructures enables precise control over the propagation of light, allowing for the development of various photonic crystals and devices with specific optical filtering and guiding properties. Photonic crystals are materials or structures that possess a periodic variation in refractive index, which gives rise to a photonic bandgap. These crystals can be designed to control the behavior of light in specific ways. For example, they can be engineered to allow only certain wavelengths of light to pass through while blocking others. This selective filtering of light is useful in applications such as optical communications, where it is necessary to transmit specific wavelengths of light while rejecting unwanted signals. In addition to filtering properties, photonic crystals can also guide and manipulate light. By introducing defects or irregularities into the crystal lattice, researchers can create waveguides and optical cavities that confine and direct light within the structure. These properties are valuable for developing photonic integrated circuits, sensors, lasers, and other devices that rely on precise control of light.

Overall, the ability of nanostructures to exhibit photonic bandgap effects opens up a wide range of possibilities for manipulating light at the nanoscale. This field of research holds promise for applications in areas such as telecommunications, optical computing, solar energy, sensing, and beyond, where the control and manipulation of light are crucial for advancing technology.

- **Nonlinear Optical Effects**: At the nanoscale, the behavior of light starts to exhibit nonlinear optical effects with greater prominence. This is primarily due to the increased intensity of light and the unique properties of nanomaterials. Nonlinear optical effects refer to the phenomena that occur when the response of a material to light is nonlinearly related to the incident light intensity. These effects can be utilized and manipulated for various applications in the field of nonlinear optics.

  One example of a nonlinear optical effect is harmonic generation. In this process, when intense light interacts with a nonlinear material, it generates new light frequencies that are integer multiples (harmonics) of the original frequency. For instance, if the incident light has a frequency of ω, harmonic generation can produce light with frequencies like 2ω, 3ω, and so on. This effect enables the generation of coherent light at frequencies that are not directly provided by the light source. It finds applications in areas such as laser systems, spectroscopy, and telecommunications. Frequency mixing is another nonlinear optical effect. It involves the interaction of two or more light waves with different frequencies, resulting in the generation of new frequencies that are the sum or difference of the original frequencies. This process is commonly used in frequency conversion applications. For example, it can be employed to convert light from one wavelength to another, which is crucial for optical communication systems

or for obtaining specific wavelengths required for certain experiments.

Nonlinear scattering is a phenomenon where the interaction of light with a nonlinear material leads to the scattering of light at different frequencies. It can result in various phenomena, such as stimulated Raman scattering and four-wave mixing. Nonlinear scattering processes have significant implications in all-optical signal processing, where information is manipulated using only optical signals, without the need for conversion to electronic signals. This field holds promise for applications in optical computing, optical data storage, and high-speed signal processing. At the nanoscale, the enhanced intensity of light and the unique properties of nanomaterials, such as their strong light-matter interactions and size-dependent properties, provide opportunities to exploit nonlinear optical effects further. Nanomaterials can be engineered to exhibit enhanced nonlinear responses, making them ideal candidates for applications in nonlinear optics, frequency conversion, and all-optical signal processing. Their small size allows for efficient light confinement and control, enabling the manipulation of light at the nanoscale.

The special characteristics of nanophotonic structures offer more exciting and promising prospects in the field of nanotechnology and material engineering. They offer the possibilities of ultra-compact circuit design, high-resolution sensors, and high-speed computation technologies.

1.2 Plasmonics

Plasmonics is the study of the detection, generation, and manipulation of optical signals at the optical frequency on the nanometer scale [1]. Plasmonics, a rapidly growing interdisciplinary field, focuses on the detection, generation, and manipulation of optical signals at the nanometer scale using the phenomenon of plasmons. Plasmons are collective oscillations of electrons in the metal-dielectric interface that can be excited by external stimuli. This field combines concepts from optics and nanotechnology to achieve enhanced control over light-matter interactions, light confinement, and various optical phenomena. The foundation of plasmonics lies in the interaction between light and free electrons in metallic nanostructures. When light interacts with these structures, it can induce a collective oscillation of electrons known as a plasmon. This plasmon oscillation creates a localized electromagnetic field at the metal-dielectric interface, leading to the confinement of light within nanoscale dimensions. This confinement allows for the manipulation and control of light at the subwavelength level, opening up exciting possibilities for numerous applications.

One of the primary advantages of plasmonics is its ability to enhance light-matter interactions. The intense electromagnetic fields associated with plasmons enable enhanced light

absorption and scattering by nanostructures. By engineering the shape, size, and composition of these structures, researchers can tailor their plasmonic properties to achieve desired optical effects. This enhanced light-matter interaction is beneficial in a wide range of applications, including sensing, spectroscopy, and solar energy conversion. Plasmonics also provides a unique platform for the localization of light. Through the excitation of surface plasmons, light can be trapped and confined within nanoscale regions, surpassing the diffraction limit of conventional optics. This property is particularly valuable in the development of nanophotonic devices, such as waveguides, sensors, and light-emitting diodes, where the ability to confine and manipulate light on the nanoscale is crucial. Moreover, plasmonic structures can exhibit extraordinary optical phenomena, such as surface-enhanced Raman scattering (SERS) [2] and plasmon-enhanced fluorescence. SERS enables highly sensitive molecular detection by enhancing the Raman scattering signal of molecules in close proximity to plasmonic nanostructures. This technique has significant implications for chemical and biological sensing, as it allows for the detection of trace amounts of substances. Plasmon-enhanced fluorescence, on the other hand, enhances the emission of fluorophores placed near plasmonic structures, leading to improved sensitivity in fluorescence-based assays and imaging techniques. In addition to these applications, plasmonics also finds utility in the field of nanophotonics. The ability to manipulate and control light at the nanoscale enables the development of compact and efficient photonic devices. Plasmonic waveguides, for instance, can guide light along subwavelength paths, facilitating the integration of optical components on a chip. This miniaturization and integration of optical elements are crucial for advancing technologies such as optical computing, data storage, and telecommunications. Researchers in plasmonics continue to explore new materials and fabrication techniques to improve the efficiency and functionality of plasmonic devices. Materials with unique plasmonic properties, including noble metals like gold and silver, as well as alternative materials such as graphene, are being investigated. Advanced fabrication methods, such as electron beam lithography and self-assembly techniques, enable precise control over the size, shape, and arrangement of plasmonic nanostructures.

1.3 Surface Plasmon Polariton

Surface plasmon polariton (SPP) is a coupled electromagnetic oscillation of photons and electrons. Transverse magnetic polarized light interacting with the metal-dielectric interface induces SPP under specific conditions. The existence of surface plasmon was first predicted by Rufus Ritchie in 1957 [3]. When an optical excitation is given in a metal-dielectric-composed object, the electromagnetic wave propagates inside both the mediums and in the metal-dielectric interface, and a surface wave is generated shown in Fig 1.1 [4]. SPP is generated when the momentum of the incident light matches the momentum of SPP mode [5]. The momentum can be matched using prism couplers [6–9], grating couplers [6–9], fiber

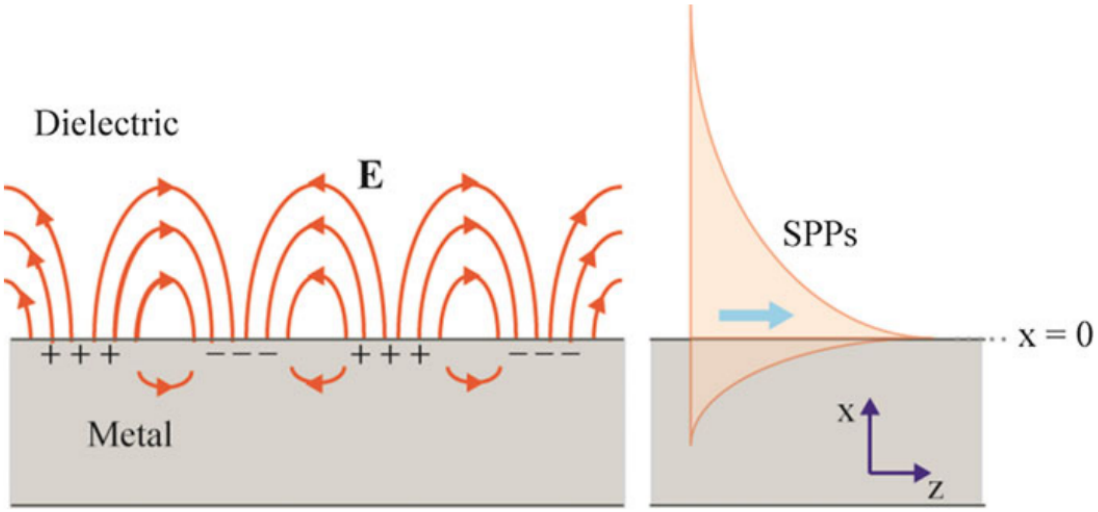

Figure 1.1: Propagation of SPP in Metal-Dielectric Interface.

and waveguide couplers [10–13]. Plasmonic devices work on the principle of SPP wave propagation, which is electromagnetic wave propagation along a metal-dielectric interface because these waves have far shorter wavelengths than regular light waves, they can interact with materials at the nanoscale [14]. Plasmonic devices, as a result, provide high-speed data transmission and processing capabilities, as well as improved bandwidth [15]. One of the most important properties of SPPs is their ability to overcome the diffraction limit [16], which is the physical limit that restricts the resolution of conventional optical devices. This means that SPPs can confine light in subwavelength dimensions, allowing for the development of nanoscale plasmonic devices with unprecedented performance [16, 17]. This wave's penetration depth is more extensive in the dielectric medium, which typically exceeds 100 nm, in contrast, the penetration depth for metals is generally less than 10 nm [18]. In addition, SPPs have been extensively used in sensing applications, such as biosensors, where they can detect small changes in the refractive index of the surrounding medium. This is possible because the amplitude of the SPP surface wave is extremely sensitive to changes in the local environment, such as the binding of a biomolecule to the sensor surface [19]. This property makes plasmonic sensors highly sensitive and selective, with potential applications in various fields, including medical diagnosis and environmental monitoring. In addition, the distinctive characteristics of SPPs make them suitable for the development of nanophotonic devices, in which light may be modulated at the nanoscale.

These SPPs are transverse magnetic (TM) plane waves that propagate along the interface of the two materials [20]. The dielectric constant of the dielectric and metal half-spaces are represented by ε_d and ε_m, respectively. In this configuration, SPPs can be described as a wave vector k that is related to the optical frequency through a dispersion relation [21],

$$k_x = k_0 \times \sqrt{\frac{\epsilon_d \times \epsilon_m}{\epsilon_d + \epsilon_m}} \tag{1.1}$$

where, k_0 is the wave-vector of free space. Assuming that the interface between the two materials is perpendicular to the z-axis and that the SPPs propagate along the x-axis, the dispersion relation describes the relationship between the wave vector k and the frequency of the light [22]. This relationship is crucial for understanding the characteristics of plasmonic devices and is key to the behavior of SPPs. The dispersion relation may be used to compute key parameters for SPPs such as propagation length, phase velocity, and group velocity. The propagation length describes how far the SPPs can propagate along the interface before they decay due to energy loss. The phase velocity is the velocity at which the SPP wavefronts propagate, while the group velocity is the velocity at which the energy of the wave packet propagates. Understanding the dispersion relation and these important parameters is crucial for the design and optimization of plasmonic devices, as it allows for the calculation of the optimal configuration and materials to use in a given application.

One of the major limiting factors of optical devices is the diffraction limit. It is the limitation of optical resolution due to diffraction and it is proportional to the wavelength of the light being observed. [23]. However, the unique properties of SPP can come in handy in this scenario. Surface plasmon polariton is a surface wave, an electromagnetic wave that propagates in the interface of two mediums. The excitation of SPP leads to strong electromagnetic field confinement and results in shorter wavelengths compared to light. And so, they are able to overcome the diffraction limit [16]. Thus, SPP can have localized field intensity and higher momentum. A shorter wavelength allows SPP to be confined in subwavelength devices such as nanosensors [17]. In addition, SPP is sensitive to changes in the environment [24]. It can detect the change of physical parameters such as temperature, and pressure and detect the presence of unknown molecules. Owing to the unique properties of surface plasmon polariton, many nanoscale devices and applications are possible. The principle of SPP propagation can be used in manufacturing optical waveguides [25–31], sources [29, 32–35], SERS [36–44], near field optics [45–52], data storage [53–56], solar cells [57–60], biosensors [10, 61–73] and chemical sensors.

1.4 Plasmonic Waveguide

The surface plasmon polariton (SPP) mentioned earlier requires guidance in a medium to ensure controlled propagation. A plasmonic waveguide is a nanoscale guiding structure that leverages the interaction between light and SPPs to confine and direct light. Unlike traditional dielectric waveguides that rely on total internal reflection, plasmonic waveguides exploit the high confinement and subwavelength propagation characteristics of SPPs

at metal-dielectric interfaces. These waveguides enable light transmission with nanoscale confinement, increased field intensity, and the potential for powerful light-matter interactions through the support of SPP modes. Plasmonic waveguides have found applications in various fields, including integrated optics, sensing, data transfer, and signal processing. By utilizing these waveguides, highly compact and efficient photonic devices can be created, offering the potential for future technological advancements. In contrast to dielectric waveguides, which guide light through total internal reflection, plasmonic waveguides operate based on the interaction between light and SPPs. SPPs are collective oscillations of electrons that occur at the metal-dielectric interface when excited by incident light. These oscillations couple with the incident light to form a hybridized SPP mode, which travels along the waveguide. The SPP mode is confined to the metal-dielectric interface and propagates with a wavelength much smaller than the free-space wavelength of light. The unique properties of SPPs allow plasmonic waveguides to confine light to nanoscale dimensions. The intense electromagnetic fields associated with SPPs are tightly confined within the waveguide, enabling the transmission of light at subwavelength scales. This subwavelength confinement is particularly advantageous for miniaturizing photonic components and achieving high device integration densities. Furthermore, the strong field confinement in plasmonic waveguides leads to increased field intensity, enhancing light-matter interactions. This characteristic is beneficial for various applications, such as sensing and spectroscopy, where the interaction of light with nanoscale objects or molecules is of interest. Plasmonic waveguides have demonstrated their potential in integrated optics, where they enable the routing and manipulation of light on chip-scale platforms. The subwavelength confinement and strong field localization facilitate the design and fabrication of highly compact photonic circuits with improved performance. Additionally, plasmonic waveguides have been employed in sensing applications. The high sensitivity of SPPs to changes in the refractive index of the surrounding medium allows for ultrasensitive detection of biological and chemical substances. By utilizing the evanescent field of the SPP mode, plasmonic waveguides can interact with analytes present in the surrounding medium, enabling label-free detection with high sensitivity. Moreover, plasmonic waveguides have been explored for data transfer and signal processing. The ability to confine light to nanoscale dimensions and guide it with low loss enables the development of high-speed and compact photonic interconnects for on-chip communication. The subwavelength confinement of plasmonic waveguides also offers the potential for enhancing nonlinear optical effects and all-optical signal processing, which can significantly impact optical computing and data processing technologies

1.4.1 MIM Waveguide

Metal insulator metal (MIM) waveguide is a highly popular waveguide system in the field of nanosensor designs. This waveguide configuration consists of a dielectric medium sand-

wiched between two metal layers, allowing for the guidance of surface plasmon polariton (SPP) waves along the metal-dielectric interface. The top view of MIM waveguide configuration is shown in Fig. 1.2.

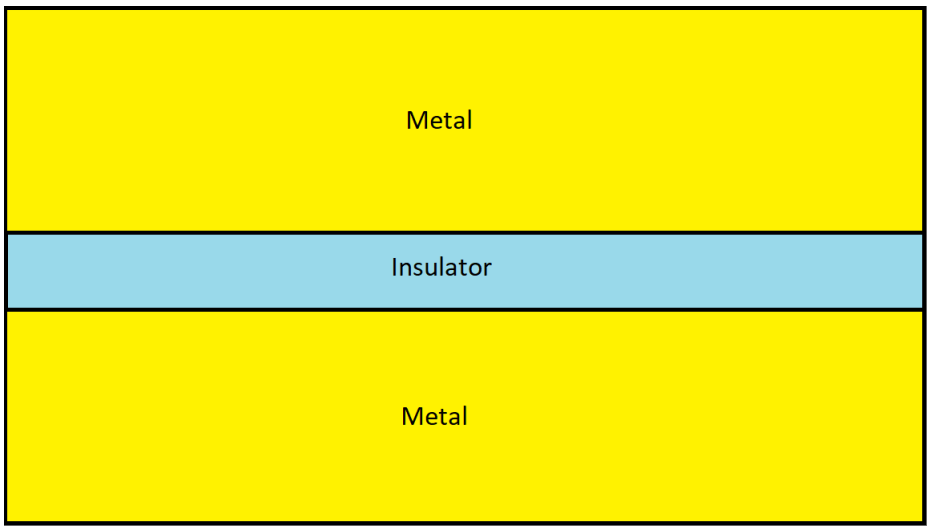

Figure 1.2: Configuration of MIM waveguide configuration.

The MIM waveguide possesses remarkable properties, including strong electromagnetic field confinement, low propagation loss, effective interference, and straightforward fabrication, making it an ideal choice for nanosensor applications [74–76]. The dispersion, propagation length, and mode confinement of MIM waveguides depend on the selection of metals and dielectric materials employed in their construction. As a result, MIM waveguides find extensive usage in various fields, including optical communications, medical imaging, biosensors, and quantum computing. The primary advantage of the MIM waveguide lies in its exceptional confinement ability, as the insulating layer restricts the propagation of electromagnetic waves to a confined region. This confinement results in improved signal integrity and interaction with surrounding materials, which is particularly advantageous in applications that require precise control over optical properties, such as integrated photonics and optical sensing. However, it is important to note that the MIM waveguide does have certain limitations. One such limitation is its relatively shorter propagation length compared to other waveguide topologies. The propagation length refers to the distance a guided wave can travel before experiencing significant attenuation. Despite this limitation, the MIM waveguide exhibits lower propagation loss, indicating that guided signals encounter minimal attenuation and result in improved signal quality with reduced transmission losses. This characteristic makes the MIM waveguide an attractive option for the production of photonic devices. The lower propagation loss of the MIM waveguide has garnered significant interest from both researchers and industry professionals alike. The ability to fabricate photonic devices using MIM structures facilitates the development of efficient and high-performing devices. Consequently, there is a growing emphasis on research in the field of hybrid waveguides, aimed at further enhancing their properties and optimizing performance. Ongoing investigations

explore various aspects, including the utilization of new materials, design modifications, and fabrication techniques. These efforts aim to advance the field of optics and enable the development of efficient and versatile devices for applications in telecommunications, data transmission, sensing, and more. Overall, MIM waveguide is a widely employed waveguide system in nanosensor designs. The MIM waveguide has found applications in optical communications, medical imaging, biosensors, and quantum computing. Its exceptional confinement ability, despite the relatively shorter propagation length, makes it an attractive choice for integrated photonics and optical sensing applications. Ongoing research into hybrid waveguides seeks to further optimize their properties and performance, focusing on materials, design, and fabrication techniques to enable the development of efficient and versatile photonic devices for various fields and industries.

1.4.2 IMI Waveguide

The Insulator Metal Insulator (IMI) waveguide presents a fascinating arrangement of waveguides that employs a metal layer positioned between two layers of dielectric material. This unique configuration gives rise to intriguing properties and applications. Notably, the IMI waveguide is capable of supporting long-range Surface Plasmon Polariton (SPP) waves, also referred to as Long Range Surface Plasmons (LRSP) [77]. These LRSP waves exhibit a remarkable ability to propagate over significant distances, making the IMI waveguide an ideal choice for designing nanodevices that require extensive wave coverage. To visualize the structure of the IMI waveguide, we can refer to Figure 1.3, which illustrates the top view. The metal layer is positioned between the two layers of dielectric material, forming a sandwich-like configuration. This arrangement imparts distinct characteristics to the waveguide, differentiating it from the Metal Insulator Metal (MIM) waveguide topology. One of the key advantages of the IMI waveguide topology is its ability to generate plasmons with an exceptionally long propagation length. The plasmons, excited by incident light, can traverse the waveguide over extended distances without significant attenuation or loss of energy. This property is particularly advantageous for optical devices that operate on large spatial scales, where the transmission of waves over long distances is crucial. The distribution of field lines within the IMI waveguide structure contributes to its enhanced propagation capabilities. The interaction between the electromagnetic waves and the metal-insulator interfaces leads to a reduced attenuation of the waves, allowing for efficient transmission. As a result, the IMI waveguide demonstrates superior propagation characteristics compared to other waveguide configurations. However, despite its remarkable ability to support long-range wave propagation, the IMI waveguide structure faces limitations when it comes to confining electromagnetic waves. In terms of confinement ability, the IMI topology falls short in comparison to the MIM waveguide. This limitation can significantly impact the sensitivity and performance of devices based on the IMI waveguide. The reduced confinement restricts the effective inter-

action between the guided wave and the surrounding materials, potentially compromising the device's overall sensitivity and efficiency. In practical applications, the choice between the MIM and IMI waveguide topologies depends on the specific requirements and objectives of the designer or researcher. If confinement ability is of utmost importance, the MIM waveguide proves to be a more suitable option. On the other hand, if the transmission of waves over extended distances is a priority, the IMI waveguide's extended propagation length becomes advantageous. Careful evaluation and consideration of these factors are crucial to determine the most appropriate waveguide topology for a given application. Overall, IMI waveguide configuration offers unique properties and advantages. It enables the support of long-range Surface Plasmon Polariton (SPP) waves, making it an excellent choice for nanodevices that require extensive wave coverage. However, the IMI waveguide's limited confinement ability poses challenges in creating highly sensitive structures. The selection between the MIM and IMI waveguide topologies depends on the specific requirements and priorities of the intended application, with designers and researchers carefully assessing their objectives to choose the most suitable waveguide topology.

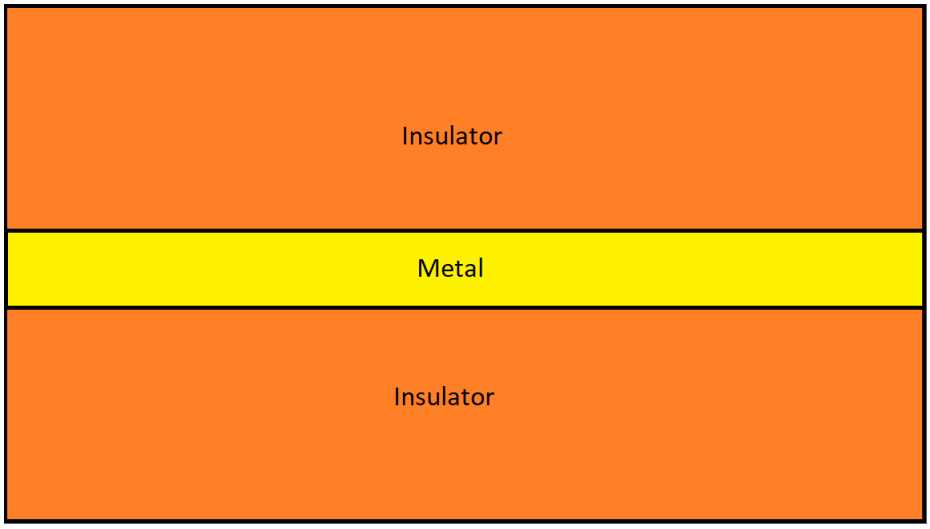

Figure 1.3: Configuration of IMI waveguide.

1.4.3 DLSPP Waveguide

The Dielectric-loaded surface plasmon polariton (DLSPP) waveguides are a unique type of waveguide configuration that combines dielectric and metallic elements to guide surface plasmon polariton (SPP) waves. These waveguides have been experimentally demonstrated, as reported in the study by Steinberger et al. [78]. They offer several advantages and are particularly useful in the near-infrared regions. The DLSPP waveguide consists of a metallic surface, typically made of materials like gold or silver, with a dielectric stripe embedded on it. The dielectric stripe serves as a guiding structure for the SPP waves, confining and directing their propagation. This configuration allows for the efficient guiding of SPP waves

along the surface of the metallic structure.

One important characteristic of the DLSPP waveguide is its figure of merit (FOM), which determines its performance and suitability for specific applications. The FOM of a waveguide is a measure of the balance between the propagation length and the mode confinement. In the case of thin dielectric loads, the DLSPP waveguide exhibits a high FOM. This means that it enables long propagation lengths for the SPP mode in the near-infrared regions. This property is desirable for applications requiring the efficient transmission of SPP waves over long distances. On the other hand, when the dielectric load is thick, the decay length of the SPP wave is reduced, sacrificing the mode confinement of the electromagnetic waves. This characteristic makes the DLSPP waveguide suitable for applications that demand large-density plasmonic devices, where high localization and compactness are required. To visualize the structure of a DLSPP waveguide, an isometric view is typically used. Figure 1.4, as presented in the study by Grandidier et al. [79], demonstrates the arrangement and components of a DLSPP waveguide. This representation helps in understanding the spatial configuration and the interaction between the dielectric stripe and the metallic surface. Overall, the DLSPP waveguides are a unique class of waveguide configurations that utilize a dielectric stripe embedded on a metallic surface to guide SPP waves. These waveguides offer advantages such as long propagation lengths in the near-infrared regions for thin dielectric loads and compactness for thick dielectric loads. DLSPP waveguides show great potential for application in integrated photonics [80, 81]. This waveguide-based coupler and splitters are already been experimentally proven [82, 83]. The dielectric material can be doped for active control of SPP mode.

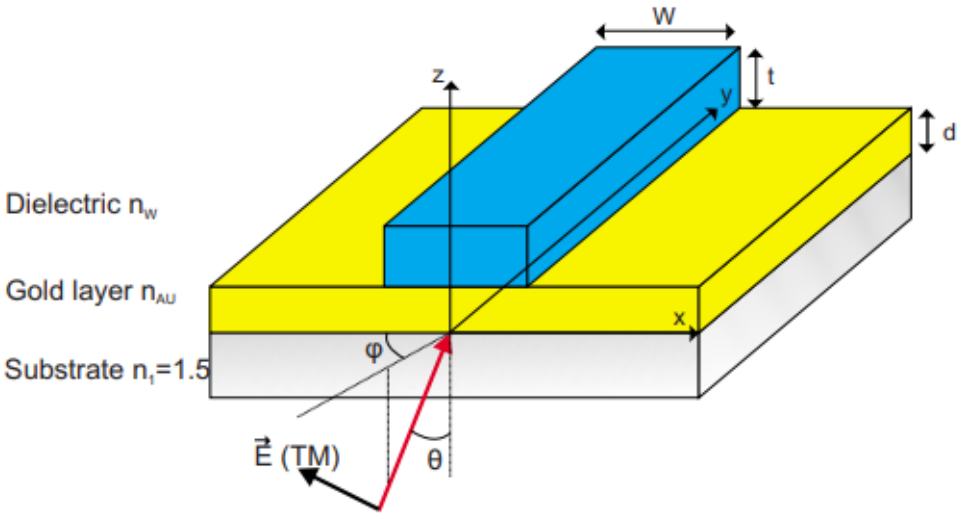

Figure 1.4: Isometric view of DLSPP waveguide.

1.4.4 Slot Waveguide

Slot waveguides are plasmonic structures that utilize a nanoscale gap or slot between two metal areas or a metal and a dielectric region. These waveguides enable the propagation of surface plasmon polaritons (SPP) while providing subwavelength light confinement. The optical mode supported by slot waveguides is highly confined within the slot itself, and its propagation direction aligns with the slot. The fundamental SPP mode exhibited by slot waveguides possesses a remarkably large propagation length. This attribute is crucial for efficient transmission of light signals over long distances. The group velocity of this mode is exceptionally high, nearly approaching the speed of light in the substrate. At optical communication wavelengths, the propagation length can reach tens of micrometers [84]. These remarkable characteristics render slot waveguides highly suitable for various optoelectronic applications. The key advantage of slot waveguides lies in their ability to confine light within a nanoscale region, far below the diffraction limit imposed by conventional dielectric waveguides. This extreme confinement of light arises from the strong electromagnetic field confinement within the narrow slot. The top view of slot waveguide configuration is shown in Fig. 1.5.

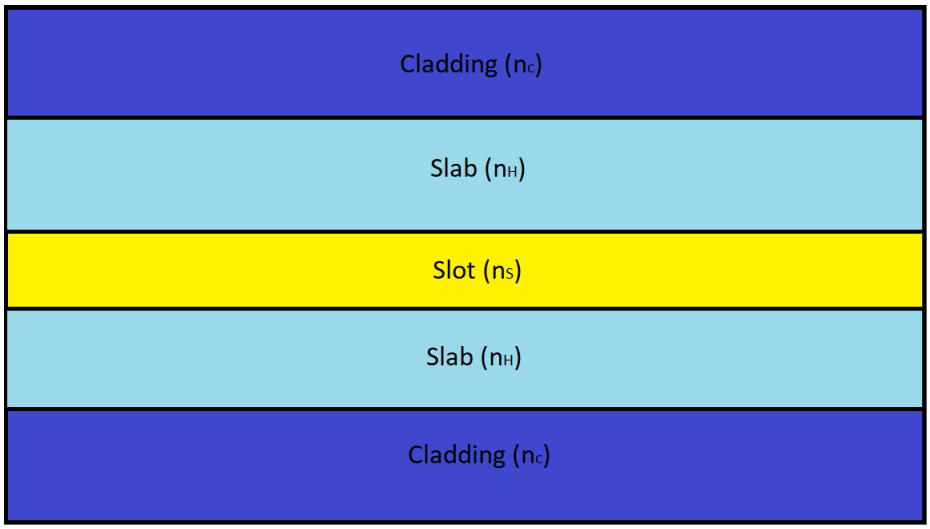

Figure 1.5: Configuration of slot waveguide.

By carefully engineering the dimensions of the slot and the surrounding materials, it is possible to achieve highly efficient light transmission and manipulation at the nanoscale. The subwavelength confinement offered by slot waveguides opens up opportunities for enhancing various optoelectronic devices. One significant application is in integrated photonic circuits, where the tight confinement of light enables the integration of multiple functional components onto a single chip. This integration leads to compact and efficient devices for data communication, sensing, and signal processing. Moreover, the high group velocity of the fundamental SPP mode in slot waveguides allows for rapid transmission of information. This feature is particularly advantageous in applications requiring high-speed data transfer,

such as optical interconnects and telecommunications. Slot waveguides can facilitate the development of next-generation optical communication systems capable of transmitting large volumes of data at unprecedented speeds. The long propagation length of the SPP mode in slot waveguides is crucial for minimizing signal loss during transmission. This extended propagation length ensures that the SPPs can travel over significant distances without significant attenuation. Consequently, slot waveguides are promising candidates for applications involving signal routing and waveguiding, enabling the efficient and reliable transfer of light signals across optical circuits. Furthermore, the unique properties of slot waveguides make them attractive for various sensing applications. The strong confinement of light within the slot enables enhanced interaction with analytes present in the vicinity of the waveguide. This property can be harnessed for developing highly sensitive sensors capable of detecting minute changes in the refractive index or the presence of specific molecules. Slot waveguides offer a platform for label-free biosensing, environmental monitoring, and chemical analysis, with potential applications in medical diagnostics and environmental sensing. Overall, slot waveguides are plasmonic structures that exploit nanoscale gaps or slots to enable the propagation of surface plasmon polaritons. These waveguides provide subwavelength light confinement, possess long propagation lengths, high group velocities, and enable efficient transmission and manipulation of light at the nanoscale. These unique features make slot waveguides well-suited for integration in optoelectronic devices, such as integrated photonic circuits, high-speed optical interconnects, and ultrasensitive sensors. The continued exploration and development of slot waveguides hold great promise for advancing various fields, including photonics, telecommunications, and biosensing.

1.4.5 Nanowire Waveguide

Waveguide structures made of metallic or dielectric nanowires with subwavelength dimensions are referred to as nanowire waveguides. These waveguides enable the confinement and propagation of light at the nanoscale, making them suitable for various applications in nanophotonics. In metallic nanowire waveguides composed of materials like gold or silver, the confinement and direction of light are achieved through the phenomenon of surface plasmon polaritons (SPPs) [85]. SPPs are formed when incident light interacts with free electrons at the metal-dielectric interface. The resulting hybrid excitations propagate along the nanowire, allowing for the localization and manipulation of light on the nanoscale. The subwavelength diameter of nanowires is crucial for the significant confinement of the SPP mode. This confinement leads to enhanced light-matter interactions and enables the manipulation of light at the nanoscale. Nanowire waveguides offer advantages in terms of space, power, and material requirements. Their small size allows for densely packed integration on a chip, making them suitable for nanoscale optical circuits and devices. The tight confinement of light within the nanowire structure reduces the power requirements for signal transmission,

resulting in energy-efficient photonic systems. Furthermore, the use of nanowires enables the utilization of small amounts of materials, making them cost-effective and compatible with nanofabrication techniques. Nanowire waveguides operating at high speeds are well-suited for applications requiring rapid signal processing or transmission. By confining light to sub-wavelength dimensions, these waveguides can overcome the diffraction limit of conventional optics, enabling the manipulation of light with high precision and resolution. Logic gates, fundamental building blocks of digital circuits, can benefit from the confinement and manipulation of light offered by nanowire waveguides [86]. Nanowire waveguides provide a compact and high-speed alternative to traditional electronic logic gates, offering advantages such as faster operation and reduced power consumption. Nanowire waveguides also hold promise in the development of photodetectors, which convert light signals into electrical signals [87]. By integrating nanowire waveguides with light-absorbing materials, efficient light coupling and detection can be achieved. The tight confinement of light within the nanowire enhances the absorption efficiency, leading to improved photodetection capabilities.

1.4.6 Hybrid Waveguide

A hybrid waveguide structure is a composite arrangement that combines different guiding mechanisms or materials to achieve specific functionalities or effects. It comprises multiple components, each with its own distinct characteristics, which are merged to form a unified waveguide structure. For instance, a hybrid waveguide can be constructed by combining a metal surface with a dielectric waveguide. Alternatively, it may consist of a dielectric nanowire separated from a metallic surface by a gap. This configuration enables subwavelength confinement and low propagation loss in two dimensions. Moreover, the hybrid mode can be confined within a size significantly smaller than the diffraction limit [29]. Consequently, hybrid waveguides can be tailored to meet the requirements of specific systems. The Metal-Insulator-Metal (MIM) and Insulator-Metal-Insulator (IMI) waveguide topologies exhibit contrasting characteristics in terms of confinement ability and propagation length. While the MIM structure offers strong confinement, it has a shorter propagation length. On the other hand, the IMI waveguide excels in achieving greater propagation length. To address the need for a device that combines high confinement, good output, and a high propagation constant, researchers have proposed hybrid waveguides. A hybrid waveguide topology typically involves two distinct dielectric mediums attached to a metallic surface. The dielectric medium with a lower refractive index is positioned between the other dielectric medium and the metallic surface. This arrangement establishes strong coupling between the lower and upper surfaces, leading to enhanced confinement. Additionally, the hybrid waveguide does not incorporate a double metallic layer, minimizing the potential for interference and reducing the likelihood of shortening the propagation length. By merging the advantages of MIM and IMI topologies, the hybrid waveguide provides a compelling solution. It of-

fers improved confinement ability, allowing for precise control over the guided wave and its interaction with surrounding materials. Simultaneously, the hybrid waveguide exhibits a higher propagation length, enabling wave transmission over longer distances with minimal attenuation. The distinctive characteristics of the hybrid waveguide topology have garnered significant interest among researchers. This area of exploration holds substantial potential for advancing the field of optics and expanding the capabilities of optical devices. By capitalizing on the strengths of both MIM and IMI structures, the hybrid waveguide serves as an attractive platform for developing innovative and high-performance optical components.

In this thesis, we have numerically investigated plasmonic refractive index nanosensors. Researchers have used MIM waveguides extensively for designing RI sensors. Hence, the MIM waveguide has been used in the RI sensor as the guiding medium for SPP propagation.

1.5 Present and Future of Plasmonics

The computation technology that we use today is the culmination of a long and continuous evolution process involving mathematics, engineering, and innovations. Throughout history, various tools and devices have been used for computation, each representing a significant advancement in its time. In ancient times, the abacus served as a primitive computational tool, allowing users to perform basic arithmetic calculations. The abacus, which dates back thousands of years, consisted of beads or stones placed on rods or wires, with each bead representing a specific value. While limited in its capabilities, the abacus provided a foundation for numerical computation and helped humans better understand mathematical concepts [88]. As technology progressed, analog computers emerged as an upgrade to abacus-based computation. These machines utilized physical phenomena, such as electrical voltages or mechanical movements, to perform calculations. Analog computers were capable of solving complex mathematical equations, providing faster and more accurate results than the abacus [89]. However, they were limited in terms of scalability and precision, as they relied on physical components and continuous values. The invention of the transistor in the mid-20th century marked a significant milestone in computation technology. Transistors are small electronic devices that can control the flow of electrical current, serving as fundamental building blocks for modern electronics. The development of transistors paved the way for the creation of more complex computational devices, such as microprocessors and processors [90].

Over the years, there has been a relentless march of material development and technological advancements, leading to the continuous shrinking of transistor sizes. This reduction in size has followed a trend described by Moore's Law, which states that the number of transistors on integrated circuits doubles approximately every two years, while the size of the transistors halves during the same period. Consequently, this trend has enabled the creation of smaller

and faster processors and electronic devices. However, as transistors approach the nanometer scale, new challenges arise. The complexity of integrated circuit (IC) manufacturing increases as the size of transistors nears the atomic scale. At such small sizes, quantum effects, such as direct quantum tunneling, can lead to undesirable phenomena like gate leakage current. When electrons can tunnel through the gate of a transistor, it can cause operational issues and compromise the reliability of the circuit [91]. Therefore, researchers and engineers face the task of finding innovative solutions to mitigate these challenges and sustain the progress of computation technology. In addition to the transistor-related challenges, the interconnectivity between transistors within a processor presents another bottleneck. Copper has been commonly used as the conductor for connecting transistors, but it faces limitations when dealing with a large number of transistors in a complex architecture. As processors continue to evolve and integrate more components, the need for efficient and reliable interconnects becomes increasingly crucial [92]. Another area of concern is the integration of optical transmission with microprocessors. Fiber optic cables have revolutionized data transmission by efficiently transmitting signals over long distances and at high speeds. However, their integration with microprocessors, which operate at much smaller scales, poses a significant challenge. The size disparity between optical transmission components and microprocessors has made it difficult to combine the two technologies seamlessly [93]. In this context, surface plasmon polaritons (SPPs) have emerged as a potential solution to address the existing challenges in computation technology. SPPs are electromagnetic waves that propagate along the surface of a metal-dielectric interface, enabling efficient transfer of information at the nanoscale. By exploiting the unique properties of SPPs, researchers aim to develop novel interconnect and communication technologies that can overcome the limitations of traditional approaches [94].

Plasmonic devices, such as refractive index (RI) sensors, have garnered significant attention due to their potential applications in various fields, including medical science, environmental science, and military defense. These devices utilize the properties of plasmons, which are collective oscillations of free electrons on a metal surface, to manipulate and control light at the nanoscale. This ability to manipulate light has opened up new possibilities for advancements in several key areas. One area where plasmonic devices show great promise is biosensing. The refractive index sensors based on plasmonics offer highly sensitive and label-free detection of biological molecules. By measuring the changes in the refractive index of the surrounding medium, these sensors can detect and analyze biological analytes such as proteins, DNA, and viruses. This has enormous implications for medical science, as it enables rapid and accurate detection of diseases, including early-stage cancers and infectious agents. Plasmonic biosensors have the potential to revolutionize diagnostics, leading to improved patient care and better disease management. Chemical sensing is another field that can benefit from plasmonic devices. Plasmonic sensors can detect and analyze various

chemical substances, including hazardous materials, pollutants, and gases. Their high sensitivity and selectivity make them valuable tools for environmental monitoring and pollution control. These sensors can be deployed in industrial settings, urban environments, and even remote locations to provide real-time data on air and water quality. By enabling early detection and monitoring of chemical hazards, plasmonic devices can help mitigate environmental risks and safeguard human health. In the realm of military defense, plasmonic devices offer intriguing possibilities. Plasmonic cloaking, based on the manipulation of light, has been proposed as a potential technology for creating invisibility. By designing materials with specific plasmonic properties, it may be possible to control the propagation of light waves and redirect them around an object, rendering it invisible to detection. While still in the realm of theoretical research, plasmonic cloaking has the potential to revolutionize stealth technology and enhance military capabilities. Plasmonics also holds great potential for advancing solar energy technology. Plasmonic solar cells, for instance, have been developed to improve the efficiency of solar panels. These cells incorporate plasmonic nanoparticles or structures that can enhance light absorption and trapping within the solar cell, leading to increased energy conversion efficiency. By harnessing plasmonic effects, solar panels can generate more electricity from sunlight, making solar power a more viable and sustainable energy source. This advancement in solar energy technology can contribute to reducing greenhouse gas emissions and combating climate change. The potential of plasmonics is indeed promising, and future manufacturing of plasmonic devices can have a positive impact on society and civilization. With ongoing research and development, plasmonic devices can be optimized for various applications, leading to breakthroughs in fields such as healthcare, environmental monitoring, and renewable energy. The integration of plasmonic devices into existing technologies and systems has the potential to enhance their performance and capabilities, ultimately benefiting humanity. However, it is important to note that there are still challenges to overcome in the practical implementation of plasmonic devices. Fabrication techniques need to be refined to enable large-scale manufacturing of these devices with consistent performance. Integration of plasmonic components with existing technologies also requires careful engineering and optimization. Additionally, the cost-effectiveness and scalability of plasmonic devices need to be addressed to facilitate their widespread adoption.

Chapter 2

Literature Review

SPPs are a collective plasma oscillation that propagates in a metal-dielectric interface. They possess some important characteristics such as electromagnetic enhancement around nanoparticles, and resonant frequency which renders them a good alternative for information transmission. Researchers have further investigated the properties of SPPs and come up with new nano-scale devices which may not only accelerate the development of processors but also other applications.

One of the revolutionary inventions of SPP-based plasmonic nanosensors is the metal-insulator-metal (MIM) waveguide incorporated refractive index (RI) nanosensor. This nanosensor detects the change in refractive index and provides optical output by means of SPP modulation. It offers strong electromagnetic confinement, fast and label-free detection, rapid detection, and easy fabrication [95]. It is possible to enhance the performance of MIM waveguide-based RI sensors by fine-tuning them in terms of geometric design or material. As a result highly localized electromagnetic fields can be achieved and hence higher sensitivity can be achieved. Higher sensitivity results in more detection of minute changes. Thus, achieving higher sensitivity by proper and careful optimization is essential for biosensing applications. One of the drawbacks of MIM-waveguide-based RI sensors is low sensitivity compared to fiber optic sensors. The fiber optic sensors are bulkier in size compared to the RI sensors. Thus researchers have put effort into modifying the sensor with a view to enhancing the sensitivity. One of the strategies adopted by the researchers is the introduction of resonators and coupling them with the MIM waveguide. The resonators come in different shapes e.g. circular ring cavities, triangular cavities, rectangular cavities, and other polygon and complex structured cavities. The inclusion of these cavities increases the coupling of electromagnetic field localization and results in higher sensitivity. Researchers improve the sensitivity of RI sensors by modifying the resonator structure with geometric designs and coupling it with the MIM waveguide [96]. By using the properties of SPP and innovative resonator designs, researchers are continuously developing new plasmonic nanosensor structures with higher sensitivity and overcoming the limitations of MIM waveguides.

Following the continuous research and development of plasmonic RI sensors, many sensor designs have been proposed featuring different shapes of ring resonators. Butt et al. [97] proposed a sensor design of a square ring resonator incorporated with a MIM waveguide and obtained a sensitivity of 1200 nm/RIU. Tang, Yue, et al. [98] proposed an RI sensor where a MIM waveguide is coupled with rectangular and ring resonators and obtained a sensitivity of 1125 nm/RIU. MR Rakhshani et al. [99] proposed a novel design of a rectangular resonator with nanodots and slot cavities and obtained a sensitivity of 892 nm/RIU. Furthermore, Rakhshani et al. presented a RI sensor by combining a MIM waveguide with a square resonator that has an array of silver nanorods embedded in it, and they measured a maximum sensitivity of 2320 nm/RIU [100]. Based on the published proposed papers, it is observed that square-shaped ring resonators demonstrate comparatively low sensitivity. Therefore, investigations of resonator structures of other geometrical shapes have been carried out. Xie, Yi-Yuan, et al. [101] proposed a topology of a MIM waveguide with a hexagonal cavity with a sensitivity of 1562.5 nm/RIU. Ghorbani et al. [102] proposed the topology of a MIM waveguide coupled with an octagonal resonator and the resulting sensitivity is 1540 nm/RIU. Zhang et al. proposed a concentric double-ring resonator that has a sensitivity of 1060 nm/RIU and a figure of merit (FOM) of 203.8 [103]. Yan et al. developed a structure of a MIM waveguide coupled with the stub and the notched ring, which has a sensitivity of 1071.4 nm/RIU [104]. Rahmatiyar et al. [105] obtained a maximum sensitivity and FOM of 1295 nm/RIU and 159.6, respectively, for refractive index sensing, by designing a ring resonator-based plasmonic sensor with tapered defects. Apart from regular geometric shapes, resonators consisting of complex geometric shapes have been designed and performance has been investigated. L Wang et al. [106] proposed the topology of a T-shaped resonator with a MIM waveguide and achieved a sensitivity of 680 nm/RIU. Researchers have been working on various nanosensor designs consisting of resonators of complex geometric structures. They are working on different resonator structures that are shown in Fig 2.1.

In Table 2.1, a comparison of the performance of plasmonic sensors is shown, including their sensitivity and Figure of Merit (FOM). It's worth noting that all the sensors listed in the table use a Metal-Insulator-Metal (MIM) design with silver as the metal part. However, when we look at the summarized data in Table 2.1, we can see that the sensitivity of these MIM-based refractive indexes (RI) sensors are not good enough for optimal performance. To make lab-on-chip devices more efficient and effective, it's important to address this limitation and aim for better sensitivity in these sensors.

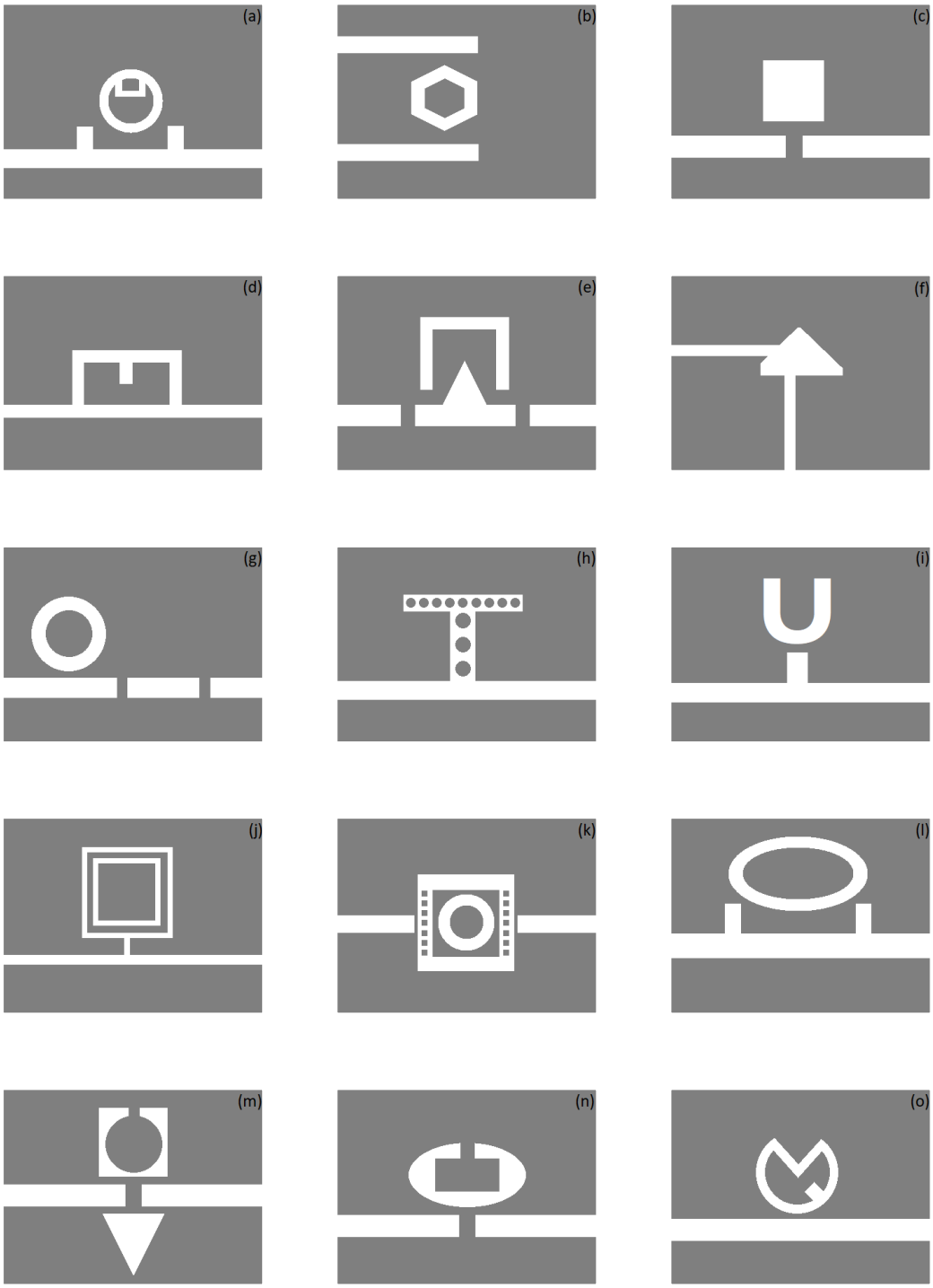

Figure 2.1: Different proposed nanosensor designs. (a) Circular Ring Containing a Rectangular Cavity, (b) Hexagonal Ring Cavity, (c). Square Cavity, (d) Rectangular Ring Resonator, (e) U-shaped Resonator, (f) Triangular Resonator, (g) Ring Cavity and Baffles (h) T-shaped Resonator, (i) U-shaped Cavity, (j) Double Square Ring Resonator (k) Rectangular and Circular Ring Resonators, (l) Elliptical Ring Resonator, (m) Square Ring and Triangle Cavity, (n) Racetrack Cavity, (o) V-ring Cavity With Groove.

Table 2.1: Comparison of Performance Metrics for Recent MIM-Based Plasmonic Refractive Index Sensors

Reference	**Year**	**Structure**	**Sensitivity**	**FOM**
Zou et al. [107]	2014	Ring Resonator	3960	-
Huang et al. [108]	2014	Disk Cavity	1320	-
Wu et al. [109]	2014	Ring Resonator	3460	-
Binfeng et al. [110]	2014	Bragg Grating	1550	-
Ni et al. [111]	2015	Tooth-shaped Cavity	733	30.5
Zafar et al. [112]	2015	Pair of Stub Resonators	1060	176.7
Xie et al. [101]	2015	Hexagonal	1562	38.6
Yan et al. [113]	2015	Ring Resonator	868	43.9
Chen et al. [114]	2015	Stub and Groove Resonator	1260	-
Li et al. [115]	2015	Rectangular	800	-
Chen et al. [116]	2015	Rectangular Ring Resonator	1000	-
Wu et al. [117]	2015	Single Defect Nanocavity	1800.4	-
Wen et al. [118]	2015	Pair of Slot-cavity Resonators	903	-
Ahmadivand et al. [119]	2015	Concentric Split Nanoring Resonators	497	118.5
Chen et al. [120]	2015	Side Cavity and Baffle	1280	-
Zhang et al. [121]	2016	Asymmetric Cavity	-	74.3
Wang et al. [122]	2016	Ring Cavity	2000	-
Pang et al. [123]	2016	Oblique Rectangular	750	53.3
Zhang et al. [124]	2016	Double Rectangular Cavity	596	7.5
Chen et al. [125]	2016	Fillet Cavity	1496	124.6
Gaur et al. [126]	2016	Bragg Grating	1535	152
Wang et al. [127]	2016	Circular Cavity and Groove Resonator	1450	-
Chen et al. [128]	2016	Nano-disc Resonator	1555	87.9
Rakhshani et al. [129]	2016	Hexagonal Ring Cavity	4270	22
Binfeng et al. [130]	2016	Circular Cavity	1277	-
Binfeng et al. [131]	2016	Square Cavity	938	-
Li et al. [132]	2016	T-shape	1090	-
Chen et al. [133]	2016	Side-coupled Cavity	1820	-
Zhang et al. [134]	2016	Rectangle Insulator Cavity	-	57
Wen et al. [135]	2016	Slot Cavities and Grooves	1131	-
Sherif et al. [136]	2016	Rectangular Cavity	1550	-
Chen et al. [137]	2017	Rectangular Cavity	1612	-
Lin et al. [138]	2017	Disk and Ring Cavity	1100	-
Mai et al. [139]	2017	Couple of Slot Cavity and Groove	800	-
Yang et al. [140]	2017	Square Cavity	1120	-
Huang et al. [141]	2017	Dual Rectangular Cavity	1200	92
Yang et al. [142]	2017	Dual Rectangular Cavity	1400	-
Zhang et al. [143]	2017	Dual Side Cavity and Groove Resonator	1900	-

Reference	Year	Structure	Sensitivity	FOM
Wu et al. [144]	2017	Hexagonal Resonator	560	178
Zhou et al. [145]	2017	Trapezoidal Cavity	750	65.2
Zhao et al. [146]	2017	Ring Cavity and Baffles	718	-
Akhavan et al. [147]	2017	Elliptical Ring Resonator	780	-
Tang et al. [98]	2017	Rectangular and Ring Resonator	1125	74
Rakhshani et al. [100]	2017	Square Resonator with Nanorods	2320	-
Yan et al. [104]	2017	Notch Ring Resonator	1071.4	12.5
Rakhshani et al. [148]	2017	Nanorods in Racetrack Resonator	2610	52
Butt et al. [97]	2018	Square Ring Resonator	1200	19.7
Zhang et al. [103]	2018	Concentric Ring Resonator	1060	203.8
Zafar et al. [149]	2018	Double Elliptical Resonator	1100	224
Jankovic et al. [150]	2018	Triangular Resonator	986	-
Zhang et al. [151]	2018	Ring Resonator	1160	-
Ghorbani et al. [102]	2018	Octagonal Ring Cavity	1540	-
Yi et al. [152]	2018	U-shaped Cavity	1000	-
Wang et al. [106]	2018	T-shaped Resonator	680	8.68
Lai et al. [150]	2018	Hexagonal Resonator	780	-
Wen et al. [153]	2018	End-Coupled Slot Cavity Resonator	950	-
Shi et al. [154]	2018	Double Tooth-Shaped Cavities Side-Coupled to Ring Cavity	1000	-
Khan et al. [155]	2018	Double L-Shaped Cavity	1360	-
Guo et al. [156]	2018	Tangent-Ring Resonators	880	-
Chen et al. [157]	2018	Ring Resonator	825	-
Liu et al. [158]	2018	Semiring-Stub-Waveguide	600	120
Zhao et al. [159]	2018	Groove and Stub Resonators	2000	-
Wang et al. [160]	2018	Ring and Stub Resonator	2000	-
Ren et al. [161]	2018	Side-Coupled U-Shaped Resonators	917	180
Mahboub et al. [162]	2018	Ring Resonator	586.8	62.6
Dong et al. [163]	2018	Arch Bridge Cavity	1500	-
Butt et al. [164]	2019	Square Ring with Nanodots	1240	20
Salah et al. [165]	2019	Double Teeth	2602.5	-
Wang et al. [166]	2019	Circular Ring with Baffle	1114.3	55.71
Lu et al. [167]	2019	Two Side-Coupled Rectangular Resonator	1295	-
Zhang et al. [168]	2019	Tooth-Coupled Ring Resonator	1200	-
Butt et al. [169]	2019	Square Ring Resonator	1367	25
Zhang et al. [170]	2019	Two Stubs and Ring Resonator	1268	280
Chou Chau et al. [171]	2019	T-shaped Resonator	8280	-

Reference	Year	Structure	Sensitivity	FOM
Li et al. [172]	2019	Semi-ring Cavity	1405	-
Chen et al. [173]	2019	Square Convex Ring Resonator	1120	-
Yu et al. [174]	2019	Ring Cavity	2000	-
Yu et al. [174]	2019	Circular Cavity	2000	-
Rakhshani et al. [175]	2019	Square Resonator	6400	-
Yang et al. [176]	2019	circular Split-ring Resonance Cavity	1500	65.2
Fang et al. [177]	2019	Semi Ring Rectangular Composite Cavity	1260.5	-
Chen et al. [178]	2019	Two Rectangular Cavities	985	54
Fang et al. [177]	2019	Rectangular Cavity and Inverted U-shaped Groove	1059.2	-
Cheng et al. [179]	2019	T-shaped, ring and split-ring Resonator	1900	-
Chen et al. [180]	2019	Defect Cavity	652	-
Rahmatiyar et al. [105]	2020	Ring Resonator with Defects	1295	159.6
Kazanskiy et al. [181]	2020	Square Ring with Nanodots	907	-
Butt el al. [182]	2020	Bow Tie Resonator	2300	-
Qi et al. [183]	2020	Umbrella Resonator	1600	193
Asgari et al. [184]	2020	Double Square Ring Resonator	1250	32.8
Achi et al. [185]	2020	Racetrack Cavity	2380	-
Butt et al. [95]	2020	Square Ring Resonator	2464	-
Qi et al. [183]	2020	Semi-annular Cavity and Cross-shaped Cavity	1600	193
Guo et al. [186]	2020	Rectangle Cavity Without Long Side	1840	51.11
Yang et al. [187]	2020	Circular Ring Cavity With Stub	1420	76.76
Liu et al. [188]	2020	D-shaped Cavity	1510	-
Li et al. [189]	2020	Tooth-shape and Semi-ring Cavity	1062	-
Sharma et al. [190]	2020	Split Ring Resonators	1965	328
Wang et al. [191]	2020	Isosceles Triangular Cavity	1200	-
Yang et al. [192]	2020	Cross-shaped Cavity	1100	-
Chauhan et al. [193]	2020	Ring Resonator	1200	-
Sagor et al. [194]	2020	Three Parallel Rectangular Cavity	1556	14.83
Wang et al. [195]	2020	Circle With Inner Core and Stub	1183.3	-
Chen et al. [196]	2020	Compact Resonant Cavity	1100	-
Wang et al. [195]	2020	Ring Resonator	1600	-
Rakshani et al. [197]	2020	Two Concentric Double-square Resonators	1380	104

Reference	Year	Structure	Sensitivity	FOM
Chen et al. [198]	2021	Circular Split-ring Resonator	1180	-
Amoosoltani et al. [199]	2021	Two Sequential Ring Resonator	1000	133
Butt et al. [200]	2021	L-shaped Resonator	1065	251.17
Zhu et al. [201]	2021	U-shaped Cavity	825	-
Hu et al. [202]	2021	Triangular Resonator	1250	88.68
Sagor et al. [203]	2021	Two Unequal Rectangular Cavities	2625.87	26.04
Chau et al. [204]	2021	Elliptical-shaped Resonator	2600	-
She et al. [205]	2021	Circular Resonator Embedded With Defective Metal Nanocube	10200	-
Chen et al. [206]	2021	Circular Split-ring Resonance Cavity	1328.8	4.8
Zhang et al. [207]	2021	Circular Ring Containing Rectangular Cavity	2300	57.5
Wu et al. [208]	2021	Defective Ring Cavity	1600	-
Liu et al. [209]	2021	Side-coupled Rectangular Cavity	1550.38	-
Bahri et al. [210]	2021	Rectangular Cavities	3010	-
Xiao et al. [211]	2021	Inverted U-shaped and Triangular Groove Cavities	840	-
Rakshani et al. [212]	2021	Two Square Nanorods Arrays and One Rectangular Resonator	1090	-
Liu et al. [213]	2021	Connected Concentric Double Rings Resonator	2260	56.5
Yu et al. [214]	2021	Racetrack Resonant Cavity	1503.7	26.8
Yu et al. [215]	2021	Split Annular Cavity Connected With Rectangular Resonator	1000	-
Chao et al. [216]	2021	Circular Ring With Air Path	2900	-
Zhou et al. [217]	2021	Two Stub Resonators and Ring Resonator	1650	117.8
Shao et al. [218]	2021	Double Ring Resonator	1885	77
Shi et al. [219]	2021	Half-ring Resonance Cavity	1723	51
Harhouz et al. [220]	2021	Oval Resonator	2844.95	-
Chao et al. [221]	2021	Rectangular and Circular Ring Resonators	3400	36
Su et al. [222]	2021	Elliptical Ring Resonator	1550	43.05
Li et al. [223]	2021	X-shaped Resonant Cavity	1303	-

Reference	Year	Structure	Sensitivity	FOM
Rohimah et al. [224]	2022	r-shaped Resonator	1333	-
Wang et al. [225]	2022	Square Ring and Triangle Cavity	2259.56	-
Li et al. [226]	2022	Whistle-shaped Cavity	1229	-
Zhang et al. [227]	2022	U-shaped Ring Resonator	2020	53.16
Bensalah et al. [228]	2022	Hexagonal Irregular Ring Resonator	2417	38
Fan et al. [229]	2022	Taiji Resonator	2016	345
Guo et al. [230]	2022	Cross-shape Cavity Resonator	1000	-
Yan et al. [231]	2022	Internal Z-ring Resonator	2234	49.65
Ren et al. [232]	2022	Double Notch and Double Convex Circle	2740	52.69
Najjari et al. [233]	2022	Waveguide With Four Teeth	1078	-
Tavana et al. [234]	2022	Semi-circular Resonant Cavity and Circular Split-Ring Resonator	579	12.46
Rohimah et al. [235]	2022	Obround-shaped Resonator	1636	-
Zhang et al. [227]	2022	U-Shaped Ring Resonator	2020	53.16
Zhou et al. [236]	2022	Rectangular Root and Double-ring with Rectangular Cavity	2280	76.7
Harhouz et al. [237]	2022	Oval Resonator	3787,9	-
Wang et al. [238]	2022	V-ring Cavity With Groove	2765	50.28
Dong et al. [239]	2022	Ring Resonator	7550	302
Shen et al. [240]	2022	Protractor Type Half Ring Cavity	1600	50
Zhou et al. [241]	2022	Double Rectangles and Annular Cavity	1990	63.2
Wang et al. [242]	2022	Petal With flower-core Ring Resonator	2000	47.62
Liu et al. [243]	2022	Elliptical, Half-ring and Half-ring With opening Cavity	1048.6	-
Wu et al. [244]	2022	Circular Ring Cavity With Stub	2520	61.46
Tathfif et al. [245]	2022	Concentric Triple Ring Resonator	7530.49	-
Wu et al. [246]	2022	Special Square and Ring Cavity	2350	-
Pan et al. [247]	2022	Rectangular and Semi-ring Resonators	1280	-

Chapter 3

Methodology

3.1 Electromagnetic Wave Theory

3.1.1 Maxwell's Fundamental Equations

Maxwell's equations are a set of fundamental equations in electromagnetism that provide a complete framework for understanding the interaction and generation of electric and magnetic fields, derived by James Clerk Maxwell. These equations unify the laws of electricity and magnetism and offer profound insights into electromagnetic phenomena. Constitutive equations are also essential in describing how matter behaves when exposed to electric and magnetic fields. These equations define the relationship between electric and magnetic fields and material properties such as electric permittivity and magnetic permeability. By including constitutive equations, Maxwell's equations can be applied to various materials, allowing for a more in-depth understanding of electromagnetic phenomena in different media.

The wave equation, derived from Maxwell's equations, governs the behavior of electromagnetic waves as they travel through space or different materials. It describes the fundamental principles underlying the propagation of electromagnetic waves in both time and space. By solving the wave equation, we can predict and analyze the characteristics of electromagnetic waves, such as their speed, direction, and intensity, as they move through various media. The wave equation includes different modes of propagation, known as TE (Transverse Electric), TM (Transverse Magnetic), and TEM (Transverse Electromagnetic). These modes are distinguished by the specific properties of the electric and magnetic fields during propagation. For instance, in TE mode, the electric field is perpendicular to the direction of propagation, while in TM mode, the magnetic field is perpendicular to the direction of propagation. The TEM mode represents cases where both electric and magnetic fields are entirely perpendicular to the direction of propagation. Understanding and applying Maxwell's equations and the wave equation, along with characterizing different modes, is crucial for comprehending and predicting the behaviour of electromagnetic waves and their interaction with matter in

various physical systems and technological applications.

Maxwell's laws encompass four fundamental electromagnetic phenomena: Faraday's law, Maxwell-Ampere's law, Gauss's law of electric field, and Gauss's law of magnetic field. These laws establish the relationship between electric and magnetic fields and provide a deep understanding of electromagnetic phenomena. The laws can be expressed in both integral and differential forms, providing versatile approaches to analyzing electromagnetic problems. In this section, we focus on the differential form of Maxwell's equations, which is used in the finite element method (FEM) for numerical analysis. By expressing Maxwell's equations in differential form, we can effectively apply FEM to analyze electromagnetic problems involving time-varying electric and magnetic fields. For time varying electric and magnetic fields, Maxwell's equations can be expressed as [248, 249],

- *Gauss's Law for Electric Fields:*

$$\nabla \cdot \mathbf{D} = \rho \tag{3.1}$$

  where ρ is the charge density.

  $\mathbf{D} = \varepsilon\mathbf{E} + \mathbf{P}$, relates the electric displacement field (D) to the electric field (E) and the polarization of the material (P), which indicates that the electric displacement is a combination of the electric field and the polarizability of the material. If there are no external charges and no electric currents present, then equation 3.1 can be expressed as:

$$\nabla \cdot \mathbf{D} = 0 \tag{3.2}$$

  This law provides a fundamental relationship between electric charges and the electric field they create. It helps to understand the behaviour of electric fields, the interaction of charges with electric fields, and the distribution of charges in various systems. It is one of the four fundamental equations of electromagnetism, collectively known as Maxwell's equations, and plays a crucial role in analyzing and solving electromagnetic problems.

- *Gauss's Law for Magnetic Fields:*

$$\nabla \cdot \mathbf{B} = 0 \tag{3.3}$$

  where $\nabla \cdot \mathbf{B}$ represents the divergence of the magnetic field $\mathbf{B}$. The law implies that the total magnetic flux through any closed surface is always zero. This means that the number of magnetic field lines entering a closed surface is equal to the number of lines exiting it. It also implies that the magnetic field lines form closed loops, circulating around current-carrying wires or magnetic materials.

- *Faraday's Law:*

$$\nabla \times \mathbf{E} = -\frac{\partial \mathbf{B}}{\partial t} \tag{3.4}$$

where $\nabla \times \mathbf{E}$ represents the curl of the electric field $\mathbf{E}$ and $\frac{\partial \mathbf{B}}{\partial t}$ is the time rate of change of the magnetic field $\mathbf{B}$. This equation describes how a changing magnetic field induces an electric field. The induced electric field forms closed loops and is directly proportional to the rate of change of the magnetic field. This phenomenon is the basis for electromagnetic induction and is responsible for various practical applications, such as electric generators, transformers, and electromagnetic wave propagation. The law implies that a changing magnetic field produces a circulating electric field, which can induce electric currents in conductors. Conversely, if an electric circuit experiences a changing magnetic field, it can generate an electromotive force (EMF) that drives electric current through the circuit.

- *Ampere-Maxwell Law:*

$$\nabla \times \mathbf{H} = \mathbf{J} + \frac{\partial \mathbf{D}}{\partial x} \tag{3.5}$$

where $\mathbf{J}$ is the current density. The Ampere-Maxwell law incorporates an additional term compared to Ampere's law, which only considers conduction currents. The added term, $\frac{\partial \mathbf{D}}{\partial x}$, accounts for the displacement current. The displacement current arises from the time-varying electric field and is essential for maintaining the consistency of Maxwell's equations and ensuring their compatibility with the principle of conservation of charge. The law states that the circulation of the magnetic field is directly related to the total current, including both the conduction current and the displacement current. It demonstrates that a changing electric field can induce a magnetic field, similar to how a changing magnetic field induces an electric field, as described by Faraday's law.

3.1.2 Formulation of Electromagnetic Wave Equations

Propagation of electromagnetic (EM) waves in a vacuum or different media with respect to time and space can be described by the wave equation, which is a second-order partial differential equation. The following derivation outlines the process of obtaining the wave equation from Maxwell's equations::

$$\nabla \times (\nabla \times \mathbf{E}) = -\frac{\partial \mathbf{B}}{\partial t} \tag{3.6}$$

Here, $\mathbf{B} = \mu\mathbf{H}$

$$\nabla \times (\nabla \times \mathbf{E}) = \nabla \times \left(-\mu \frac{\partial \mathbf{H}}{\partial t}\right) \tag{3.7}$$

We know that, $\nabla \times (\nabla \times \mathbf{E}) = \nabla(\nabla \cdot \mathbf{E}) - \nabla^2\mathbf{E}$ and $\nabla \times \mathbf{E} = \frac{\partial \mathbf{E}}{\partial t}$.

Now to simplify Equation 3.7 , we can express it as follows:

$$\nabla(\nabla \cdot \mathbf{E}) - \nabla^2\mathbf{E} = -\mu\varepsilon\frac{\partial^2\mathbf{E}}{\partial t^2} \tag{3.8}$$

This is the wave equation for the electric field, where μ is the magnetic permeability and ε is the electric permittivity of the medium. The wave equation describes the behavior of EM waves by relating the spatial and temporal variations of the electric field. It indicates that the second derivative of the electric field with respect to time is proportional to the Laplacian of the electric field and the product of the magnetic permeability and electric permittivity. Solving the wave equation allows us to determine the characteristics of EM waves, such as their propagation speed, wavelength, and frequency. Gauss's law is being applied to derive wave equations for the electric and magnetic fields.

According to Gauss's law, the divergence of the electric field (E) is zero $(\nabla\mathbf{E} = 0)$ in a region with a constant permittivity over space. Based on this, the wave equation for the electric field ($\mathbf{E}$) is obtained as follows:

$$\nabla^2\mathbf{E} - \mu\varepsilon\frac{\partial^2\mathbf{E}}{\partial t^2} = 0 \tag{3.9}$$

Similarly, the wave equation for the magnetic field ($\mathbf{H}$) can be derived as:

$$\nabla^2\mathbf{H} - \mu\varepsilon\frac{\partial^2\mathbf{H}}{\partial t^2} = 0 \tag{3.10}$$

Here, ∇^2 represents the Laplacian operator, which describes the spatial variation of the field. $\frac{\partial^2\mathbf{E}}{\partial t^2}$ and $\frac{\partial^2\mathbf{H}}{\partial t^2}$ represent the second partial derivatives of $\mathbf{E}$ and $\mathbf{H}$ with respect to time, respectively. μ is the magnetic permeability of the medium, and ε_0 is the permittivity of free space.
If the variation of the dielectric profile, which is related to the electric field, is negligible over distance, the wave equation for the electric field can be expressed as follows:

$$\nabla^2\mathbf{E} - \frac{\varepsilon}{c^2}\frac{\partial^2\mathbf{E}}{\partial t^2} = 0 \tag{3.11}$$

This equation is a simplified form that assumes a constant dielectric profile and incorporates the speed of light in the medium.

3.1.2.1 Electromagnetic Wave propagation

In the context of Maxwell's equations, when matter is present, specifically when there are free electrons and atoms containing protons and electrons. Maxwell's equations describe the fundamental principles of electromagnetism, relating electric and magnetic fields to their sources. One of Maxwell's equations, known as Gauss's law for electric fields, states that

the divergence of the electric field (**E**) is proportional to the charge density (ρ) divided by the electric constant (ε_0). Mathematically, it can be expressed as follows:

$$\nabla \cdot \mathbf{E} = \frac{\rho}{\varepsilon_0}$$

Here, $\nabla \cdot \mathbf{E}$ represents the divergence of the electric field, which measures how much the electric field spreads out or converges at a given point in space. In the presence of matter, the equation you provided suggests that the divergence of the electric field ($\nabla \cdot \mathbf{E}$) may no longer be zero. Instead, it becomes proportional to the charge density (ρ) divided by the electric permittivity of the medium (ε_0). The term ρ represents the charge density, which is the amount of electric charge per unit volume. The electric permittivity (ε_0) is a fundamental constant that characterizes the electrical properties of the medium in which the electromagnetic field exists. It determines how the electric field interacts with matter.

When matter is present, the presence of free electrons and atoms with protons and electrons affects the behavior of the electric field, resulting in a nonzero divergence. This modification reflects the influence of charges within the medium on the electric field distribution. It is important to note that the modified form of the equation you provided is valid in the presence of matter. In vacuum or situations where matter is not present, the standard form of Gauss's law for electric fields ($\nabla \cdot \mathbf{E} = 0$) holds true, but it does not hold universally.
In materials, the relationship describing the curl of the magnetic field changes. The modified equation is as follows:

$$\nabla \times \mathbf{B} = \varepsilon_0 \mu_0 \frac{\partial \mathbf{E}}{\partial t} + \mu_0 \mathbf{J}_f + \nabla \times \mathbf{M} + \frac{\partial \mathbf{P}}{\partial t} \tag{3.12}$$

This equation introduces additional terms enclosed within the square brackets, which are related to the properties of matter. These terms include:

- *Free electric current density ($\mathbf{J}_f$)*: It represents the density of electric current flowing freely in the material. This term accounts for the presence of charges that are not bound to any specific atoms or molecules but can move through the material.

- *Magnetization current density ($\nabla \times \mathbf{M}$)*: It describes the current induced in the material due to the presence of a magnetic field. When a material is subjected to a magnetic field, the magnetic moments of its constituent atoms or molecules align, creating a magnetization. This alignment gives rise to a circulating current that contributes to the overall magnetic field.

- *Polarization current density ($\frac{\partial \mathbf{P}}{\partial t}$)*: It represents the current induced in the material due to the time-varying polarization. Polarization refers to the separation of positive and negative charges within the material in response to an applied electric field. When the polarization changes over time, it gives rise to a polarization current.

By including these additional terms in the equation, it explicitly shows how electromagnetic waves behave differently when propagating through materials compared to vacuum. The presence of these terms indicates the interaction between light and matter, where the properties of the material affect the propagation of electromagnetic waves. We know that, in the absence of magnetization and free current density,

$$\nabla \times \mathbf{E} = -\frac{\partial \mathbf{B}}{\partial t} \tag{3.13}$$

$$\nabla \times \mathbf{B} = \varepsilon_0 \mu_0 \frac{\partial \mathbf{E}}{\partial t} + \mu_0 \frac{\partial \mathbf{P}}{\partial t} \tag{3.14}$$

By taking the curl of equation 3.13, we obtain:

$$\nabla \times (\nabla \times \mathbf{E}) = -\frac{\partial}{\partial t}(\nabla \times \mathbf{B}) \tag{3.15}$$

By taking the negative time derivative of equation 3.14, we find:

$$-\frac{\partial}{\partial t}(\nabla \times \mathbf{B}) = -\varepsilon_0 \mu_0 \frac{\partial^2 \mathbf{E}}{\partial t^2} - \mu_0 \frac{\partial^2 \mathbf{P}}{\partial t^2} \tag{3.16}$$

When comparing equations 3.15 and 3.16, we observe that the following relationship holds true:

$$\nabla \times (\nabla \times \mathbf{E}) = -\varepsilon_0 \mu_0 \frac{\partial^2 \mathbf{E}}{\partial t^2} - \mu_0 \frac{\partial^2 \mathbf{P}}{\partial t^2} \tag{3.17}$$

We know, the general vector relation is like $\nabla \times (\nabla \times \mathbf{F}) = -\nabla^2 \mathbf{F} + \nabla(\nabla \cdot \mathbf{F})$. Similar to this relation we have:

$$-\nabla^2 \mathbf{E} + \nabla(\nabla \cdot \mathbf{E}) = -\varepsilon_0 \mu_0 \frac{\partial^2 \mathbf{E}}{\partial t^2} - \mu_0 \frac{\partial^2 \mathbf{P}}{\partial t^2} \tag{3.18}$$

Nonetheless, when dealing with homogeneous isotropic neutral materials stimulated by light, the resulting fields retain their divergence-free characteristic. Based on these assumptions, we have formulated a wave equation 3.19 that bears resemblance to the equation observed in a vacuum. However, it includes an additional term associated with polarization:

$$-\nabla^2 \mathbf{E} = -\varepsilon_0 \mu_0 \frac{\partial^2}{\partial t^2}(\mathbf{E} + \frac{\mathbf{P}}{\varepsilon}) \tag{3.19}$$

In materials exhibiting linear, isotropic, and instantaneous polarization response, $\mathbf{P(t)} = \varepsilon_0 \chi_r \mathbf{E(t)}$, the relationship between the electric field and its spatial and temporal derivatives can be expressed in a simplified form as follows.

$$\nabla^2 \mathbf{E} = \varepsilon_0 \mu_0 \left(1 + \chi_r\right) \frac{\partial^2 \mathbf{E}}{\partial t^2} \tag{3.20}$$

The equation states that when an electric field changes quickly over time, it also changes

rapidly in space and the susceptibility of a material represents its ability to polarize in response to an external electric field. A higher susceptibility implies a more pronounced polarization response, which, in turn, results in shorter wavelengths.

3.1.2.2 Wave Relation with Refractive Index

A scalar plane wave of the form $\mathbf{E}(t, z) = \mathbf{E}_r \cos(kz - \omega t)$ is substituted into the simplified equation 3.20. Here, $\mathbf{E}(t, z)$ represents the electric field as a function of time (t) and position (z), $\mathbf{E}_r$ is the magnitude of the electric field, k is the wave vector, and ω is the angular frequency. When we substitute this plane wave into the equation 3.20, we obtain a modified expression that relates the temporal and spatial derivatives of the electric field. The plane wave assumption allows us to simplify the equation and analyze the behavior of the electric field in terms of its oscillations in time and space. We can explore the characteristics of the electric field within the material. The cosine function represents the oscillating nature of the wave, with kz representing the phase term that describes the position of the wave in both space and time and ωt representing the phase term that describes the temporal component.

$$\nabla^2 \left(\mathbf{E}_r \cos(kz - \omega t)\right) = \varepsilon_0 \mu_0 \left(1 + \chi_r\right) \frac{\partial^2}{\partial t^2} \left(\mathbf{E}_r \cos(kz - \omega t)\right) \tag{3.21}$$

If we take double spacial derivative in the left side of equation 3.21, then we'll get -k^2. Similarly, if we take double time derivative in the right side of equation 3.21, then we'll get -ω^2.

Now, if we divide both sides of the equation by the common terms, we will obtain the following expression:

$$\frac{\omega}{k} \equiv v_p = \frac{c}{\sqrt{1 + \chi_r}} \tag{3.22}$$

The impact of the polarizability of a material on the propagation of light waves.

- When $\chi_r = 0$ (no polarizable material): In this case, the equation 3.22 simplifies to $\frac{\omega}{k} \equiv v_p = c$, which means the wave propagates with a phase velocity equal to the speed of light in vacuum, denoted by c. In other words, when there is no polarizable material present, the speed of light is not affected, and it behaves as it does in empty space.

- When $\chi_r \neq 0$ (light propagating inside a material with nonzero χ): In this scenario, the equation 3.22 shows that the speed of the wave (represented by v_p) is reduced by a factor of $\sqrt{1 + \chi_r}$. The term χ_r quantifies the influence of the polarizable material on the wave propagation. Additionally, the wavelength of the light wave is also affected. When light passes through a material with nonzero χ, the wavelength becomes shorter

or reduced compared to its wavelength in vacuum. The reduction factor $\sqrt{1+\chi_r}$ leads to a decrease in the wavelength.

$$\begin{aligned} \frac{\omega}{k} &= \frac{\omega}{2\pi/\lambda} = \frac{c}{\sqrt{1+\chi_r}} \\ \Rightarrow \lambda &= \frac{2\pi c}{\omega}\frac{1}{\sqrt{1+\chi_r}} \\ &= \frac{\lambda_0}{\sqrt{1+\chi_r}} \end{aligned} \tag{3.23}$$

Inside a polarizable material, both the speed of light and the wavelength experience a reduction by the same factor "$\sqrt{1+\chi_r}$". This factor is known as the refractive index, denoted by 'n'. In the scenario of an idealized instantaneous response, the relationships can be represented as follows:

$$v = \frac{c}{\sqrt{1+\chi_r}} \equiv \frac{c}{n} \tag{3.24}$$

where v is the reduced speed of light, c is the speed of light in vacuum, χ_r is the electric susceptibility of the material, and n is the refractive index. This equation illustrates that the speed of light inside the material is reduced compared to its speed in vacuum. In a similar manner, the wavelength within the material can be expressed as follows:

$$\lambda = \frac{\lambda_0}{\sqrt{1+\chi_r}} = \frac{\lambda_0}{n} \tag{3.25}$$

where λ is the reduced wavelength, λ_0 is the wavelength in vacuum, χ_r is the electric susceptibility, and n is the refractive index. As frequency (f) remains constant for a given light source, we see that the wavelength (λ) inside the material is reduced compared to its wavelength in vacuum. The equations 3.25 and 3.24 show that for a polarizable material with an instantaneous response, the speed of light and the wavelength are both reduced by the refractive index factor $\sqrt{1+\chi_r}$. The refractive index is defined as the ratio of the speed of light in vacuum to the reduced speed of light inside the material, or alternatively, the ratio of the wavelength in vacuum to the reduced wavelength inside the material.

3.1.3 Formulation of Wave Propagation Mode

Suppose we consider the wave propagating along the x direction in the Cartesian coordinate system, assuming that there is no spatial variation in the y direction. The electric field (**E**) and magnetic field (**H**) are expressed as vector quantities in terms of their components in a Cartesian coordinate system. The electric field (**E**) can be expressed in terms of its Cartesian components in the following manner:

$$\mathbf{E} = \mathbf{E}_x\hat{a}_x + \mathbf{E}_y\hat{a}_y + \mathbf{E}_z\hat{a}_z \tag{3.26}$$

where $\mathbf{E}_x$, $\mathbf{E}_y$, and $\mathbf{E}_z$ represent the magnitudes of the electric field components in the x, y, and z directions, respectively. The $\hat{a}_x$, $\hat{a}_y$, and $\hat{a}_z$ are unit vectors pointing in the positive x, y, and z directions, respectively. In a similar fashion, the magnetic field ($\mathbf{H}$) can be decomposed into its Cartesian components as follows:

$$\mathbf{H} = \mathbf{H}_x\hat{a}_x + \mathbf{H}_y\hat{a}_y + \mathbf{H}_z\hat{a}_z \tag{3.27}$$

Here, $\mathbf{H}_x$, $\mathbf{H}_y$, and $\mathbf{H}_z$ represent the magnitudes of the magnetic field components in the x, y, and z directions, respectively.

By assuming a harmonic time dependence, $\frac{\partial}{\partial t} = -j\omega$ and solving Ampere's law and Faraday's law, we obtain the following expression:

$$\frac{\partial \mathbf{E}_z}{\partial y} - \frac{\partial \mathbf{E}_y}{\partial z} = j\omega\mu_0\mathbf{H}_x \tag{3.28}$$

This equation 3.28 relates the spatial variations of the electric field components in the y and z directions to the spatial variation of the magnetic field component in the x direction. It states that the change in electric field in the y direction with respect to changes in the z direction is proportional to the rate of change of the magnetic field in the x direction. Here, j represents the imaginary unit, ω is the angular frequency, μ_0 is the permeability of free space, and $\mathbf{H}_x$ is the x component of the magnetic field.

$$\frac{\partial \mathbf{E}_x}{\partial z} - \frac{\partial \mathbf{E}_z}{\partial x} = j\omega\mu_0\mathbf{H}_y \tag{3.29}$$

$$\frac{\partial \mathbf{E}_y}{\partial x} - \frac{\partial \mathbf{E}_x}{\partial y} = j\omega\mu_0\mathbf{H}_z \tag{3.30}$$

These equations describe similar relationships as Equation 3.28, but for different pairs of electric and magnetic field components. Equation 4.18 states that the change in electric field in the x direction with respect to changes in the z direction is proportional to the rate of change of the magnetic field in the y direction. Equation 3.30 states that the change in electric field in the y direction with respect to changes in the x direction is proportional to the rate of change of the magnetic field in the z direction.

$$\frac{\partial \mathbf{H}_z}{\partial y} - \frac{\partial \mathbf{H}_y}{\partial z} = j\omega\varepsilon_0\mathbf{E}_x \tag{3.31}$$

$$\frac{\partial \mathbf{H}_x}{\partial z} - \frac{\partial \mathbf{H}_z}{\partial x} = j\omega\varepsilon_0\mathbf{E}_y \tag{3.32}$$

$$\frac{\partial \mathbf{H}_y}{\partial x} - \frac{\partial \mathbf{H}_x}{\partial y} = j\omega\varepsilon_0\mathbf{E}_z \tag{3.33}$$

These equations relate the spatial variations of the magnetic field components to the spatial variation of the electric field components. Equation 3.31 states that the change in magnetic field in the z direction with respect to changes in the y direction is proportional to the rate of change of the electric field in the x direction. Equation 3.32 states that the change in magnetic field in the x direction with respect to changes in the z direction is proportional to the rate of change of the electric field in the y direction. Equation 3.33 states that the change in magnetic field in the y direction with respect to changes in the x direction is proportional to the rate of change of the electric field in the z direction. Here, ε_0 is the permittivity of free space.

As the propagation is in the x direction in the form of $e^{j\beta x}$, where β represents the propagation constant, the derivative with respect to x can be expressed as $\frac{\partial}{\partial x} = -j\beta$. Moreover, as there is no spatial variation along the y direction, the derivative with respect to y, denoted as $(\frac{\partial}{\partial y})$ becomes zero. Hence, the equation can be simplified as follows:

$$\frac{\partial \mathbf{E}_y}{\partial z} = j\omega\mu_0 \mathbf{H}_x \tag{3.34}$$

$$\frac{\partial \mathbf{E}_x}{\partial z} - j\beta \mathbf{E}_z = j\omega\mu_0 \mathbf{H}_y \tag{3.35}$$

$$j\beta \mathbf{E}_y = j\omega\mu_0 \mathbf{H}_z \tag{3.36}$$

$$\frac{\partial \mathbf{H}_y}{\partial z} = j\omega\varepsilon_0 \mathbf{E}_x \tag{3.37}$$

$$\frac{\partial \mathbf{H}_x}{\partial z} - j\beta \mathbf{H}_z = j\omega\varepsilon_0 \mathbf{E}_y \tag{3.38}$$

$$j\beta \mathbf{H}_y = j\omega\varepsilon_0 \mathbf{E}_z \tag{3.39}$$

By characterizing the solutions into TM and TE modes, we can distinguish between two types of electromagnetic wave behavior based on their polarization properties. TM modes represent wave configurations where the electric field is confined to a specific plane perpendicular to the wave's direction of travel and the magnetic field lines form loops around the direction of propagation. On the other hand, TE modes describe wave configurations where the magnetic field is confined to a plane perpendicular to the direction of propagation, while the electric field lines extend in the direction of propagation.

3.1.4 Unveiling the Primary Propagation Mode of Surface Plasmon Polaritons: A TM or TE Conundrum

3.1.4.1 Transverse Magnetic Mode

Electric field $\mathbf{E}_x$ and $\mathbf{E}_z$ for TM modes are respectively,

$$\mathbf{E}_x = -j\frac{1}{\omega\varepsilon_0\varepsilon}\frac{\partial \mathbf{H}_y}{\partial z} \tag{3.40}$$

$$\mathbf{E}_z = -\frac{\beta}{\omega\varepsilon_0\varepsilon}\mathbf{H}_y \tag{3.41}$$

The transverse magnetic (TM) wave equation can be represented as:

$$\frac{\partial^2 \mathbf{H}_y}{\partial z^2} + (k_0^2 - \beta^2)\mathbf{H}_y = 0 \tag{3.42}$$

For $z > 0$, the TM solutions for metal and dielectric will be:

$$\mathbf{H}_z(z) = A_2 e^{j\beta x} e^{-k_2 x} \tag{3.43}$$

$$\mathbf{E}_x(z) = jA_2\frac{1}{\omega\varepsilon_0\varepsilon}k_2 e^{j\beta x} e^{-k_2 z} \tag{3.44}$$

$$\mathbf{E}_z(z) = -A_1\frac{\beta}{\omega\varepsilon_0\varepsilon} e^{j\beta x} e^{-k_2 z} \tag{3.45}$$

For $z < 0$, the transverse magnetic (TM) solutions for both the metal and dielectric can be expressed as follows:

$$\mathbf{H}_y(z) = A_1 e^{j\beta x} e^{-k_1 z} \tag{3.46}$$

$$\mathbf{E}_x(z) = -jA_1\frac{1}{\omega\varepsilon_0\varepsilon}k_1 e^{j\beta x} e^{-k_1 z} \tag{3.47}$$

$$\mathbf{E}_z(z) = -A_1\frac{\beta}{\omega\varepsilon_0\varepsilon} e^{j\beta x} e^{-k_1 z} \tag{3.48}$$

The continuity of the tangential components of the magnetic field ($\mathbf{H}_y$) and electric field ($\mathbf{E}_z$) at the interface between a metal and a dielectric. The continuity condition gives rise to the following equation:

$$A_1 = A_2 \tag{3.49}$$

This equation states that the amplitudes of the $\mathbf{H}_y$ field on the metal side (A_1) and the dielectric side (A_2) are equal. A_1 and A_2 represent the magnitudes of the magnetic field components on their respective sides.

Moreover, there exists a relationship between the wave numbers in the dielectric (k_1) and the metal (k_2) as expressed by the equation:

$$\frac{k_2}{k_1} = -\frac{\varepsilon_d}{\varepsilon_m} \tag{3.50}$$

Here, ε_d and ε_m are the dielectric permittivity and the metal permittivity, respectively. The negative sign indicates that the phase of the wave is reversed when passing from the metal

to the dielectric. Based on these conditions, the surface wave known as the Surface Plasmon Polariton (SPP) exists at the metal-dielectric interface. The SPP (Surface Plasmon Polariton) possesses a propagation constant represented as β. This constant, denoted as β, can be calculated by utilizing the subsequent expressions:

$$k_2^2\varepsilon = \beta^2 - k_0^2\varepsilon_d \tag{3.51}$$

This equation relates the wave number (k_1) in the dielectric, the permittivity of the metal (ε_m), the propagation constant (β), and the free space wave number (k_0).
Similarly, The relationship between the wave number (k_2) in the metal and β can be expressed as:

$$k_1^2\varepsilon = \beta^2 - k_0^2\varepsilon_m \tag{3.52}$$

The propagation constant (β) can be obtained by solving these equations, and it is determined by the permittivities of the metal and the dielectric (ε_m and ε_d), as well as the wave number in free space (k_0). These equations describe the dispersion relation for the propagation of Surface Plasmon Polaritons (SPPs) at the metal-dielectric interface.

$$\beta = k_0\sqrt{\frac{\varepsilon_m\varepsilon_d}{\varepsilon_m + \varepsilon_d}} \tag{3.53}$$

So, SPP can be propagated in TM mode

3.1.4.2 Transverse Electric Mode

The equations for the magnetic field components $\mathbf{H}_x$ and $\mathbf{H}_z$ for TE (Transverse Electric) modes can be expressed as follows:

$$\mathbf{H}_x = -j\frac{1}{\omega\mu_0}\frac{\partial \mathbf{E}_y}{\partial z},$$
$$\mathbf{H}_z = \beta\frac{1}{\omega\mu_0}\mathbf{E}_y$$

The TE (Transverse Electric) wave equation can be expressed as follows:

$$\frac{\partial^2 \mathbf{E}_y}{\partial z^2} + \left(k_0^2\varepsilon - \beta^2\right)\mathbf{E}_y = 0 \tag{3.54}$$

For negative values of z, ($z > 0$), the transverse electric (TE) solutions for both metals and

dielectrics can be expressed as follows:

$$\mathbf{E}_y(z) = A_2 e^{j\beta x} e^{-k_2 z}, \tag{3.55}$$

$$\mathbf{H}_x(z) = -jA_2 \frac{\beta}{w\mu_0} k_2 e^{j\beta x} e^{-k_2 z}, \tag{3.56}$$

$$\mathbf{H}_z(z) = -A_2 \frac{\beta}{w\mu_0} k_2 e^{j\beta x} e^{-k_2 z}, \tag{3.57}$$

For negative values of z, ($z < 0$), the transverse electric (TE) solutions for both metal and dielectric materials can be described as follows:

$$\mathbf{E}_y(z) = A_1 e^{j\beta x} e^{-k_1 z}, \tag{3.58}$$

$$\mathbf{H}_x(z) = -jA_1 \frac{\beta}{w\varepsilon_{01}} k_1 e^{j\beta x} e^{-k_1 z}, \tag{3.59}$$

$$\mathbf{H}_z(z) = -A_1 \frac{\beta}{w\varepsilon_0\varepsilon_1} k_2 e^{j\beta x} e^{-k_1 z}, \tag{3.60}$$

In electromagnetics, the continuity equations for the electric field ($\mathbf{E}_y$) and magnetic field ($\mathbf{H}_x$) components are important in analyzing the behavior of electromagnetic waves at interfaces between different media. The continuity conditions ensure that the fields are continuous across the boundary and help determine the existence of surface modes and surface plasmon polaritons (SPPs) for different polarization states. The continuity condition for the electric field in the y-direction ($\mathbf{E}_y$) and the magnetic field in the x-direction ($\mathbf{H}_x$) can be expressed as follows:

$$A_1(k_1 + k_2) = 0 \tag{3.61}$$

where A_1 is the amplitude of the incident wave, and k_1 and k_2 are the wave vectors in the two media separated by the interface. This equation implies that either A_1 is zero or the sum of k_1 and k_2 is zero for the continuity to be satisfied.

For TE polarization, the electric field is perpendicular to the plane of incidence, meaning $\mathbf{E}_y = 0$. In this case, the continuity equation reduces to $k_1 + k_2 = 0$. Since the real part of a wave vector represents its phase velocity and determines whether the wave is evanescent (decaying) or propagating, having a positive real part for k_1 and k_2 is necessary for wave confinement.

Consequently, for TE polarization, if $A_1 = A_2 = 0$ (both the incident and transmitted waves are absent), the continuity condition is satisfied, and no surface modes exist.

So, SPP can not be propagated in TE mode

3.2 Material Modeling

At high frequencies, the properties of materials, such as the relative permittivity (ε_r) and refractive index (n), become frequency-dependent. In order to mathematically describe this frequency dependency, various models have been developed, including the Drude model, Lorentz model, and Lorentz-Drude model. These models offer a means to accurately characterize plasmonic materials like Silver and Gold, which are widely utilized. The appropriate tabulated values are used to model their behavior. Numerical simulation tools like COMSOL Multiphysics Software employ the finite element method, which discretizes the system boundary into a triangular mesh and approximates the field within that boundary. To simulate transparent boundaries for incoming and outgoing signals, scattering boundary conditions are implemented. Scattering parameters are then utilized to evaluate important quantities such as transmittance and reflectance in two-port electromagnetic wave-based devices. Through mode analysis and boundary mode analysis, the fundamental mode propagation can be predicted, allowing for the calculation of parameters like the propagation constant and other associated properties.

3.2.1 Lorentz Model

The Lorentz material model, also referred to as the Lorentzian or Lorentz-Oscillator model, is a widely employed framework for understanding how materials react to electromagnetic fields. It is an important material model for comprehending the behavior of dielectric materials and has diverse applications in physics, such as optics, electromagnetics, and condensed matter physics. In the Lorentz model, the fundamental premise is that particles or clusters of particles present in a material can be represented as harmonic oscillators. These oscillators possess inherent resonant frequencies and interact with the incident electromagnetic field, resulting in a complex dielectric response. At the core of this model lies the assumption that the distribution of electronic charges within the material undergoes oscillations around an equilibrium position in response to an applied electric field.

Atoms consist of a central, positively charged nucleus containing protons and neutrons. The nucleus carries a total electric charge of $+eZ$, where Z represents the atomic number. Surrounding the nucleus, a neutral atom contains Z electrons. These electrons are bound to the nucleus through Coulomb interaction forces and orbit around it, following the spatial distribution principles described by quantum mechanics. In atoms with high atomic numbers, some of the electrons are tightly bound to the nucleus and orbit it at a close proximity. These electrons are referred to as core electrons. Other electrons occupy larger orbits, encircling both the positively charged nucleus and the core electrons that are tightly bound. Consequently, these outer electrons experience a reduced net positive charge from the nucleus, resulting in weaker Coulomb binding forces acting upon them. The outermost electrons,

known as valence electrons, are responsible for maintaining the overall neutrality of the atom. These electrons experience the least attractive forces from the nucleus and are therefore more easily movable. As a consequence, valence electrons often contribute the most to the polarization response of atoms, as they are the most responsive to external influences and are involved in interactions with other atoms or molecules.

The Lorentz model is a simplified mechanical model of an atom that incorporates key assumptions to understand its behavior. This model is based on four main assumptions.
Firstly, the Lorentz model assumes that the movement of the atom's core can be neglected. This assumption is reasonable because the core mass is significantly larger than the electron mass by over three orders of magnitude. Therefore, the core's motion has minimal impact on the overall behavior of the atom. Secondly, the model considers only the valence electrons, disregarding the behavior of core electrons. It assumes that the core electrons are tightly bound and unresponsive to the electromagnetic wave. This assumption implies that the valence electrons are the primary particles involved in the atom's interactions. The third assumption of the Lorentz model is that the valence electrons are bound to the core by an effectively harmonic binding potential. In the absence of an external electric field, the electrons reach a steady state and occupy a minimum-energy configuration around the core. Deviations from this equilibrium position result in a restoring force that acts to bring the electrons back to equilibrium. This restoring force is assumed to be linearly dependent on the displacement from equilibrium, following Hooke's Law:

$$\mathbf{F} = K\mathbf{x} \tag{3.62}$$

Here, K represents the spring constant, which quantifies the strength of the binding force. The linear force response in the Lorentz model implies that the potential energy increases quadratically as the position of the electrons increases, leading to a harmonic binding potential. Lastly, the Lorentz model assumes that the atom responds isotropically, meaning it responds equally in all directions, and only along the applied driving force. This assumption allows the electron's position to be described using a scalar r(t), which represents the distance from the core. By assuming isotropic behavior, the model simplifies the atom's response to external forces and facilitates analysis.
In summary, when an alternating electric field is applied, then it behaves like a spring. We can express all the forces by the following equation,

$$\begin{aligned} \mathbf{F}_{\text{acceleration}} + \mathbf{F}_{\text{damping}} + \mathbf{F}_{\text{restoration}} &= \mathbf{F}_{\text{ext}} \\ m\frac{\partial^2 \mathbf{x}}{\partial t^2} + m\gamma\frac{\partial \mathbf{x}}{\partial t} + m\omega_0^2\mathbf{x} &= q\mathbf{E} \end{aligned} \tag{3.63}$$

By applying Fourier analysis to Equation 3.63, we obtain the following expression:

$$\begin{aligned} m(-j\omega)^2\mathbf{x}(\omega) + m\gamma(-j\omega)\mathbf{x}(\omega) + m\omega_0^2\mathbf{x}(\omega) &= q\mathbf{E}(\omega), \\ -\frac{m}{\omega^2}\mathbf{x}(\omega) - jm\gamma\omega\mathbf{x}(\omega) + m\omega_0^2\mathbf{x}(\omega) + m\omega_0^2\mathbf{x}(\omega) &= q\mathbf{E}(\omega), \\ [-\omega^2 + \omega_0^2 - j\gamma\omega]\mathbf{x}(\omega) &= \frac{q}{m}\mathbf{E}(\omega), \\ [\omega_0^2 - \omega^2 - j\gamma\omega]\mathbf{x}(\omega) &= \frac{q}{m}\mathbf{E}(\omega) \end{aligned} \tag{3.64}$$

The equation 3.64 allows us to obtain the function $\mathbf{x}(\omega)$,

$$\mathbf{x}(\omega) = \frac{q}{m}\frac{\mathbf{E}(\omega)}{\omega_0^2 - \omega^2 - j\gamma\omega} \tag{3.65}$$

The equation expressing the dipole moment (μ) can be written as follows:

$$\mu = q\mathbf{x}(\omega), \mu = \frac{q^2}{m}\frac{\mathbf{E}(\omega)}{\omega_0^2 - \omega^2 - j\gamma\omega} \tag{3.66}$$

The polarization $\mathbf{P}(\omega)$ is determined by the product of the number of dipoles and Equation 3.64,

$$\begin{aligned} \mathbf{P}(\omega) &= N\mu, \\ \mathbf{P}(\omega) &= \frac{Nq^2}{m}\frac{E(\omega)}{\omega_0^2 - \omega^2 - j\gamma\omega} \end{aligned} \tag{3.67}$$

The general formula for polarization is as follows:

$$\mathbf{P} = \varepsilon_0\chi(\omega)\mathbf{E}(\omega) \tag{3.68}$$

Upon comparing Equation 3.67 and Equation 3.68, we can observe the following relationship:

$$\mathbf{P} = \varepsilon_0\chi(\omega)\mathbf{E}(\omega) = \frac{Nq^2}{m}\frac{\mathbf{E}(\omega)}{\omega_0^2 - \omega^2 - j\gamma\omega} \tag{3.69}$$

The susceptibility can be determined using Equation 3.69,

$$\chi(\omega) = \frac{Nq^2}{m\varepsilon_0}\frac{1}{\omega_0^2 - \omega^2 - j\gamma\omega} \tag{3.70}$$

We again know that,

$$\chi(\omega) = \varepsilon_r(\omega) - 1 \tag{3.71}$$

Finally, we have obtained that,

$$\varepsilon_r(\omega) - 1 = \frac{Nq^2}{m\varepsilon_0}\frac{1}{\omega_0^2 - \omega^2 - j\gamma\omega}, \\ \varepsilon_r(\omega) = 1 + \frac{Nq^2}{m\varepsilon_0}\frac{1}{\omega_0^2 - \omega^2 - j\gamma\omega} \tag{3.72}$$

The expression $\frac{Nq^2}{\varepsilon_0 m}$ in Equation 3.72 represents the plasma frequency, denoted as ω_p^2. So it can be derived as follows:

$$\varepsilon_r(\omega) = 1 + \frac{\omega_p^2}{\omega_0^2 - \omega^2 - j\gamma\omega} \tag{3.73}$$

We can separate the real and imaginary components of the permittivity, denoted as $\varepsilon_r(\omega)$ as follows:

$$\varepsilon_r'(\omega) = 1 + \omega_p^2\frac{(\omega_0^2 - \omega^2)}{(\omega_0^2 - \omega^2)^2 + \gamma^2\omega^2} \tag{3.74}$$

$$\varepsilon_r''(\omega) = \omega_p^2\frac{\omega\gamma}{(\omega_0^2 - \omega^2)^2 + \gamma^2\omega^2} \tag{3.75}$$

The graphical representation of real and imaginary are shown in Fig. 3.1 where ω_p = 2, ω_0 = 2, and γ = 0.3.

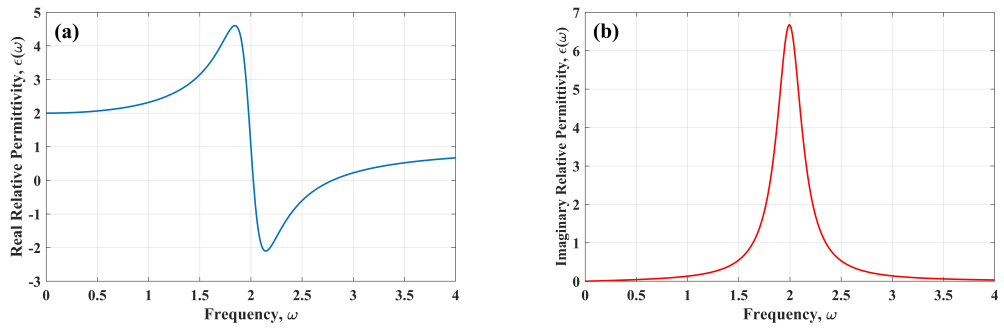

Figure 3.1: a. The real part of permittivity b. The imaginary part of permittivity.

The real part of the dielectric function, $\varepsilon'(\omega)$, represents the dispersion or frequency-dependent behavior of the material, while the imaginary part, $\varepsilon''(\omega)$, accounts for the energy loss or absorption in the material. The complex dielectric function can be used to calculate various important material properties. The refractive index (n) and the complex propagation constant (k) of a material can be obtained from the dielectric function as follows:

$$n(\omega) = \sqrt{\frac{1}{2}\left(\sqrt{\varepsilon'(\omega)^2 + \varepsilon''(\omega)^2} + \varepsilon'(\omega)\right)} \tag{3.76}$$

$$k(\omega) = \sqrt{\frac{1}{2}\left(\sqrt{\varepsilon'(\omega)^2 + \varepsilon''(\omega)^2} - \varepsilon'(\omega)\right)} \tag{3.77}$$

3.2.2 Drude Model

The Drude material model, commonly referred to as the Drude-Lorentz model, is a classical framework used to elucidate the response of metals and conductors when subjected to electromagnetic fields. It offers a simplified representation of the electrical conductivity and optical characteristics exhibited by these materials. According to the Drude model [250], the conduction electrons in a metal behave as a free electron gas and experience collisions with the lattice ions. In the Drude model, the macroscopic current density ($\mathbf{J}$) in a material is related to the applied electric field ($\mathbf{E}$) through Ohm's law:

$$\mathbf{J}(t) = \sigma \mathbf{E}(t) \tag{3.78}$$

where $\mathbf{J}(t)$ represents the current density as a function of time, $\mathbf{E}(t)$ is the applied electric field, and σ is the electrical conductivity of the material. The Drude model incorporates the concept of relaxation time (τ), which represents the average time between electron collisions. It assumes that after each collision, the electron's velocity is randomized, resulting in a net zero drift velocity on average. The relaxation time is inversely proportional to the scattering rate of electrons and can be related to the electrical conductivity as follows:

$$\sigma = \frac{ne^2\tau}{m} \tag{3.79}$$

where n is the number density of conduction electrons, e is the elementary charge, and m is the effective mass of the conduction electrons. In metals, the majority of electrons exist in a state of freedom, as they are not strongly bound to the atomic nuclei. Unlike in other materials, the restoring force acting on these electrons can be considered negligible due to the weak interaction with the surrounding lattice. Consequently, the concept of a natural frequency (ω_0) becomes irrelevant in the context of metals. To describe the behavior of electrons in metals under the influence of electromagnetic fields, the Drude model emerges as a useful framework. The Drude model can be derived from the more general Lorentz model by setting $(\omega_0 = 0)$. This modification accounts for the absence of a characteristic natural frequency in metals. By neglecting the influence of a natural frequency $(\omega_0 = 0)$ in the Lorentz model, the Drude model captures the unique properties exhibited by metals. In this simplified model, the restoring force component associated with the harmonic motion of electrons is disregarded. Instead, the Drude model focuses on the collective behavior of free electrons in response to external fields, particularly emphasizing their electrical conductivity and optical properties. The expression for the complex dielectric function, denoted as $\varepsilon(\omega)$,

of a Drude material can be represented as follows:

$$\begin{aligned} \varepsilon(\omega) &= 1 + \frac{\omega_p^2}{-\omega^2 - i\gamma\omega}, \\ \varepsilon(\omega) &= 1 - \frac{\omega_p^2}{\omega^2 + i\gamma\omega} \end{aligned} \tag{3.80}$$

where ω_p is the plasma frequency, and γ is the collision frequency.The plasma frequency can be expressed as follows:

$$\omega_p = \sqrt{\frac{ne^2}{\varepsilon_0 m}} \tag{3.81}$$

and the collision frequency can be expressed as the reciprocal of the relaxation time:

$$\gamma = \frac{1}{\tau} \tag{3.82}$$

Now, we can split the real and imaginary parts from the permittivity $(\varepsilon_r(\omega))$ as follows:

$$\varepsilon_r'(\omega) = 1 - \frac{\omega_p^2}{\omega^2 + \gamma^2} \tag{3.83}$$

$$\varepsilon_r''(\omega) = \frac{\gamma\omega_p^2}{\omega(\omega^2 + \gamma^2)} \tag{3.84}$$

The real part of the dielectric function, $\varepsilon'(\omega)$, represents the dispersion or frequency-dependent behavior of the material, while the imaginary part, $\varepsilon''(\omega)$, accounts for the energy loss or absorption in the material. The complex dielectric function can be used to calculate various optical properties of Drude materials. For example, the refractive index (n) and the propagation constant (k) can be derived as follows:

$$n(\omega) = \sqrt{\frac{1}{2}\left(\sqrt{\varepsilon'(\omega)^2 + \varepsilon''(\omega)^2} + \varepsilon'(\omega)\right)} \tag{3.85}$$

$$k(\omega) = \sqrt{\frac{1}{2}\left(\sqrt{\varepsilon'(\omega)^2 + \varepsilon''(\omega)^2} - \varepsilon'(\omega)\right)} \tag{3.86}$$

These properties describe how light interacts with Drude materials, such as the reflection, transmission, and absorption of light. The Drude model is a simplified representation of the behavior of metals and conductors, neglecting some quantum effects and material-specific details. In metals, the valence electrons are delocalized and can move freely throughout the crystal lattice. This mobility gives rise to the phenomenon of electrical conductivity, which is a fundamental property of metals. The plasma frequency (w_p) directly relates to this conductivity through the relationship between the frequency and the dielectric response of

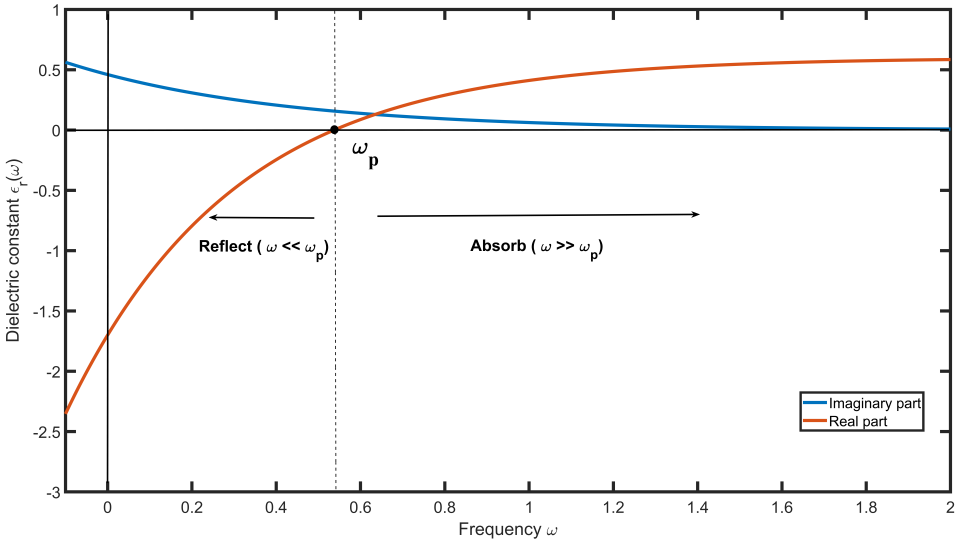

Figure 3.2: Real and Imaginary Part of Drude Model

the material. At frequencies below w_p, metals exhibit high reflectivity because the incident photons are unable to excite the conduction electrons. This phenomenon is responsible for the shiny appearance of metals. However, above the plasma frequency, metals become more transparent, leading to reduced reflectivity and increased absorption of light.

3.2.3 Lorentz-Drude Model

The Drude model is a classical model widely employed to elucidate the behavior of conductors and metals in the presence of electromagnetic fields. It offers a simplified yet insightful understanding of electrical conductivity and optical properties in these materials. Despite its simplicity, the Drude model serves as a fundamental framework for comprehending the response of conductors to external perturbations. However, it has limitations in capturing the detailed frequency-dependent behavior of real materials.

To address this limitation, the Lorentz-Drude model has been developed and found to provide excellent agreement with experimental observations across a broad range of materials. It has been successfully employed to reproduce experimental data related to important optical properties such as the refractive index, absorption spectra, and other characteristics. The remarkable agreement between the Lorentz-Drude model and experimental data validates its effectiveness in describing and predicting the behavior of real materials. The Lorentz-Drude model incorporates the interactions between electrons within a material, which play a pivotal role in determining the material's response to electromagnetic fields, particularly in metals and conductors. By considering electron-electron interactions, the model can capture the collective behavior of electrons and describe phenomena such as plasmon resonances, which are crucial for understanding the optical properties of these materials. In materials, the di-

electric response exhibits a frequency-dependent behavior due to the electron behavior under the influence of electromagnetic fields. The Lorentz-Drude model successfully accounts for this frequency dependence by incorporating resonance frequencies and damping coefficients associated with the oscillators. This enables a more realistic representation of the dielectric properties of materials over a wide range of frequencies. A key aspect of the Lorentz-Drude model lies in the consideration of damping coefficients associated with the oscillators, which encapsulate the energy dissipation and absorption processes that occur when materials interact with electromagnetic fields. By incorporating damping, the model accurately describes the attenuation and absorption of electromagnetic waves within a material, offering insights into the energy dissipation mechanisms at play. The Lorentz-Drude model, with its ability to incorporate electron-electron interactions, frequency-dependent responses, and damping effects, provides a comprehensive framework for studying the optical properties of materials. It offers a deeper understanding of phenomena such as plasmonic resonances and provides valuable insights into the absorption and attenuation of electromagnetic waves within materials. This model serves as a powerful tool for the design and characterization of materials with tailored optical properties for a range of applications in photonics, optoelectronics, and beyond. The expression for the electric field density $\mathbf{D}$ in the frequency domain, considering both models, can be reformulated as follows:

$$\mathbf{D}(\omega) = \varepsilon_0 \left(1 + \frac{\omega_p}{j\gamma\omega - \omega^2} + \frac{\omega_p^2}{\omega_0^2 + j\omega\gamma - \omega^2}\right) \mathbf{E}(\omega) \tag{3.87}$$

where ε_0 is the vacuum permittivity, ω_p is the plasma frequency, Γ is the damping factor, ω is the angular frequency, ω_0 is the resonant frequency, and $\mathbf{E}(\omega)$ is the electric field in the frequency domain. The real and imaginary part of the dielectric constant is shown in Fig. 3.2.

The formulation of the dielectric constant (ε_r) in the Lorentz-Drude model can be expressed as follows [251]:

$$\varepsilon_r(\omega) = 1 - \frac{\Omega_p^2}{\omega(\omega - i\Gamma_0)} + \sum_{j=1}^{k} \frac{f_j \omega_p^2}{(\omega_j^2 - \omega^2) + i\omega\Gamma_j} \tag{3.88}$$

In the context of this study, the symbols ω_j, ω_p, f_j, Γ_j, and Γ_0 represent the resonance frequency, plasma frequency, oscillator strength, damping frequency, and damping constant, respectively. It is worth noting that Ω_p specifically refers to the plasma frequency of free electrons, while the symbol k is used to represent the oscillation number. The real part of the dielectric function, $\varepsilon'(\omega)$, represents the dispersion or frequency-dependent behavior of the material, while the imaginary part, $\varepsilon''(\omega)$, accounts for the energy loss or absorption in the material.

3.3 Formulation of Surface Plasmon Polariton

3.3.1 Propagation and Decaying Property of SPP

Surface plasmon polaritons (SPPs) are electromagnetic waves that propagate along the interface between a metal and a dielectric material. They arise from the coupling between electromagnetic waves and collective oscillations of free electrons at the metal-dielectric interface, known as surface plasmons. SPPs have attracted significant attention due to their ability to confine light at the nanoscale, which has important implications for various fields such as nanophotonics, sensing, and surface-enhanced spectroscopy. The provided equation describes the propagation of an electromagnetic wave with a complex dielectric constant. It is derived by incorporating the complex dielectric constant into Maxwell's equations. The outcome of this derivation can be summarized by the following expression:

$$\nabla^2 \mathbf{E}(x,t) = \mu\varepsilon \frac{\partial^2}{\partial t^2}\mathbf{E}(x,t) \tag{3.89}$$

where $\mathbf{E}$ represents the electric field, and ∇^2 and $\frac{\partial^2}{\partial t^2}$ denote the Laplacian and second partial derivative with respect to time, respectively.
Now, μ can be replaced as $\mu_0\mu_r$ and ε can be replaced as $\varepsilon_0\varepsilon_r$ in Equation 3.89,

$$\nabla^2 \mathbf{E}(x,t) = \mu_0\mu_r\varepsilon_0\varepsilon_r \frac{\partial^2}{\partial t^2}\mathbf{E}(x,t) \tag{3.90}$$

We know that,

$$c = \frac{1}{\sqrt{\mu_0\varepsilon_0}} \tag{3.91}$$

$$n = \sqrt{\mu_r\varepsilon_r} \tag{3.92}$$

Based on Equation 3.90, the following expression can be derived as follows:

$$\nabla^2 \mathbf{E}(x,t) = \frac{n^2}{c^2}\frac{\partial^2}{\partial t^2}\mathbf{E}(x,t) \tag{3.93}$$

A class of solutions to the wave equation, characterized by propagation along the x-axis, can be mathematically represented as follows:

$$\mathbf{E}(x,t) = \mathbf{E}_0 exp(ikx - iwt) \tag{3.94}$$

where $\mathbf{E}_0$ is the electric field amplitude, $\mathbf{k}$ is the wavevector, and ω is the angular frequency. By substituting Equation 3.94 into Equation 3.93 and considering the left-hand side portion

of the equation, we obtain:

$$\frac{\partial^2 \mathbf{E}}{\partial x^2} = -k^2 \mathbf{E} \tag{3.95}$$

Similarly, for the portion on the right-hand side, we will obtain:

$$\frac{\partial^2 \mathbf{E}}{\partial t^2} = -\omega^2 \mathbf{E} \tag{3.96}$$

The dispersion law for the plane wave can be derived from equations 3.95 and 3.96 as follows:

$$\begin{aligned} -k^2 \mathbf{E} &= \frac{n^2}{c^2}(-\omega^2 \mathbf{E}) \\ k^2 &= \frac{n^2}{c^2}(\omega^2) \\ k &= \pm \frac{\omega}{c} n \\ k &= \pm \frac{\omega}{c}(n' + in'') \end{aligned} \tag{3.97}$$

The complex refractive index, denoted as n, can be expressed as $n' + in''$, where n is the real part of the refractive index, and n'' is the imaginary part of the refractive index. Now after substituting the wave vector value into Equation 3.94:

$$\begin{aligned} &\mathbf{E} = \mathbf{E}_0 \exp(ikx - iwt), \\ &\mathbf{E} = \mathbf{E}_0 \exp\left(i\left(\frac{\omega}{c}(n' + in'')x - iwt\right)\right), \\ &\mathbf{E} = \mathbf{E}_0 \exp\left(i\frac{\omega}{c}n'x - \frac{\omega}{c}n''x - iwt\right), \\ &\mathbf{E} = \mathbf{E}_0 \exp\left(i\frac{\omega}{c}n'x - iwt\right) \exp\left(-\frac{\omega}{c}n''x\right), \\ &\mathbf{E} = \mathbf{E}_0 \exp\left(i\beta x - iwt\right) \exp\left(-\frac{\omega}{c}n''x\right), \end{aligned} \tag{3.98}$$

where the 1st exponential term $exp(-i\beta x - iwt)$ represents the propagation of the wave with propagation constant β. The 2nd exponential term $exp(-\frac{w}{c}n''x)$ represents the decay of the electric field amplitude as the wave propagates in the x-direction away from the metal-dielectric interface and it represents the absorption and energy loss in the SPP mode as it propagates along the interface. The graphical representation can be seen in Fig. 3.3.

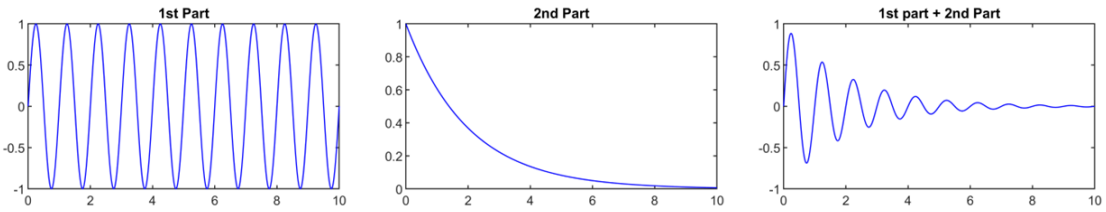

Figure 3.3: Propagation property of SPP.

3.3.2 Understanding SPP Propagation at Metal-Insulator Interface

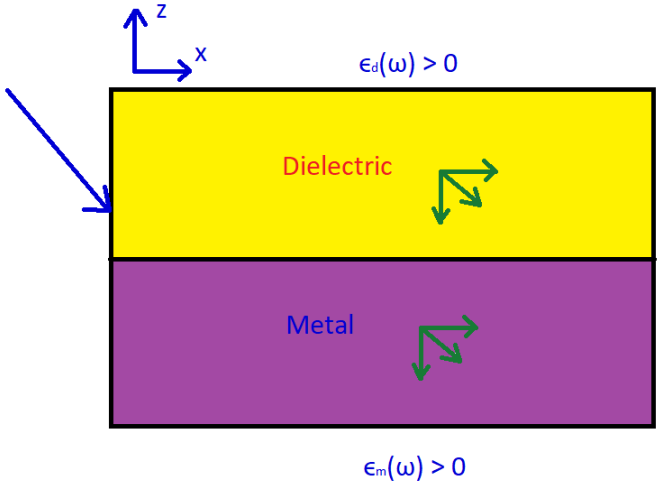

Figure 3.4: Wave Vector of SPP propagtion in Metal-Insulator Interface.

Figure 3.4 depicts the wave vector of Surface Plasmon Polariton (SPP) propagation at the metal-insulator interface. The representation of the wave vector in the metal and dielectric is as follows:

$$\mathbf{K}_d = (\mathbf{K}_{1x}, 0, -\mathbf{K}_{1z})$$

$$\mathbf{K}_m = (\mathbf{K}_{2x}, 0, -\mathbf{K}_{2z})$$

For the metal, we can express it as follws:

$$\mathbf{K}_{2x}^2 + \mathbf{K}_{2z}^2 = \frac{n^2\omega^2}{c^2} = \varepsilon_m \mathbf{K}_0^2 \tag{3.99}$$

This equation represents the relationship between the wave vector components $\mathbf{K}_{2x}$ and $\mathbf{K}_{2z}$, the refractive index n, the angular frequency ω, the speed of light c, and the permittivity ε_m of the metal. Additionally, we have the following:

$$\mathbf{K}_{2z}^2 = \varepsilon_m \mathbf{K}_0^2 - \mathbf{K}_{2x}^2 \tag{3.100}$$

Equation 3.100 provides a specific expression for $\mathbf{K}_{2z}^2$ in terms of $\mathbf{K}_{2x}^2$ and ε_m.
We know that for metals, the permittivity (ε_m) is negative, and if $\mathbf{K}_{2x}^2$ is positive, then $\mathbf{K}_{2z}^2$ will be negative, indicating an imaginary value. This imaginary component in the wave vector implies an evanescent behavior, suggesting that the wave decays exponentially within the metal. Such behavior is a characteristic of surface plasmon polaritons (SPPs), which are collective electron oscillations at the metal-dielectric interface.

So, based on the obtained results, we can conclude that when the wave vector components in the metal, $\mathbf{K}_{2x}^2$ and $\mathbf{K}_{2z}^2$, have opposite signs due to the negative permittivity (ε_m) of metals, the wave cannot propagate through the metal. Instead, it experiences total internal reflection at the metal-dielectric interface. Therefore, light incident on a metal will be predominantly reflected rather than transmitted through the material.

3.3.3 Determining the Resonant Wavelength for SPPs

Assuming a TM mode wave, where the magnetic field propagates in the y-axis direction, the magnetic field within the metal and dielectric can be described as follows:

$$\mathbf{H}_{1y} = h_1 e^{ik_{1x}x} e^{-k_{1z}z} \tag{3.101}$$

$$\mathbf{H}_{1y} = h_1 e^{ik_{1x}x} e^{-k_{1z}z} \tag{3.102}$$

Here, h_1 represents the amplitude of the magnetic field, k_{1x} represents the wave vector component in the x-axis direction, and k_{1z} represents the wave vector component in the z-axis direction. The wave vector in its generalized form can be expressed as follows:

$$\mathbf{K}_{iz} = (K_{ix}^2 - \varepsilon_i K_0^2)^1/2 \tag{3.103}$$

Now, for dielectric,

$$\mathbf{K}_{1z} = (K_{1x}^2 - \varepsilon_d K_0^2)^1/2 \tag{3.104}$$

Now, for metal,

$$\mathbf{K}_{2z} = (K_{2x}^2 - \varepsilon_m K_0^2)^1/2 \tag{3.105}$$

As, ε_d is positive and ε_m is negative, so Eq. 3.104 and 3.105, we'll get that SPP decays faster in metal than dielectric.
According to the Ampere-Maxwell law,

$$\nabla \times \mathbf{H} = \mu_0 \mathbf{J} + \frac{\partial \mathbf{D}}{\partial t} \tag{3.106}$$

Here, the current density $\mathbf{J} = 0$. Hence, the equation can be expressed as follows:

$$\nabla \times \mathbf{H} = \frac{\partial \mathbf{D}}{\partial t} \tag{3.107}$$

Now, we know that $\mathbf{D} = \varepsilon \mathbf{E}$ and $\mathbf{E} = \mathbf{E}_0 \exp(ikx - i\omega t)$. By replacing these expressions, the equation can be reformulated as follows:

$$\nabla \times \mathbf{H} = -i\omega\varepsilon \mathbf{E} \tag{3.108}$$

The relationships stated below can be expressed using the curl equation:

$$\nabla \times \mathbf{H} = \begin{pmatrix} \hat{x} & \hat{y} & \hat{z} \\ \frac{\partial}{\partial x} & \frac{\partial}{\partial y} & \frac{\partial}{\partial z} \\ 0 & \mathbf{H}_z & 0 \end{pmatrix} = -i\omega\varepsilon \mathbf{E}$$

$$\text{-}\frac{d}{dz}\mathbf{H}_y \hat{x} + \frac{d}{dx}\mathbf{H}_y \hat{z} = -i\omega\epsilon \mathbf{E}$$

$$\text{-}\mathbf{K}_{1z}\mathbf{H}_{1y}\hat{x} + i\mathbf{K}_{1x}\mathbf{H}_{1y}\hat{z} = -i\omega\epsilon \mathbf{E}$$

$$\text{-}\omega\epsilon \mathbf{E} = i\mathbf{K}_{1z}\mathbf{H}_{1y}\hat{x} - \mathbf{K}_{1x}\mathbf{H}_{1y}\hat{z}$$

$$\text{-}\mathbf{E}_1 = \frac{\mathbf{H}_{1y}}{\epsilon_d \omega}(i\mathbf{K}_{1z}\hat{x} - \mathbf{K}_{1x}\hat{z})$$

Similarly, we can determine $\mathbf{E}_2$,

$$E_2 = \frac{\mathbf{H}_{2y}}{\epsilon_m \omega}(-iK_{2z}\hat{x} + K_{1x}\hat{z})$$

At the initial point (z = 0), when considering the interface between the two media, we can assume that $\mathbf{H}_{1y}$ and $\mathbf{H}_{2y}$ are almost equal. Consequently, $\mathbf{E}_1$ and $\mathbf{E}_2$ will also be equal. By equating the x component, we can derive the following equation:

$$\begin{aligned} \frac{\mathbf{K}_{1z}}{\epsilon_d} &= -\frac{\mathbf{K}_{2z}}{\epsilon_m} \\ \frac{\mathbf{K}_{1z}}{\mathbf{K}_{2z}} &= -\frac{\epsilon_d}{\epsilon_m} \end{aligned} \tag{3.109}$$

To support the existence of Surface Plasmon Polaritons (SPPs), the ratio of $\mathbf{K}_{1z}^2$ (from Eq. 3.104) to $\mathbf{K}_{2z}^2$ (from Eq. 3.105) needs to be equal. This leads to the following expression:

$$\mathbf{K}_{1x}^2 = \mathbf{K}_{2x}^2 = \mathbf{K}_x^2 \tag{3.110}$$

The wave vector expression for propagation in the x-direction becomes:

$$\mathbf{K}_{1x}^2 = \left(\frac{\epsilon_m \epsilon_d}{\epsilon_m + \epsilon_d} \right) \mathbf{K}_0^2 \tag{3.111}$$

As the wave vector $\mathbf{K}$ approaches infinity, at resonance:

$$\mathbf{K} \to \infty$$

Therefore, it means that,

$$\epsilon_m + \epsilon_d = 0$$

$$\epsilon_m = -\epsilon_d$$

Let's assume that $\epsilon_d = 1$, so we can conclude that:

$$\epsilon_m = -1$$

$$1 - \frac{w_p^2}{w^2} = -1$$

$$\frac{w_p^2}{w^2} = 2$$

After solving the equation for w, we obtain:

$$w = \frac{w_p}{\sqrt{2}}$$

Likewise, when considering the resonant wavelength λ, we can express it as follows:

$$\lambda = \frac{\lambda_p}{\sqrt{2}}$$

3.3.4 Formulation of Dielectric Loss

When a dielectric is subjected to an alternating field, the three components of polarizations, namely electronic, ionic, and orientational polarizations, contribute to a complex dielectric constant. The dielectric constant now comprises both real and imaginary components and is expressed as follows:

$$\varepsilon_r = \varepsilon_r' - j\varepsilon_r'' \tag{3.112}$$

In this section, we aim to demonstrate that the imaginary part of the dielectric constant gives rise to the absorption of energy by the material from the alternating field.

Consider a parallel plate capacitor with a dielectric material having the dielectric constant ε, with ε' and ε'' representing the real and imaginary parts, respectively. Let the capacitor be subjected to an alternating field $\mathbf{E}_0 \cos(\omega t)$, and at any instant, the charge density per unit area of the plates be $\pm\mathbf{Q}(t)$, and the flux density be $\mathbf{D}(t)$. According to Gauss's law, we obtain:

$$\mathbf{D}(t) = \mathbf{Q}(t) \tag{3.113}$$

The current density is then given by the time derivative of $\mathbf{D}(t)$:

$$\mathbf{J}(t) = \frac{d\mathbf{D}(t)}{dt} \tag{3.114}$$

Since $\mathbf{E}(t)$ represents the electric field intensity at any instant t, it can be written as $\mathrm{Re}[\mathbf{E}_e]$. Therefore, for a complex dielectric constant, we can express the flux density $\mathbf{D}(t)$ as follows:

$$\mathbf{D}(t) = \mathrm{Re}[\epsilon_0 \epsilon_r E_0 e^{j\omega t}] \tag{3.115}$$

Or,

$$\mathbf{D}(t) = \epsilon_0 \epsilon_r \mathrm{Re}[\mathbf{E}_0 e^{j\omega t}] \tag{3.116}$$

By substituting Equation 3.112 into Equation 3.116, we can express the current density $\mathbf{J}(t)$ as follows:

$$\mathbf{J}(t) = \varepsilon_0 \mathrm{Re}[\varepsilon_r' - j\varepsilon_r'']j\omega \mathbf{E}_0 e^{j\omega t} = [\omega \varepsilon_0 \epsilon_r'' \mathbf{E}_0 \cos(\omega t) - \omega \varepsilon_0 \epsilon_r' \mathbf{E}_0 \sin(\omega t)] \tag{3.117}$$

Note that the imaginary part ϵ'' of the dielectric constant determines the current component that is in phase with the applied alternating field, while the real part ϵ' of the dielectric constant is out of phase by 90° with the applied field.

The instantaneous power per unit volume absorbed by the material is given by $\mathbf{J}(t)\mathbf{E}(t)$. Therefore, the power absorbed by the material per second per unit volume can be expressed as:

$$\mathbf{W}(t) = \frac{1}{2\pi} \int_0^{2\pi} \mathbf{J}(t)\mathbf{E}(t)\, d(wt) \tag{3.118}$$

Substituting the value of $J(t)$ from Equation 3.117, we obtain:

$$\mathbf{W}(t) = \frac{1}{2\pi} \int_0^{2\pi} [\omega\epsilon_0\epsilon_r''\mathbf{E}_0^2 \cos^2(\omega t) - \omega\epsilon_0\epsilon_r'\mathbf{E}_0^2 \sin^2(\omega t)]\, d(wt) \tag{3.119}$$

Simplifying the integral, we obtain:

$$\mathbf{W}(t) = \frac{\omega}{2}\epsilon_0\epsilon_r''\mathbf{E}_0^2 \tag{3.120}$$

This equation clearly shows that the energy absorbed by the dielectric material from the alternating field is directly proportional to the imaginary part of the dielectric constant ϵ'', and it is referred to as dielectric loss.

It is customary to characterize the dielectric losses in a dielectric material at a particular frequency and temperature using a factor known as the loss tangent $\tan\delta$. The loss tangent is expressed as follows:

$$\tan\delta = \frac{\epsilon_r''}{\epsilon_r'} \tag{3.121}$$

The loss tangent provides a measure of the dissipation of energy in the dielectric material and is commonly used to quantify the dielectric loss at a given frequency and temperature.

3.4 Simulation Modeling

Most of the physical phenomena, such as wave propagation, fluid dynamics, and thermal analysis, are inherently time and space-dependent. These phenomena can be mathematically described by partial differential equations (PDEs). However, when dealing with complex geometries and inhomogeneous media, finding analytical solutions to these PDEs becomes exceedingly difficult. To overcome this challenge, numerical methods are employed to approximate the solutions by discretizing the system boundaries. In this regard, computer programs play a vital role in aiding these numerical approximations.

3.4.1 Finite Element Method

One popular numerical approach used to solve PDEs is the finite element method (FEM). The FEM is known for its accuracy and efficiency, particularly when dealing with irregular shapes. The method involves dividing the domain of interest into smaller, interconnected regions called finite elements. By discretizing the domain, the PDEs can be transformed into a system of algebraic equations that can be solved using computational algorithms. The

FEM's ability to handle complex geometries and inhomogeneous media is achieved through the local approximation of the unknown functions within each finite element. These approximations, often represented by piecewise polynomials, enable the FEM to accurately capture the behavior of the physical system under consideration. Compared to other numerical approaches such as the finite difference method and the method of moments, the FEM offers several advantages [252]. Firstly, the FEM can handle irregular shapes more effectively, as the finite elements can be tailored to match the geometry of interest. Secondly, the FEM allows for the use of different types of finite elements within a single simulation, accommodating variations in material properties or geometric features. Finally, the FEM's ability to adaptively refine the mesh can enhance accuracy in regions of interest while reducing computational costs in less critical areas.
In general, the finite element method (FEM) can be divided into four steps [253]:

1. **Discretization of the Solution Boundary:** The first step in FEM involves dividing the solution boundary into a finite number of elements. Each element is a small subdomain that collectively covers the entire solution domain. This process is known as meshing or discretization. By discretizing the domain, the continuous problem is transformed into a discrete problem that can be solved numerically.

2. **Derivation of Governing Equations:** Once the solution boundary has been discretized, the next step is to derive the governing equations for a typical element. These equations are derived by applying the principles of physics and considering the behavior of the physical system within each element. Depending on the type of problem being analyzed, different governing equations may be used, such as the Navier-Stokes equations for fluid dynamics or the heat equation for thermal analysis.

3. **Assembly of Element Equations:** After obtaining the governing equations for each element, the next step is to assemble all the elements in the solution boundary. This involves combining the individual element equations to form a system of equations that represents the behavior of the entire system. By assembling the equations, the interactions between neighboring elements are taken into account, allowing for a comprehensive analysis of the system as a whole.

4. **Solution of the System Equations:** The final step in FEM is to solve the system of equations obtained from the assembly step. This involves resolving the equations to obtain the numerical solution for the problem at hand. Various numerical techniques can be employed to solve the system equations, including direct methods like Gaussian elimination or iterative methods like the conjugate gradient method. The choice of solution method depends on factors such as the size and complexity of the system, as well as the desired accuracy and computational efficiency.

The four steps outlined above provide a general framework for performing finite element analysis. By following these steps, engineers and scientists can analyze complex physical phenomena and obtain numerical solutions for a wide range of problems.
Let us consider a generalized wave equation given by:

$$\nabla^2 \mathbf{V} + k^2 \mathbf{V} = g, \tag{3.122}$$

where $\mathbf{V}$ represents the unknown field potential that needs to be determined using a numerical method, g denotes the source term, and k represents the wavenumber of the media.
To simplify the problem, we will consider the Laplace's equation, which is a special case of the generalized wave equation, given by:

$$\nabla^2 \mathbf{V} = 0, \tag{3.123}$$

assuming $k = g = 0$.
The Laplace's equation represents a steady-state condition where the field potential $\mathbf{V}$ does not vary with time. It is commonly used to solve problems where there are no sources or sinks of the field within the domain. By assuming $k = g = 0$, we eliminate any external sources or wave propagation effects, simplifying the problem to finding the solution for the Laplace's equation. Solving the Laplace's equation is important in various fields, including electrostatics, heat conduction, and fluid flow, as it allows us to determine the distribution of the field potential in the absence of sources or time-varying phenomena. Numerical methods, such as the finite element method mentioned earlier, can be employed to discretize the domain and solve the resulting system of equations obtained from the discretization process. These methods enable us to approximate the solution to the Laplace's equation and obtain the field potential $\mathbf{V}$.

3.4.1.1 Discretization of the Solution Boundary

In this section, we will consider a very simple 2D system boundary represented by three triangular finite elements, as shown in Figure 3.5. This example will help illustrate the application of the finite element method (FEM) in approximating the solution within the region.
To approximate the solution within the region, we will use the following expression:

$$\mathbf{V}(x, y) \approx \sum_{e=1}^{N} \mathbf{V}_e(x, y), \tag{3.124}$$

where $\mathbf{V}(x, y)$ represents the true solution, $\mathbf{V}_e(x, y)$ represents the solution within each finite element e, and N denotes the number of finite elements. In this specific problem region, we will keep N equal to 3.

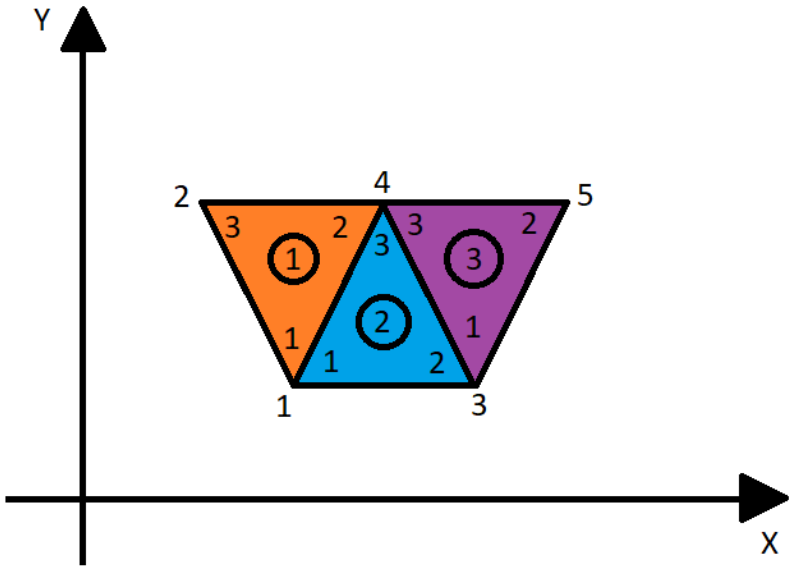

Figure 3.5: 2D system boundary represented by three triangular finite elements.

By dividing the region into smaller triangular elements and approximating the solution within each element, we can construct a piecewise representation of the true solution $\mathbf{V}(x, y)$ using the individual solutions within each finite element. This approach allows us to capture the behavior of the solution in a more localized manner and accurately represent complex geometries. The choice of triangular elements in this example is common in 2D FEM analysis due to their simplicity and ability to approximate irregular shapes effectively. However, it's important to note that in practice, more complex meshing techniques and higher-order elements are often used to achieve higher accuracy and better representation of the true solution. The solution $\mathbf{V}_e(x, y)$ within a triangular element e can be expressed as a polynomial function. Specifically, for a triangular element, $\mathbf{V}_e(x, y)$ can be approximated as follows:

$$\mathbf{V}_e(x, y) = a + bx + cy, \tag{3.125}$$

where a, b, and c are constant values that need to be determined to accurately represent $\mathbf{V}_e$ at any point within the element. The expression in Equation (3.125) represents a linear variation of $\mathbf{V}_e$ within the triangular element. This linear approximation is commonly employed due to its simplicity and efficiency, particularly in the context of FEM. By assuming a linear variation, the electric field $\mathbf{E}_e$ within the element can be approximated as well. Since the electric field is the negative gradient of the potential, it can be expressed as follows:

$$\mathbf{E}_e = -\nabla \mathbf{V}_e. \tag{3.126}$$

This assumption implies that the electric field is uniform within the element, meaning it does not vary significantly across the element. This assumption simplifies the calculation of the electric field within the element and is a common approximation made in FEM analysis.

It's important to note that while a linear approximation is used in this example, higher-order polynomial approximations can be employed for more accurate representations of the solution within each element. Additionally, other shape functions, such as quadratic or cubic functions, can also be utilized to improve the accuracy of the approximation.
In summary, within a triangular element, the solution $\mathbf{V}_e(x, y)$ can be approximated by a polynomial function. The linear approximation is commonly employed, allowing for efficient calculations. The assumption of a uniform electric field within the element simplifies the analysis and is often made in FEM applications.

3.4.1.2 Governing Equation Formulation

In the formulation of the governing equation for the finite element method, let's consider a single element from Figure 3.5 as shown in Figure 3.6.

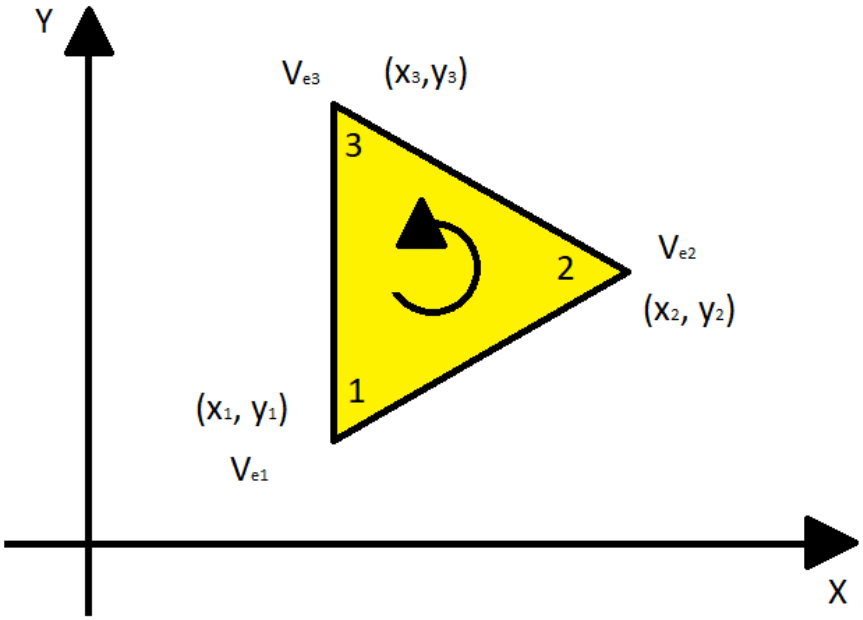

Figure 3.6: A single triangular element with three nodes.

To represent the potentials at the three nodes, we can use a vector notation:

$$[\mathbf{V}_e] = \begin{bmatrix} \mathbf{V}_{e1} \\ \mathbf{V}_{e2} \\ \mathbf{V}_{e3} \end{bmatrix} \tag{3.127}$$

where $\mathbf{V}_{e1}$, $\mathbf{V}_{e2}$, and $\mathbf{V}_{e3}$ represent the potentials at nodes 1, 2, and 3, respectively.
The potentials at the nodes can be expressed using a matrix notation:

$$[\mathbf{V}_e] = \begin{bmatrix} 1 & x_1 & y_1 \\ 1 & x_2 & y_2 \\ 1 & x_3 & y_3 \end{bmatrix} \begin{bmatrix} a \\ b \\ c \end{bmatrix} \tag{3.128}$$

where x_1, x_2, and x_3 are the x-coordinates of the nodes, and y_1, y_2, and y_3 are the y-coordinates of the nodes. The coefficients a, b, and c represent the constants that need to be determined to fully define the potentials within the element. By solving the above equation, we can obtain the values of a, b, and c, which will allow us to determine the potentials at any point within the element.

$$\begin{pmatrix} a \\ b \\ c \end{pmatrix} = \begin{pmatrix} 1 & x_1 & y_1 \\ 1 & x_2 & y_2 \\ 1 & x_3 & y_3 \end{pmatrix}^{-1} \begin{pmatrix} \mathbf{V}_{e1} \\ \mathbf{V}_{e2} \\ \mathbf{V}_{e3} \end{pmatrix} \tag{3.129}$$

Replacing the constant into Eq. 3.124, we obtain

$$\mathbf{V}_e = \sum_{i=1}^{3} \alpha_i(x, y)\mathbf{V}_{ei} \tag{3.130}$$

In the given context, the element shape functions α_1, α_2, and α_3 can be expressed as follows:

$$\alpha_1 = \frac{1}{2A}\left[(x_2y_3 - x_3y_2) + (y_2 - y_3)x + (x_3 - x_2)y\right], \tag{3.131}$$

$$\alpha_2 = \frac{1}{2A}\left[(x_3y_1 - x_1y_3) + (y_3 - y_1)x + (x_1 - x_3)y\right], \tag{3.132}$$

$$\alpha_3 = \frac{1}{2A}\left[(x_1y_2 - x_2y_1) + (y_1 - y_2)x + (x_2 - x_1)y\right] \tag{3.133}$$

where A represents the area of the element (e). The area A is given by:

$$A = \frac{1}{2}\left[(x_2 - x_1)(y_3 - y_1) - (x_3 - x_1)(y_2 - y_1)\right].$$

In the above equations, α_i represents the element shape function for node i, which describes the variation of the solution within the element. These shape functions are derived based on the element geometry and are used to interpolate the values of the solution at different points within the element. The area A is calculated using the coordinates of the three nodes (x_1, y_1), (x_2, y_2), and (x_3, y_3). The area value is positive when the nodes are numbered counterclockwise, which is the convention commonly followed. These shape functions and the element area are fundamental components in the finite element method. They are used to express the solution within the element and play a crucial role in the formulation of the governing equations and the overall analysis.

By employing the Laplace equation, the corresponding per unit length energy can be ex-

pressed as follows:

$$\mathbf{W}_e = \frac{1}{2}\int \varepsilon |\mathbf{E}_e|^2 dS = \frac{1}{2}\int \varepsilon |\nabla \mathbf{V}_e|^2 dS \tag{3.134}$$

where ε is the permittivity of the medium, $\mathbf{E}_e$ denotes the electric field within the element, and $\mathbf{V}_e$ represents the potential at any point within the element. The energy $\mathbf{W}_e$ is obtained by integrating the square of the electric field magnitude or the square of the gradient of the potential over the element domain. This energy quantity is often used in finite element analysis to evaluate the behavior and properties of the electrical field within the system. In the equation, $|\mathbf{E}_e|$ represents the magnitude of the electric field, and $|\nabla \mathbf{V}_e|$ represents the magnitude of the gradient of the potential. The integration is performed over the element domain, which is determined by the shape and size of the element. The permittivity ε characterizes the electrical properties of the medium, and it is a material-specific constant that relates the electric field to the electric displacement within the medium. Calculating the energy $\mathbf{W}_e$ provides valuable insights into the behavior and distribution of the electric field within the element.

From Eq. 3.130, we obtain:

$$\nabla \mathbf{V}_e = \sum_{i=1}^{3} \mathbf{V}_{ei} \nabla \alpha_i \tag{3.135}$$

Matrix form of the derived equation, placing Eq. 3.134 into Eq. 3.135 is,

$$\mathbf{W}_e = \frac{1}{2}\varepsilon [\mathbf{V}_e]^t [\mathbf{C}^{(e)}][\mathbf{V}_e] \tag{3.136}$$

In this context, the superscript t denotes the transpose of $\mathbf{V}_e$,

$$\mathbf{C}_{ij}^{(e)} = \int (\nabla \alpha_i \cdot \nabla \alpha_j) dS \tag{3.137}$$

The symbol $\mathbf{C}_e$ represents the element coefficient matrix, which is defined as follows:

$$|\mathbf{C}^{(e)}| = \begin{bmatrix} \mathbf{C}_{11}^{(e)} & \mathbf{C}_{12}^{(e)} & \mathbf{C}_{13}^{(e)} \\ \mathbf{C}_{21}^{(e)} & \mathbf{C}_{22}^{(e)} & \mathbf{C}_{23}^{(e)} \\ \mathbf{C}_{31}^{(e)} & \mathbf{C}_{32}^{(e)} & \mathbf{C}_{33}^{(e)} \end{bmatrix} \tag{3.138}$$

Each element $\mathbf{C}_{ij}^{(e)}$ in the matrix corresponds to a particular physical property or parameter that characterizes the behavior of the finite element model.

It's important to note that in a larger mesh with multiple elements, the potentials at the shared nodes between adjacent elements must be compatible to ensure continuity of the solution across the boundaries. This is typically achieved through the assembly of the global system of equations and applying appropriate boundary conditions.

3.4.1.3 Assembly of Element Equations

To address the overall boundary solution, N number of elements from a single element can be accumulated. The total energy of the accumulated elements is represented as follows:

$$\mathbf{W} = \sum_{e=1}^{N} \mathbf{W}_e = \frac{1}{2}\varepsilon[\mathbf{V}]^T[\mathbf{C}][\mathbf{V}], \tag{3.139}$$

where $[\mathbf{V}]$ is a column vector representing the accumulated nodal potentials:

$$[\mathbf{V}] = \begin{bmatrix} \mathbf{V}_1 \\ \mathbf{V}_2 \\ \mathbf{V}_3 \\ \vdots \\ \mathbf{V}_n \end{bmatrix},$$

and n denotes the total number of nodes in an element. N is the total number of elements within the solution boundary, and $[\mathbf{C}]$ presents the global coefficient matrix consisting of the element coefficient matrix.

Considering the global numbering, the global coefficient matrix of size 5×5 is expressed as:

$$[\mathbf{C}] = \begin{bmatrix} \mathbf{C}_{11} & \mathbf{C}_{12} & \mathbf{C}_{13} & \mathbf{C}_{14} & \mathbf{C}_{15} \\ \mathbf{C}_{21} & \mathbf{C}_{22} & \mathbf{C}_{23} & \mathbf{C}_{24} & \mathbf{C}_{25} \\ \mathbf{C}_{31} & \mathbf{C}_{32} & \mathbf{C}_{33} & \mathbf{C}_{34} & \mathbf{C}_{35} \\ \mathbf{C}_{41} & \mathbf{C}_{42} & \mathbf{C}_{43} & \mathbf{C}_{44} & \mathbf{C}_{45} \\ \mathbf{C}_{51} & \mathbf{C}_{52} & \mathbf{C}_{53} & \mathbf{C}_{54} & \mathbf{C}_{55} \end{bmatrix}$$

Here, $\mathbf{C}_{ij}$ presents the coupling of i and j. For an element, the inter-element boundary potentials are identical. Hence, $\mathbf{C}_{ij}$ will have involvement from the associated elements of node i and j.

The global coefficient will be zero without direct correspondence with the nodes. The global coefficient matrix is symmetric, given by:

$$\mathbf{C}_{ij} = \mathbf{C}_{ji}.$$

The expression of the global coefficient matrix in terms of the element coefficient matrix is:

$$[\mathbf{C}] = \begin{bmatrix} \mathbf{C}_{11}^{(1)} + \mathbf{C}_{11}^{(2)} & \mathbf{C}_{13}^{(1)} & \mathbf{C}_{12}^{(2)} & \mathbf{C}_{12}^{(1)} + \mathbf{C}_{13}^{(2)} & 0 \\ \mathbf{C}_{31}^{(1)} & \mathbf{C}_{33}(1) & 0 & \mathbf{C}_{32}(1) & 0 \\ \mathbf{C}_{21}^{(2)} & 0 & C_{22}^{(2)} + \mathbf{C}_{11}^{(3)} & \mathbf{C}_{23}^{(2)} + \mathbf{C}_{13}^{(3)} & \mathbf{C}_{12}^{(3)} \\ \mathbf{C}_{21}^{(1)} + \mathbf{C}_{31}^{(2)} & \mathbf{C}_{23}^{(1)} & \mathbf{C}_{32}^{(2)} + \mathbf{C}_{31}^{(3)} & \mathbf{C}_{22}^{(1)} + \mathbf{C}_{33}^{(2)} + \mathbf{C}_{33}^{(3)} & \mathbf{C}_{32}^{(}3) \\ 0 & 0 & \mathbf{C}_{21}^{(3)} & \mathbf{C}_{23}^{(3)} & \mathbf{C}_{22}^{(3)} \end{bmatrix}$$

Here, $\mathbf{C}_{ij}$ represents the coupling between nodes i and j. The subscripts (1), (2), and (3) refer to the respective elements. The global coefficient matrix is formed by combining the coefficients of the element matrices. The diagonal elements of the global matrix are the sum of the corresponding diagonal elements of the element matrices, while the off-diagonal elements involve the interactions between the elements. The matrix is symmetric due to the symmetry property of the coefficients.

3.4.1.4 Solution of the System Equations

To meet the requirements of the Laplace equations, the solution region should have minimum total energy. So, partial differentiation of each node value will yield zero. Hence,

$$\frac{\partial \mathbf{W}}{\partial \mathbf{V}_k} = 0, \quad k = 1, 2, \ldots, n. \tag{3.140}$$

By performing the partial derivative of $\mathbf{W}$ in terms of $\mathbf{V}_1$, we can obtain:

$$\frac{\partial \mathbf{W}}{\partial \mathbf{V}_k} = 0 = \mathbf{V}_1\mathbf{C}_{11} + \mathbf{V}_2\mathbf{C}_{12} + \mathbf{V}_3\mathbf{C}_{13} + \mathbf{V}_4\mathbf{C}_{14} + \mathbf{V}_5\mathbf{C}_{15}. \tag{3.141}$$

So, the generalized expression is

$$\frac{\partial \mathbf{W}}{\partial \mathbf{V}_k} = 0 = \sum_{i=1}^{n} \mathbf{V}_i\mathbf{C}_{ik}. \tag{3.142}$$

Considering node 1 as independent, from Equation 3.141, it is formulated as

$$\mathbf{V}_1 = -\frac{1}{\mathbf{C}_{11}} \sum_{i=2}^{5} \mathbf{V}_i\mathbf{C}_{ik}.$$

Hence, the generalized form is

$$\mathbf{V}_k = -\frac{1}{\mathbf{C}_{kk}} \sum_{\substack{i=1 \\ i \neq k}}^{n} \mathbf{V}_i\mathbf{C}_{ik}.$$

Here, k denotes the independent node. Without the connection between node i and k, $\mathbf{C}_{ik}$ is zero. Nodes directly connected with k will have $\mathbf{V}_k$. The initial values of the potential will remain unchanged, while unknown potentials will be set to zero. During the numerical calculation, all the free nodes are approximated using the initial values in the first iteration. In the subsequent iterations, the approximated values are replaced with the initial values. This iteration continues until a tolerable error in the approximation is achieved.

Electric field energy is the energy associated with an electric field in a specific region of space. It represents the potential energy stored in the electric field due to the arrangement

of charges or the presence of electric potential differences [254]. The electric field energy density, represented by $\mathbf{W}_E$, is the amount of energy per unit volume stored in the electric field [255]. It is calculated using the formula:

$$\mathbf{W}_E = \frac{1}{2}\epsilon_0 |\mathbf{E}|^2 \tag{3.143}$$

where ϵ_0 is the vacuum permittivity and E is the magnitude of the electric field vector. This equation shows that the electric field energy density is directly proportional to the square of the electric field magnitude and inversely proportional to the vacuum permittivity. The factor of $\frac{1}{2}$ arises because the electric field energy results from the interaction between charges, and each charge contributes equally to the total energy. To calculate the total electric field energy within a specific volume, one must integrate the energy density over that volume. The total energy U is given by:

$$U = \iiint \mathbf{W}_E \, dV \tag{3.144}$$

where the triple integral is taken over the entire volume of interest. The concept of electric field energy is essential in various applications and phenomena. It helps us understand the behavior of electric fields and their effects on charged particles and systems. For example, in capacitors, electric field energy is stored in the electric field between the capacitor plates when a potential difference is applied. This energy can be released when the capacitor discharges. Electric field energy is also crucial in studying the interaction between electric fields and matter. It provides insights into the forces experienced by charged particles, their dynamics in electric fields, and the behavior of dielectric materials in electric fields.

3.5 Boundary Conditions

3.5.1 Scattering Boundary Conditions

Scattering Boundary Condition is a condition applied at the simulation window to create a transparent boundary for the incoming and outgoing (scattered) signals. It allows the simulation to accurately model the behavior of waves interacting with the boundary. The outgoing (scattered) wave, for which the simulation window is perfectly transparent, can be expressed in different coordinate systems.

In the case of a plane wave, the outgoing wave can be written as:

$$\mathbf{E} = \mathbf{E}_{\text{SC}} e^{-j\mathbf{k}(\mathbf{n}\cdot\mathbf{r})} + \mathbf{E}_0 e^{-j\mathbf{k}(\mathbf{K}\cdot\mathbf{r})} \tag{3.145}$$

where $\mathbf{E}_{\text{SC}}$ is the scattered field, $\mathbf{E}_0$ represents the incident plane wave propagating along the $\mathbf{k}$ direction, and $\mathbf{n}$ is the unit normal vector pointing outwards from the simulation window.

The term $\mathbf{E}_{\text{SC}}e^{-j\mathbf{k}\cdot\mathbf{nr}}$ represents the scattered wave, while $\mathbf{E}_0 e^{-j\mathbf{k}\cdot\mathbf{Kr}}$ represents the incident wave. This plane scattered wave condition allows the transparent transmission of the incident wave at any angle, while the outgoing (scattered) waves are perfectly transparent for the perpendicularly incident wave and partially transparent for obliquely incident outgoing (scattered) waves.

In the case of a cylindrical wave, the outgoing wave can be expressed as:

$$\mathbf{E} = \mathbf{E}_{\text{SC}}e^{-j\mathbf{k}\frac{(\mathbf{n}\cdot\mathbf{r})}{\sqrt{r}}} + \mathbf{E}_0 e^{-j\mathbf{k}(\mathbf{K}\cdot\mathbf{r})} \tag{3.146}$$

where $\sqrt{r}$ accounts for the cylindrical wave nature. This cylindrical scattered wave condition ensures the transparent behavior of the outgoing waves while considering the cylindrical coordinate system.

Similarly, in the case of a spherical wave, the outgoing wave can be described as:

$$\mathbf{E} = \mathbf{E}_{\text{SC}}e^{-j\mathbf{k}\frac{(\mathbf{n}\cdot\mathbf{r})}{r_s}} + \mathbf{E}_0 e^{-j\mathbf{k}(\mathbf{K}\cdot\mathbf{r})} \tag{3.147}$$

where r_s represents the spherical wave nature. This spherical scattered wave condition allows the transparent behavior of the outgoing waves while considering the spherical coordinate system.

In all these expressions, the scattered field $\mathbf{E}_{\text{SC}}$ and the incident field $\mathbf{E}_0$ play crucial roles in determining the behavior of the waves at the simulation window. The transparent boundary condition ensures that the incoming waves are not reflected or absorbed at the boundary but instead continue to propagate through the simulation region. It allows the accurate simulation of wave interactions and propagation in a larger domain. The scattering boundary condition is particularly useful for simulating electromagnetic wave propagation, acoustic wave propagation, and other wave phenomena. By considering the appropriate coordinate system and expressing the outgoing (scattered) waves in terms of the scattered field and incident field, the condition enables the simulation to accurately capture the behavior of waves at the boundary. It enables the simulation of wave propagation and scattering phenomena in a finite computational domain, allowing researchers to study the behavior of electromagnetic waves in various practical scenarios. The significance of scattering boundary conditions in solving electromagnetic wave problems can be understood through the following points:

1. **Realistic Simulation:** Electromagnetic waves often encounter boundaries in real-world scenarios, such as objects, structures, or open spaces. By applying scattering boundary conditions, researchers can simulate these scenarios and accurately capture the interaction between waves and boundaries. This enables the study of wave propagation, scattering, and diffraction phenomena, providing insights into the behavior of electromagnetic waves in complex environments.

2. **Transparent Boundary:** Scattering boundary conditions provide a transparent bound-

ary for incoming and outgoing waves. This means that incident waves are not reflected or absorbed at the boundary but continue to propagate through the computational domain. This transparent behavior allows researchers to focus on the interaction of waves with the objects or structures of interest, without disturbances caused by spurious reflections.

3. **Conservation of Energy:** Scattering boundary conditions ensure that energy is conserved in the computational domain. By allowing the transmission of incident waves through the boundary, they maintain the balance between incident, transmitted, and scattered fields. This conservation of energy is essential for obtaining accurate and physically meaningful results in electromagnetic simulations.

4. **Numerical Stability:** When solving electromagnetic wave problems numerically, scattering boundary conditions help maintain numerical stability. They prevent wave reflections and associated numerical artifacts that could lead to instabilities or inaccuracies in the simulation. By incorporating transparent boundaries, scattering boundary conditions enhance the convergence and reliability of numerical methods used for solving Maxwell's equations.

5. **Flexible Modeling:** Scattering boundary conditions offer flexibility in modeling different types of boundaries and geometries. They can be applied to various boundary shapes, such as planar, curved, or irregular surfaces, allowing researchers to simulate a wide range of scenarios encountered in practical electromagnetic wave problems. This flexibility enables the investigation of wave interactions with complex objects, such as antennas, scattering structures, or waveguides.

6. **Wave Scattering Analysis:** Scattering boundary conditions facilitate the analysis of wave scattering phenomena. By studying the characteristics of the scattered field, researchers can extract valuable information about the interaction between electromagnetic waves and objects. This analysis includes determining scattering cross-sections, identifying resonance phenomena, and studying the influence of different object geometries and materials on wave scattering behavior.

3.5.2 Port Boundary Conditions

Ports are the boundary conditions applied in electromagnetic devices to present input and output terminals. Scattering parameters are associated with these boundary conditions. To ensure consistent power flow through the respective ports, the fields $\mathbf{E}_1$, $\mathbf{E}_2$, $\mathbf{E}_3$, etc. are normalized. The power flow can be determined using the time-average Poynting vector, given by:

$$\mathbf{S}_{\text{av}} = \frac{1}{2}\text{Re}(\mathbf{E} \times \mathbf{H}^*) \tag{3.148}$$

The total power radiating from the port can be calculated by considering the orthogonal component of the Poynting vector, denoted by $\mathbf{n}$. The expression for the power flow is:

$$n \cdot \mathbf{S}_{\text{av}} = \mathbf{n} \cdot \frac{1}{2}\text{Re}(\mathbf{E} \times \mathbf{H}^*) \tag{3.149}$$

Under the cutoff frequency, the radiated power is zero, making it impossible to normalize the fields. However, in this region, the S-parameters can be considered trivial, and therefore, their calculation is not required.

For TE waves, the electric field is given by

$$\mathbf{E} = -\mathbf{Z}_{TE}\mathbf{E} \times \mathbf{H} \tag{3.150}$$

Here, $\mathbf{Z}_{TE}$ represents the wave impedance, which is defined as

$$\mathbf{Z}_{TE} = \frac{\omega\mu}{\beta} \tag{3.151}$$

In this equation, ω represents the angular frequency of the wave, μ denotes the permeability, and β is the propagation constant. The power flow through the port can be expressed as

$$\begin{aligned} \mathbf{n} \cdot \mathbf{S}_{\text{av}} &= \mathbf{n} \cdot \frac{1}{2}\text{Re}(\mathbf{E} \times \mathbf{H}^*) \\ &= -\frac{1}{2}\text{Re}(\mathbf{E} \cdot (\mathbf{n} \times \mathbf{H}^*)) \\ &= \frac{1}{2Z_{TE}}|\mathbf{E}|^2 \end{aligned} \tag{3.152}$$

In this equation, $\mathbf{n}$ represents the normal vector, $\mathbf{S}_{\text{av}}$ is the time-average Poynting vector, $\mathbf{E}$ and $\mathbf{H}$ are the electric and magnetic fields respectively. Equation 3.152 shows that the power flow through the port is equal to half of the wave impedance $\mathbf{Z}_{TE}$ times the magnitude squared of the electric field $|\mathbf{E}|^2$. For TM waves, the magnetic field is given by

$$\mathbf{H} = \frac{1}{\mathbf{Z}_{TM}}\mathbf{n} \times \mathbf{E} \quad (3.70) \tag{3.153}$$

Here, $\mathbf{Z}_{TM}$ represents the wave impedance, which is defined as

$$\mathbf{Z}_{TM} = \frac{\beta}{\omega\epsilon} \tag{3.154}$$

In this equation, β represents the propagation constant, ω denotes the angular frequency of the wave, and ϵ is the permittivity. The power flow through the port can be expressed as

$$\begin{aligned}\mathbf{n}\cdot\mathbf{S}_{\text{av}} &= \frac{1}{2}\mathbf{n}\cdot\text{Re}(\mathbf{E}\times\mathbf{H}^*)\\ &= \frac{1}{2\mathbf{Z}_{TM}}\mathbf{n}\cdot\text{Re}(\mathbf{E}\times(\mathbf{n}\times\mathbf{E}^*))\\ &= \frac{1}{2\mathbf{Z}_{TM}}|\mathbf{n}\times\mathbf{E}|^2\end{aligned} \tag{3.155}$$

In this equation, $\mathbf{n}$ represents the normal vector, $\mathbf{S}_{\text{av}}$ is the time-average Poynting vector, $\mathbf{E}$ is the electric field. Equation 3.155 shows that the power flow through the port is equal to half of the wave impedance $\mathbf{Z}_{TM}$ times the magnitude squared of the vector $\mathbf{n}\times\mathbf{E}$.

3.6 Performance Metrices

3.6.1 Transmittance

Transmittance refers to the power transmitted through the sensor structure relative to the incident power. When light interacts with a refractive index sensor, a portion of the incident power is reflected, a portion is transmitted, and a portion is absorbed. The transmittance specifically quantifies the transmitted power. It is calculated as the ratio of the power transmitted through the sensor to the power incident on the sensor. Usually in a refractive index sensor, there is a waveguide. In the waveguide, from one side electromagnetic waves enter which is called as input port and from another side of the waveguide, all these waves leave and that is called the output port. Integral of the energy flux density in each port is known as the power at each port. Mathematically, Transmittance can be expressed as:

$$\begin{aligned}T &= P_{out}/P_{in},\\ P_{out} &= \int P_{oavx}dS_2,\\ P_{in} &= \int P_{oavx}dS_1\end{aligned} \tag{3.156}$$

P_{oavx} is the x-axis component of time-averaged power. A component of the E field acting along the surface in the same direction as the wave vector is required to generate a surface plasmon. SPR can only be induced when the polarization state is normal/perpendicular to the boundary between metal and dielectric. In practice, the TM-polarized incident wave can flow through the bus waveguide port and be measured at the output port.

In terms of S-parameter, transmittance can be defined as the square of the transmission coefficient from input port to output port. Mathematically, transmittance can be expressed as:

$$T = |S_{21}|^2 \tag{3.157}$$

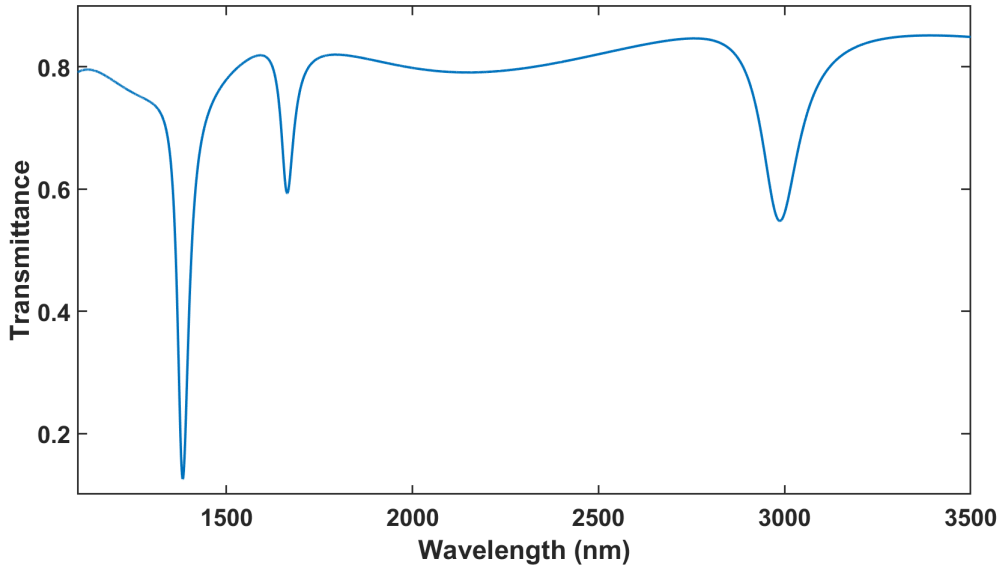

Figure 3.7: Transmittance of a sensor

Fig. 3.7 shows the transmittance curve for a refractive index value of a sensor. This transmittance curve value can vary depending on the design of the sensor. At the wavelength where resonance occurs, we can see dips in the transmittance curves. In the figure, we can see three dips all together. First one has the biggest dip because at that wavelength the resonance between the waveguide and sensor is the most. Second dip is a bit small because the resonance is not that strong but the third dip is bigger than the second one.

3.6.2 Sensitivity

The sensitivity of a refractive index sensor relates to its ability to detect minor changes in the refractive index of the surrounding medium. It is a critical design and performance metric that quantifies the sensor's measurement precision. A refractive index sensor's sensitivity is normally assessed by the shift in the resonance wavelength per unit change in the refractive index of the material being sensed. The perceived mediums are dielectric in nature, and each substance has various dielectric materials. A material's refractive index can also change depending on physical conditions, such as temperature. On the other hand, the resonance wavelength of a sensor is the wavelength at which SPPs are well coupled with the resonator, which results in a standing wave field pattern. It is the specific wavelength at which the sensor exhibits maximum sensitivity to changes in the refractive index.

The formula of the refractive index sensor's sensitivity is given below:

$$S = \frac{\Delta\lambda_{res}}{\Delta n} \tag{3.158}$$

Here, $\Delta\lambda$ represents the shift in resonance wavelength where the transmission curve shows a valley. Δn represents the change in the refractive index of the dielectric material that is being sensed. The unit of sensitivity is expressed in nm/RIU.

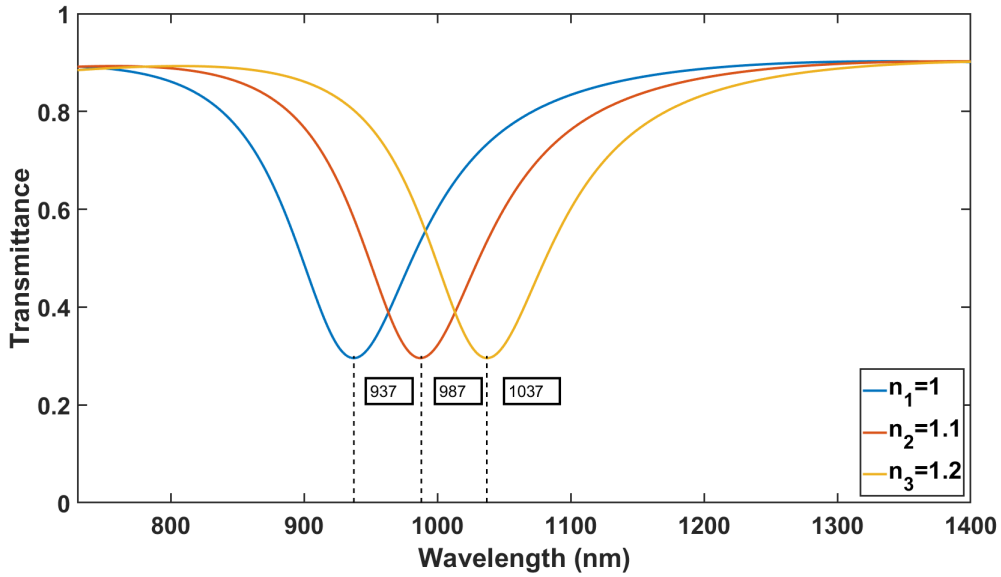

Figure 3.8: Sensitivity

From Fig. 3.8, we can see that there are three transmittance curves shown for three different refractive indexes. The blue curve shows the transmittance curve of a dielectric material that has a refractive index value of 1. It has a resonance wavelength of 937 nm which means that at that value, there will be a valley in the transmission curve showing a strong resonance between the waveguide and the resonator. The orange curve shows the transmittance curve of a dielectric material that has a refractive index value of 1.1. It has a resonance wavelength of 987 nm which means that at that value there will be a valley in the transmission curve showing a strong resonance between the waveguide and the resonator. The yellow curve shows the transmittance curve of a dielectric material that has a refractive index value of 1.2. It has a resonance wavelength of 1037 nm which means that at that value there will be a valley in the transmission curve showing a strong resonance between the waveguide and the resonator.

Now for the curve of blue and orange, the shift in resonance wavelength is (987-937) = 50 nm and the change in refractive index is (1.1-1)=0.1. So, the sensitivity value is (50/0.1) = 500 nm/RIU. For the curve of orange and yellow, shift in resonance wavelength is (1037-987) = 50 nm and change in refractive index is (1.2-1.1)=0.1. So, the sensitivity value is (50/0.1) = 500 nm/RIU. And for the curve of blue and yellow, shift in resonance wavelength is (1037-937) = 100 nm and change in refractive index is (1.2-1)=0.2. So, the sensitivity

value is (100/0.2) = 500 nm/RIU. This is how sensitivity is calculated from the transmittance curve given for different refractive indexes.

3.6.3 Figure of Merit

The figure of merit (FOM) is a data used to assess the overall performance of Refractive index sensors. It combines the sensor's sensitivity to refractive index changes with its sensing resolution to provide an in-depth evaluation of its capabilities. The FOM is defined as the ratio of the sensitivity (S) to the full width at half maximum (FWHM) of the transmittance curve. Whenever the sensitivity of a RI sensor increases, it is usually assumed that FOM will also increase but that is not always the case. Whenever the sensitivity of a RI sensor is increased due to changes in its design, a trade off occurs with the FWHM value. The FWHM value also usually increases. As a result, the FOM value usually degrades or remains the same. It reduces the sensing resolution and affects the ability to precisely measure changes in the refractive index. So when we are considering the performance parameters of a RI sensor, FOM value should also be considered with the sensitivity value. Mathematically, FOM can be expressed as:

$$FOM = \frac{S}{FWHM} \tag{3.159}$$

Sensitivity is defined as the ability of the sensor to detect minor changes in the refractive index of the surrounding medium as it has been described in the previous section. On the other hand Full width half maximum refers to the width of a transmittance curve at the average value of the whole transmittance curve.

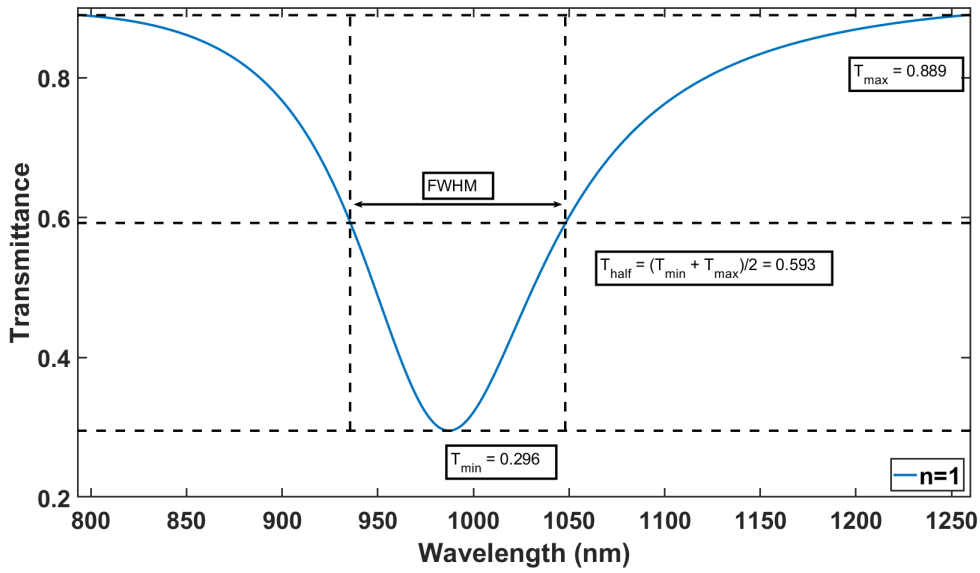

Figure 3.9: Calculation of FWHM for Symmetrical Curve

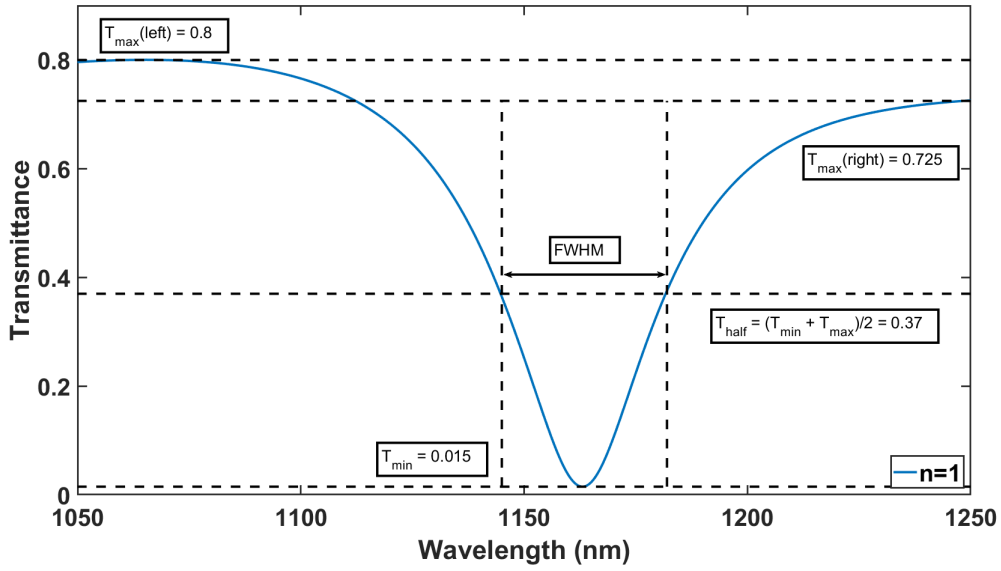

Figure 3.10: Calculation of FWHM for Asymmetrical Curve

In Fig. 3.9, we can see a symmetrical transmittance dip in the figure. Let us assume that the sensitivity value of this transmittance curve is 500 nm/RIU. Now in this curve, The highest value of the transmittance curve Tmax is 0.889 and the lowest value Tmin is 0.296. So the average or at the half point of the transmittance curve, the value is (0.889+0.296)/2 = 0.593. So at the transmittance value of 0.593, whatever the value of the width of the transmittance curve is, it is called the full width at half maximum.

The value of FWHM for an asymmetrical curve is a bit different. In Fig. 3.10, we can see that The transmittance curve is not symmetrical. The highest value of transmittance is different at two sides. The left side has a higher value of maximum transmittance and the right side has a lower value than the left side. So all the calculation is the same as before but for the value of maximum transmittance T_{max}, we will consider the lower value because up to the lower value, the transmittance curve exists on both sides but after that up to the higher value, no transmittance curve exists on the right side. So the highest value of the transmittance curve T_{max} is 0.725 and the lowest value T_{min} is 0.015. So the average or at the half point of the transmittance curve, the value is (0.725+0.015)/2 = 0.37. So at the transmittance value of 0.37, whatever the value of the width of the transmittance curve is, it is called the full width at half maximum for the asymmetrical transmittance curve.

3.6.4 Quality Factor

The Q factor, commonly referred to as the quality factor, is a dimensionless metric that describes the sharpness or selectivity of resonant dips. The ratio of the resonant peak wavelength to the full width at half maximum (FWHM) bandwidth is described as the Q factor. Mathematically, Q factor can be expressed as:

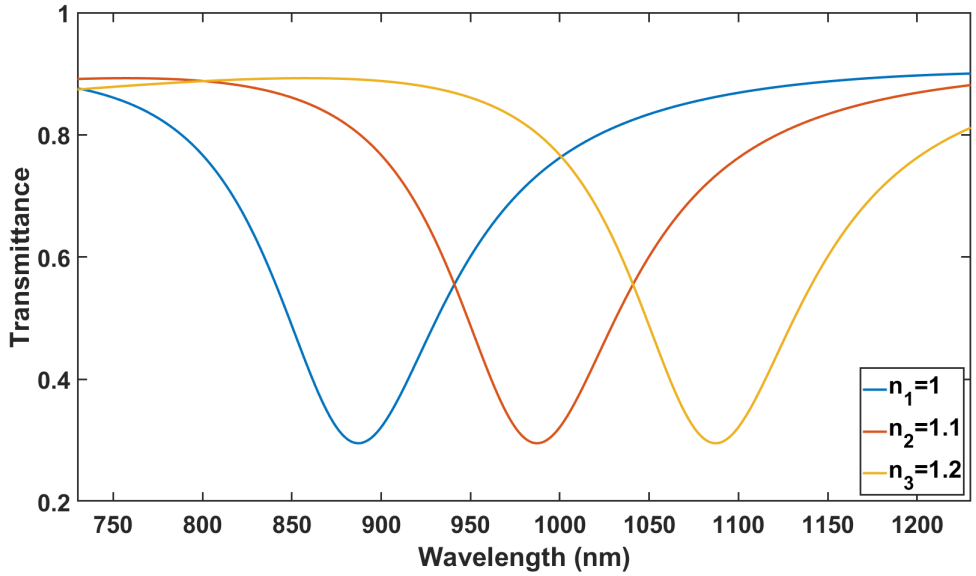

Figure 3.11: High Q-factor

$$Q = \frac{\lambda_{res}}{FWHM} \tag{3.160}$$

The resonance peak wavelength of a sensor is the value of wavelength where SPPs are well coupled with the resonator which results in a standing wave field pattern. It is the specific wavelength at which the sensor exhibits maximum sensitivity to changes in the refractive index. Due to the resonance between the waveguide and the resonator a dip is observed in the transmittance curve. This dip has a specific sharpness and and as a result in a sensor which is more selective in detecting changes in the refractive index of the surrounding medium. This means that the sensor can more effectively distinguish small changes in the refractive index of the medium being measured.

Fig. 3.11 and 3.12 both show three transmittance curves of different refractive indexes. In both cases the resonant peak wavelengths are almost the same but for the first one the FWHM values are more compared to the later three ones. As a result, the later ones show more sharpness and their quality to detect small changes in the refractive index of the medium is more. So simply the three curves in the later portions shows more quality factor.

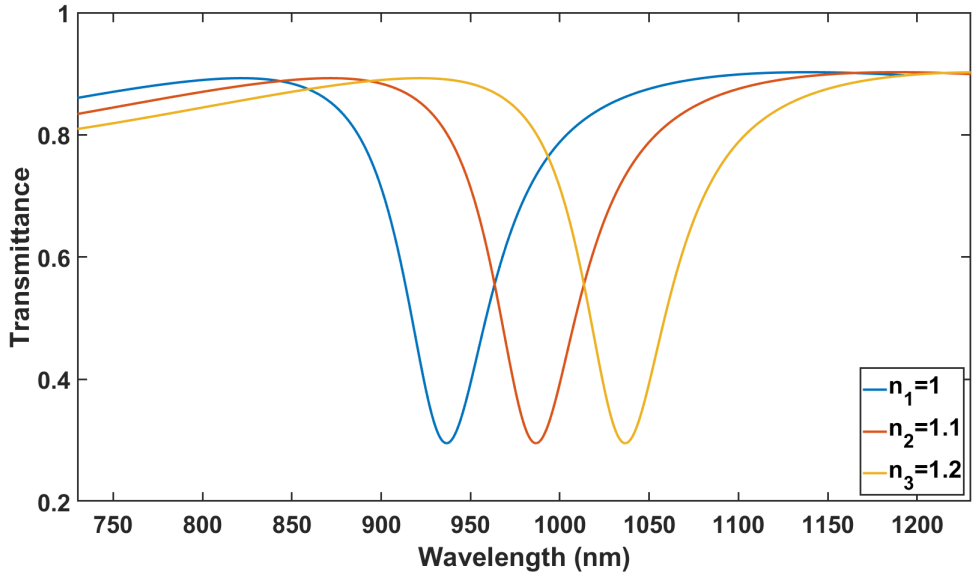

Figure 3.12: Low Q-factor

3.6.5 Sensing Resolution

A refractive index sensor's sensing resolution refers to the smallest change in refractive index that the sensor can detect or resolve. It is a key measure of the sensor's performance and sensitivity to changes in the refractive index of the medium in which it is placed. A sensor with a higher sensing resolution can detect smaller changes in refractive index, whereas a sensor with a lower sensing resolution would need to detect bigger changes in refractive index.

Sensing resolution is the ratio of the minimum ratio of the optical spectral analyzer to the value of sensitivity. Mathematically, sensing resolution can be expressed as:

$$SR = \frac{\Delta\lambda}{S} \tag{3.161}$$

where, $\Delta\lambda$ is the minimum resolution of the optical spectrum analyzer. Commercially, the value of the optical spectral analyzer is usually assumed to be 0.001 nm. Higher the value of sensing resolution, more the capability of detecting small changes.

3.6.6 Excitation Ratio

The excitation ratio (ER) is defined as the difference between the maximum and minimum values of transmittance value. It quantifies the dynamic range or the extent of change in the sensor's transmittance value. A higher excitation ratio indicates a larger difference between the maximum and minimum transmittance values, which implies that the sensor can detect and respond to a broader range of refractive index changes. It is generally desired as it allows for more accurate and precise measurements. Mathematically, Excitation Ratio can

be expressed as:

$$ER = T_{max} - T_{min} \tag{3.162}$$

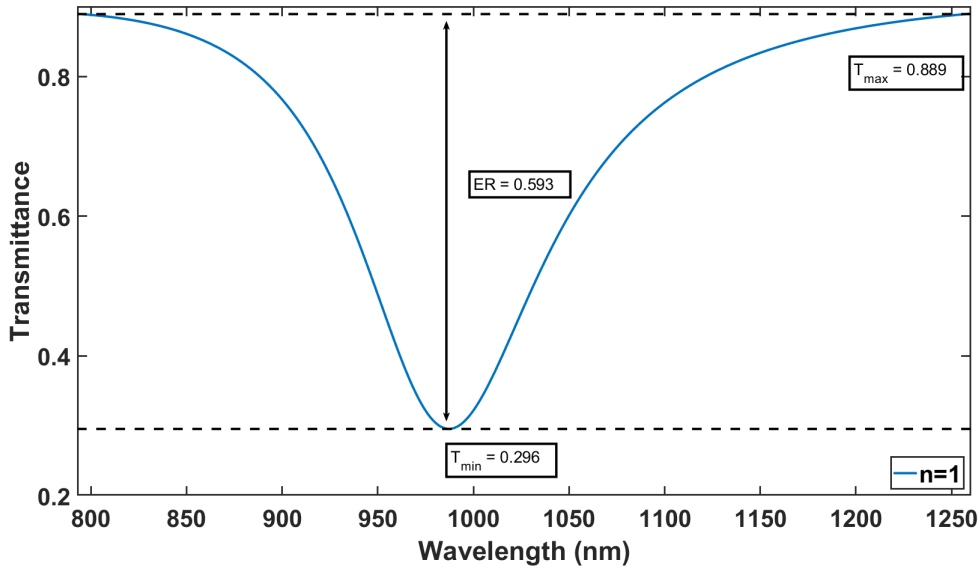

Figure 3.13: Excitation Ratio for Symmetrical Curve

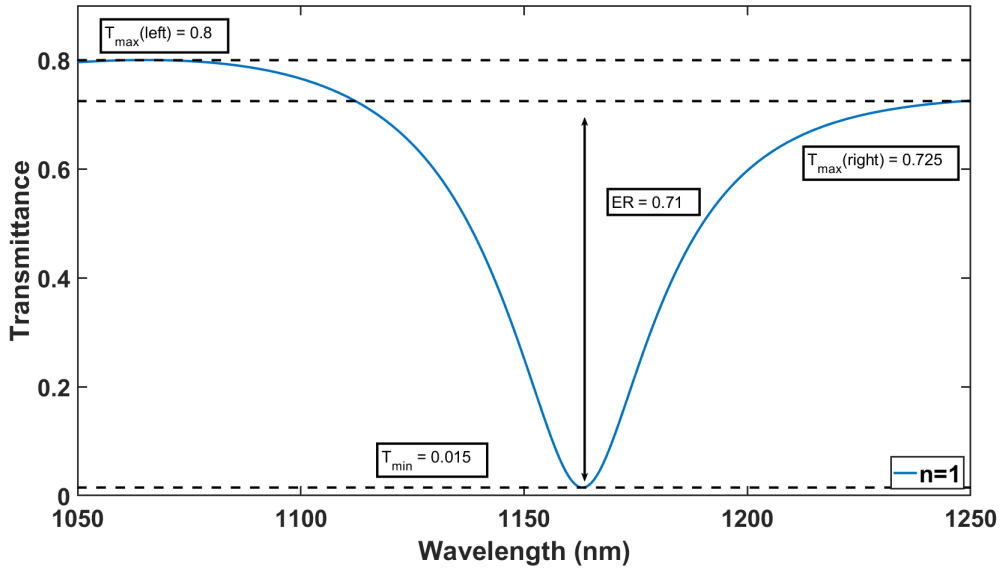

Figure 3.14: Excitation Ratio for Asymmetrical Curve

Fig. 3.13 shows the transmittance curve of the sensor for a specific refractive index value which is symmetrical in nature. Now if we want to know the excitation ratio value for this case then the maximum transmittance value is T_{max} = 0.889 and minimum value is T_{min}= 0.296. So the excitation ratio for this case is (0.889-0.296) = 0.593. For the case of an asymmetrical curve it is a bit different. Fig. 3.14, we can see that The transmittance curve

is not symmetrical. The highest value of transmittance is different at two sides. The left side has a higher value of maximum transmittance and the right side has a lower value than the left side. So all the calculation is the same as before but for the value of maximum transmittance T_{max}, we will consider the lower value because up to the lower value, the transmittance curve exists on both sides but after that up to the higher value, no transmittance curve exists on the right side. So the highest value of the transmittance curve Tmax is 0.725 and the lowest value T_{min} is 0.015. So the excitation ratio for this case is (0.725-0.015) = 0.71.

3.7 RI Sensor Fabrication Process

The fabrication process of refractive index (RI) sensors involves a series of intricate steps aimed at creating plasmonic nanosensors that can detect and quantify minute changes in the refractive index of the surrounding medium. These sensors harness the remarkable phenomenon known as localized surface plasmon resonance (LSPR), which occurs when plasmonic nanoparticles interact with electromagnetic waves, leading to strong resonant scattering and absorption. The RI sensor fabrication process encompasses a comprehensive range of techniques and methodologies, carefully orchestrated to optimize sensor performance and sensitivity. It typically commences with the synthesis of plasmonic nanoparticles, where materials with excellent plasmonic properties, such as gold or silver, are often chosen due to their ability to exhibit intense plasmonic responses in the desired wavelength range. The nanoparticles are then functionalized to enhance their stability, biocompatibility, and functionality by modifying their surface with specific ligands, antibodies, or DNA strands. In parallel, the substrate upon which the plasmonic nanosensors will be constructed undergoes meticulous preparation, involving thorough cleaning and potential surface modifications to facilitate nanoparticle adhesion and introduce specific surface chemistries. The subsequent step involves the controlled deposition of the plasmonic nanoparticles onto the prepared substrate, employing various techniques such as spin coating, dip coating, or drop-casting, with parameters carefully adjusted to optimize nanoparticle density and uniformity. To achieve enhanced sensing capabilities and tailored functionalities, advanced patterning techniques, including electron beam lithography or photolithography, are often employed to precisely define the geometry and arrangement of the plasmonic nanosensors, enabling the creation of sensor arrays or specific patterns. Optionally, a protective layer, such as a polymer or silica coating, can be applied to encapsulate the plasmonic nanosensors, shielding them from environmental factors, improving stability, and preventing nanoparticle aggregation. Throughout the fabrication process, rigorous characterization techniques such as scanning electron microscopy (SEM), atomic force microscopy (AFM), and spectroscopic measurements are employed to analyze the morphology, structure, and optical properties of the fabricated RI sensors. Subsequently, the sensors' performance is evaluated using diverse testing methods such as surface-enhanced Raman spectroscopy (SERS), surface plasmon resonance (SPR),

or localized surface plasmon resonance (LSPR). The optimization and iteration phase follows, where the fabrication process and sensor design are refined and improved based on the characterization and testing results. This iterative approach ensures the development of highly sensitive and versatile RI sensors, primed for a wide array of applications ranging from biosensing and environmental monitoring to chemical analysis and beyond. There are several methods of the fabrication process that are used in plasmonic nanosensor production. Some of the mostly used processes are discussed,

3.7.1 Nanoimprint Lithography (NIL)

Nano-imprint lithography (NIL) is a cutting-edge nanofabrication technique that has revolutionized the field of nanoscale patterning. It offers a cost-effective, high-resolution, and large-scale manufacturing approach, making it particularly advantageous for applications in plasmonic refractive index (RI) sensor fabrication.

Nano-imprint lithography is a nanofabrication technique that enables the replication of intricate nanoscale patterns onto a substrate. It relies on a process akin to molding, where a mold, or template, with the desired pattern is pressed into a polymer material, creating a precise replica of the pattern. NIL can be categorized into two main approaches: thermal NIL (T-NIL) and UV-curable NIL (UV-NIL). T-NIL involves heating the polymer material above its glass transition temperature, allowing it to flow and conform to the mold's surface. UV-NIL, on the other hand, employs a UV-curable resist, which is exposed to UV light during the imprinting process to initiate cross-linking and solidify the pattern. Both techniques offer high-resolution patterning capabilities, with feature sizes reaching sub-10 nm scales.

The process of nano-imprint lithography consists of several key steps, including mold fabrication, imprinting, and pattern transfer. The following outlines a generalized description of the process:

- **Mold Fabrication:** The mold, also known as the template, is fabricated using advanced techniques such as electron beam lithography or focused ion beam milling. The mold can be made from materials such as silicon, quartz, or nickel, and it contains the desired nanoscale pattern.
- **Imprinting:** A polymer material, typically a thermoplastic or UV-curable resist, is applied onto a substrate, forming a thin film. The mold is then pressed into the polymer material with controlled force and temperature, ensuring proper contact and pattern transfer. In thermal NIL, the polymer is heated to facilitate flow, while in UV-NIL, UV light is used to cure the resistance and create a solidified replica of the mold pattern.
- **Pattern Transfer:** After imprinting, the mold is carefully separated from the polymer material, leaving behind a patterned layer adhered to the substrate. Additional pro-

cessing steps such as etching or deposition may be employed to transfer the pattern to the underlying substrate or modify the patterned layer.

Nano-imprint lithography plays a pivotal role in the fabrication of plasmonic RI sensors, enabling the precise patterning required for enhanced sensing performance. Plasmonic RI sensors exploit the phenomenon of localized surface plasmon resonance (LSPR), where the interaction between light and plasmonic nanoparticles results in highly sensitive refractive index measurements. By integrating NIL into plasmonic RI sensor fabrication, the following benefits can be achieved:

- **Enhanced Sensor Performance:** Nano-imprint lithography allows for the creation of well-defined patterns, enabling precise control over the arrangement and geometry of plasmonic nanoparticles. This precise control enhances the interaction between light and nanoparticles, resulting in improved sensitivity and selectivity of the RI sensor.
- **Scalability and Reproducibility:** NIL offers a highly scalable fabrication process, allowing for the mass production of plasmonic RI sensors. The replication of patterns using molds ensures reproducibility, enabling consistent sensor performance across multiple devices.
- **Versatile Sensor Design:** Nano-imprint lithography enables the patterning of plasmonic sensors with diverse geometries and arrangements, facilitating the development of sensor arrays and customizable architectures. This versatility allows for the design and optimization of plasmonic RI sensors tailored to specific applications, such as biosensing, environmental monitoring, or chemical analysis.

Nano-imprint lithography has emerged as a powerful technique for nanoscale patterning, revolutionizing the field of plasmonic RI sensor fabrication. Its ability to achieve high-resolution patterns, scalability, and reproducibility makes it a valuable tool in the development of sensitive and versatile RI sensors. As research and advancements in nano-imprint lithography continue, we can anticipate even more remarkable achievements in the field of plasmonic sensing, paving the way for innovative applications and breakthroughs in various scientific and technological domains.

3.7.2 Electron Beam Lithography (EBL)

Electron beam lithography (EBL) is a cutting-edge nanofabrication technique that has revolutionized the field of nanoscale patterning. With its exceptional resolution and precision, EBL enables the creation of intricate patterns at sub-10 nanometer scales, making it an invaluable tool in plasmonic refractive index (RI) sensor fabrication.

Electron beam lithography is a nanofabrication technique that utilizes a focused beam of electrons to pattern a substrate with extraordinary precision. By selectively exposing a resist material to the electron beam, EBL enables the creation of high-resolution patterns, surpassing the limitations of optical lithography. EBL systems typically employ a scanning electron microscope (SEM) equipped with a sophisticated electron beam column, capable of generating fine electron beams with diameters as small as a few nanometers.

The process of electron beam lithography involves several key steps, including resist coating, electron beam exposure, development, and pattern transfer. The following outlines a generalized description of the process:

- **Resist Coating:** A resist material is applied onto a substrate, typically using spin coating or vapor deposition techniques. The resist serves as a photosensitive layer, capable of undergoing chemical changes upon exposure to the electron beam.
- **Electron Beam Exposure:** The resist-coated substrate is loaded into the electron beam lithography system. A finely focused electron beam is scanned across the surface of the resist, selectively exposing specific areas according to the desired pattern. The electron beam's intensity, dwell time, and scanning speed are precisely controlled to achieve the desired pattern resolution and accuracy.
- **Development:** After electron beam exposure, the resist undergoes a development process to remove either the exposed or unexposed areas, depending on the resist type. This step reveals the desired pattern in the resist material, creating a mask for subsequent processing steps.
- **Pattern Transfer:** The patterned resist can serve as a mask for transferring the pattern onto the underlying substrate. Techniques such as etching or deposition are employed to remove or deposit material selectively, replicating the pattern in the substrate.

Electron beam lithography plays a crucial role in the fabrication of plasmonic RI sensors, enabling the precise and intricate patterning required for enhanced sensing performance. Plasmonic RI sensors exploit the phenomenon of localized surface plasmon resonance (LSPR), where the interaction between light and plasmonic nanoparticles results in highly sensitive refractive index measurements.

Electron beam lithography stands as a powerful technique for nanoscale patterning, revolutionizing the field of plasmonic RI sensor fabrication. Its unmatched resolution, precision, and versatility empower researchers and engineers to push the boundaries of plasmonic sensing, enabling highly sensitive and tailored RI sensors. As advancements in electron beam lithography continue to unfold, we can expect even greater strides in the development of

plasmonic RI sensors, opening up new avenues for groundbreaking applications in biosensing, environmental monitoring, and beyond

3.7.3 Focused Ion Beam Milling (FIB)

Focused Ion Beam (FIB) milling is a cutting-edge nanofabrication technique that has revolutionized the field of nanoscale patterning. With its exceptional precision and control, FIB milling enables the creation of intricate patterns at sub-10 nanometer scales, making it an invaluable tool in the fabrication of plasmonic refractive index (RI) sensors.

Focused Ion Beam milling is a nanofabrication technique that utilizes a focused beam of ions to selectively remove material from a substrate. Unlike traditional lithography methods, FIB milling allows for direct, maskless patterning with unparalleled precision. The primary ion species employed in FIB milling is typically gallium (Ga+), due to its high milling rate and controllability. The FIB milling process involves several key steps, including substrate preparation, ion beam scanning, and pattern transfer. The following provides a generalized description of the process:

- **Substrate Preparation:** The substrate to be patterned is first prepared by cleaning and possibly coating it with a protective layer. The choice of substrate material depends on the specific application, such as silicon, glass, or polymers.
- **Ion Beam Scanning:** The substrate is loaded into the FIB milling system, which typically combines an ion column with a scanning electron microscope (SEM) for imaging and precise control. A finely focused ion beam is scanned across the surface of the substrate, selectively milling away material in accordance with the desired pattern. The ion beam's acceleration voltage, current density, and dwell time are precisely controlled to achieve the desired milling depth and accuracy.
- **Pattern Transfer:** After the FIB milling process, the patterned resist can serve as a mask for transferring the pattern onto the underlying substrate. Techniques such as etching or deposition are employed to remove or deposit material selectively, replicating the pattern in the substrate.

Focused Ion Beam milling plays a vital role in the fabrication of plasmonic RI sensors, enabling precise and intricate patterning required for enhanced sensing performance. Plasmonic RI sensors exploit the phenomenon of localized surface plasmon resonance (LSPR), where the interaction between light and plasmonic nanoparticles results in highly sensitive refractive index measurements.

Focused Ion Beam milling stands as a powerful technique for nanoscale patterning, revolutionizing the field of plasmonic RI sensor fabrication. Its unmatched precision, control, and

three-dimensional capabilities empower researchers and engineers to push the boundaries of plasmonic sensing, enabling highly sensitive and tailored RI sensors. As advancements in FIB milling continue to unfold, we can expect even greater strides in the development of plasmonic RI sensors, opening up new avenues for groundbreaking applications in biosensing, environmental monitoring, and various other scientific and technological domains.

3.7.4 Reactive Ion Etching (RIE)

Reactive Ion Etching (RIE) is an advanced nanofabrication technique that has transformed the field of precision etching. With its exceptional control and selectivity, RIE enables the fabrication of intricate patterns and structures at the nanoscale. This technique plays a vital role in plasmonic refractive index (RI) sensor fabrication, offering precise etching capabilities necessary for the development of high-performance sensors.

Reactive Ion Etching is a dry etching technique that employs chemically reactive ions to selectively remove material from a substrate. It is particularly advantageous due to its anisotropic etching characteristics, allowing for high aspect ratio features and precise control over etching depth. RIE is typically performed in a low-pressure plasma environment, where a mixture of reactive gases, such as oxygen, fluorine, or chlorine, is introduced to enhance the etching process. The choice of gas depends on the material being etched and the desired etch characteristics.

The process of Reactive Ion Etching involves several key steps, including substrate preparation, plasma generation, and etch profile control. The following provides a generalized description of the process:

- **Substrate Preparation:** The substrate to be etched is prepared by cleaning and possibly coating it with a protective layer. The choice of substrate material depends on the specific application, ranging from silicon to metal films or dielectrics.
- **Plasma Generation:** The prepared substrate is loaded into the RIE system, which typically consists of a vacuum chamber with specialized electrodes. A radio frequency (RF) or microwave power source is applied to generate a low-pressure plasma within the chamber. The reactive gas is introduced into the plasma, leading to the formation of chemically reactive ions.
- **Etch Profile Control:** The reactive ions bombard the substrate surface, resulting in the selective removal of material. Etching selectivity is achieved through the use of mask layers or by adjusting the composition of the reactive gas mixture. The etch rate and profile can be controlled by optimizing process parameters such as gas flow rates, pressure, power, and substrate temperature.

Reactive Ion Etching plays a crucial role in the fabrication of plasmonic RI sensors, enabling precise and controlled etching necessary for enhanced sensing performance. Plasmonic RI sensors exploit the phenomenon of localized surface plasmon resonance (LSPR), where the interaction between light and plasmonic nanoparticles results in highly sensitive refractive index measurements.

Reactive Ion Etching stands as a powerful technique for precision etching, revolutionizing the field of plasmonic RI sensor fabrication. Its exceptional control, selectivity, and ability to create intricate structures empower researchers and engineers to push the boundaries of plasmonic sensing, enabling highly sensitive and tailored RI sensors. As advancements in Reactive Ion Etching continue to unfold, we can expect even greater strides in the development of plasmonic RI sensors, opening up new avenues for groundbreaking applications in biosensing, environmental monitoring, and various other scientific and technological domains.

3.7.5 Atomic Layer Deposition (ALD)

Atomic Layer Deposition (ALD) has emerged as a groundbreaking nanofabrication technique, offering exceptional control over thin film deposition with atomic-scale precision. This technique has revolutionized various fields, including plasmonic refractive index (RI) sensor fabrication, by enabling the deposition of conformal and uniform coatings on complex three-dimensional structures.

Atomic Layer Deposition is a vapor-phase deposition technique that enables the controlled growth of thin films on substrates with atomic-scale precision. Unlike other deposition methods, ALD operates by sequentially exposing the substrate to alternating precursor gases in a self-limiting manner. Each precursor deposition step consists of precisely dosed and timed pulses, ensuring a controlled atomic layer thickness growth. The self-limiting nature of ALD enables precise control over film thickness, composition, and uniformity. The ALD process involves several key steps, including substrate preparation, precursor exposure, and purging. The following provides a detailed description of the process:

- **Substrate Preparation:** The substrate to be coated is prepared by cleaning and possibly surface treatment to enhance film adhesion. The choice of substrate material depends on the specific application, ranging from silicon to metal films or dielectrics.
- **Precursor Exposure:** The prepared substrate is loaded into the ALD reactor, which typically consists of a vacuum chamber equipped with precursor delivery systems. The chamber is evacuated, and the substrate is heated to the desired temperature for optimal precursor reactivity. The first precursor is introduced into the chamber, selectively adsorbing onto the substrate surface in a self-limiting manner. The excess precursor

is removed by purging with an inert gas, leaving a monolayer of the precursor on the substrate surface.

- **Second Precursor Exposure and Repeat Cycles:** The chamber is purged again to remove any remaining precursor and reaction by-products. The second precursor is introduced into the chamber, reacting with the adsorbed monolayer from the previous step to form a solid film. Excess second precursor and reaction by-products are purged from the chamber. The above steps are repeated in a cycle until the desired film thickness is achieved.

ALD plays a critical role in the fabrication of plasmonic RI sensors, enabling precise and controlled deposition of functional films necessary for enhanced sensing performance. Plasmonic RI sensors exploit the phenomenon of localized surface plasmon resonance (LSPR), where the interaction between light and plasmonic nanoparticles results in highly sensitive refractive index measurements.

Atomic Layer Deposition stands as a powerful technique for precise thin film deposition, revolutionizing the field of plasmonic RI sensor fabrication. Its atomic-scale control, conformal coating capabilities, and versatility empower researchers and engineers to push the boundaries of plasmonic sensing, enabling highly sensitive and tailored RI sensors. As advancements in ALD continue to unfold, we can expect even greater strides in the development of plasmonic RI sensors, opening up new avenues for groundbreaking applications in biosensing, environmental monitoring, and various other scientific and technological domains. The precise and controlled deposition provided by ALD paves the way for further advancements in plasmonic sensing, fueling innovations in the field of optical sensing and paving the path toward highly efficient and versatile RI sensors of the future.

3.7.6 Molecular Beam Epitaxy (MBE)

Molecular Beam Epitaxy (MBE) stands as a pioneering technique in the realm of nanoscale material growth, offering unparalleled control over thin film deposition. By leveraging the precise manipulation of molecular beams, MBE enables the fabrication of high-quality crystalline structures with atomic-scale precision. In the context of plasmonic refractive index (RI) sensor fabrication, MBE plays a pivotal role, allowing for the development of tailored materials and heterostructures that enhance sensing performance.

Molecular Beam Epitaxy is a technique that enables the controlled growth of thin films and heterostructures with atomic-scale precision. Unlike other deposition methods, MBE operates under ultra-high vacuum conditions to ensure a clean and controlled growth environment. In MBE, molecular or atomic beams are directed towards a heated substrate, where

they undergo adsorption, diffusion, and desorption processes, resulting in the formation of epitaxial layers with exceptional crystalline quality and well-defined interfaces. The MBE process involves several key steps, including substrate preparation, molecular or atomic beam generation, and growth control. The following provides a detailed description of the process:

- **Substrate Preparation:** The substrate to be epitaxially grown is carefully prepared, undergoing cleaning processes to remove contaminants and achieve a pristine surface. The choice of substrate material is critical, considering factors such as lattice matching, crystal structure, and desired functionalities.
- **Molecular or Atomic Beam Generation:** In MBE, molecular or atomic beams are generated using effusion cells or electron beam evaporators. The source materials are heated, causing the evaporation or sublimation of the desired molecular or atomic species. The evaporated species form a beam and are directed toward the substrate surface.
- **Growth Control:** The substrate is heated to a temperature appropriate for the desired material growth. The molecular or atomic beams impinge on the heated substrate surface, where they undergo various surface reactions. Adsorption, diffusion, and incorporation processes lead to the growth of crystalline layers with atomic-scale precision. The growth is carefully controlled by adjusting the fluxes of the molecular or atomic beams, substrate temperature, and growth time.

Molecular Beam Epitaxy plays a vital role in the fabrication of plasmonic RI sensors, enabling the precise growth of tailored materials and heterostructures necessary for enhanced sensing performance. Plasmonic RI sensors harness the phenomenon of localized surface plasmon resonance (LSPR), where the interaction between light and plasmonic nanostructures results in highly sensitive refractive index measurements.

Molecular Beam Epitaxy stands as a powerful technique for precise material growth, pushing the frontiers of plasmonic RI sensor fabrication. Its atomic-scale control, tailored material growth capabilities, and interface engineering empower researchers and engineers to advance the field of plasmonic sensing, enabling highly sensitive and tailored RI sensors. As advancements in MBE continue to unfold, we can expect even greater strides in the development of plasmonic RI sensors, opening up new avenues for groundbreaking applications in biosensing, environmental monitoring, and various other scientific and technological domains. The precision and versatility offered by MBE pave the way for further advancements in plasmonic sensing, fueling innovations in the field of optical sensing and propelling the development of highly efficient and versatile RI sensors of the future.

Chapter 4

Advancements in Sensor Technology: Design, Optimization, and Real-world Implementations

4.1 Importance of Design and Optimization

It is crucial to carefully design and optimize the structural parameters of refractive index sensor designs in order to maximize the performance parameters of these sensors. Scientists and engineers strive to achieve significant advancements in the interaction between light and matter within these sensors by carefully selecting and designing parameters and configurations, particularly through the incorporation of baffles, stubs, and nanorods. These recent advancements in refractive index sensors have opened up a wide range of applications, with a specific focus on detecting biological and chemical substances and measuring various physical quantities. While the designing of sensors is very important for good performance, it is equally important to consider the tolerance level of the fabrication methods used as well. So it is important to optimize the geometric parameters of the sensor for maximizing sensor performance and meeting the tolerance limit of fabrication technology at the same time. The geometric parameters encompass the size, shape, and placement of the sensor, as well as the overall structure. The performance of the sensor also depends on the materials used in the sensor. Researchers diligently work towards enhancing the efficacy and efficiency of the interaction between light and matter within the sensor by carefully selecting and enhancing the sensor's geometric parameters, leading to improved sensitivity and detection capabilities.

One of the methods of improving the performance of the refractive index is integrating nanorods alternatively known as nanodots into their structures. They possess unique optical characteristics that can enhance the sensor's performance. These elongated nanoscale structures exhibit significant localized surface plasmon resonance, allowing for enhanced electromagnetic confinement and interaction with the analytes. By incorporating nanorods

into the sensor's design, researchers can significantly enhance its sensitivity to variations in the refractive index of the surrounding medium, leading to improved sensing capabilities. The size and number of nanorods are directly correlated with the sensitivity of the sensor. It is also important to place the nanorods in the correct places of the sensor in order to maximize the light-matter interaction. Integration of nanorods can increase the sensitivity of the sensor by up to 61% compared to a sensor without nanorods [104,126,166]. Another method of improving sensor performance is to introduce baffles in the cavity. Baffles can introduce additional SPP modes which is known as gap plasmon resonance. The discontinuity of the cavity structure significantly enhances SPP wave by the excitation of EM wave [221].

The integration of nanorods and baffles into refractive index sensors has opened up a wide array of applications. These sensors have the ability to detect various biological substances, such as proteins, DNA, and cells, monitor chemical processes, detect chemical pollutants and heavy metal ions in water, and also investigate and monitor food quality. Their enhanced sensitivity and selectivity make them invaluable tools in biological research, environmental monitoring, healthcare, and industrial operations.

While sensor design is essential the tolerance of the manufacturing procedure must also be taken into consideration. Fabrication procedures might cause a deviation from the designed structure and introduce impurities in the sensor. These flaws can be caused by various reasons such as material restrictions, process variances, or equipment constraints. As a result, it is critical to tune the structural characteristics to guarantee that the sensor can still offer remarkable results despite these manufacturing limitations. Optimizing geometric structure necessitates a thorough understanding of the fabrication process and its possible drawbacks. Researchers may adapt the sensor's design to compensate for any deviations that may arise during production by taking fabrication tolerances into account. This procedure may include altering the sensor's size, materials, or geometries to guarantee that its performance stays strong and dependable. Additionally, optimization strategies can solve scalability and cost-effectiveness challenges. The structural characteristics may be tuned for large-scale manufacture while ensuring consistent performance across several sensors. This scalability is critical for practical applications requiring the deployment of a large number of sensors in real-world environments.

4.2 Real-world Scope of Plasmonic Refractive Index Sensor

In order to successfully use refractive index-based sensors with optimized structural parameters, several important factors must be considered, along with their many potential applications. It is worth noting that real-world implementation of these sensors requires collab-

oration between researchers, engineers, and industry experts. Additionally, advancements in manufacturing processes, material science, and integration techniques play a crucial role in achieving higher output and cost efficiency. These sensors offer improved performance, reliability, and advanced functionalities that can address critical challenges and lead to significant societal and technological advancements. To delve further into this subject, here are several aspects worth exploring:

- **Medical Applications:** The refractive index sensors can be used in various biomedical applications, such as point-of-care diagnostics, disease detection, and monitoring. These sensors can detect specific biological substances like proteins, DNA, or cells with high sensitivity and precision. For example, in the field of cancer diagnostics, refractive index sensors can detect biomarkers indicative of specific types of cancer, enabling early detection and personalized treatment. Refractive index sensors can also be used for blood glucose monitoring, blood group classification, detecting protein concentration in cells and urine, detecting contamination in biological components, etc.

- **Food Quality Monitoring:** To ensure the safety and quality of foods, these sensors can detect contaminants, allergens, or adulterants in food and beverages which in terms allowing for rapid and reliable detection of potential risks and ensuring compliance with food safety regulations. For instance, RI sensors can be used in detecting adulteration in honey, lactose in milk, protein in meat products, fat in dairy products evaluating the freshness of fruit and vegetables, sugar concentration in chocolate and sweet products, etc.

- **Environmental Monitoring:** RI sensors can detect and monitor pollutants, toxins, and hazardous substances in air, water, or soil which can provide real-time data on the presence and concentration of these substances, aiding in environmental assessment, pollution control, and ensuring public safety as in detecting chemical pollution and heavy metal ions in water, soil moisture, salinity of seawater etc.

- **Industrial Processes and Manufacturing:** RI sensors can detect changes in the refractive index of chemical solutions, enabling real-time monitoring of reactions and ensuring product quality and consistency. The sensor can be used in monitoring chemical solutions, liquid concentration measurement, drug concentration measurement, monitoring the refractive index of adhesives and sealants, fuel quality investigation etc.

- **Security and Defense:** These sensors can detect and identify dangerous substances, explosives, and biological agents, helping to improve early warning systems and security measures.

- **Energy and Optoelectronics:** Optimized RI sensors are useful in the development of efficient energy systems and optoelectronic devices. They can be embedded into solar cells to boost light absorption and energy conversion efficiency. These sensors can also help with the design and optimization of photonic devices such as optical waveguides, sensors, and integrated circuits.

- **Agriculture & Precision Farming:** Refractive index sensors allow precision farming techniques in the agriculture industry. These sensors may be used to monitor soil composition, moisture levels, and nutrient concentrations by adjusting the structural characteristics as in crop quality assessment, detecting the presence of pesticides, and monitoring temperature and humidity for ensuring an ambient environment for plants. This data may assist farmers in making smart choices about irrigation, fertilization, and crop management, resulting in increased yields, resource efficiency, and sustainability.

- **Structural Integrity Monitoring:** Refractive index sensors can be integrated into infrastructure systems for structural integrity monitoring. By optimizing the structural parameters, these sensors can detect changes in the refractive index of materials used in bridges, buildings, or pipelines. This enables the early identification of structural defects, cracks, or corrosion, facilitating timely maintenance and preventing catastrophic failures.

4.3 Sensor Design with Modified Rectangular Resonator with Baffles and Nanorod

4.3.1 Designing Structure and Methodology

The top view of the initially proposed structure has been illustrated in a two-dimensional (2D) diagram in Fig. 4.1. Refractive index sensing depends on the light-matter interaction between the waveguide and the material being sensed [256]. Table 4.22 provides the details of the geometric parameters used in designing the sensor.

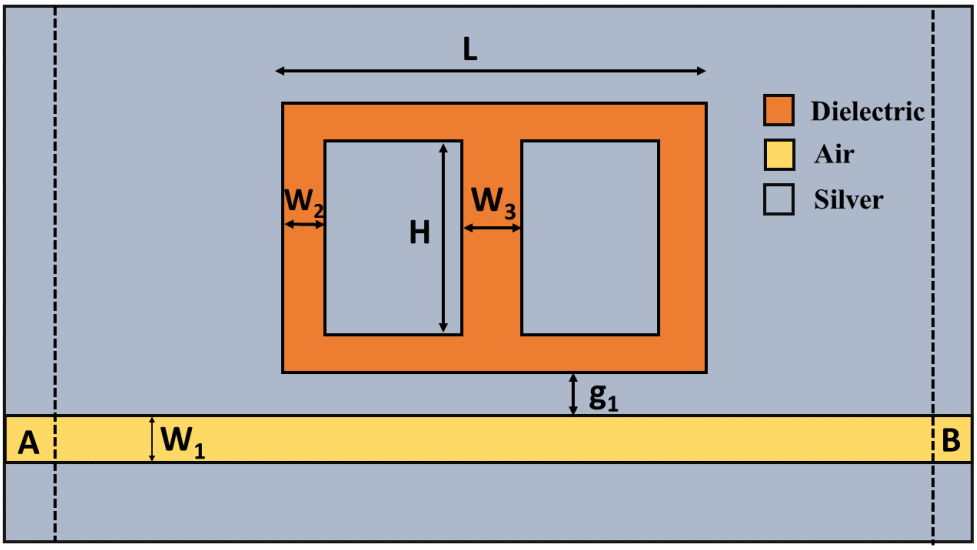

Figure 4.1: Initial structure of the sensor.

Table 4.1: Geometric properties of the resonator at the initial stage.

Name of the Parameter	Symbol	Value (nm)
Length of the resonator	L	400
Height of the connector	H	200
Gap between resonator and waveguide	g_1	20
Width of the waveguide	w_1	45
Width of the resonator	w_2	55
Width of the connector	w_3	110

Typically, silver and gold are employed for refractive index sensing. Silver is preferred due to its higher sensitivity compared to gold [257]. The numerical simulation is executed using COMSOL Multiphysics 5.6 software. In the review article by Butt et al. [18], it was discovered that nearly all MIM sensors are simulated in 2D. When the height of a device

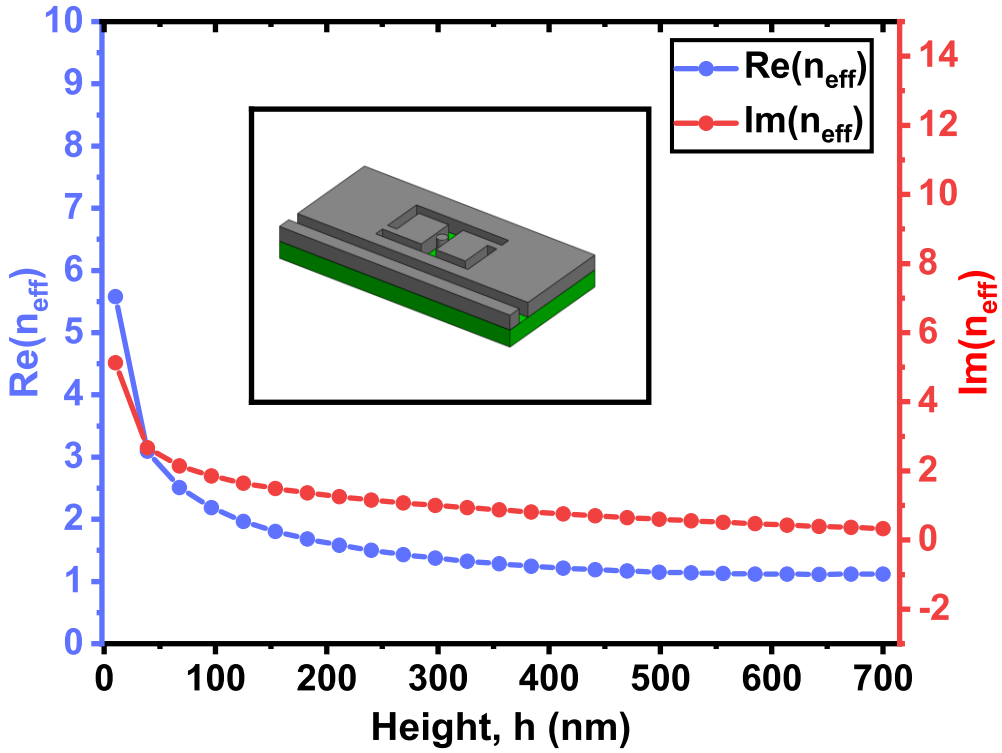

Figure 4.2: Relationship between height (h) and effective refractive index n_{eff} (both real and imaginary parts) for $n = 1$.

exceeds 800 nm, the 2D results can be extrapolated to a 3D scenario, and the performance characteristics are nearly identical [258]. In scenarios where the height of the device is greater than 800 nm, 2D device analysis can provide accurate results without the need for time-consuming and computationally costly 3D simulations. Danaie et al. [258], Hassan et al. [259] and Zhang et al. [103] demonstrated that the outcomes of 2D and 3D simulations coincide as the effective refractive index becomes constant after a certain height. With the variation of height, both $Re(n_{eff})$ and $Im(n_{eff})$ change, which in turn, affects the sensitivity and loss in the system [103]. To investigate this effect, the height (h) of our proposed structure is varied at a wavelength of 1615 nm and filled the cavity with a dielectric whose refractive index is 1. The resulting effect on n_{eff} is plotted in Fig. 4.2, which shows that both $Re(n_{eff})$ and $Im(n_{eff})$ gradually decrease with a decrease in modal power at the metal interface. This decrease stabilizes after a certain height (approximately 500 nm). As the height increases, $Im(n_{eff})$ decreases and approaches to a very small value. The stabilization of n_{eff} results in lower system loss and longer propagation length, which is desirable for many optical applications [259].

The scattering boundary condition in the simulation setup absorbs the outgoing waves and prevents unwanted reflections, avoiding interference in the simulated results and producing reliable data. Extra-fine triangular meshing is used to improve the simulation's resolution and accuracy, breaking down the simulation into finer-grained components [260]. The finite

element method (FEM) is implemented in this framework so that the electromagnetic wave equations involving material interfacing can be solved numerically. To solve partial differential equations (PDEs), FEM breaks down the solution domain into discrete, elementary components, resembling the behavior of waves as they interact with different materials, and facilitating in-depth analysis of complex systems [261].

The Lorentz-Drude model provides a useful theoretical framework to analyze the structural properties of metals, including their electronic structure and optical response, and is widely employed in materials science to investigate metals behavior at the atomic and molecular levels. The model illustrates the behavior of electrons through a set of equations that take into consideration the impact of collisions between electrons and the lattice vibrations of the metal. The Lorentz-Drude model enables the calculation of an essential parameter known as the complex dielectric function, $\hat{\varepsilon}_r(\omega)$ (4.1), which describes how the material responds to electromagnetic radiation at different frequencies by considering two types of electrons: free electrons and bound electrons. The first term in the model, $\hat{\varepsilon}_r^{(f)}(\omega)$ (4.2), represents the response of the free electrons, which can be explained by the Drude model, and the second term, $\hat{\varepsilon}_r^{(b)}(\omega)$ (4.3), represents the response of the bound electrons, which can be explained by the Lorentz model. The real part characterizes the ability of the material to hold energy when subjected to an electric field, while the imaginary part describes the material's ability to dissipate energy [262].

$$\hat{\varepsilon}_r(\omega) = \hat{\varepsilon}_r^{(f)}(\omega) + \hat{\varepsilon}_r^{(b)}(\omega) \tag{4.1}$$

$$\hat{\varepsilon}_r^{(f)}(\omega) = 1 - \frac{\Omega_p^2}{\omega(\omega - i\Gamma_0)} \tag{4.2}$$

$$\hat{\varepsilon}_r^{(b)}(\omega) = \sum_{j=1}^{k} \frac{f_j \omega_p^2}{\omega_j^2 - \omega^2 + i\omega\Gamma_j} \tag{4.3}$$

where, f_j is the oscillator strength of the j-th oscillator in the material, ω_j is to the natural frequency of the j-th oscillator in the material, ω is the frequency of the electromagnetic radiation, ω_p is the plasma frequency of the material, Γ_j is the damping constant associated with the j-th harmonic oscillator of the materia, Γ_0 is the damping constant at zero frequency, and Ω_p is the plasma frequency of free electrons in the material. All the parameters with their respective values have been provided in Table 4.2 [262].

As the width of the waveguide is much smaller than the incident wavelength, other modes cannot propagate or be sustained in the waveguide, and the waveguide can only support the most fundamental transverse magnetic (TM) mode [263]. SPPs are excited in TM mode from the input port A in Fig. 4.1. The subsequent equation (4.4) provides a way to express the dispersion relation for the TM mode.

Table 4.2: Lorentz-Drude parameters for Silver (Ag).

Parameters		**Values**
Plasma frequency ($\hbar\omega_p$)		9.010 eV
Collision frequency (Γ_0)		0.048 eV
Oscillator strength (f_j)	f_0	0.845
	f_1	0.065
	f_2	0.124
	f_3	0.011
	f_4	0.840
	f_5	5.646
Resonant frequency (ω_j)	ω_1	0.816 eV
	ω_2	4.481 eV
	ω_3	8.185 eV
	ω_4	9.083 eV
	ω_5	20.29 eV
Damping frequency (Γ_j)	Γ_0	0.048 eV
	Γ_1	3.886 eV
	Γ_2	0.452 eV
	Γ_3	0.065 eV
	Γ_4	0.916 eV
	Γ_5	2.419 eV

$$\epsilon_d\sqrt{n_{\text{eff}}^2-\epsilon_m}+\epsilon_m\sqrt{n_{\text{eff}}^2-\epsilon_d}\tanh\left(\frac{W\pi\sqrt{n_{\text{eff}}^2-\epsilon_d}}{\lambda}\right)=0 \tag{4.4}$$

where, ϵ_d is the permitivity of the dielectric, while ϵ_m is the permitivity of the material, n_{eff} is the effective refractive index, W is the width of the waveguide, and λ corresponds to the wavelength of the guided light [264].

The Maxwell equations and waveguide boundary conditions can be used to calculate the (n_{eff}) in the MIM structure. The following equations can be solved to obtain the expression for (n_{eff}):

$$\mathrm{k_d}\epsilon_\mathrm{m}\tanh\left(\frac{\mathrm{k_d}W}{2}\right)+\epsilon_\mathrm{d}\mathrm{k_m}=0 \tag{4.5}$$

$$\mathrm{k_{d,m}}=\sqrt{\beta_{\text{SPP}}^2-\epsilon_{\mathrm{d,m}}k_0^2} \tag{4.6}$$

$$n_{\text{eff}}=\frac{\beta_{\text{SPP}}}{k_0} \tag{4.7}$$

where, $\mathrm{k_d}$ and $\mathrm{k_m}$ refer to the transverse propagation constants of the dielectric and metal layers, respectively, and β_{SPP} is the propagation constant. The term k_0 represents the wave vector in free space, which is defined as the reciprocal of the wavelength of the excitation light, λ, and $k_0 = \frac{2\pi}{\lambda}$ [263]. The effective refractive index (η_{eff}) depends on the MIM

waveguide structure, geometry, and materials of the waveguide being used [265].

The resonant wavelength of a plasmonic resonator can be determined using standing wave theory, which relates the effective length of the resonator to the resonant wavelength (λ_{res}) and the mode order (m). Specifically, the resonant wavelength can be calculated using the following equation (4.8):

$$\lambda_{res} = \frac{2n_{eff}L}{m - \frac{\phi_{ref}}{\pi}} \tag{4.8}$$

where, L is the resonator's effective length, n_{eff} is the effective refractive index of the SPP mode, ϕ_{ref} is the phase shift due to the traveling of SPP, and m is a positive integer that denotes the mode order of the SPP resonance [266]. By understanding the resonant wavelength and its shift, we can gain insights into the interactions between the sensor and its surrounding environment. Changes in the medium's refractive index (n) can lead to a shift in the resonant wavelength, which can be utilized to identify and measure analytes in the sample. To design and optimize plasmonic sensors for a variety of applications, it is essential to understand the resonant wavelength and its shifting properties.

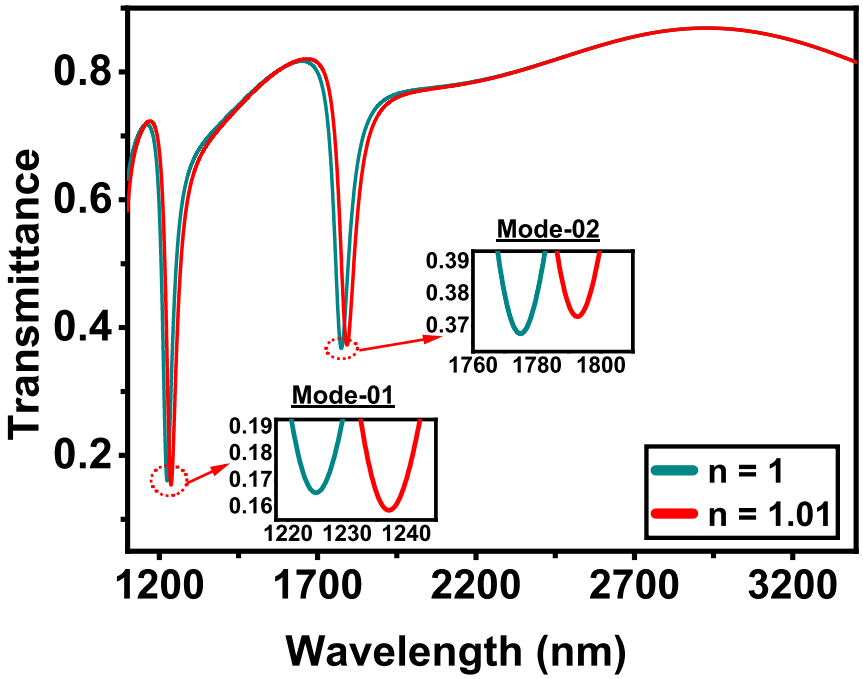

Figure 4.3: Transmittance characteristics for initial structure

4.3.2 Sensing Parameters and Optimization

4.3.2.1 Selection of Suitable Structure

Initially, we optimized our sensor for the refractive index values of n = 1 and n = 1.01. The value 1.01 was chosen to demonstrate that a change in refractive index results in a change

in the resonant wavelength. This value was arbitrarily selected for the initial evaluation of the sensor. After analyzing the structure depicted in Fig. 4.1, we observe that it exhibits a low sensitivity profile, as shown in Fig. 4.3, with two resonant dips having sensitivity values of 1232.05 nm/RIU and 1786.53 nm/RIU, respectively. However, the structure was further modified and investigated with a view to maximizing sensitivity.

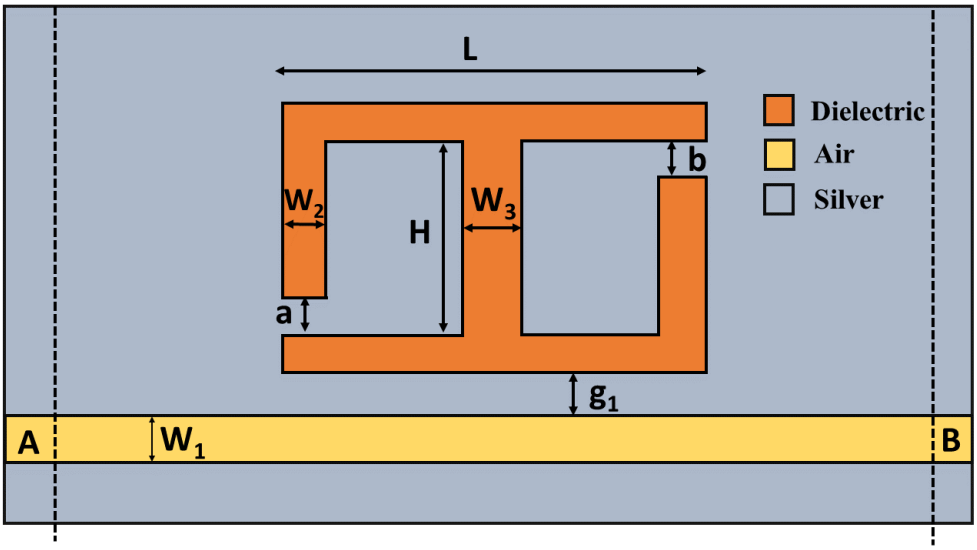

Figure 4.4: Modified structure with baffles.

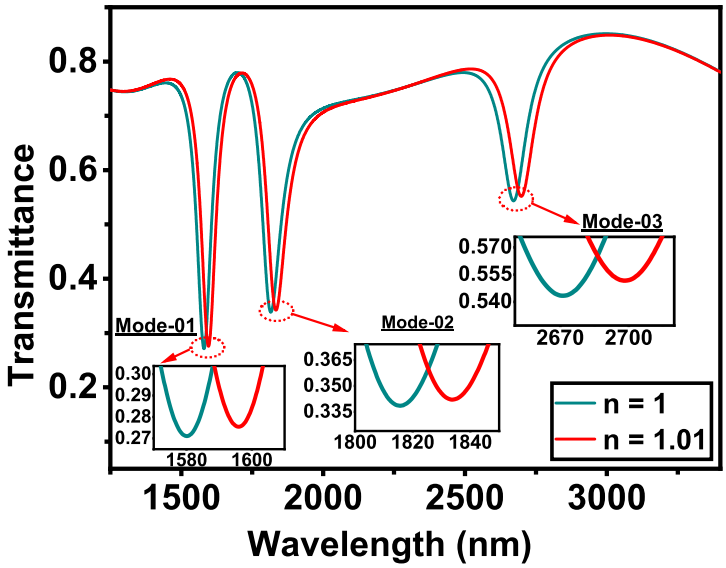

Figure 4.5: Transmittance characteristics for modified structure with baffles

The structure was modified by introducing two baffles positioned on opposite sides of the rectangle depicted in Fig. 4.4. The size of the left-side baffle denoted as ‘a’, was assumed to be 40 nm initially, while the size of the right-side baffle, denoted as ‘b’, was also assumed to be 55 nm initially. In a rectangular ring resonator, changing the size of the Ag baffles alters

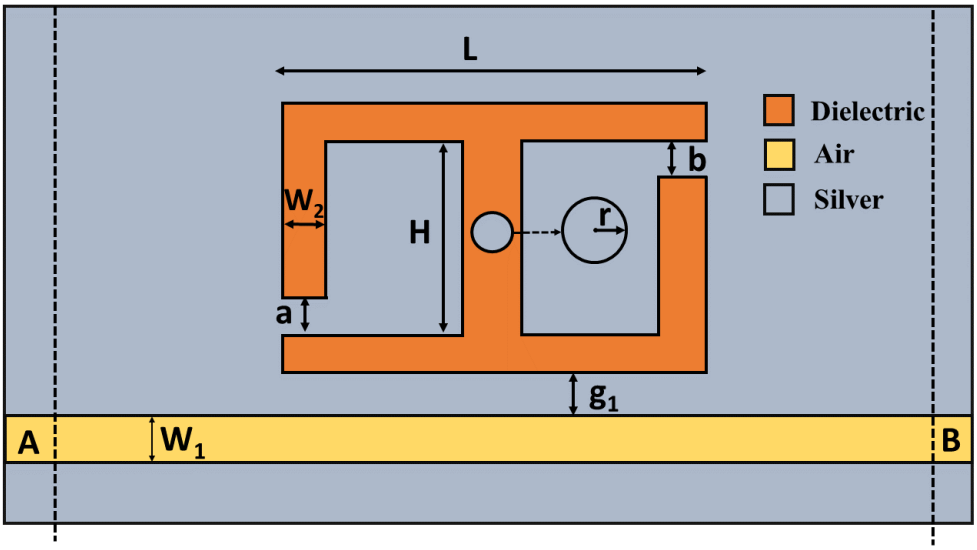

Figure 4.6: Modified structure with single nanorod.

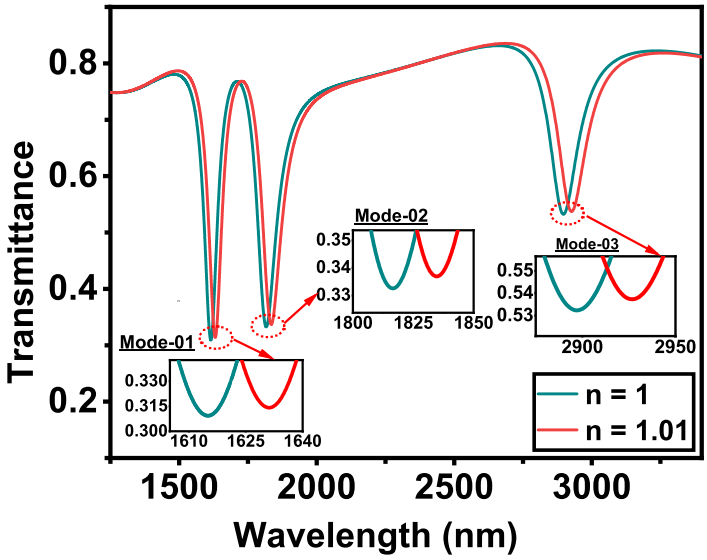

Figure 4.7: Transmittance characteristics for modified structure with single nanorod

the SPPs mode and produces various resonance mode. Ag baffles placed inside a rectangular ring cavity can create a GPR mode and make it possible to tune the SPPs modes [221]. By incorporating these baffles, an improvement in the sensitivity profile is observed, as shown in Fig. 4.5, resulting in the identification of three distinct resonant dips with sensitivity values of 1571.52 nm/RIU, 1824.68 nm/RIU, and 2611.15 nm/RIU, respectively. However, FOM is not up to the mark, so we worked on further improving it. By placing a nanorod into the resonator structure, with its radius denoted as 'r' and assumed to be 30 nm as shown in Fig. 4.6, significant changes are observed in the transmission spectra, as well as notable improvements in both sensitivity and FOM values, as shown in Fig. 4.7. Specifically, the sensitivity values increased to 1614.27 nm/RIU, 1816.45 nm/RIU, and 2883.63 nm/RIU, respectively. When exploring the modified structure with multiple nanorods, where the spacing between

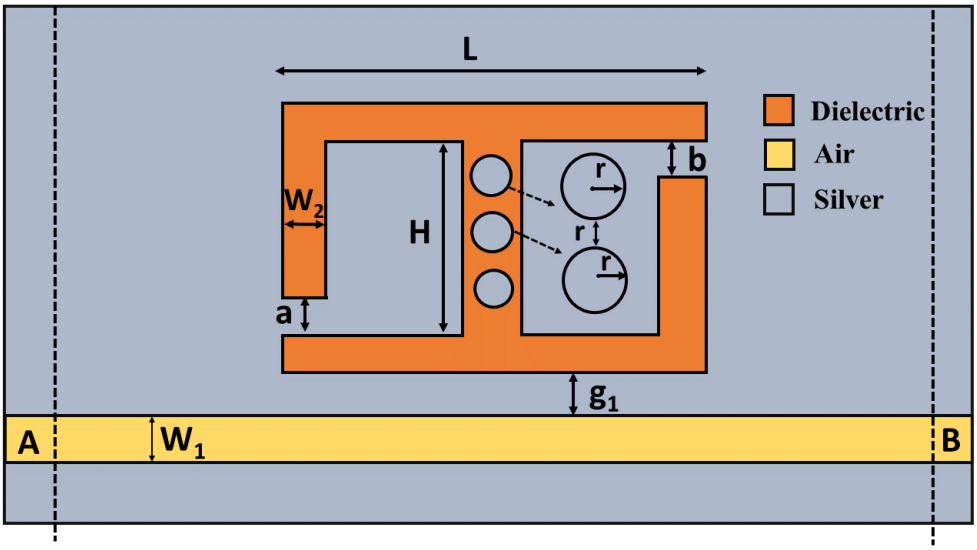

Figure 4.8: Modified structure with multiple nanorods.

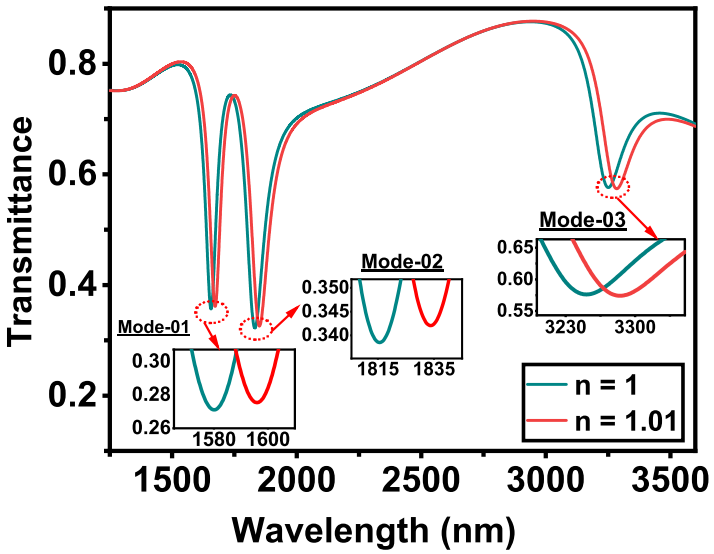

Figure 4.9: Transmittance characteristics for modified structure with multiple nanorods

the nanorods is equal to the radius of the nanorod (r), as depicted in Fig. 4.8, it is observed that the results do not align with our expectations when compared to the performance of the modified structure with a single nanorod. The FOM value in mode-3 is significantly reduced, as shown in Fig. 4.9. The electric field distributions of the single nanorod configuration for three resonant dips are shown in Fig. 4.10 (a-c) and the electric field distributions for multiple nanorods configuration for all three resonant dips are shown in Fig. 4.10 (d-f), respectively. Following the study, we chose to make our final design with one nanorod and two baffles, and the initial resonator shape is shown in Fig. 4.6.

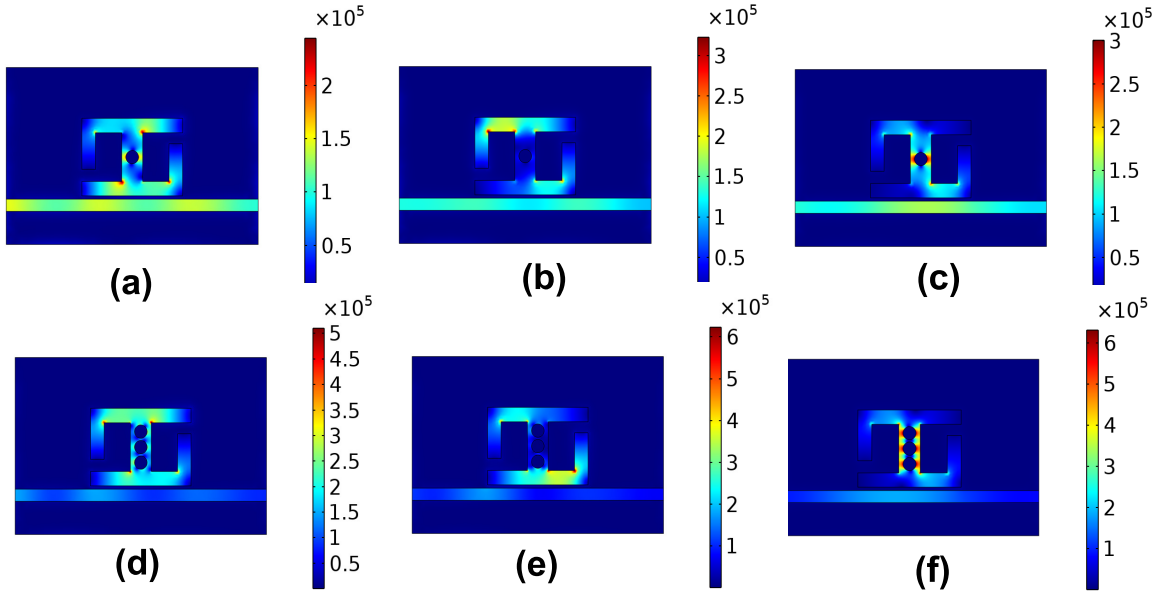

Figure 4.10: Electric field distribution (V/m), a. λ = 1594.67 nm, single nanorod b. λ = 1787.32 nm, single nanorod c. λ = 2854.74 nm, single nanorod and d. λ = 1657.18 nm, multiple nanorods e. λ = 1832.07 nm, multiple nanorods f. λ = 3250.92 nm, multiple nanorods.

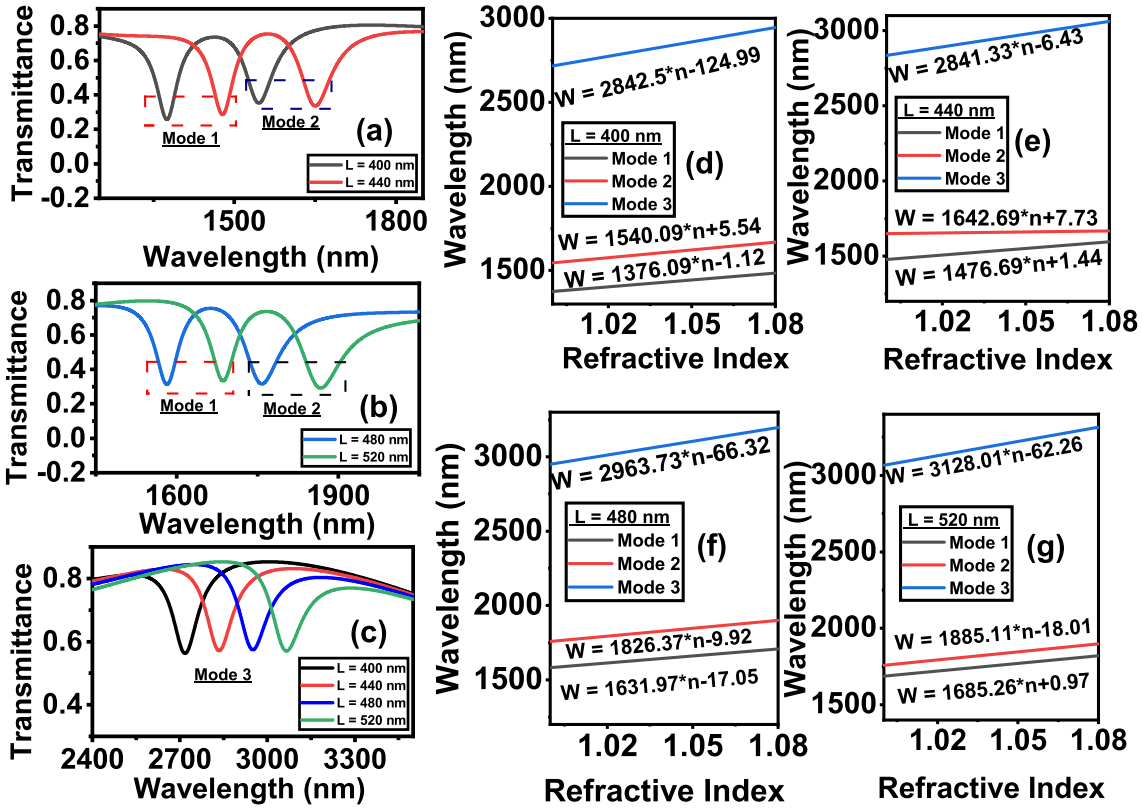

Figure 4.11: (a-c) Transmittance characteristics for different values of L and (d-g) shows resonant wavelength relation with refractive index.

4.3.2.2 Fine-tuning of the resonator structure for improved performance

The sensor's structural parameters can be optimized to achieve the optimal geometry for maximum sensitivity. It requires an iterative approach of simulating new configurations until the desired outcome is achieved.

The length of the resonator was varied between 400 nm and 520 nm with 40 nm intervals to analyze the impact of the resonator's length (L) on the sensor's performance. Fig. 4.11 (a-c) shows that increasing the resonator's length results in a redshift in the wavelength. Additionally, Fig. 4.11 (d-g) depicts the relationship between the refractive index and resonant dip for different values of L. In Fig. 4.11 (g), all three dips exhibit maximum sensitivity when the length of the resonator is 520 nm. However, at this dimension, the FOM was significantly decreased, which led us to choose L = 480 nm as our preferred length, as shown in Fig. 4.11(f). The optimal combination of sensitivity and FOM is achieved at L = 480 nm.

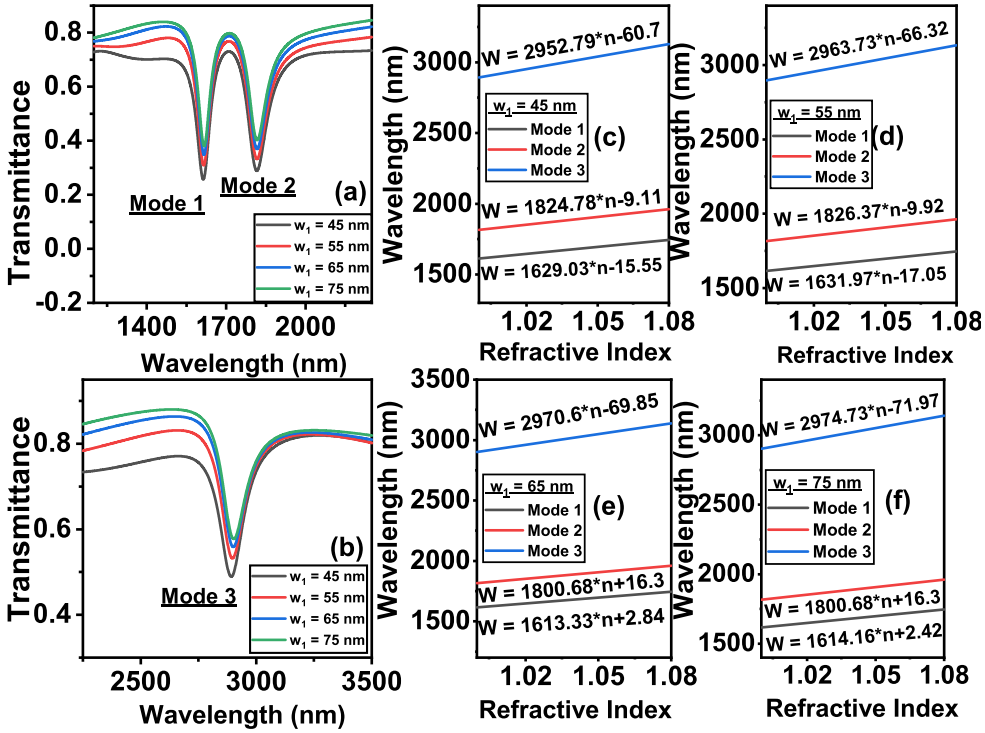

Figure 4.12: (a-b) Transmittance characteristics for different values of w_1 and (c-f) shows resonant wavelength relation with refractive index.

To ensure optimal performance of the sensor, the width (w_1) of the waveguide was swiped in small increments, ranging from 45 nm to 75 nm in steps of 10 nm. The results, shown in Fig. 4.12 (a-b), indicate that increasing the waveguide width had a detrimental effect on the transmittance characteristics, and the resonant dip decreased as the width increased. In order to determine the optimal width of the waveguide, the resonant dip versus refractive index was plotted for different values of waveguide width, as illustrated in Fig. 4.12 (c-f). Based on the analysis, w_1 = 55 nm is chosen because it provides a moderate FOM and sensitivity for all the resonant dips.

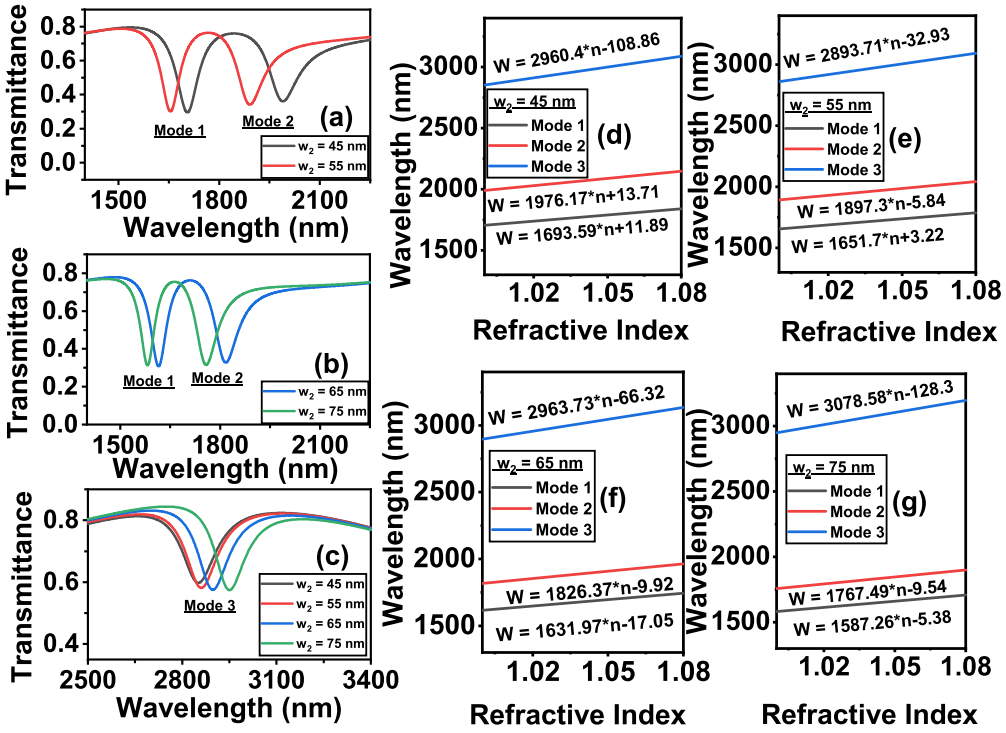

Figure 4.13: (a-c) Transmittance characteristics for different values of w_2 and (d-g) shows resonant wavelength relation with refractive index.

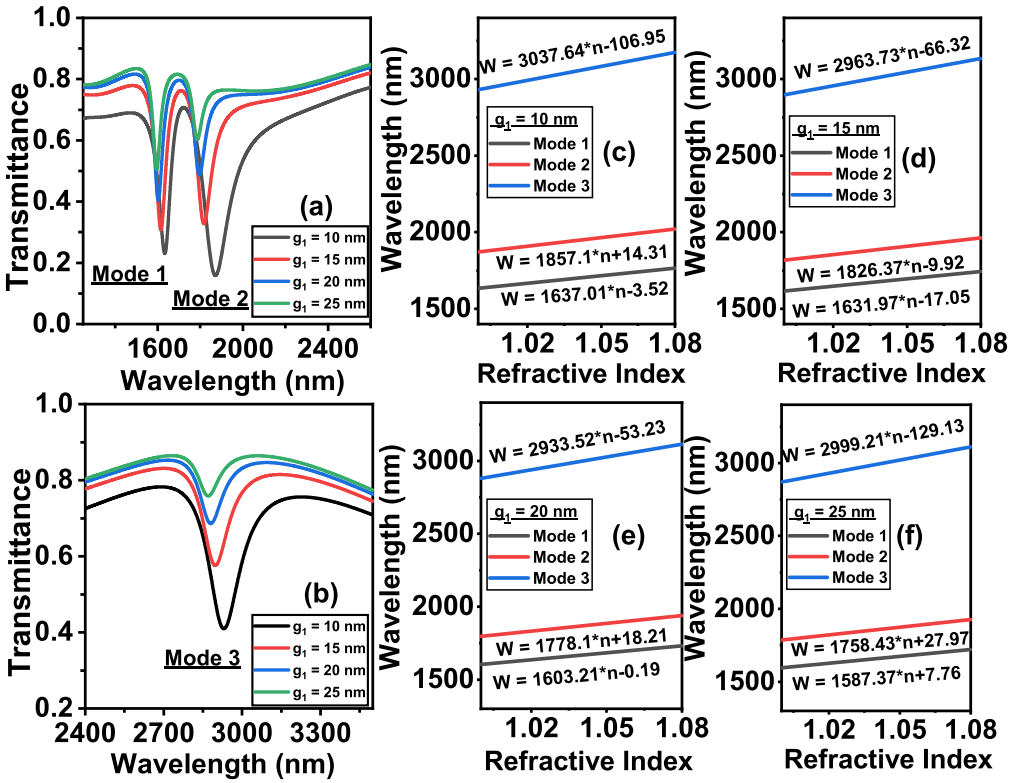

Figure 4.14: (a-b) Transmittance characteristics for different values of g_1 and (c-f) shows resonant wavelength relation with refractive index.

To assess the effect of the resonator's width (w_2) on the sensor's performance, the width of the resonator was varied from 45 nm to 75 nm with a step size of 10 nm. A blueshift towards longer wavelengths was observed for the first two dips by increasing the width of the resonator, as shown in Fig. 4.13 (a-c), but a redshift was observed for the last dip. Additionally, Fig. 4.13 (d-g) shows the resonant dip versus refractive index graphs for different values of the resonator width. According to our analysis, the sensor provides an optimal balance between sensitivity and figure of merit (FOM) when the resonator width is 65 nm.

The transmittance spectra illustrated in Fig. 4.14 (a-b) indicate that changing the distance between the waveguide and resonator (g_1) had a significant impact on the resonant dip, resulting in degraded performance. The graphs of resonant dip versus refractive index for different values of g_1 were plotted to further analyze the effect of the waveguide-resonator distance on the sensor's performance, as shown in Fig. 4.14 (c-f). An optimal waveguide-resonator distance of g_1 = 15 nm was revealed by our analysis, providing moderate FOM and sensitivity for all the resonant dips.

The effect of variations in the connector height (H) from 200 nm to 260 nm on the sensor's performance is illustrated in Fig. 4.15 (a-c), which shows a significant decline in the resonant dips. The graphs of resonant dip versus refractive index for different values of the connector height are plotted in Fig. 4.15 (d-g). The results indicate that the FOM is significantly deteriorated by increasing the connector height. Our analysis shows that the optimal connector height for the best outcome of the sensor's performance is H = 220 nm.

The effect of changing the connector width (w_3) on the sensor's performance is demonstrated in Fig. 4.16 (a-b). The transmittance characteristics are simulated for different values of connector width from 90 nm to 120 nm, with a step size of 10 nm. Fig. 4.16 (c-f) demonstrates the relationship of resonant dip versus refractive index for different values of connector width. According to our findings, there is a significant decline in sensitivity when the value of the connector width is increased. We concluded that the optimal connector width for the sensor is w_3 = 100 nm, based on the results. Maximum sensitivity values were observed for mode-1, mode-2, and mode-3 at 1631.97 nm/RIU, 1826.37 nm/RIU, and 2963.73 nm/RIU, respectively. Higher-order modes exhibit higher sensitivity due to their enhanced power and capacity to trigger a stronger surface plasmon resonance. When compared to the fundamental resonant mode, higher-order modes are more sensitive to variations in the refractive index because they have a stronger evanescent field [267, 268]. Therefore, it can be concluded that mode-3 has greater sensitivity compared to mode-1 and mode-2.

Exploring the impact of varying the size of the left baffle "a" on the sensor's performance is depicted in Fig. 4.17 (a-b). The simulation studies indicate that an increase in the left baffle size from 30 nm to 60 nm results in an improvement in the resonant dips. Fig. 4.17 (c-f)

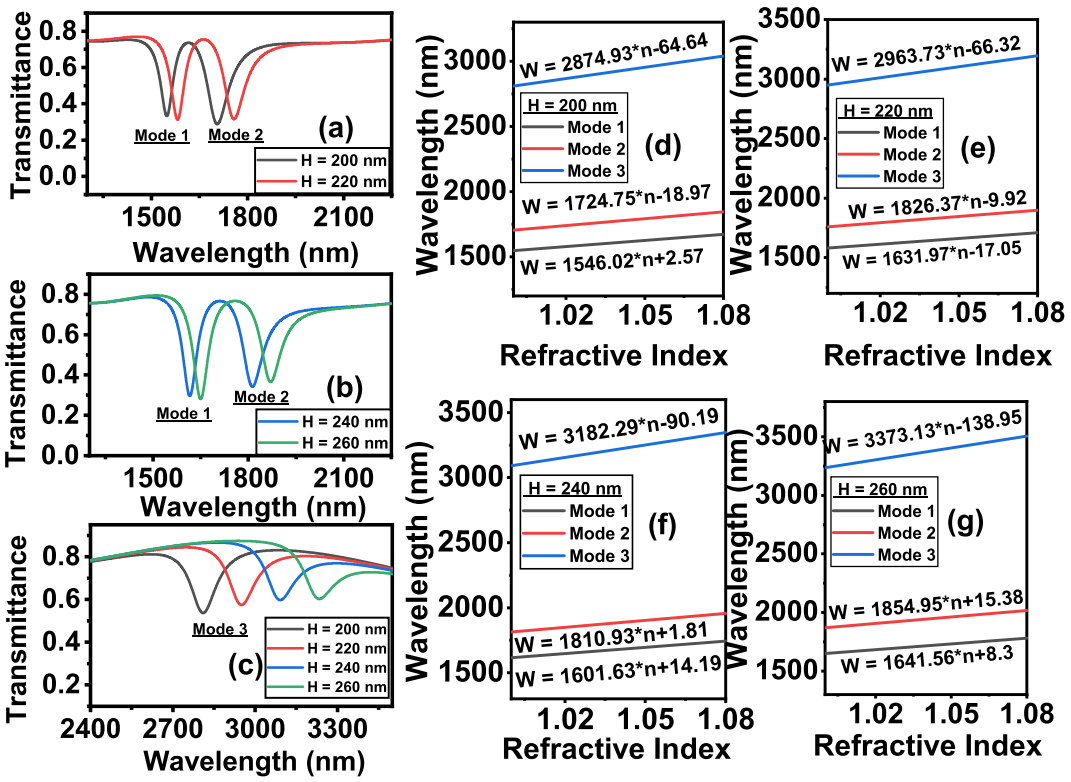

Figure 4.15: (a-c) Transmittance characteristics for different values of H and (d-g) shows resonant wavelength relation with refractive index.

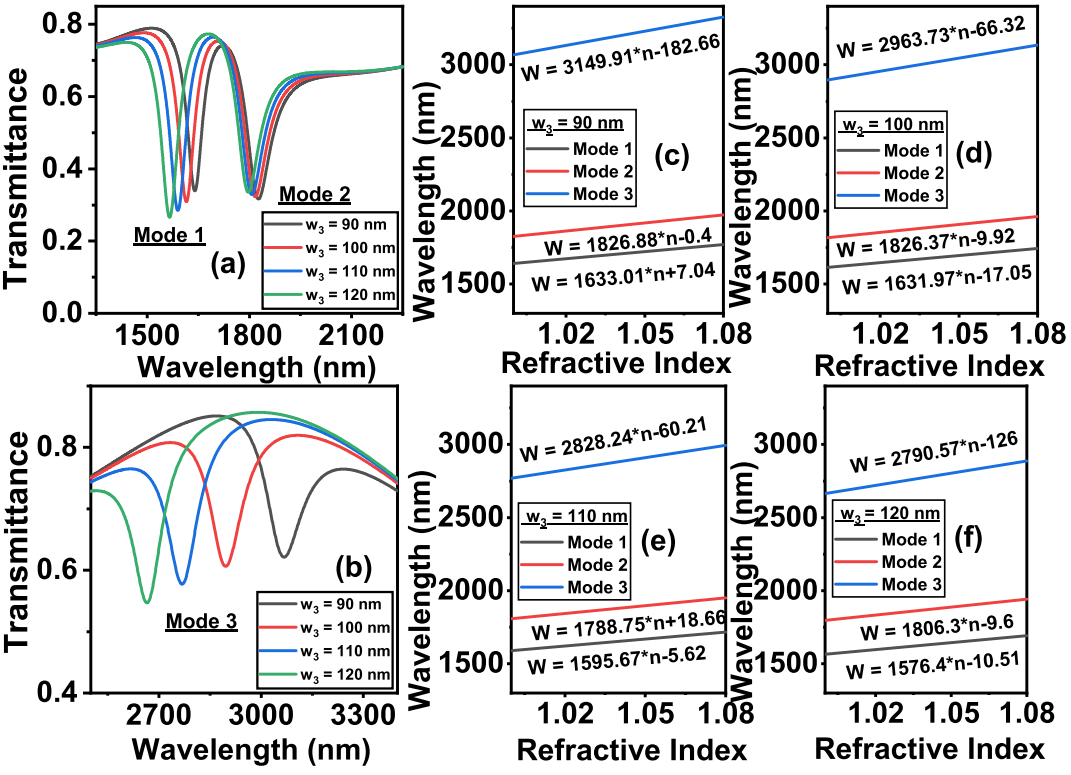

Figure 4.16: (a-b) Transmittance characteristics for different values of w_3 and (c-f) shows resonant wavelength relation with refractive index.

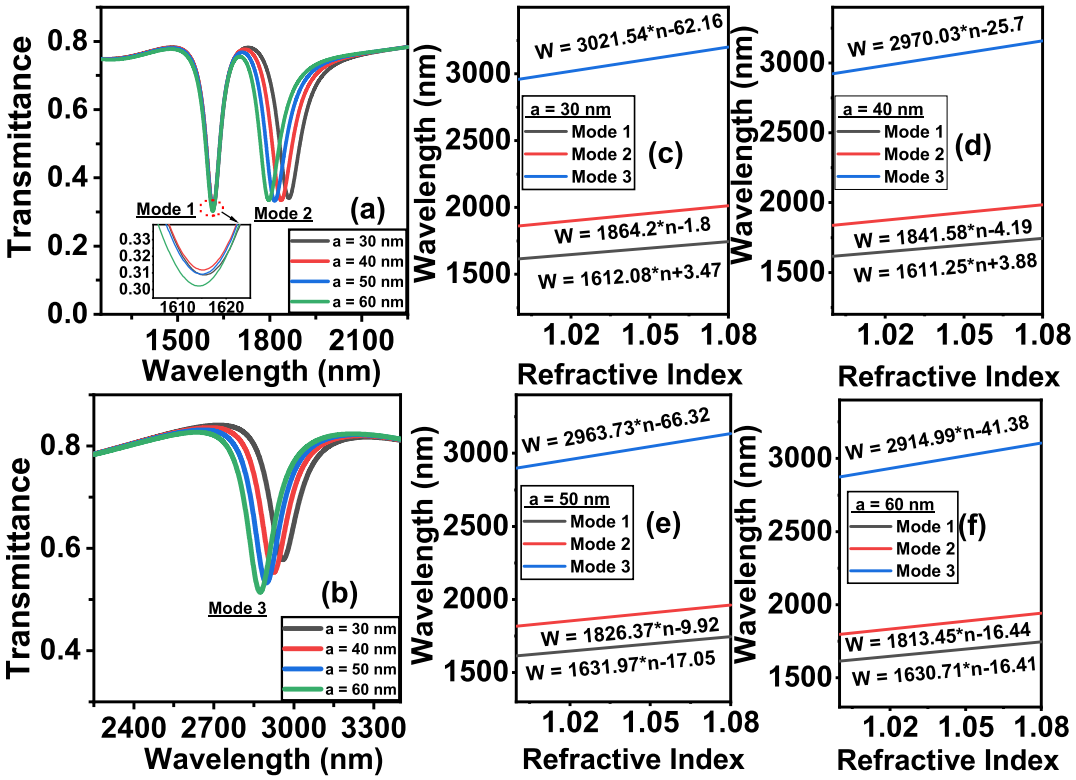

Figure 4.17: (a-b) Transmittance characteristics for different values of 'a' and (c-f) shows resonant wavelength relation with refractive index.

depicts the relationship between the resonant wavelength and refractive index, revealing a reduction in sensitivity as the baffle size increases. As per the simulation study, left baffle size of a = 50 nm offers the most favorable balance between sensitivity, and FOM, delivering optimal performance for our sensor. The right-side baffle "b" has an effect on the performance parameters shown in Fig. 4.18 (a-f) which is equivalent to that of the left-side baffle. Following the discussion, b = 55 nm is chosen for optimum performance in terms of both sensitivity and FOM.

The transmittance characteristics of a nanorod with varying radius (r) from 27.5 nm to 35 nm are illustrated in Fig. 4.19 (a-b), while Fig. 4.19 (c-f) illustrates the relationship between resonant wavelength and refractive index for different values of 'r'. According to the simulation study, sensitivity is enhanced as the radius increases. The optimal radius, r = 32.5 nm is selected to ensure a balanced sensitivity and FOM. The physical basis of the observation is that nanorods narrow the path of surface plasmon polaritons (SPPs), increasing their interaction with analyte molecules. This results in a stronger evanescent field and enhanced light-matter interaction, ultimately leading to higher sensitivity of the sensor [164].

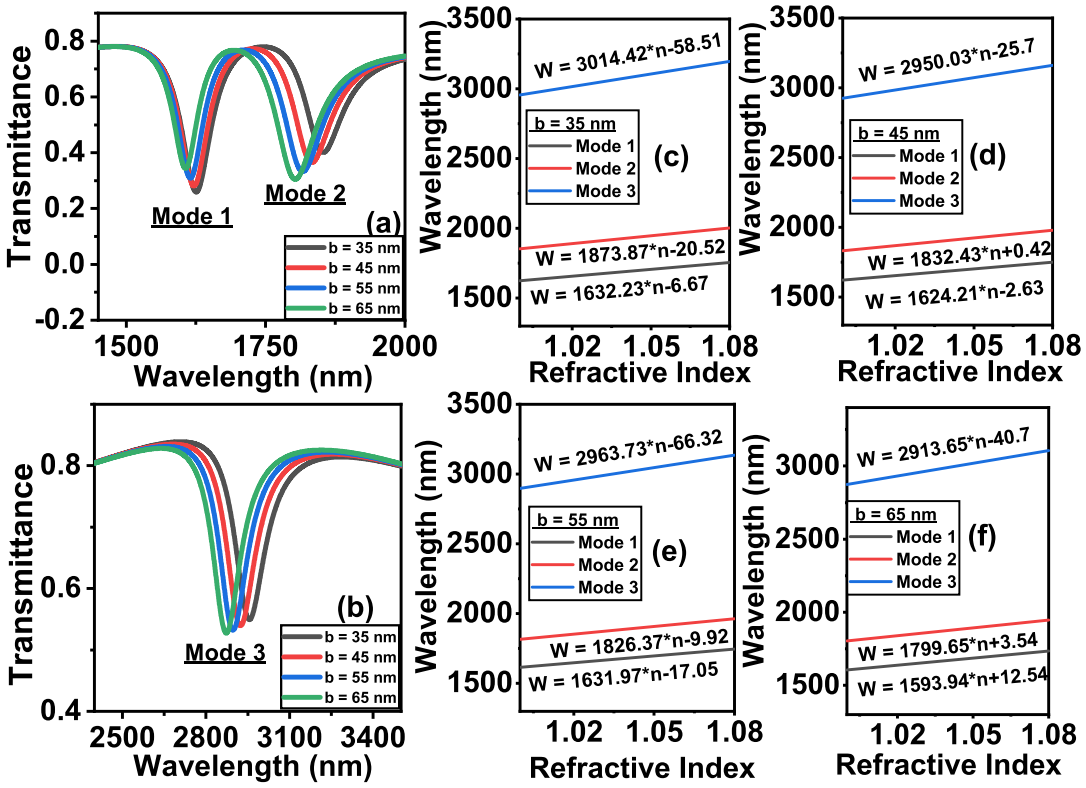

Figure 4.18: (a-b) Transmittance characteristics for different values of 'b' and (c-f) shows resonant wavelength relation with refractive index.

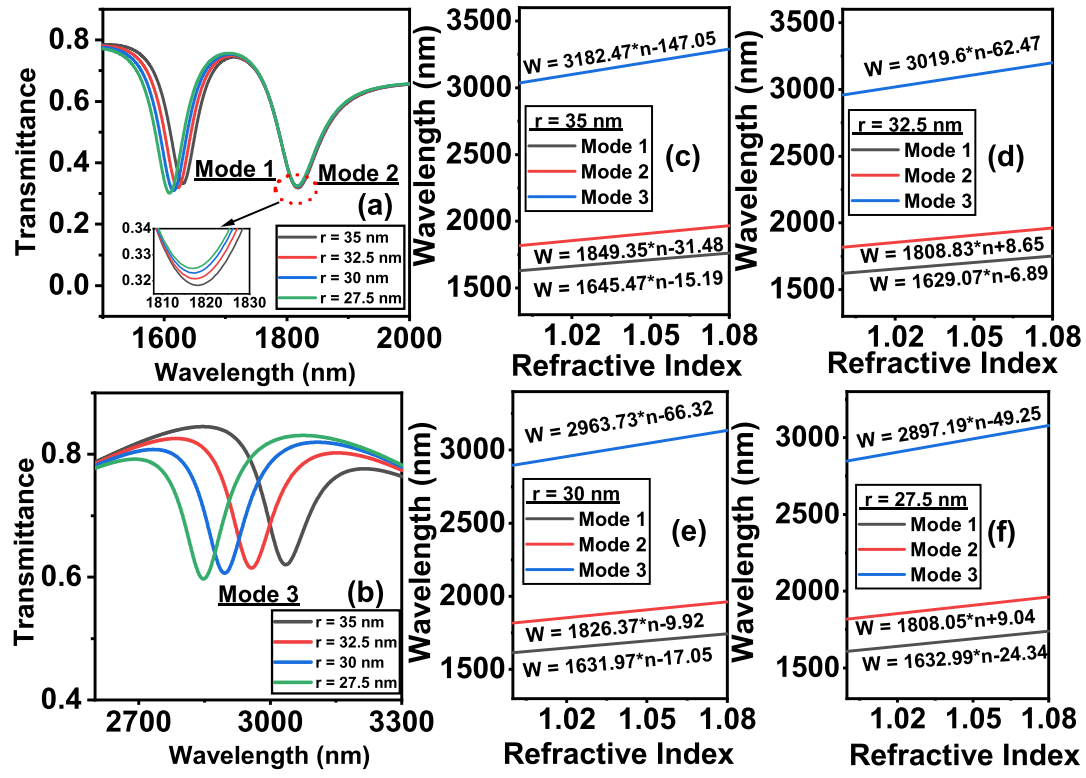

Figure 4.19: (a-b) Transmittance characteristics for different values of 'r' and (c-f) shows resonant wavelength relation with refractive index.

4.3.2.3 Final Parameters Selection and Result Analysis

Following the optimization procedure, the optimized parameters are presented in Table 4.23, which yield the most effective combination that produces the best outcome. The transmission spectra for the optimized parameters are illustrated in Fig. 4.20 for different values of refractive index. The sensor exhibits a very high sensitivity, with a maximum recorded value of 2963.73 nm/RIU, with a corresponding FOM of 25.1. In Fig. 4.21 (a-c), the electric field distributions for all three resonant modes are illustrated, while Fig. 4.21 (d-f) shows the magnetic field distributions for all three resonant modes. The results of our suggested sensor are compared with recent works of RI sensors shown in Table 4.24.

Table 4.3: Final geometric parameters of the structure.

Name of the Parameter	Symbol	Initial Value (nm)	Final Value (nm)
Length of the resonator	L	400	480
Height of the connector	H	200	220
Gap between resonator and waveguide	g_1	20	15
Width of the waveguide	w_1	45	55
Width of the resonator	w_2	55	65
Width of the connector	w_3	110	100
Left Side Baffle	a	-	50
Right Side Baffle	b	-	55
Radius of the Nanorod	r	-	32.5

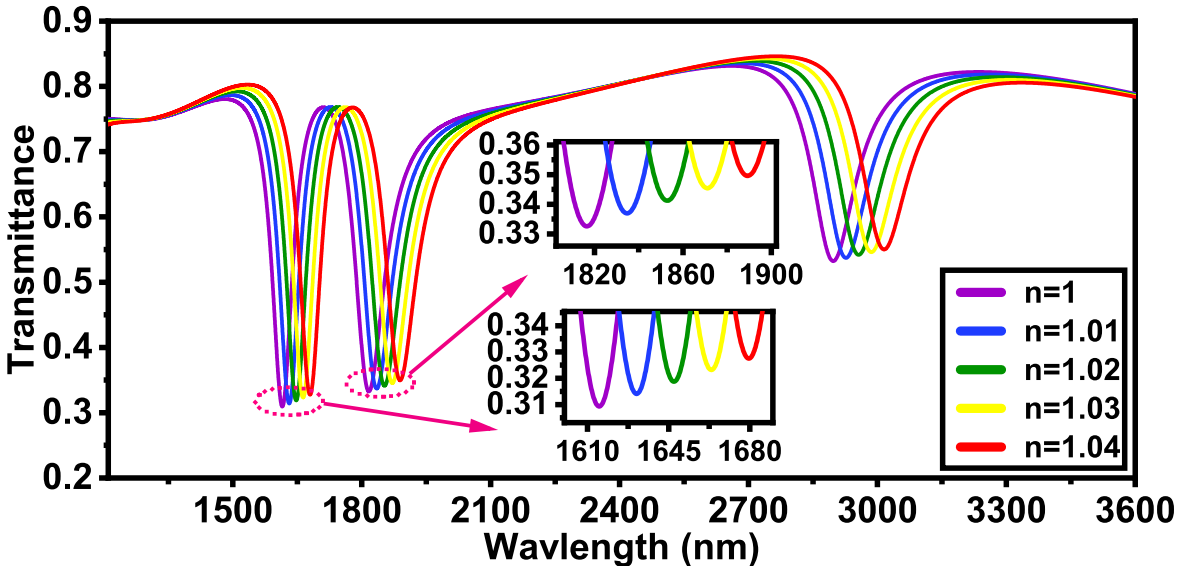

Figure 4.20: Transmittance characteristics different values of refractive index for the optimized structure.

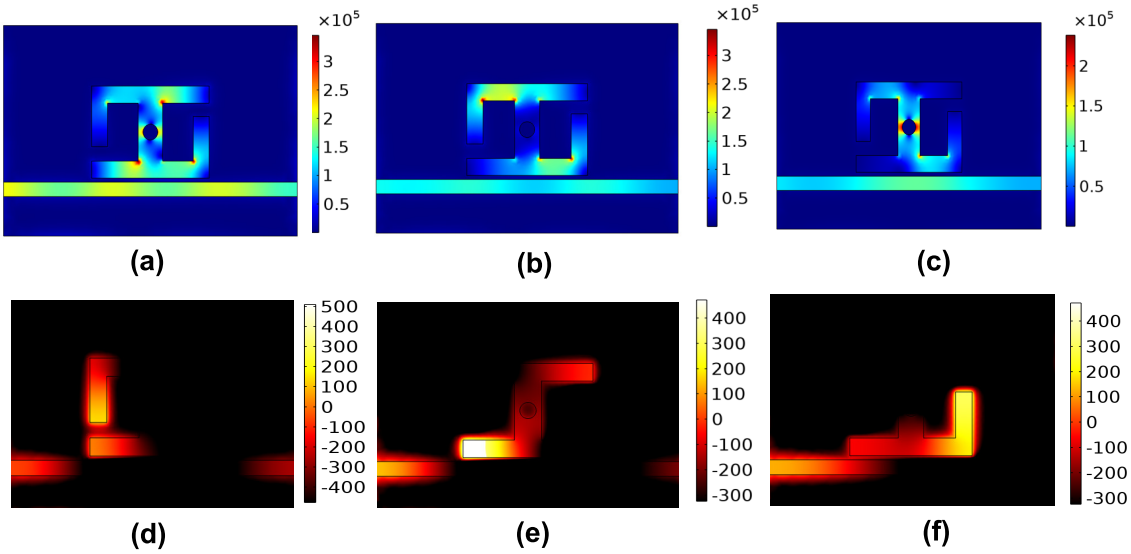

Figure 4.21: Electric field distribution (V/m) for n = 1 a. resonant wavelength = 1614.92 nm b. resonant wavelength = 1816.45 nm c. resonant wavelength = 2897.41 nm and magnetic field distribution, H_z (A/m) for n = 1 d. resonant wavelength = 1614.92 nm e. resonant wavelength = 1816.45 nm f. resonant wavelength = 2897.41 nm.

Table 4.4: Comparison of the sensing performance of the proposed sensor and recent literature.

References	**Year**	**Sensitivity (nm/RIU)**
Zafar et al. [112]	2015	1060
Rakhshani et al. [100]	2017	2320
Butt et al. [269]	2018	800
Butt et al. [97]	2018	1200
Jankovic et al. [150]	2018	986
Butt et al. [169]	2019	1367
Zhang et al. [168]	2019	1200
Zhang et al. [170]	2019	1268
Yang et. al [192]	2020	1100
Rahmatiyar et al. [105]	2020	1295
Maryam et al. [270]	2020	1260
Chou et. al [271]	2020	2080
Butt et al. [272]	2021	1400
Kazanskiy et al. [273]	2021	700
C. Wu et al. [208]	2021	1600
Rohimah et al. [224]	2022	1333
Butt et al. [274]	2022	1350
Proposed Sensor	2023	2963.73

4.3.3 Fabrication Process

Nanoimprint Lithography (NIL) is one of the effective techniques for fabricating plasmonic nanosensors due to its simplicity, low cost, and effectiveness in achieving high sensitivity. In this technique, solid-phase thermoplastic polymers such as polymethylmethacrylate (PMMA) can be used as an imprint resin because of its ability to form high-resolution patterns. First, the resin is placed over a Si substrate, and the mold design is transferred onto the resin layer. This process requires a temperature higher than $170\,^{\circ}\mathrm{C}$ and a high pressure of $50\,\mathrm{bars}$ [275]. When the mold is stamped onto the resin layer, the thickness remains the same at the places of the design. The residual resin layer, where the thickness reduces, can be removed by oxygen plasma etching with an O_2 flow rate of $30\,\mathrm{mL\,min^{-1}}$ and $300\,\mathrm{W}$ power for 6 minutes. Finally, an Ag layer is added using electron-beam evaporation, and the imprint resin is removed by ultrasonic agitation in acetone [276]. The fabrication process for the proposed structure is visually illustrated in Fig. 4.22.

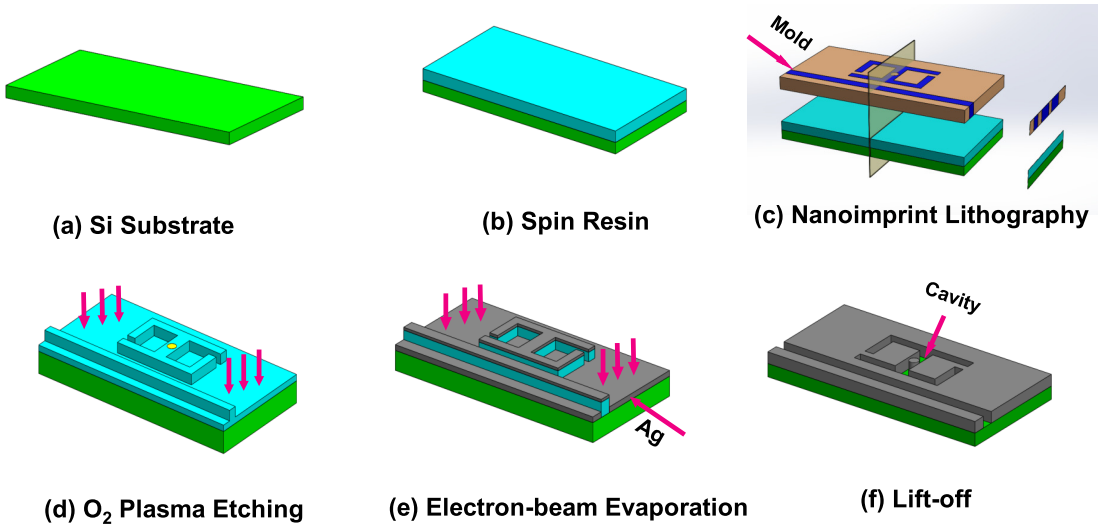

Figure 4.22: Fabrication process of the sensor a. Si Substate b. Spin Resin c. Nanoimprint Lithography d. O_2 Plasma Etching e. Electron-beam Evaporation f. Lift-off

4.3.4 Applications

For bio-sensing applications, resonant mode-3 is chosen, which has the maximum sensitivity. Mode-3 has a higher evanescent field which enables it to detect even small changes in refractive index with greater accuracy.

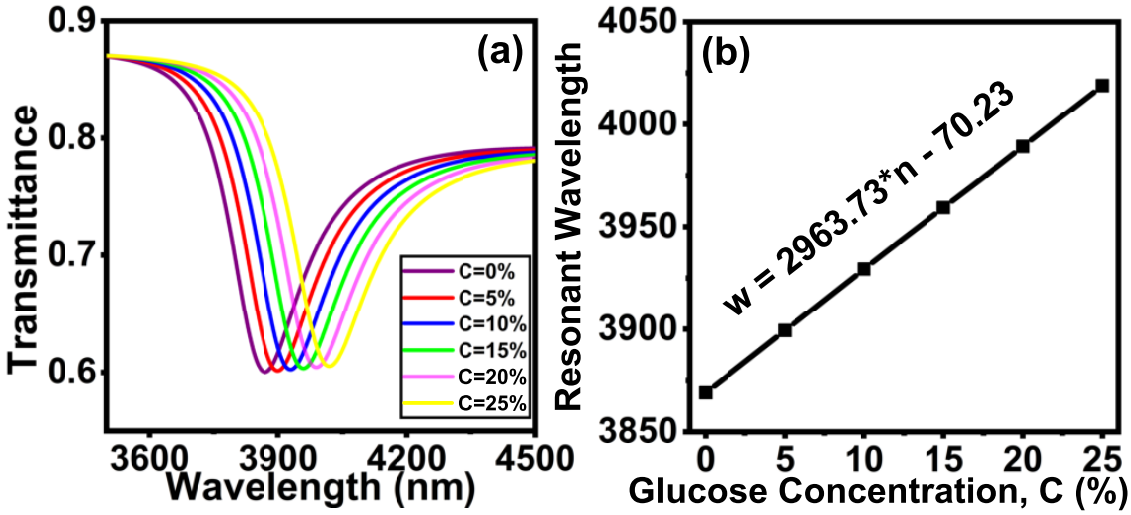

Figure 4.23: a. Transmittance characteristics for different glucose concentration percentages b. Relationship of resonant wavelength with glucose concentration (C%).

4.3.4.1 Detection of Diabetes Severity

Blood glucose concentration is the total quantity of glucose (a sugar) in a given volume of blood. The concentration of glucose in the blood is closely controlled to maintain a steady level since glucose is a vital source of energy for the body. Blood glucose normal ranges shift throughout the day, depending on when the previous meal was eaten and other personal characteristics including age and health. The following equation (4.9) calculates glucose concentration percentage,

$$n = 0.2015 \times C\% + 1.3292 \tag{4.9}$$

Here, in Eq.4.9, n is the refractive index, and C% is the glucose concentration percentage [277]. The variation of transmittance spectra is shown in Fig. 4.23 (a) and the linear relation between resonant wavelength and glucose concentration is shown in Fig. 4.23 (b).

By utilizing this relationship, it is possible to calculate the unknown concentration percentage of glucose. The percentage of glucose concentration converted to mmol/L can be used to rapidly and easily assess the severity of diabetes. We need to know the molecular weight of glucose as well as the density of the solution in order to convert the molar concentration of glucose solutions to mmol/L. At standard conditions (room temperature and atmospheric pressure), pure glucose (also known as anhydrous dextrose) has a density of approximately 1.54 g/mL and a molecular weight of approximately 180.16 g/mol. The following equation (4.10) can easily determine the diabetes level (mmol/L),

$$Diabetes\ level = \frac{(Conc.\ \%) \times (density\ in\ g/mL) \times 1000}{molecular\ weight} \tag{4.10}$$

In the following table (4.5), mmol/L values indicate diabetes levels, which may be used to

evaluate whether a person is healthy, prediabetic or diabetic [278].

Table 4.5: Primary diagnosis of Diabetes.

Condition	Range	Concentration (%)	Refractive Index
Healthy	<7.8 mmol/L	<0.912%	<1.3310
Prediabetes	7.8-11 mmol/L	0.912-1.286%	1.3310-1.3317
Diabetes	>11 mmol/L	>1.286%	>1.3317

For individuals with diabetes, it is important to monitor not only their electrolytes but also their blood glucose levels, as insulin is linked to potassium balance and blood glucose regulation. Various sensors based on MIM technology have been developed to measure unknown sample concentrations in human blood [277]. These sensors offer advantages such as nanoscale integration capability, label-free detection, low cost, and simplicity of use [149, 279]. However, previous research in this area has only focused on measuring specific substances in a solution without taking into account the size of blood corpuscles (which are in the range of micrometers), anticoagulants used, and the effect of other substances present in complex human blood on the detection process. Before refractive index sensing can be performed, several steps must be taken to prepare the sample. These steps typically include purification, molecular separation, and concentration enhancement [280].

Using a centrifuge, the initial stage in the purification process is to separate the plasma from the mixture of blood and anticoagulant (often 2% EDTA). Plasma makes up around 55% of the total volume of blood and is made up of a variety of elements, including water, proteins, viruses, bacteria, electrolytes, and glucose [281]. Once the plasma has been separated, the next step is to filter it further by removing unwanted substances. This is achieved through molecular separation, specifically utilizing ultrafiltration and nanofiltration techniques. By using a membrane with progressively smaller pore diameters, the method of nanofiltration enables the selective separation of molecules depending on their size and charge. Using nanofiltration, glucose, and electrolytes like Na^+ and K^+ can be separated from the ultrafiltered solution [282]. After the molecular separation step, the glucose sample can be placed inside the sensor's cavity to measure the refractive index, allowing the detection of the glucose concentration [259].

4.3.4.2 Anemia Type Detection

Hemoglobin (Hb) concentration is a measurement of the amount of hemoglobin in the blood, an essential protein that transports oxygen from the lungs to the body's tissues. A low hemoglobin level may indicate anemia, which occurs when the body does not have enough red blood cells (RBC) or Hb to carry oxygen to its tissues [283]. The relation between Hb

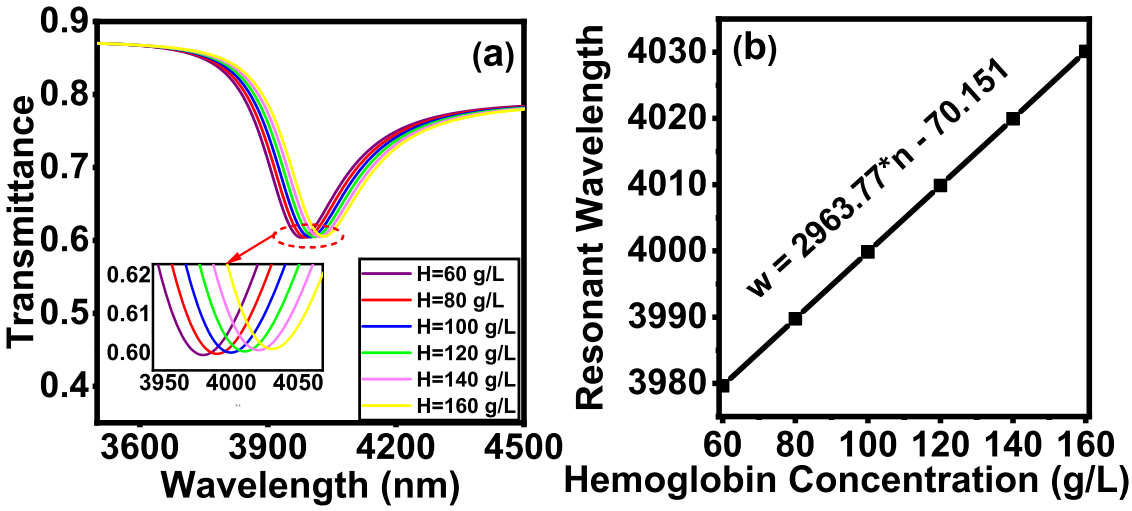

Figure 4.24: a. Transmittance characteristics for different Hemoglobin concentrations b. Relationship of resonant wavelength with Hb concentration.

concentration and refractive index is given by the following equation (4.11),

$$n = 1.38 + \frac{1}{5766.5}(H - H_{normal}) \tag{4.11}$$

Here, for a human body, the standard hemoglobin level (H_{normal}) is 140 g/L with a corresponding refractive index of 1.38 [284]. Fig. 4.24 (a) shows the transmittance characteristics for different Hb concentrations. Furthermore, it can be seen from Fig. 4.24 (b) that the Hb concentrations and the resulting changes in resonant wavelength are directly proportional, and the spacing between resonance wavelengths is 10 nm. Thus, the refractive index may be calculated from an unspecified Hb concentration. Optical spectrum analyzers can distinguish these closely spaced wavelengths individually. In order to diagnose anemia, this can be used to measure the amount of Hb in a blood sample.

Table 4.6 shows a clear idea about the anemia classification when Hb concentration decreases beyond H_{normal} value [285]. A high hemoglobin content, on the other hand, may suggest polycythemia, a disease in which the body creates too many red blood cells, which can raise the risk of blood clotting [286].

Table 4.6: Primary classification of Anemia

Condition	Range	Refractive Index
Healthy	>120 g/L	>1.376
Minor	100-120 g/L	1.373-1.376
Moderate	80-100 g/L	1.369-1.373
Acute	<80 g/L	<1.369

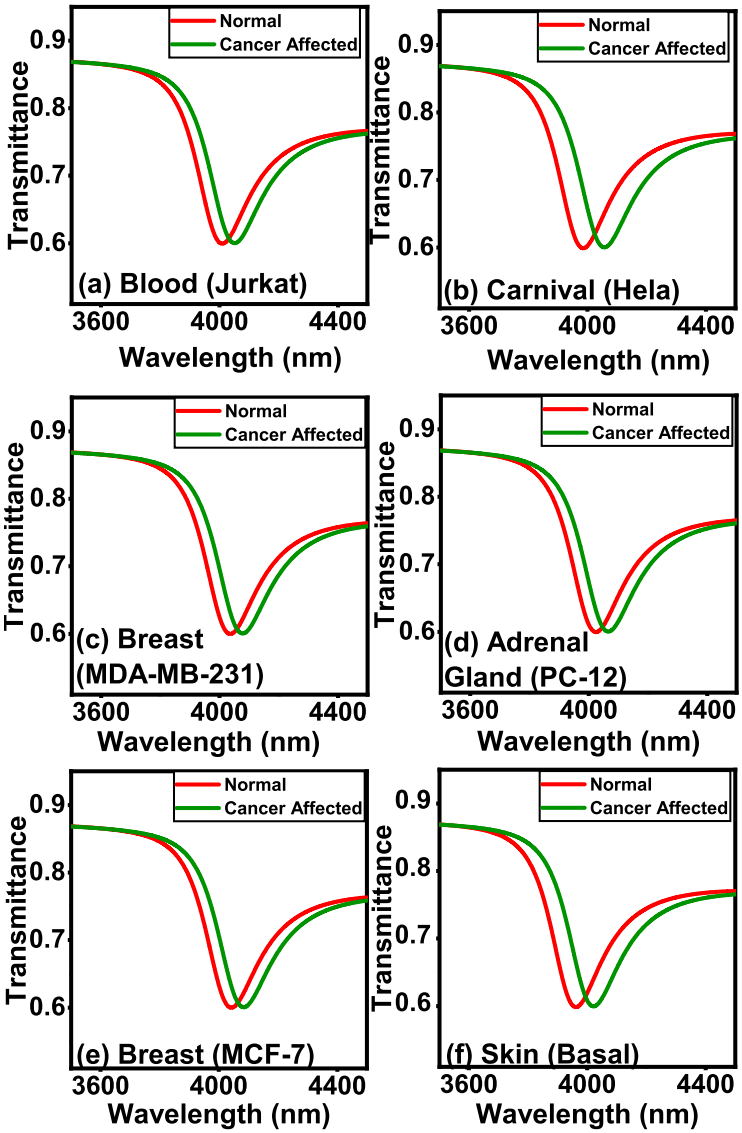

Figure 4.25: Comparison of Transmittance Characteristics between Normal and Cancerous Cells in Various Regions (a. Blood (Jurkat), b. Carnival (Hela), c. Breast (MDA-MB-231), d. Adrenal Gland (PC-12), e. Breast (MCF-7), f. Skin (Basal).

4.3.4.3 Cancer Cell Detection

Cancer is a disease that refers to abnormal cell growth and division in the body. For effective treatment, early identification and diagnosis of cancer are essential. Refractive index measurement can be one of the methods to identify cancer cells. According to the research, cancer cells (Jurkat, Hela, Basal, etc) have a different refractive index than healthy ones [287–290]. So, it is possible to determine whether the cells in a sample are malignant or normal by evaluating the sample's refractive index. The differences between healthy and cancerous cells in terms of refractive index and resonant wavelength are pointed out in Table 4.7. The shift in resonant wavelength that occurs in cancerous cells is seen in Fig. 4.25.

Table 4.7: Detection of cancer affected cell

Cell Name	Cell Type	Refractive Index		Resonant Wavelength (nm)	
		Normal	Cancer	Normal	Cancer
Jurkat	Blood	1.376	1.39	4009.44	4050.95
Hela	Carnival	1.368	1.392	3985.76	4057.04
Basal	Skin	1.36	1.38	3961.78	4021.39
MDA-MB-231	Breast	1.385	1.399	4036.42	4077.88
MCF-7	Breast	1.387	1.401	4042.46	4084.05
PC-12	Adrenal Gland	1.381	1.395	4024.38	4066.21

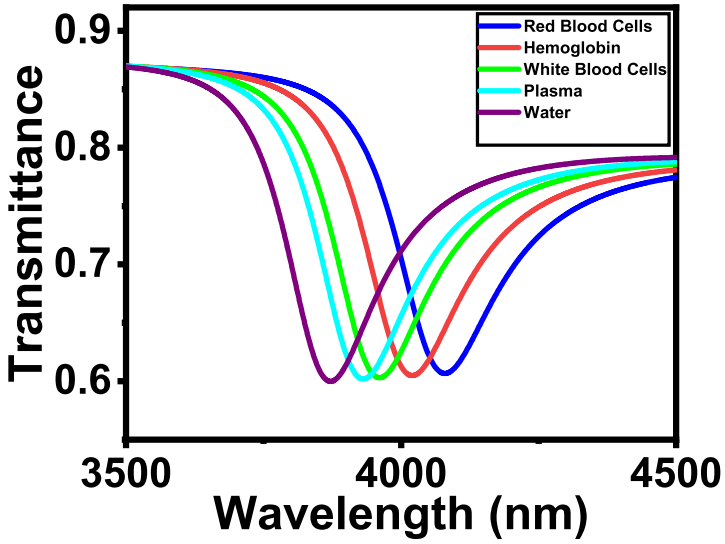

Figure 4.26: Transmittance characteristics for different components of blood.

4.3.4.4 Detection of Biological Components

i. Blood Components

There are various components in blood that have different refractive indices as shown in table 4.8 that can be utilized to analyze and detect the presence of the blood components. For example, red blood cells have a greater refractive index than the surrounding fluid. The data presented in table 4.8 may be used to detect anemia, infections, and blood disorders. Fig. 4.26 demonstrates the transmittance profile for different blood components.

Table 4.8: Various components of blood.

Blood Components	Refractive Index [291]	Resonant Wavelength (nm)
Water	1.33	4079.47
Red Blood Cells	1.4	4020.41
White Blood Cells	1.36	3960.79
Hemoglobin	1.38	3930.97
Plasma	1.35	3871.81

ii. Brain Components

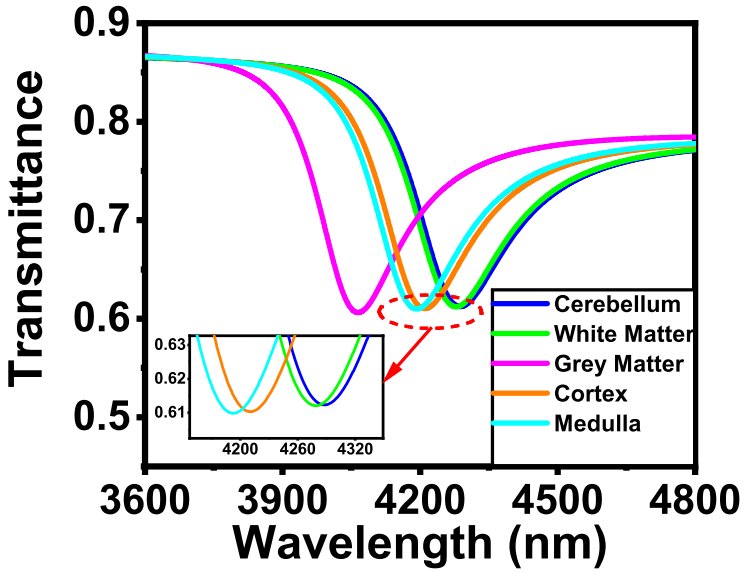

Figure 4.27: Transmittance characteristics for different components of brain.

Brain components have different values of refractive index and resonant wavelength as shown in Fig. 4.27. Table 4.9 shows the transmittance profile for different brain components. This can be used to distinguish between different brain components.

Table 4.9: Various components of brain.

Brain Components	Refractive Index [292]	Resonant Wavelength (nm)
Cerebellum	1.470	4287.96
White Matter	1.467	4279.04
Grey Matter	1.395	4064.78
Cortex	1.444	4210.55
Medulla	1.438	4192.39

iii. Intracellular Components

Table 4.10: Various intracellular components.

Intracellular Components	Refractive Index [293]	Resonant Wavelength (nm)
Water	1.33	3871.81
Protein	1.4	4079.47
Lipid	1.42	4138.83
DNA	1.44	4198.43
Bi-lipid Membrane	1.46	4258.21

To detect intracellular components using a RI sensor, we need to prepare the sample appropriately. Homogenization releases intracellular components, and filtering removes large

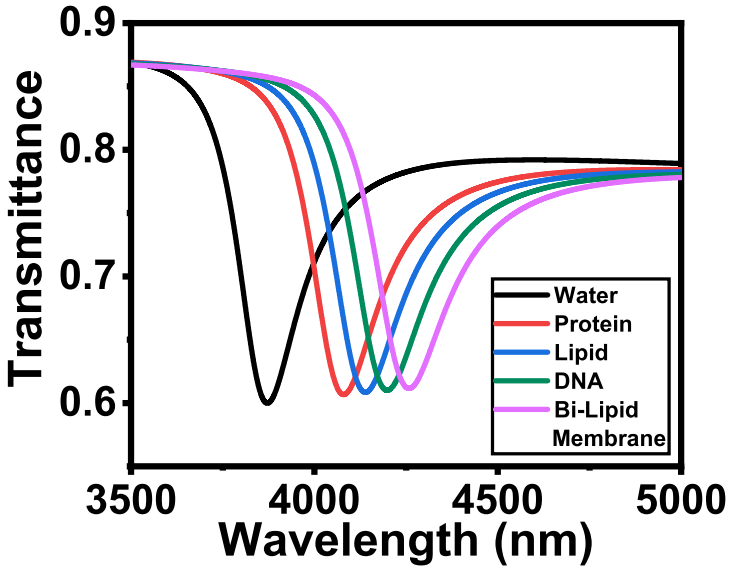

Figure 4.28: Transmittance characteristics for different components of intracellular components.

debris and cell membranes [294]. The intracellular components are introduced into the RI sensor. When optical excitation is given, a shift of resonant wavelength is observed depending on its refractive index. The sample's refractive index can be determined from the shift of resonant wavelength which can be seen in table 4.10, and transmittance spectra have been shown in Fig. 4.28.

iv. Different Tissues

Different types of tissue have different refractive indices due to their unique chemical and molecular structures. The transmittance spectra in Fig. 4.29 show how the resonant wavelength changes and the tissues can be identified from their refractive index. By comparing the refractive index of unknown tissue sample with the values in table 4.11, it is possible to identify the unknown tissue type. To get accurate refractive index values, tissue preparation, and measurement must be standardized [295].

Table 4.11: Various types of tissues.

Tissues Name	Refractive Index [296]	Resonant Wavelength (nm)
Muscle	1.3713	3995.20
Liver	1.3791	4018.39
Pancreas	1.3517	3936.94
Dermis	1.3818	4026.78

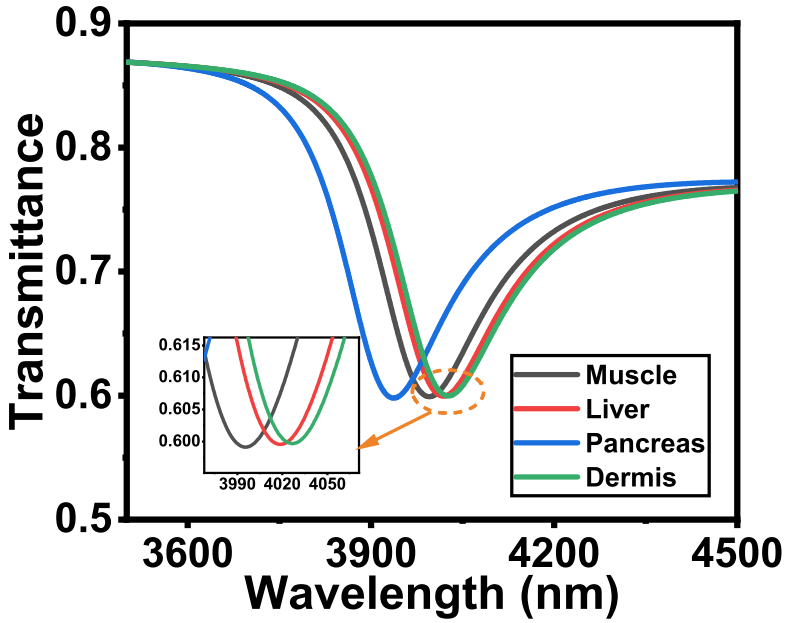

Figure 4.29: Transmittance characteristics for different types of tissues.

4.4 Sensor Design with Opposing-Face Semi-Circular Ring Resonators Integrated with Nanorods

4.4.1 Structure Model, Methodology and Performance Metrices

The top viewpoint of our initial proposed design, which contains a MIM bus waveguide coupled with an opposing-face semi-circular ring resonator, is shown in Fig. 4.30. This resonator structure is created by combining two semi-annular cavities and connecting their open ends to two rectangular cavities. The geometric parameters of this design are R, d, W, and g, which indicate the outer radius of the semi-annular cavities, the width of the semi-annular and rectangular cavities, waveguide width, and the gap between resonator and waveguide. The waveguide contains air, and the resonator is filled with a dielectric material such that the change in resonant wavelength may be monitored by altering the refractive index of the dielectric material. Table 4.12 shows the initial values of the geometric parameters for this design. According to Fig. 4.30, the blue, grey, and yellow zones are silver, dielectric material, and air, respectively. The transmittance spectrum of the proposed design was computed

Table 4.12: Initial values of the geometric parameters.

Name of the geometric parameter	Symbol	Value
Outer radius of the semi-annular cavities	R	200 nm
Width of the semi-annular and rectangular cavities	d	50 nm
Waveguide width	W	50 nm
Gap between resonator and waveguide	g	24 nm

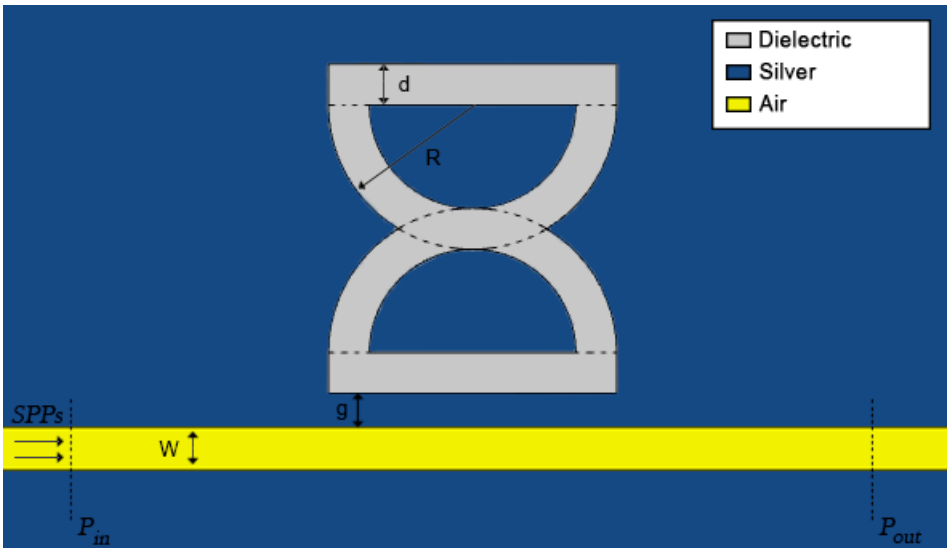

Figure 4.30: Initial structure of the design.

using the 2-D Finite Element Method (FEM) in COMSOL software. Except for the ports through which SPPs arrive and exit, scattering boundary conditions are used throughout the design to consume outgoing electromagnetic wave energy with minimum reflection. Extra-fine triangular meshing was employed to improve simulation accuracy.

SPPs are excited from the input port in transverse magnetic mode (TM). In this paper, the waveguide width is fixed at W = 50 nm. Since the waveguide width is much smaller than the incident wavelength, only the fundamental transverse magnetic mode (TM_0) can exist [297]. The dispersion equation of the fundamental TM mode in the MIM waveguide is given below [298].

$$k_1 W = 2\arctan(\frac{\epsilon_{in}\alpha}{\epsilon_M k_1}) \tag{4.12}$$

with k_1, α, and ϵ_{in} defined by momentum conservations.

$$k_1 = \sqrt{k_0^2(\epsilon_{in} - \beta^2)},\ \alpha = \sqrt{\beta^2 - k_0^2\epsilon_M},\ \epsilon_{in} = n^2. \tag{4.13}$$

Here, W represents the waveguide width. ϵ_{in} and ϵ_M define the dielectric constants of the dielectric material and the metal, respectively. $k_0 = \frac{2\pi}{\lambda}$ is the wave number and $\beta = k_0 n_{eff}$ is the propagation constant for SPPs, where λ is the wavelength of the wave and n_{eff} is the effective refractive index of the waveguide.

$T = (S_{21})^2$ is the transmittance where S_{21} is the transmission coefficient from input port P_{in} to output port P_{out} [299]. The excitation ratio (ER) is the difference between the maximum and minimum transmittance values. Higher the value of the ER, the better the performance of the sensor. The most commonly used performance parameters are sensitivity (S) and figure of merit (FOM). The capability of measuring any change in resonant wavelength with respect to

any change in refractive index is called sensitivity. It is defined as $S = \Delta\lambda/\Delta n$, where $\Delta\lambda$ is the change in resonant wavelength due to Δn amount of refractive index change. Moreover, FOM $= S/$FWHM, where FWHM is the full width at the half point of the transmission dip. Another performance parameter is the quality factor, which is defined as $Q = \lambda_m/$FWHM, where λ_m is the resonant wavelength.

4.4.2 Results Analysis

4.4.2.1 Optimization of the Design without Nanodots

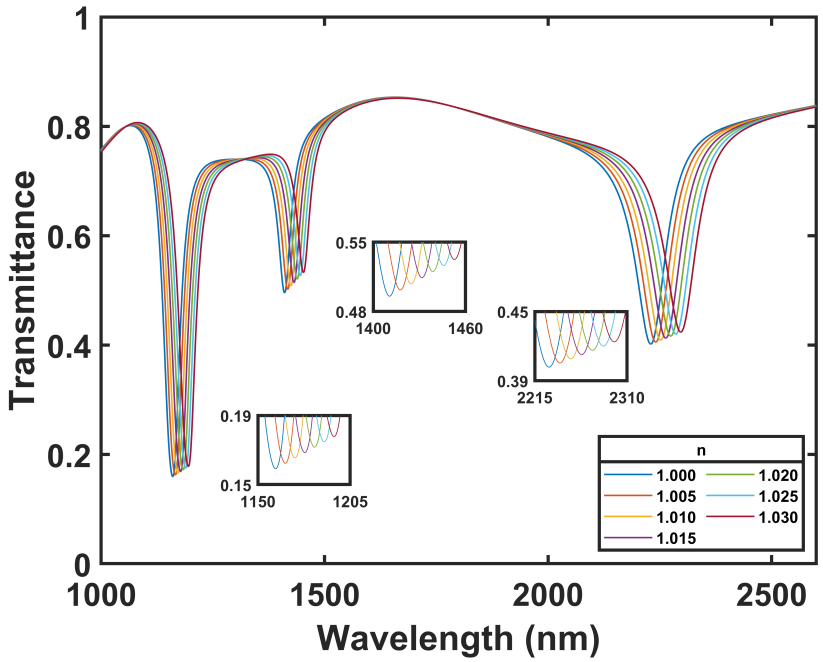

(a)

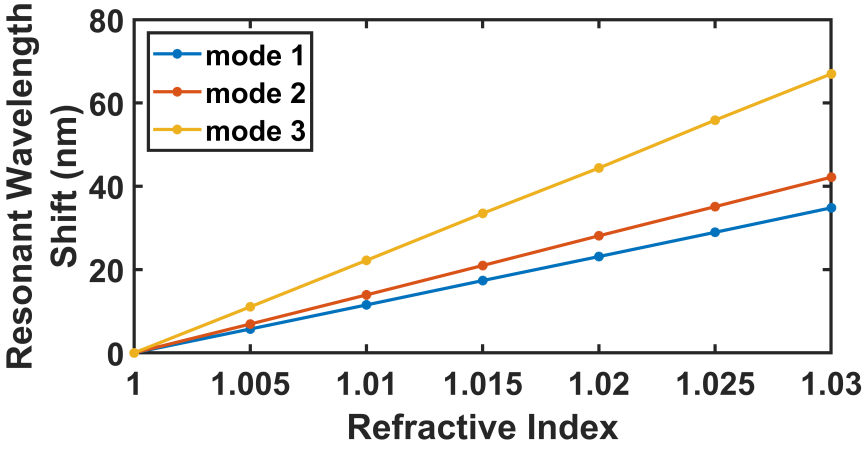

(b)

Figure 4.31: (a) Transmittance characteristic of our initial design for the initial geometric parameter values at different values of n (b) Resonant wavelength shift with a variation in n.

The transmittance values of the sensor and the resonant wavelength at which transmittance dips occur are determined by the structure and the geometric parameter values. An opposing-face semi-circular ring resonator was constructed using the initial values listed in Table 4.12. Different combinations of geometric parameters were used to see how they affected the transmittance curve. Based on that, the geometric parameters that provide the best balance of the crucial performance parameters are selected.

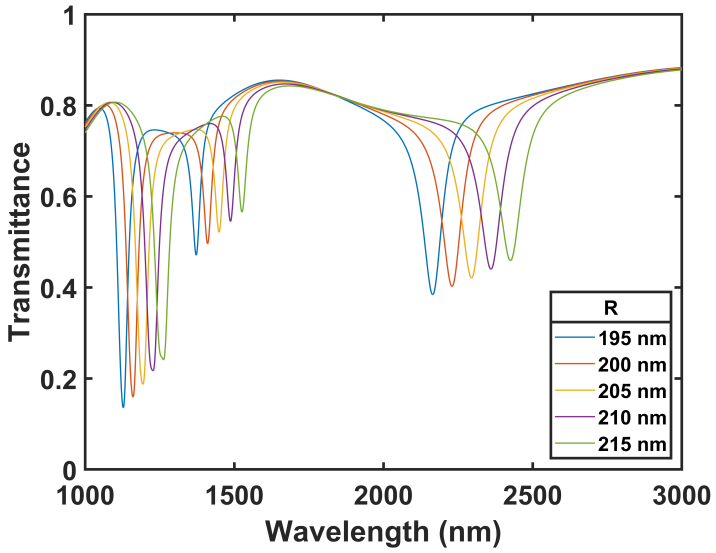

(a)

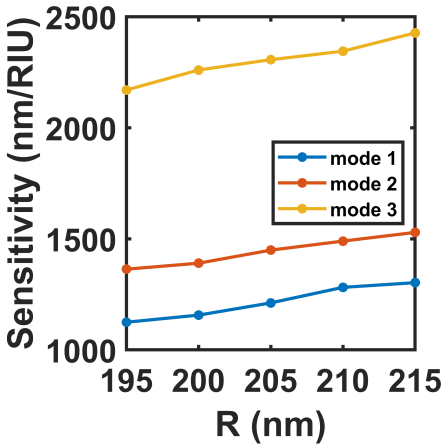

(b)

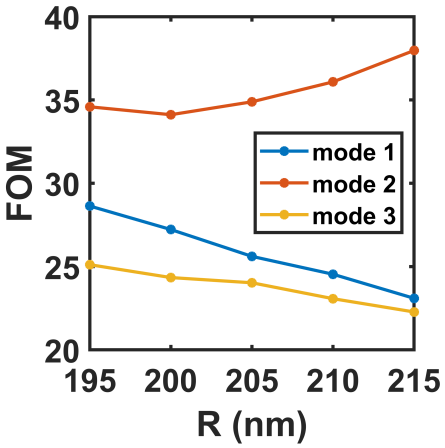

(c)

Figure 4.32: (a) Transmittance characteristic for diverse values of R (b) Sensitivity values for diverse values of R (c) FOM for diverse values of R.

To demonstrate the effect of increasing the refractive index value of dielectric material, Fig. 4.31(a) displays the transmittance curve of this resonator with initial geometric parameters in the wavelength range of 1000 nm to 2600 nm for refractive index value n changing from 1 to 1.03 with a space of 0.005. For the n = 1 scenario, three transmission dips are identified at 1160.61 nm, 1410.64 nm, and 2229.8 nm, which can be labelled as modes 1, 2, and 3. There is a redshift in all three modes as the refractive index value rises. Fig. 4.31(b) illustrates

the linear connection between the shift in resonant wavelength and the change in refractive index that meets equation 4.8, which states that n_{eff} is proportional to λ_m. As the refractive index value grows, so does the resonant wavelength, resulting in a redshift.

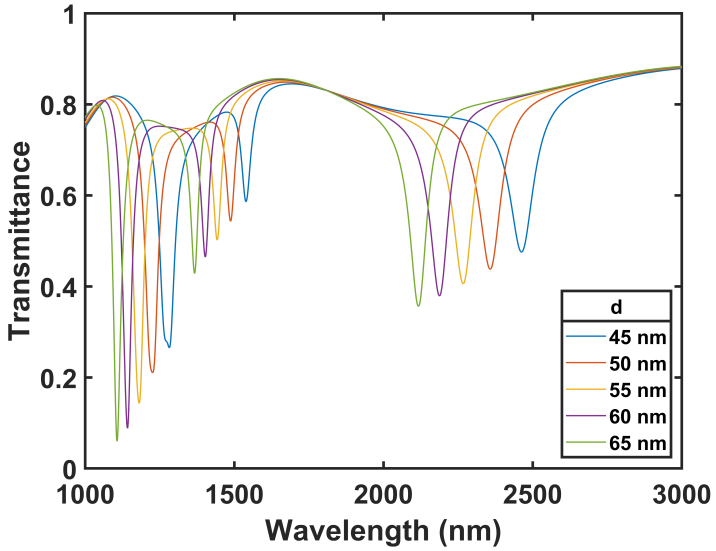

(a)

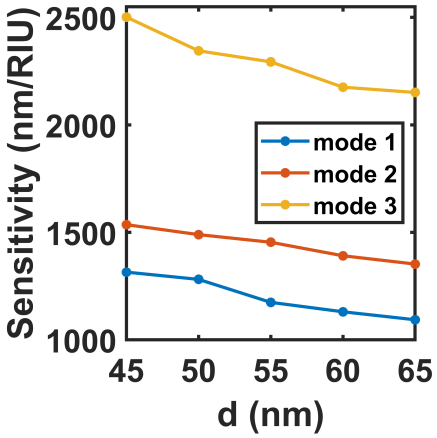

(b)

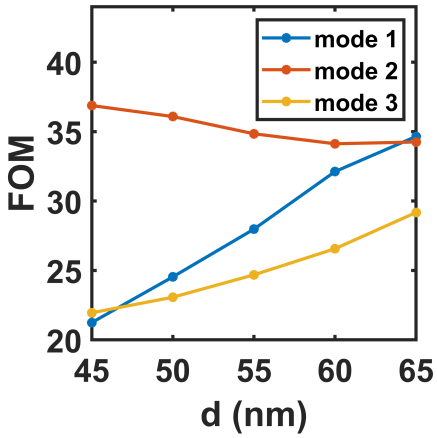

(c)

Figure 4.33: (a) Transmittance characteristic for diverse values of d (b) Sensitivity values for diverse values of d (c) FOM for diverse values of d.

The change in transmittance curve for the modulation of R value from 195 nm to 215 nm with a 5 nm interval meanwhile keeping d and g constant at 50 nm and 24 nm, respectively, is depicted in fig. 4.32(a). Increasing the value of R causes a redshift in the resonant wavelength for all three modes. Because increasing the value of R increases the effective length of the resonator and as a result, redshift in the resonant wavelength is justified by equation 4.8, which indicates that L is proportional to λ_m. Fig. 4.32(b) indicates that increasing the value of R raises the sensitivity values for all three modes. Fig. 4.32(c), on the other hand, indicates that increasing the value of R decreases FOM for modes 1 and 3, but increases

FOM for mode 2. As it is observed, the FOM values are within an acceptable range for all R values for all three modes, hence, sensitivity and resonator size were focused on when determining the best R value. Increasing the value of R increases sensitivity, but having a huge resonator is pointless, thus a balance between sensitivity and resonator size must be made. 210 nm was determined as the most optimized R value, and the sensitivity and FOM values are 1281.39 nm/RIU and 24.54 for mode 1, 1489.59 nm/RIU and 36.09 for mode 2, 2344.58 nm/RIU and 23.07 for mode 3.

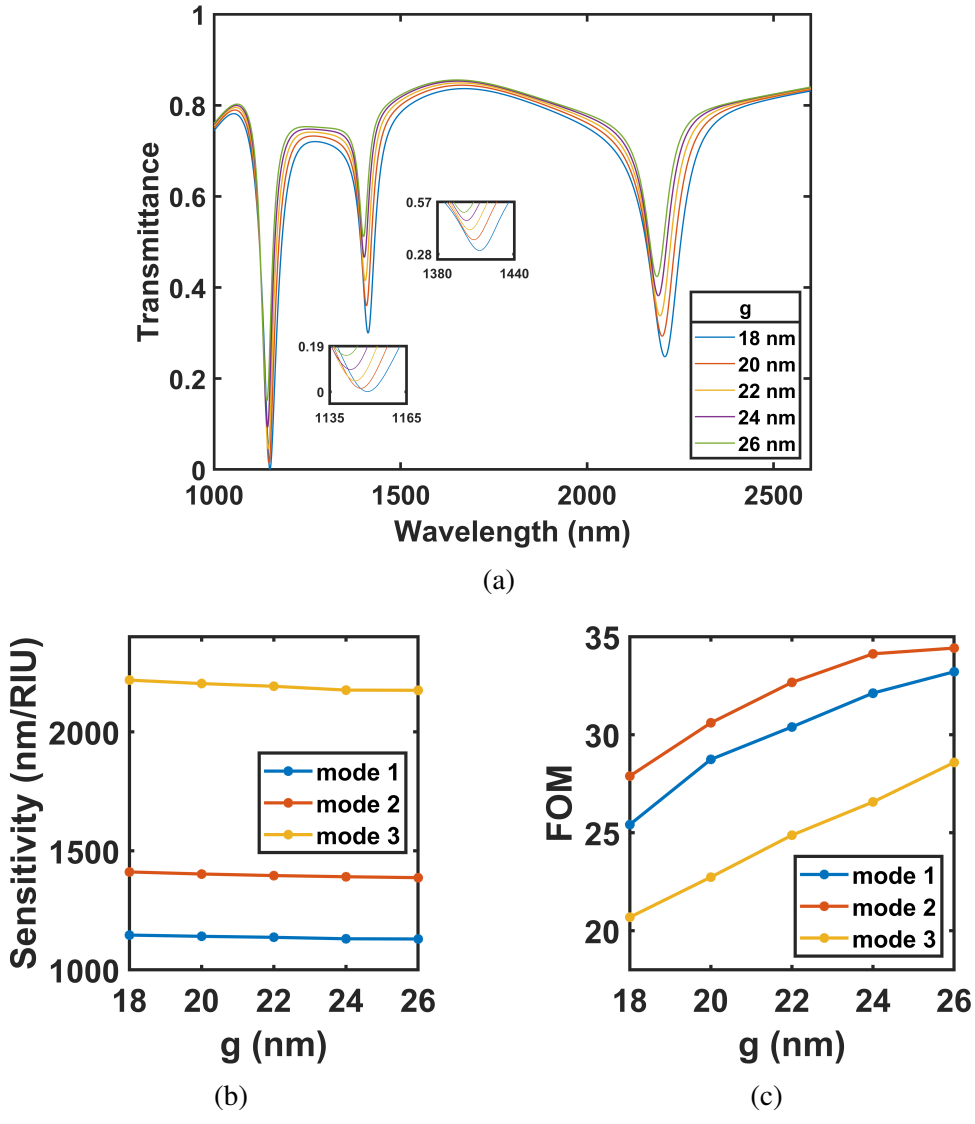

Figure 4.34: (a) Transmittance characteristic for diverse values of g (b) Sensitivity values for diverse values of g (c) FOM for diverse values of g.

Fig. 4.33(a) depicts the change in transmittance curve for a 5 nm interval change in the d value from 45 nm to 65 nm while keeping R and g constant at 210 nm and 24 nm, respectively. Increasing d causes a blueshift in the resonant wavelength for all three modes. As seen in Fig. 4.33(b), increasing the value of d reduces the sensitivity values for all three

modes. Fig. 4.33(c), on the other hand, illustrates that raising the value of d increases FOM in modes 1 and 3, but decreases FOM in mode 2. Sensitivity and FOM values were focused on when determining the best value of d. Increasing the value of d reduces sensitivity in all modes, however, FOM values increase in modes 1 and 3 while the fall in FOM value in mode 2 is not significant. 60 nm was picked as the best-optimized d value, and the sensitivity and FOM values are 1130.65 nm/RIU and 32.12 for mode 1, 1391.25 nm/RIU and 34.12 for mode 2, and 2175.42 nm/RIU and 26.57 for mode 3.

The variation in the transmittance curve for the fluctuation of the g value from 18 nm to 26 nm with a 2 nm interval while keeping R constant at 210 nm and d constant at 60 nm is shown in Fig. 4.34(a). When the amount of g is increased, there is a minor blueshift in the resonant wavelength for all three modes, but the ER reduces dramatically. When the coupling distance between the waveguide and resonator grows, the energy exchanging efficiency between the waveguide and resonator drops, and thus the ER decreases. As shown in Fig. 4.34(b), raising the value of g reduces the sensitivity values for all three modes, but the decrease is not statistically significant. Fig. 4.34(c) furthermore illustrates that increasing the value of g increases FOM in all three modes. The ER and FOM values were prioritized when determining the optimal value of g. Increasing the amount of g decreases the ER while increasing the FOM value for all three modes. As a result, an acceptable combination of FOM and ER must be determined. 20 nm was determined as the most optimum value of g, and the sensitivity and FOM are 1140.88 nm/RIU and 28.74 for mode 1, 1402.76 nm/RIU and 30.6 for mode 2, 2202.79 nm/RIU and 22.73 for mode 3.

The transmittance curve of optimal values of R, d, and g for n values ranging from 1 to 1.03 with a 0.005 interval is shown in Fig. 4.35(a). The normalized magnetic field intensity, $|H_z|$ (A/m) at n = 1 is shown in Fig. 4.35(b),(c),(d) for the resonant wavelengths of modes 1, 2, and 3, which are 1147.14 nm, 1408.52 nm, and 2201.39 nm, respectively. The normalized magnetic field intensity, $|H_z|$ (A/m) for off-resonance mode at a wavelength of 1660 nm is displayed in Fig. 4.35(e). Fig. 4.35(b),(c),(d) demonstrate that SPPs are well coupled with the resonator at resonant wavelengths, resulting in standing-wave field patterns between the waveguide and resonator. SPPs are confined to the left portion of the waveguide due to the high ER of mode 1, but as the ER drops in modes 2 and 3, SPPs can pass a little amount to the right side of the waveguide. SPPs are not coupled with the resonator at off-resonance peaks, as illustrated in Fig. 4.35(e), and most of them pass only via the waveguide.

4.4.3 Optimization of the Design after Adding Nanodots

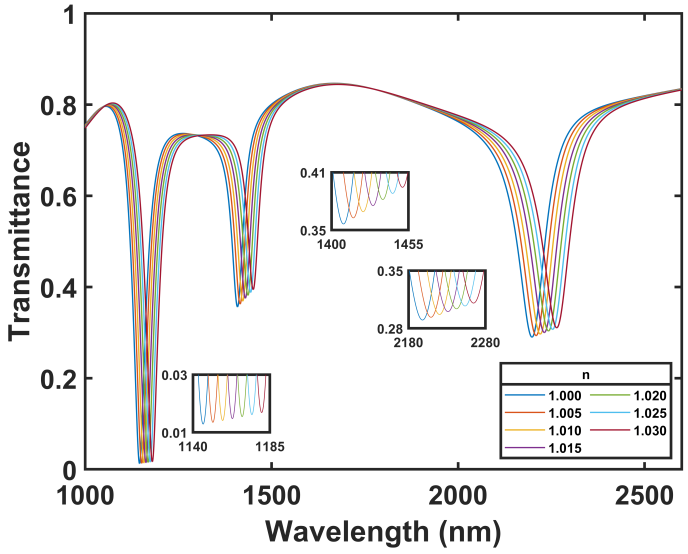

(a)

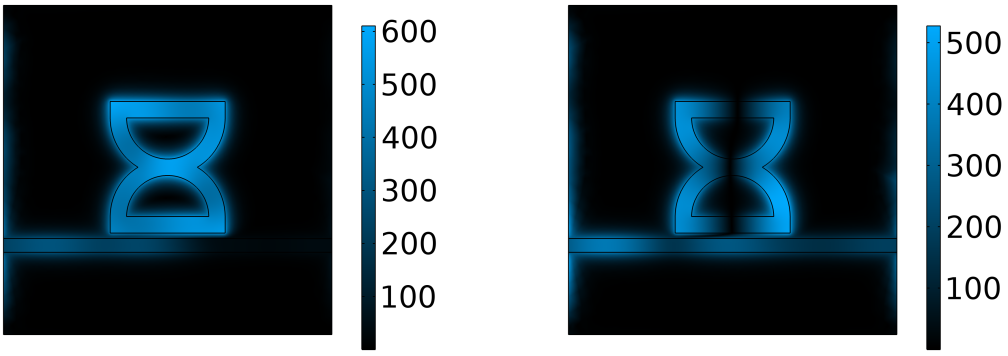

(b)

(c)

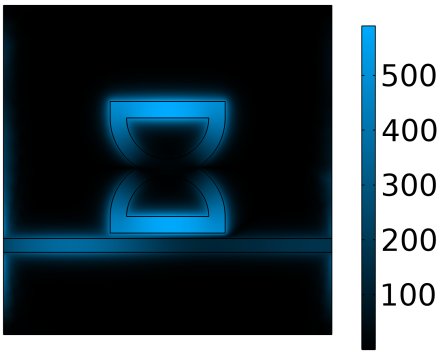

(d)

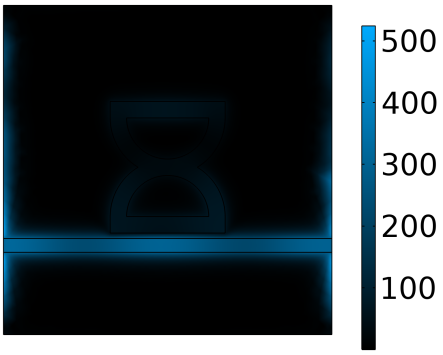

(e)

Figure 4.35: (a) Transmittance characteristic of our initial design for optimized geometric parameter values at different values of n (b) Normalized magnetic field intensity, $|H_z|$ (A/m) for n = 1 at wavelength = 1147.14 nm (c) Normalized magnetic field intensity, $|H_z|$ (A/m) for n = 1 at wavelength = 1408.52 nm (d) Normalized magnetic field intensity, $|H_z|$ (A/m) for n = 1 at wavelength = 2201.39 nm (e) Normalized magnetic field intensity, $|H_z|$ (A/m) for n = 1 at wavelength = 1660 nm.

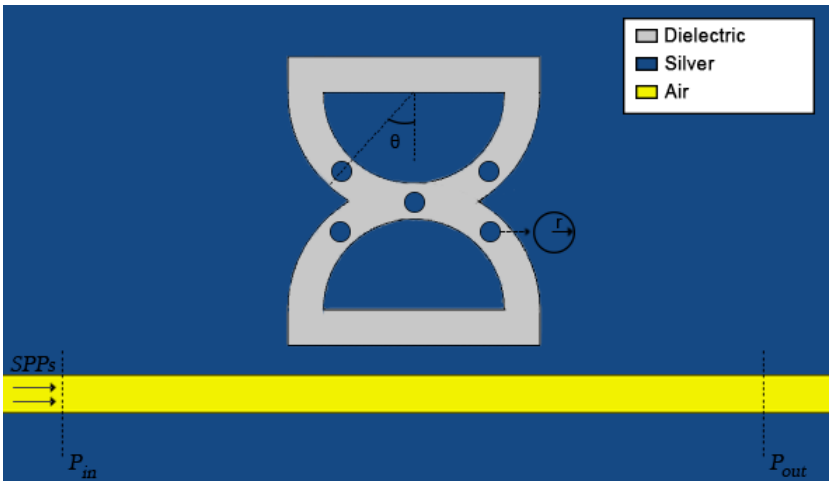

(a)

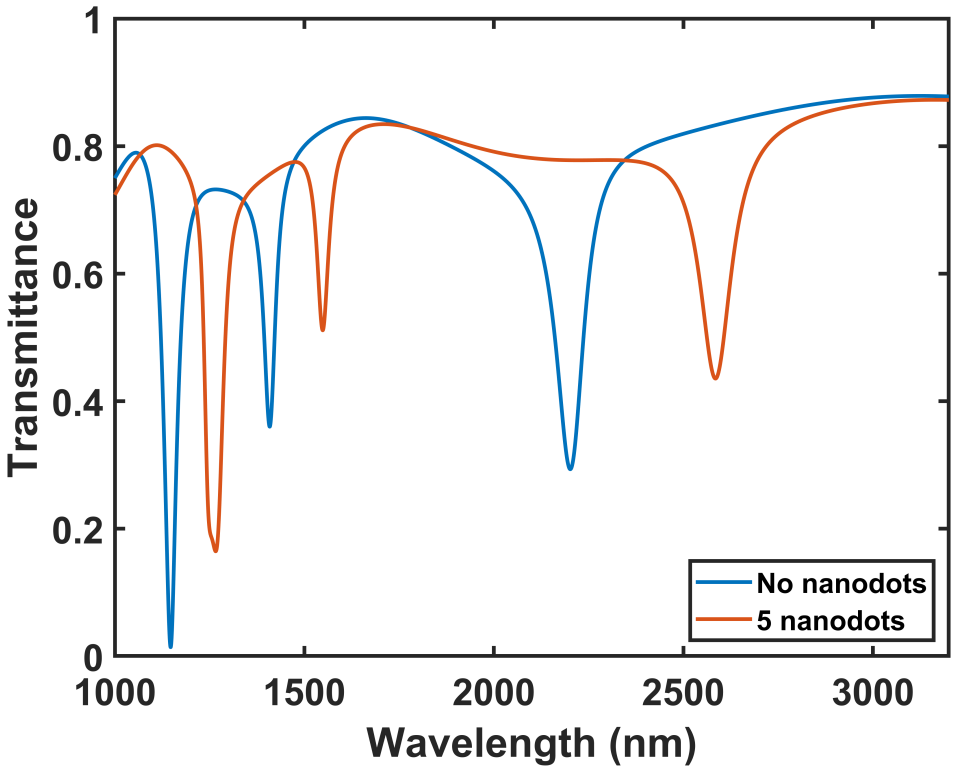

(b)

Figure 4.36: (a) Structure of the proposed design with added nanodots (b) Transmittance characteristic for initial design with no nanodots and final design with five added nanodots for $n = 1$.

A configuration with five nanodots is proposed to increase sensitivity without significantly lowering the ER. The nanodots have a radius of r, and one nanodot is at the center of the structure, while the other four nanodots are at a θ angle from the y-axis on both sides, with the same center as the half-circles. Fig. 4.36(b) indicates a redshift in the resonant wavelength with a minor drop in the ER when nanodots of r = 20 nm and $\theta = 45°$ are used.

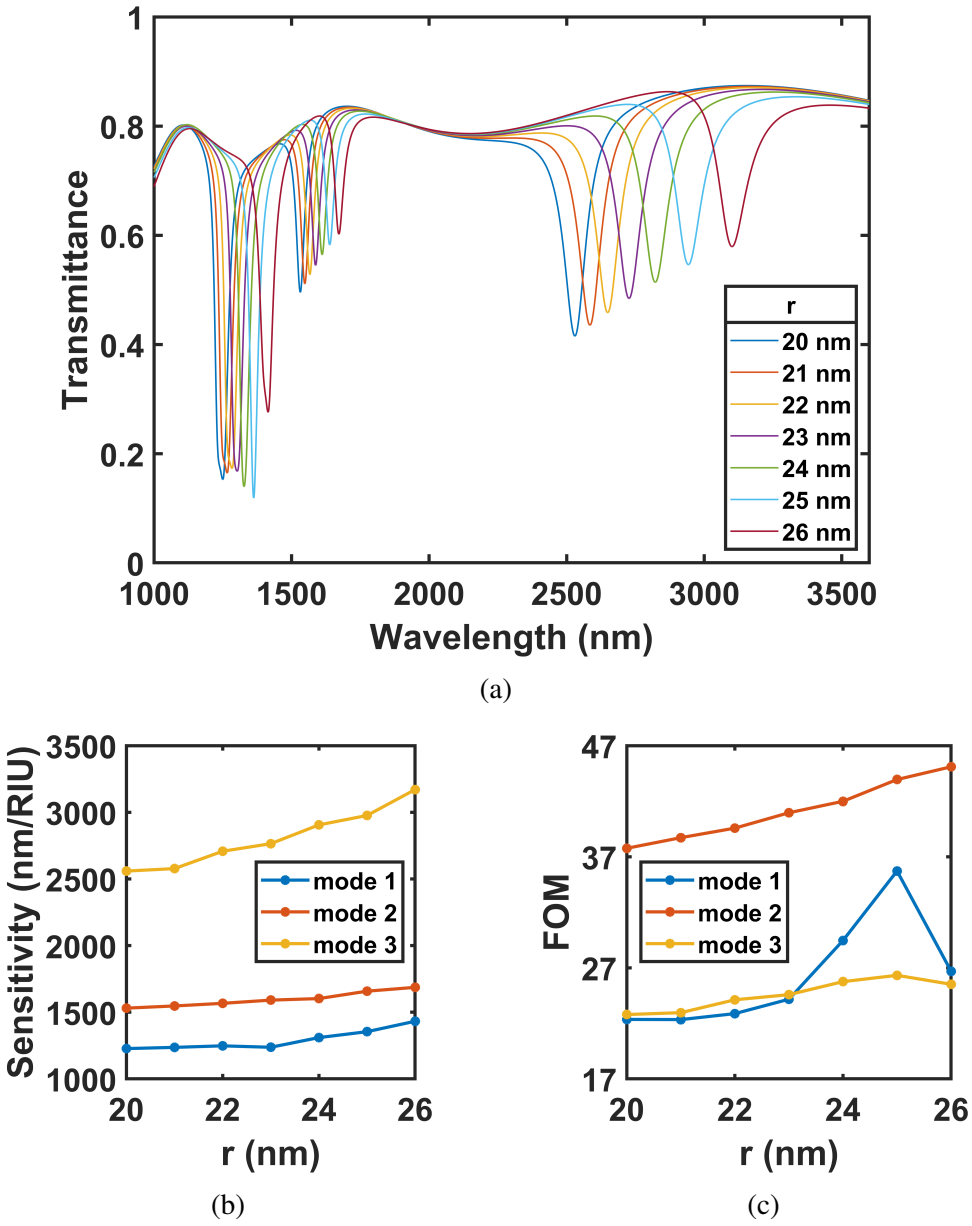

Figure 4.37: (a) Transmittance characteristic for diverse values of r (b) Sensitivity values for diverse values of r (c) FOM for diverse values of r.

The change in transmittance curve for the variation of r value from 20 nm to 26 nm with a gap of 1 nm meanwhile reserving the optimal values of R, d, and g fixed at 210 nm, 60 nm, and 20 nm correspondingly with an initial θ angle of 45° is shown in Fig. 4.37(a). Increasing the radius of nanodots r causes a redshift in the resonant wavelength for all three

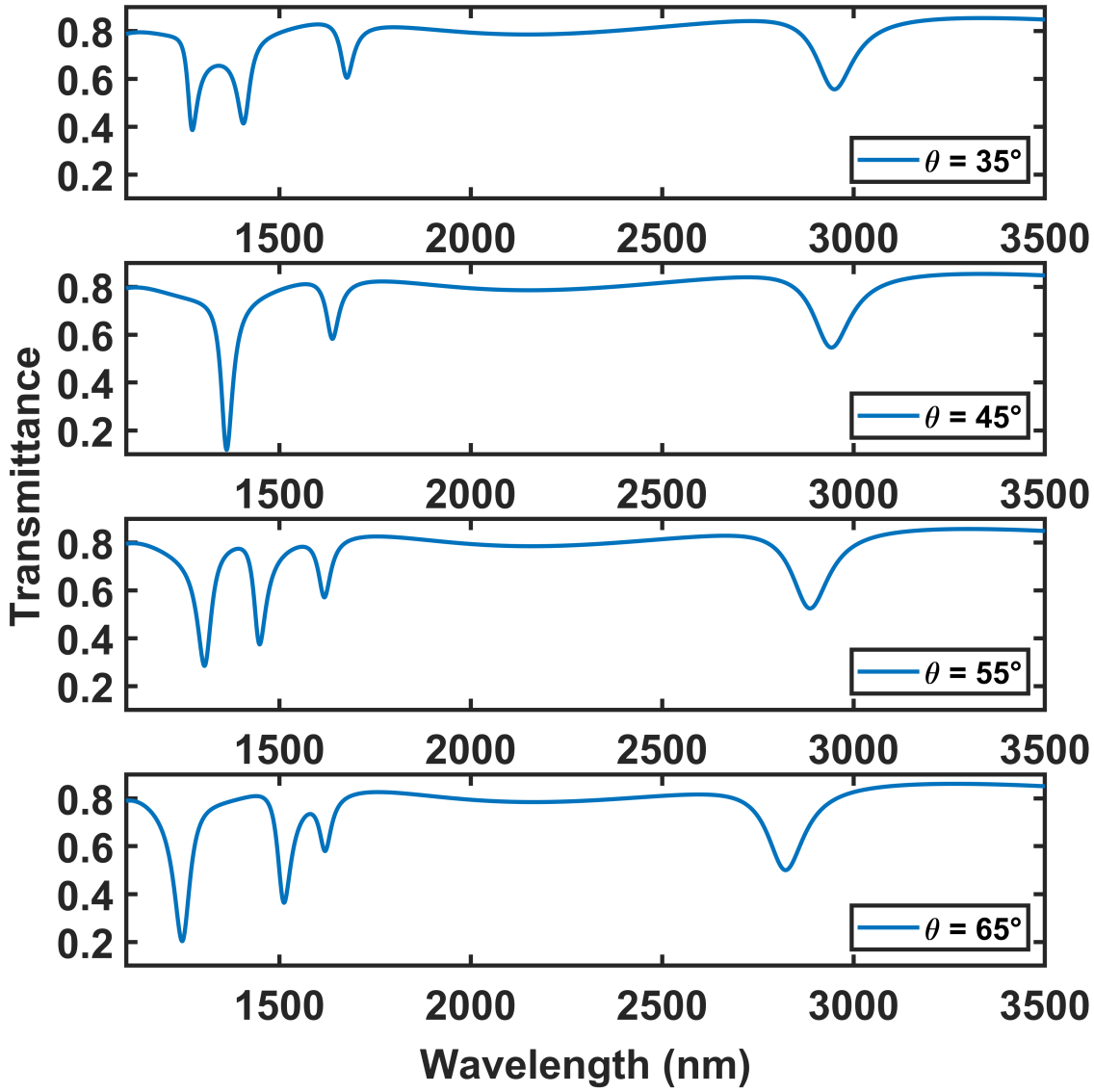

Figure 4.38: Transmittance characteristic for diverse values of θ.

modes. Fig. 4.37(b) depicts the sensitivity values for various r values, meanwhile Fig. 4.37(c) depicts the FOM values for various r values. In mode 2, increasing r enhances both sensitivity and FOM. In mode 1, raising r has little influence on sensitivity from 20 nm to 23 nm, however, the sensitivity continues to increase after that, up to 26 nm. On the other hand in mode 3, increasing r raises the sensitivity values. It is observed that the FOM of modes 1 and 3 increases from 20 nm to 25 nm and after that reduces at 26 nm. Fig. 4.37(a) shows that the ER was nearly constant for r values ranging from 20 nm to 25 nm in mode 1, although it reduced dramatically at 26 nm. As a result, the most optimum combination of sensitivity, FOM and ER can be seen for all three modes at $r = 25$ nm. The sensitivity and FOM are 1353.98 nm/RIU and 35.72 for mode 1, 1657.8 nm/RIU and 43.95 for mode 2, 2975.96 nm/RIU and 26.32 for mode 3.

Table 4.13: Optimized values of the geometric parameters.

Name of the geometric parameter	**Symbol**	**Initial value**	**Final value**
Outer radius of the semi-annular cavities	R	200 nm	210 nm
Width of the semi-annular and rectangular cavities	d	50 nm	60 nm
Waveguide width	W	50 nm	50 nm
Gap between resonator and waveguide	g	24 nm	20 nm
Radius of the nanodots	r	20 nm	25 nm
Angle of non-center nanodots with y-axis from the center of half-circle	θ	45°	45°

Table 4.14: Comparison with recently proposed sensors

References	**Year**	**Sensitivity (nm/RIU)**	**FOM**
Yan et al. [300]	2017	1071.4	14.29
Zhang et al. [301]	2018	1160	73
Wang et al. [302]	2019	1114.3	55.71
Butt et al. [303]	2020	2300	31.5
Chou Chau et al. [304]	2021	2473	34.181
Proposed design	2023	2975.96	26.32

The effect on the transmittance curve of shifting the value of θ from 35° to 65° with a 10° interval while keeping the optimal values of R, d, g, and r fixed at 210 nm, 60 nm, 20 nm, and 25 nm, respectively, is shown in Fig. 4.38. Increasing the θ angle shows a blueshift in the resonant wavelength for modes 2 and 3. At 35°, the mode 1 transmittance dip is separated into two transmittance dips with smaller ER. When the value is increased to 45°, the two transmittance dips shift towards each other and merge to form a single transmittance dip with a larger ER. However, raising the θ angle up to 65° indicates that the two transmittance dips shift away from each other and the ER of both transmittance dips is smaller than the ER of the singular transmittance dip at 45°. 45° was chosen as the optimal value of θ for considering the effect of ER.

Table 4.13 displays the initial and final values for all geometric parameters after optimization. sensitivity values for modes 1, 2, and 3 are 1353.98 nm/RIU, 1657.8 nm/RIU, and 2975.96 nm/RIU, respectively. The final FOM values for modes 1, 2, and 3 are 35.72, 43.95, and 26.32, respectively. The addition of nanodots raised sensitivity by 18.68%, 18.18%, and 35.1%, and FOM by 24.29%, 43.63%, and 15.79% for modes 1, 2, and 3. Table 4.14 shows that the suggested sensor surpasses several of the recently proposed sensors in terms of having a high sensitivity with an acceptable FOM.

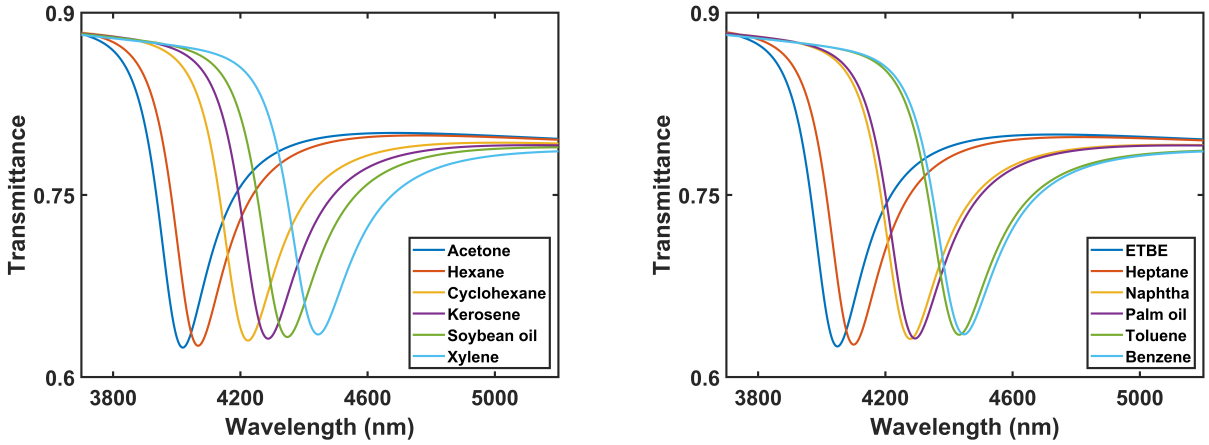

Figure 4.39: Transmittance curve for different chemical pollutants.

Table 4.15: Refractive index and resonant wavelength of different chemical pollutants.

Chemical pollutant	Refractive index	Resonant wavelength (nm)
Acetone	1.359	4018.91
ETBE	1.369	4048.95
Hexane	1.375	4067.38
Heptane	1.386	4100.31
Cyclohexane	1.427	4224.13
Naphtha	1.445	4278.16
Kerosene	1.448	4287.21
Palm oil	1.45	4293.43
Soybean oil	1.468	4347.79
Toluene	1.496	4432.45
Xylene	1.5	4444.23
Benzene	1.501	4447.31

4.4.4 Applications

4.4.4.1 Detection of chemical pollutants in seawater

During the operation of refining and chemical factories, various hazardous compounds fall into the water, which quickly travels to the sea and disperses, causing economic and environmental difficulties. Table 4.15 lists some of these contaminants and their refractive index values, most of which are insoluble or only partially soluble in water [305]. Because different chemical pollutants have distinct refractive index values, they will have different resonant wavelengths, and this feature can be utilized to quickly identify chemical pollutants that are scattered in seawater. The transmittance curves for all of the chemical pollutants are displayed in Fig. 4.52(a),(b) and the resonant wavelengths for each are listed in Table 4.15.

Table 4.16: Refractive index and resonant wavelength of different concentrations of heavy metal ion solutions.

Heavy metal ion		Concentration (ppm)		
		500	**700**	**1000**
Zn^{2+}	Refractive index	1.3351	1.3365	1.3380
	Resonant wavelength (nm)	3946.8	3951.12	3955.64
Pb^{2+}	Refractive index	1.3356	1.3370	1.3388
	Resonant wavelength (nm)	3948.37	3952.69	3958
Hg^{2+}	Refractive index	1.3359	1.3374	1.3392
	Resonant wavelength (nm)	3949.35	3953.87	3959.18

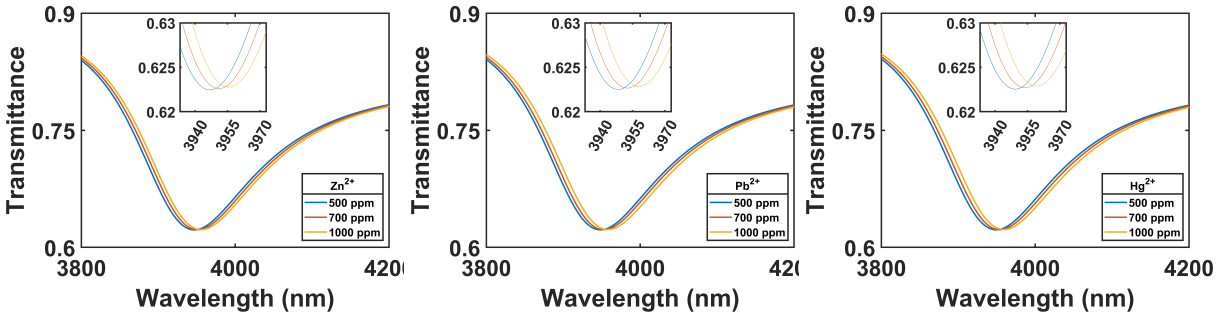

(a) (b) (c)

Figure 4.40: Transmittance curve for different concentrations of heavy metal ion solutions (a) Zn^{2+} (b) Pb^{2+} (c) Hg^{2+}.

4.4.4.2 Detection of various concentrations of heavy metal ion solutions

Zinc (Zn) is a heavy metal that helps to maintain a healthy metabolism, immune system, and regular human growth. On the other hand, lead (Pb) and mercury (Hg) are two toxic heavy metals that have exclusively negative effects on the human body. A modest amount of heavy metal ions in the body may have no effect, but there is a limit to the number of heavy metal ions someone may digest since, at higher concentrations, they can induce poisoning in the human body, including zinc [306]. Zinc overdose can induce gastrointestinal irritation, fever, chest pain, exhaustion, muscle stiffness, and other health problems. Mercury causes autonomic dysfunction and aberrant cell division, whereas lead causes organ damage, immune system suppression, and may even result in death. To avoid these hazards to the human body, identification of these heavy metal ions at high concentrations in water is required. The refractive index values of heavy metal ion solutions of Zn^{2+}, Pb^{2+}, and Hg^{2+} at concentrations of 500 ppm, 700 ppm, and 1000 ppm are shown in Table 4.16. As the refractive index value increases with the concentration of heavy metal ion solutions, the concentration can be readily estimated by altering the resonant wavelength. Table 4.16 shows the resonant wavelengths for different concentrations of heavy metal ion solutions. Fig. 4.40(a),(b),(c) depict the transmittance curves for various concentrations of Zn^{2+}, Pb^{2+}, and Hg^{2+} solutions.

4.4.4.3 Concentration of Sugar Water

Refractive index sensors can be utilized to measure the concentration of sugar water. The refractive index of a liquid is related to its composition and concentration. As the concentration of dissolved substances, such as sugar, changes in the water, the refractive index also varies. By calibrating the refractive index sensor with known concentrations of sugar water, a correlation can be established between the refractive index and the sugar concentration. This correlation allows for the measurement of sugar concentration in unknown samples based on their refractive index values. The following equation gives us a relation between the refractive index and different concentration of sugar water [307].

$$n = \frac{C + 726.48}{547.21} \tag{4.14}$$

Figure 4.41 shows the transmittance curve and table 4.17 shows the corresponding resonant wavelength for different concentration of sugar water.

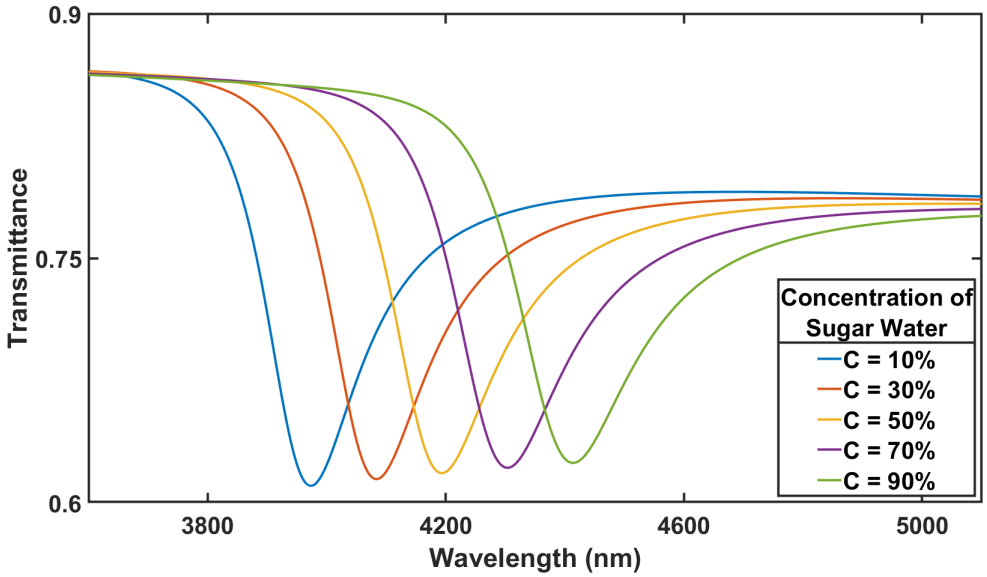

Figure 4.41: Transmittance characteristics for different sugar water concentration percentages.

Table 4.17: Resonant wavelength for different concentration of sugar water.

Sugar Water Concentration	Resonant wavelength (nm)
10%	3973.24
30%	4084.34
50%	4194.45
70%	4305.84
90%	4412.62

4.4.4.4 Concentration of NaCl Solution

Refractive index sensors can also be employed to measure the concentration of NaCl (salt) solutions. Similar to sugar water, the refractive index of a NaCl solution changes with variations in its concentration. To determine the concentration of NaCl using a refractive index sensor, a calibration curve is typically established by measuring the refractive index of NaCl solutions with known concentrations. This curve allows for the correlation between refractive index and NaCl concentration to be determined. The following equation gives us a relation between the refractive index and different concentration of NaCl solution [307].

$$n = \frac{C + 709.21}{532.13} \tag{4.15}$$

Figure 4.42 shows the transmittance curve and table 4.18 shows the corresponding resonant wavelength for different concentration of NaCl solution.

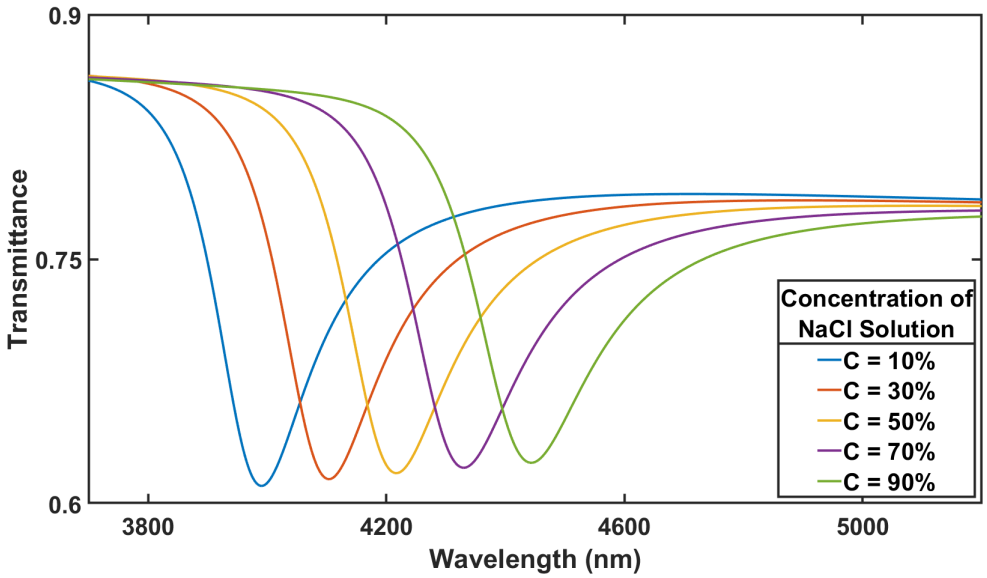

Figure 4.42: Transmittance characteristics for different NaCl solution concentration percentages.

Table 4.18: Resonant wavelength for different concentration of NaCl solution.

Concentration of NaCl Solution	Resonant wavelength (nm)
10%	3991.66
30%	4103.47
50%	4219.34
70%	4328.38
90%	4443.69

4.4.4.5 Concentration of Alcohol

Refractive index sensors can be utilized to measure the concentration of alcohol in a liquid solution. The refractive index of a substance, including alcohol, is known to vary with changes in concentration. To measure the concentration of alcohol using a refractive index sensor, a calibration process is typically conducted. This involves measuring the refractive index of alcohol solutions with known concentrations and establishing a correlation between the refractive index and alcohol concentration. Once the calibration curve is established, the refractive index of an unknown alcohol solution can be measured using the sensor. By comparing the measured refractive index to the calibration curve, the corresponding alcohol concentration can be determined. The following equation gives us a relation between the refractive index and different concentration of alchohol from 0% to 40% at $30°C$ [308].

$$n = 1.333 + C \times 0.000566 \tag{4.16}$$

Figure 4.43 shows the transmittance curve and table 4.19 shows the corresponding resonant wavelength for different concentration of alchohol.

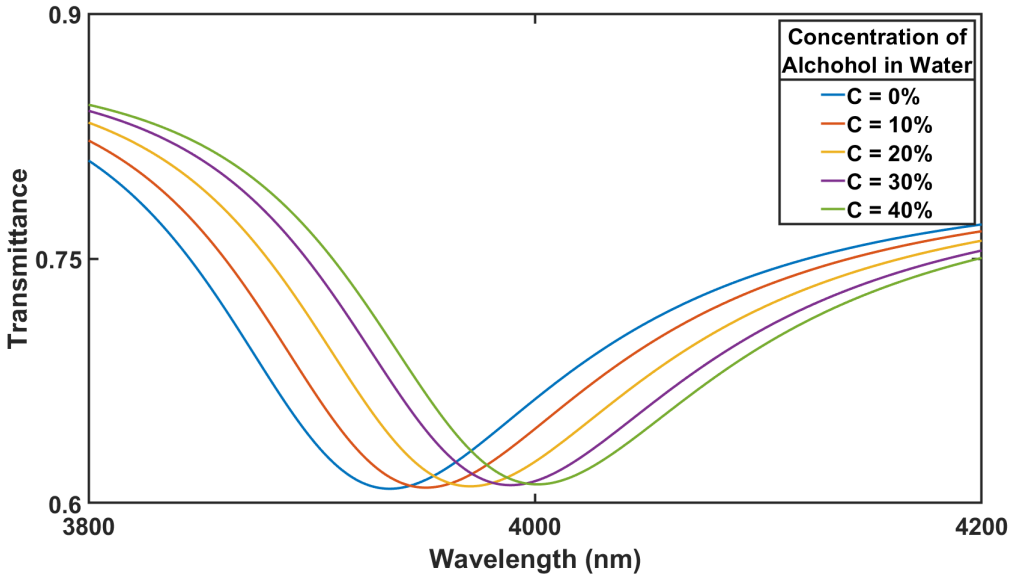

Figure 4.43: Transmittance characteristics for alchohol concentration percentages.

Table 4.19: Resonant wavelength for different concentration of alchohol.

Concentration of Alchohol	Resonant wavelength (nm)
0%	3934.83
10%	3952.34
20%	3972.65
30%	3988.45
40%	4001.87

4.4.4.6 Concentration of Water in Heavy Oil

Refractive index sensors can be employed to measure the water concentration in heavy oil samples. Water content is a crucial parameter to monitor in heavy oil, as it affects its quality and can impact various processes and applications. To measure water concentration using a refractive index sensor, a calibration process is typically performed. This involves preparing heavy oil samples with known water concentrations and measuring their corresponding refractive indices. A correlation between refractive index and water concentration can then be established. The following equation gives us a relation between the refractive index and different concentration of water in heavy oil [309].

$$n = 1.518 - C \times 0.0019 \tag{4.17}$$

Figure 4.44 shows the transmittance curve and table 4.20 shows the corresponding resonant wavelength for different concentration of water in heavy oil.

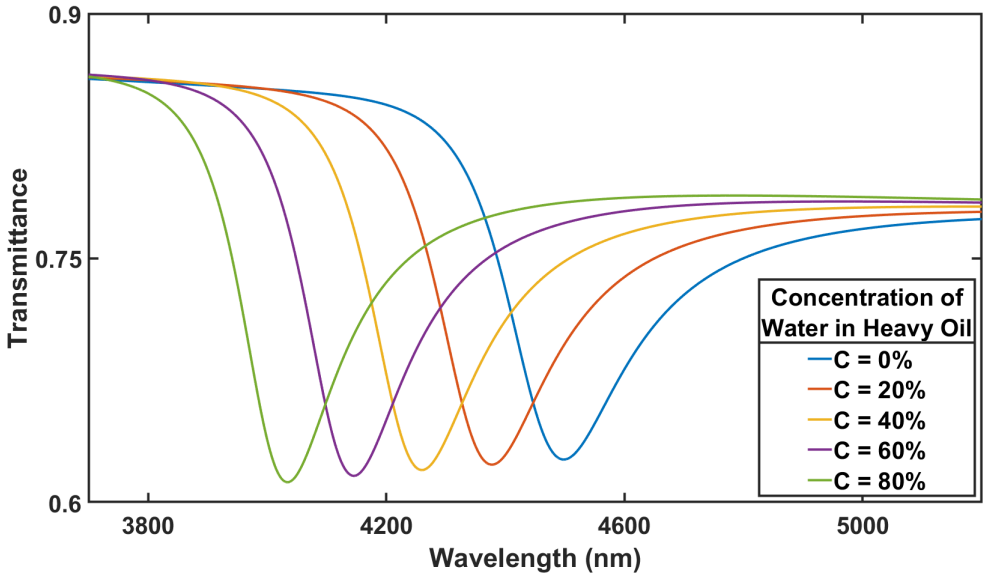

Figure 4.44: Transmittance characteristics for different water concentration percentages in heavy oil.

Table 4.20: Resonant wavelength for different concentration of water in heavy oil.

concentration of Water in Heavy Oil	Resonant wavelength (nm)
0%	4033.34
20%	4146.45
40%	4262.84
60%	4376.67
80%	4497.23

4.4.4.7 Different Alcohol Detection

Refractive index sensors can be utilized to distinguish and detect different alcohols, including methanol, ethanol, propanol, butanol, pentanol, and phenol. The refractive index of a substance is influenced by its molecular composition and can exhibit distinct values for different alcohols. To detect and differentiate these alcohols using a refractive index sensor, a calibration process is typically carried out. This involves measuring the refractive indices of standard solutions or pure samples of each alcohol of interest. The refractive index of an unknown sample can be measured using the sensor, and by comparing it to the calibration curve or reference table, the corresponding alcohol can be identified [310].

Table 4.21: Refractive index and resonant wavelength of different types of alchohol.

Different Alcohol	Refractive index	Resonant wavelength (nm)
Methanol	1.33	3926.23
Ethanol	1.36	4017.86
Propanol	1.38	4077.34
Butanol	1.4	4135.75
Pentanol	1.41	4167.24
Phenol	1.53	4530.46

Figure 4.45 shows the transmittance curve and table 4.21 shows the corresponding resonant wavelength and refractive index values for different types of alchohol.

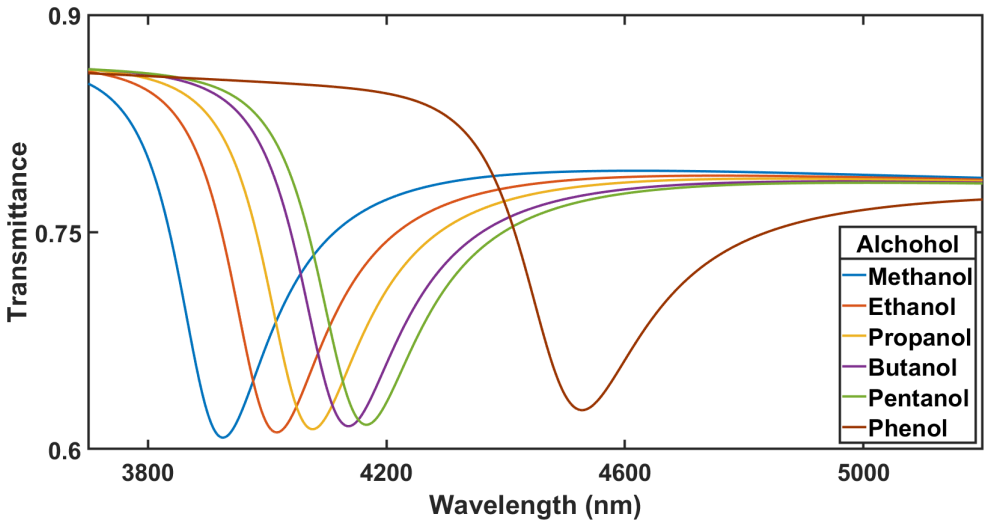

Figure 4.45: Transmittance characteristic for different alchohol.

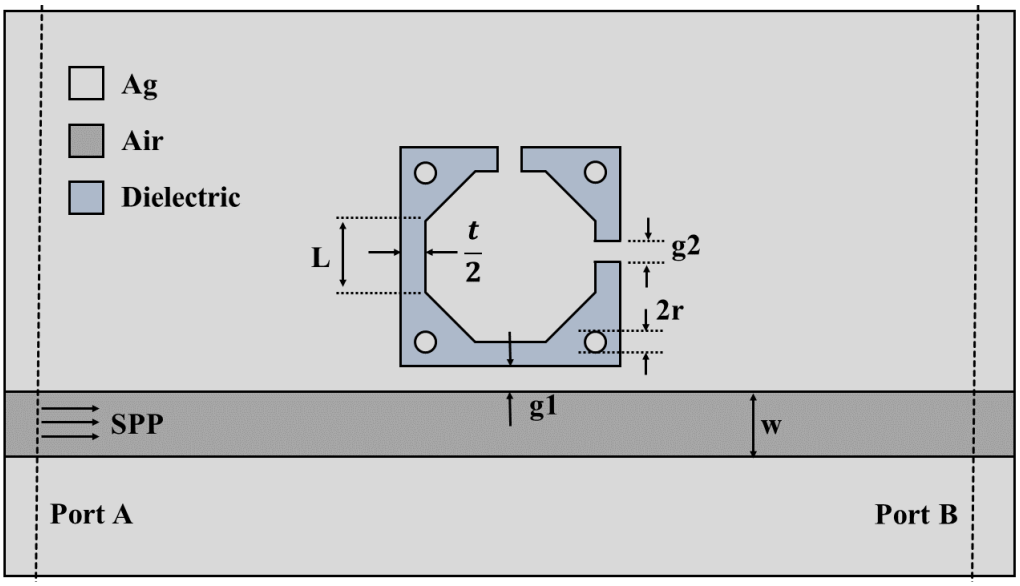

Figure 4.46: Structure of The Proposed Design.

4.5 Sensor Design with Modified Octagonal-shape Resonator with Nanorods

4.5.1 Sensor Geometry and Theoretical Analysis

The proposed geometric structure of the sensor consists of a straight MIM waveguide coupled with an octagonal cavity resonator inside a square disk along with silver nanodots and two slits as illustrated in figure 4.46. The proposed design is illustrated in a 2-D top view. The design parameters are shown in table 4.22. COMSOL Multiphysics 5.6 has been used

Table 4.22: Initial parameter values of the 2-D geometric structure

Symbol	Parameter	Value (nm)
L	Length of the arm of octagon	95
w	Width of the waveguide	90
t	Distance between outer square and inner octagon	50
g_1	Gap between waveguide and resonator	10
g_2	Width of the slit	40
r	Radius of the nanorods	10

to assess the 2D design of the proposed sensor. 2D simulation of the design is performed in order to save computational time and memory usage. EM wave frequency domain (ewfd) and boundary mode analysis have been chosen for study. The FEM algorithm has been employed in order to analyze the sensor. Extra fine triangular meshing has been used to obtain precise results [181]. The boundaries are set as scattering boundaries in order to ensure minimal reflection [311].

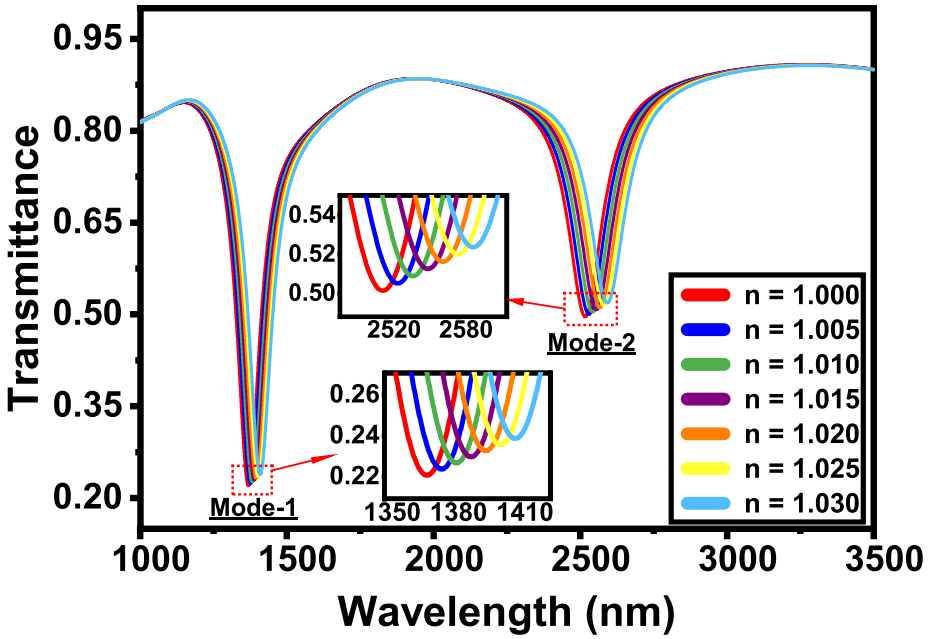

Figure 4.47: Transmittance characteristics of the optimized design for different values of the refractive index of the dielectric material.

SPPs are transverse magnetic (TM) waves [312] and TM_0 mode of MIM waveguide can be described as [98],

$$tanh(kw) = \frac{-2kp\alpha_c}{k^2 + p^2 + \alpha_c^2} \tag{4.18}$$

where, the width of the MIM waveguide is expressed by w, $k = \frac{2\pi}{\lambda}$ is the wave vector, $p = \frac{\epsilon_i}{\epsilon_m}$ where ϵ_i and ϵ_m are the dielectric constants and $\alpha_c = \sqrt{[k_0^2(\epsilon_i - \epsilon_m) + k^2]}$.

4.5.2 Sensor Design Optimization

The sensing performance parameters i.e. Transmittance, Sensitivity, and FOM vary depending on the structure of the resonator. These parameters are sensitive to the change of any geometric parameter. In order to achieve optimal transmittance and sensitivity, the geometric parameters are tuned and evaluated in an iterative approach. The transmittance characteristic of the optimized structure is shown in figure 4.47. In the following discussion, considering from the left the two observed dips in the transmittance characteristics curve are considered mode 1 and mode 2 respectively. The optimization is carried out when the refractive index of the sensing medium is chosen as n = 1. For the discussion, the resonant wavelength is denoted as λ_{res}.

The first parameter considered for tuning is the length of the arm of the octagon (L). The initial dimension was 95 nm. For the initial dimension, the sensitivity for mode 1 and mode 2 are 1016.463 nm/RIU and 1709.63 nm/RIU, and FOM values are 13.17 and 10.24 respectively. The value of the parameter L was varied from 93 nm to 107 nm and eight equally

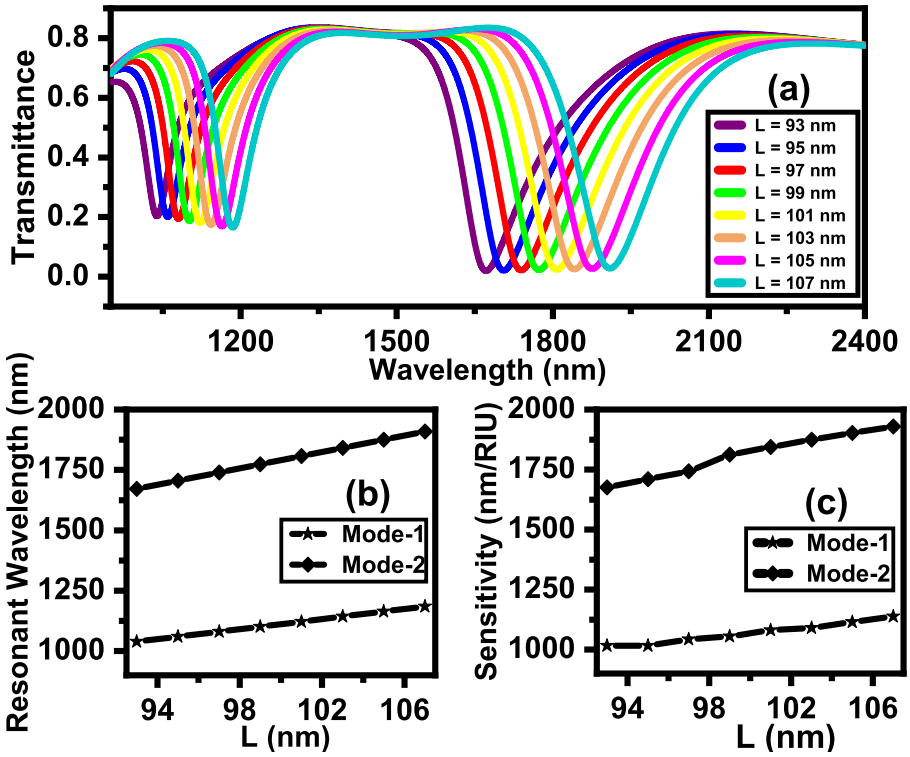

Figure 4.48: (a) Transmittance characteristics (b) Resonant wavelength and (c) Sensitivity for different values of length of the arm of octagon L.

distant values were taken in between the limits. The effect of changing the value of L on the sensing parameters is presented in figure 4.48.

The transmittance of the first dip increases while that of the second dip remains unchanged as the value of L increases. But the sensitivity and λ_{res} of both modes increase almost linearly as the value of the L increases. Upon observing the change in performance parameters when the length of the octagon is 103 nm the corresponding sensitivity for mode 1 and mode 2 are 1085.49 nm/RIU, 1889.273 nm/RIU, and FOM values are 17.41 and 12.72 respectively which is the best case considering highest sensitivity and highest FOM. Moreover, increasing the value of L furthermore does not change sensitivity and FOM much. Hence, 103 nm is chosen as the optimal value for the length of one arm of the octagon. After the iterative optimization, the maximum sensitivity and FOM have been improved by 0.25% and 19.49% respectively.

The distance between the square and inner octagon cavity (t) has significant effects on the transmittance characteristics, λ_{res}, and sensitivity which is illustrated in figure 4.49. Initially, the value of t was considered as 36 nm, while the value of L is 103 nm and the other parameters are the same as table 4.22. In this case, the resulting sensitivity and FOM for mode 2 were 1886.82 nm/RIU and 12.47 respectively. With a step size of 8 nm, the parameter was changed ranging from 20 nm to 76 nm. While the value of t is increased, for both modes the λ_{res} and the sensitivity undergoes a significant reduction while transmittance dip increases.

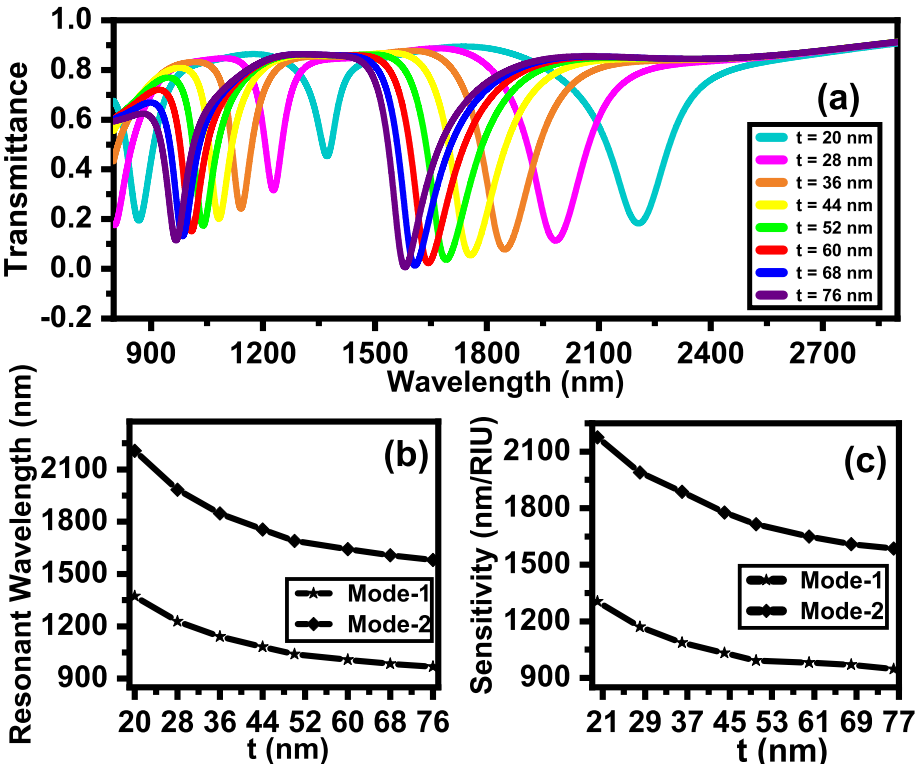

Figure 4.49: (a) Transmittance characteristics (b) Resonant wavelength λ_{res} and (c) Sensitivity for different values of distance between the square and inner octagon cavity t.

In order to get obtain an optimum sensitivity with suitable transmittance, the value of t is finalized as 50 nm where the sensitivity for mode 1 and mode 2 was recorded as 991.33 nm/RIU and 1713.95 nm/RIU respectively and the FOM values were 13.91 and 12.74. After optimization, although the sensitivity in mode 2 deteriorated by 10% and FOM improved by 2.1%.

After the optimization of previous parameters, silver nanodots were introduced in the design as it is known for improving the sensitivity [95]. The possible reason is, SPPs are constrained by nanorods, which improves their interaction with analyte molecules [164]. As a result, the evanescent field is strengthened and the interaction between light and matter is improved, eventually improving the sensor's sensitivity. Initially, four silver nanodots having a size 12 nm radius (r) were placed near the corners of the square. The change of the values of the parameters with respect to the radius of the nanodots is presented in figure 4.50. An increase in radius resulted in an increase in sensitivity and λ_{res} in mode 2 while the transmittance dip decreases. However, in mode 1 the resonant wavelength and sensitivity were not much affected. The value of r was set as 10 nm for optimal transmittance and sensitivity. It resulted in sensitivity values of 1013.64 nm/RIU and 1744.26 nm/RIU which is an increase of 2.25% and 1.76% for mode 1 and mode 2 respectively.

Two slits are placed on the top and right side of the resonator with a view to detecting changes in performance parameters. The introduction of slits with 17.5 nm width resulted in a rapid

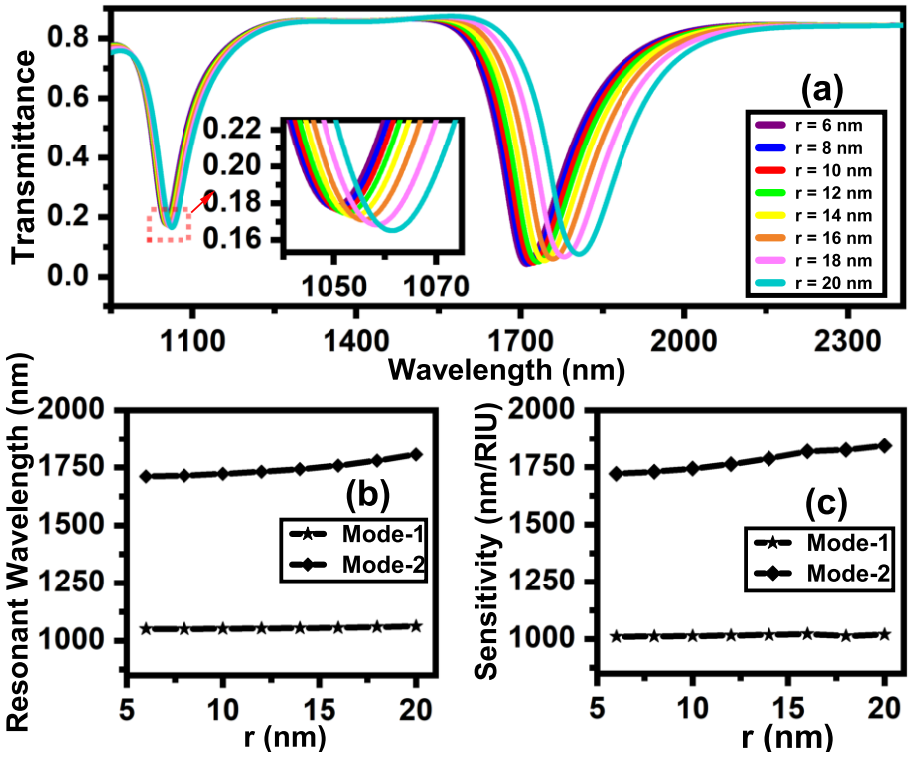

Figure 4.50: (a) Transmittance characteristics (b) Resonant wavelength λ_{res} and (c) Sensitivity for different values of radius of nanodots r.

increase of both λ_{res} and sensitivity. For both modes, the recorded sensitivity after adding slits are 1346.21 and 2595.57. The value of the width g2 was varied for further investigation ranging from 10 nm to 62.5 nm with a step size of 7.5 nm. The effect of changing g2 on transmittance characteristics, λ_{res}, and sensitivity are illustrated in figure 4.51. An increase of g_2 resulted in a decrease in λ_{res} and sensitivity while the transmittance improved. For optimal transmittance and sensitivity, the value of 40 nm was chosen to be the optimal value of the width of the slits. For mode 1 and mode 2, the recorded sensitivity values are 1344.11 nm/RIU and 2527.6 nm/RIU respectively which indicates the sensitivity values improved by 32.6% and 44.9% respectively.

Based on the observations of varying different parameters, the studies yielded the values of geometric parameters for which the best and optimal results are obtained. The optimized and finalized values for different parameters are shown in table 4.23.

The transmittance characteristics curves for different configurations of slit positions (Up-Left, Up-Right, Down-Left, Down-Right) are illustrated in figure 4.52(a) for mode 1 and 4.52(b) for mode 2 respectively. The Down-Left configuration exhibits sensitivity values of 1263.5 nm/RIU and 2548.5 nm/RIU for mode 1 and mode 2 respectively. The Down-Right configuration exhibits sensitivity values of 1265.3 nm/RIU and 2555.4 nm/RIU which are higher than the previous configuration. The Up-Left configuration exhibits sensitivity values of 1334.7 nm/RIU and 2506.6 nm/RIU. In this configuration, the sensitivity value

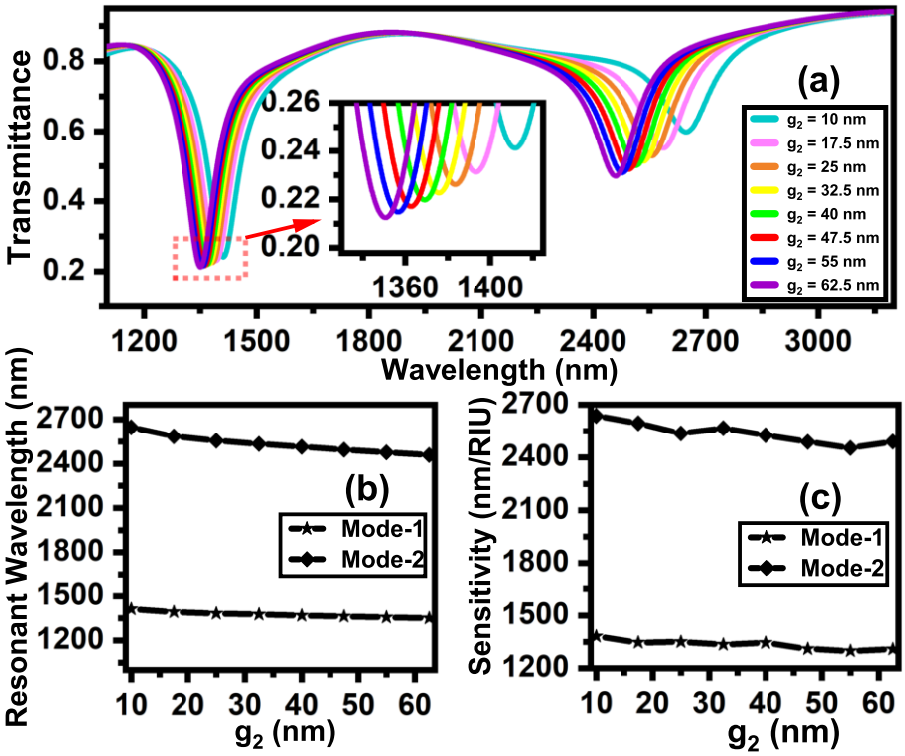

Figure 4.51: (a) Transmittance characteristics (b) Resonant wavelength λ_{res} and (c) Sensitivity for different values of width of the slits g_2.

of mode 1 is improved by 5.48% but the sensitivity value of mode 2 is reduced by 1.9% compared to the Down-Right configuration. Lastly, the Up-Right configuration exhibits sensitivity values of 1344.11 nm/RIU and 2527.6 nm/RIU respectively which is higher than the previous configuration in terms of sensitivity value. The magnetic field distributions for different configurations of slit positions are illustrated in figure 4.52(c-f). Therefore, the Up-Right configuration is considered the optimal configuration for maximum sensitivity for both modes.

4.5.3 Result Analysis

After the optimization of geometric parameters, the sensitivity values of mode 1 and mode 2 are 1344.11 nm/RIU and 2527.6 nm/RIU respectively. The recorded FOM values are 13.13 and 16.24 respectively. The sensing resolution of mode 2 is 3.956×10^{-7} RIU which implies that the sensor is capable of detecting minuscule changes in the refractive index of an unknown material.

The proposed sensor design manifests higher sensitivity than many previously reported designs based on MIM waveguide. A comparative study is shown in table 4.24.

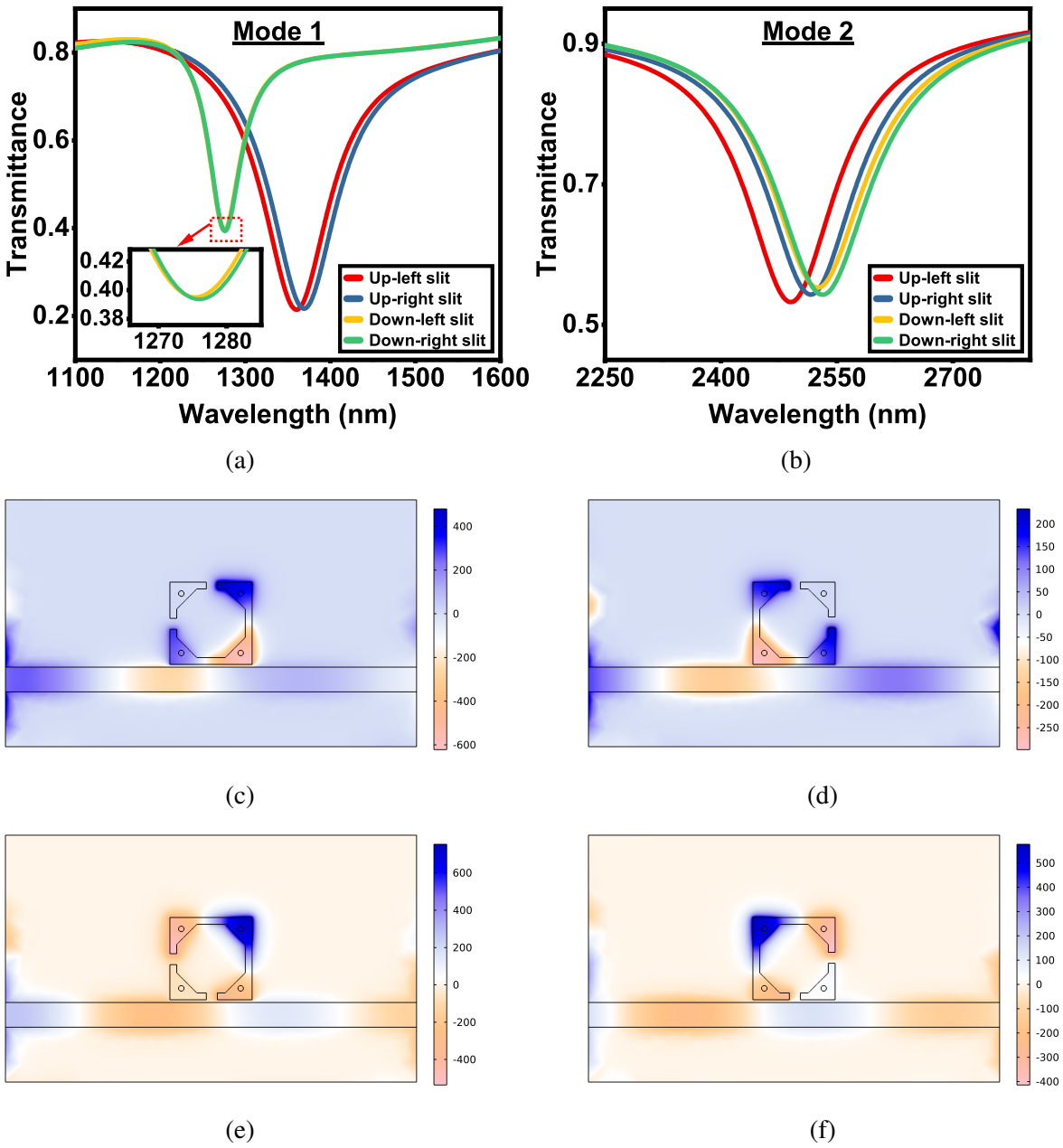

Figure 4.52: a. Transmittance characteristics of mode 1 for different slit configurations. b. Transmittance characteristics of mode 2 for different slit configurations. c. Magnetic Field Distribution (A/m) for Up and Left slit configuration. d. Magnetic Field Distribution (A/m) for Up and Right slit configuration. e. Magnetic Field Distribution (A/m) for Down and Left slit configuration. f. Magnetic Field Distribution (A/m) for Down and Right slit configuration.

Table 4.23: Optimal parameter values of the 2-D geometric structure

Symbol	Parameter	Initial Value (nm)	Optimal Value (nm)
L	Length of the arm of octagon	95	103
w	Width of the waveguide	90	90
t	Distance between outer square and inner octagon	36	50
g_1	Gap between waveguide and resonator	10	10
g_2	Width of the slit	17.5	40
r	Radius of the nanodots	12.5	10

Table 4.24: Comparison of the sensitivity with previously published MIM structured refractive index sensor designs

References	Year	Sensitivity (nm/RIU)
S Yan et al. [104]	2017	1071.4
Z Zhang et al. [103]	2018	1060
Butt et al. [169]	2019	1367
Z Li et al. [172]	2019	1405
Y Fang et al. [313]	2020	1940
R Al Mahmud et al. [314]	2021	2325
B Li et al. [226]	2022	1229
S Rohimah et al. [224]	2022	1333
This design	2023	2527.6

4.5.4 Application Scopes of the Proposed Sensor

The sensor has two dips in the transmittance characteristics graph shown in figure 4.47 labeled as mode 1 and mode 2. However, for sensing applications, higher-order modes offer some advantages over fundamental resonant mode because it can excite stronger SPR and they exhibit comparatively higher sensitivity due to their larger evanescent field.

4.5.4.1 Detection of Water in Honey

Honey is one of nature's most complex carbohydrate compounds. It is a sweet and viscous liquid that is produced by honeybees from flower nectar. Unfortunately, for economic gain honey is adulterated in many countries by sellers or distributors. Consumption of such honey may result in health concerns and a lack of nutrition. Water is one of the most commonly used adulterants found in honey. It alters the dielectric properties of honey [315]. Water is also a quality criterion that indicates resistance to yeast fermentation [316]. The percentage of water can be calculated from the measured refractive index using the following equation [317],

$$\%W = 608.277 - 395.743 \times n \tag{4.19}$$

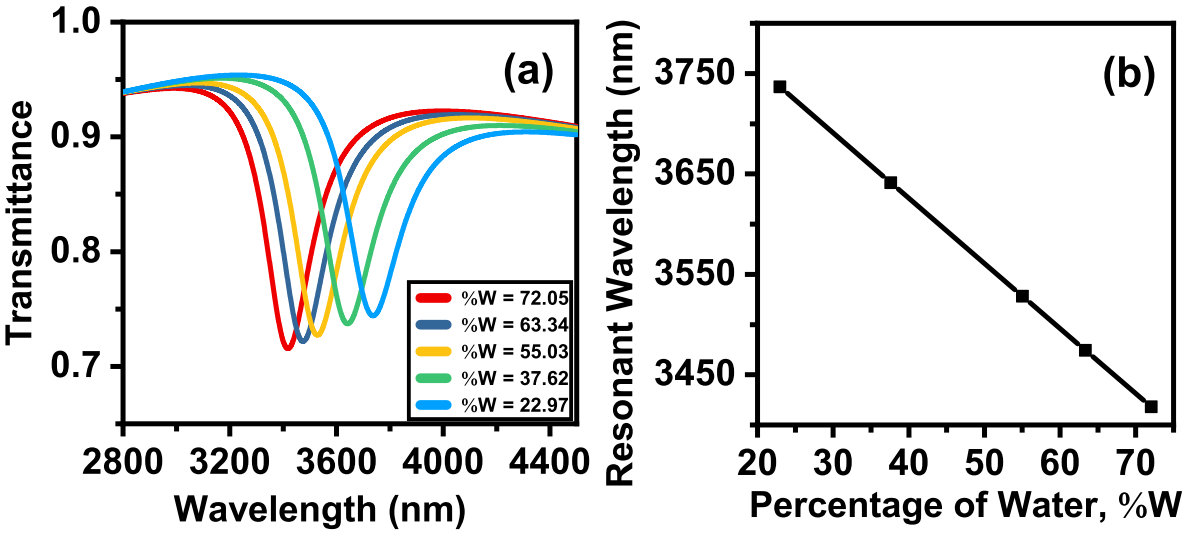

Figure 4.53: (a) Transmittance characteristics for different percentages of water, (b) Relationship between resonant wavelength and different percentages of water.

Here, n is the refractive index of the honey sample and $\%W$ is the percentage of water present in the honey sample.

The refractive index for different percentages of water in honey samples is shown in table 4.25. This can be used to measure the water percentage of honey sample. The transmittance

Table 4.25: Measurement of Water Percentage in Honey Sample

Percentage of Water (%W)	**Refractive Index** [317]	**Resonant Wavelength, λ_{res} (nm)**
72.05	1.355	3418.2
63.34	1.377	3474.5
55.03	1.398	3528.4
37.62	1.442	3641.4
22.97	1.479	3736.8

characteristics with respect to the percentage of water are shown in figure 4.53(a) and the relation between λ_{res} and the percentage of water is shown in figure 4.53(b) which follows a linear relationship that can be detected by a modern spectral analyzer [259]. Thus, the proposed sensor has the potential to measure water concentration in honey samples.

4.5.4.2 Measurement of Lactose Concentration in Solution

Lactose is a molecule consisting of glucose and galactose monosaccharides. It is mostly found in milk and other milk-based products [318]. Lactose consumption facilitates mineral absorption [319] and supports immune functions [320]. But up to 70% of the world's population have lactose intolerance [321]. Undigested lactose present in the large intestine undergoes fermentation and forms hydrogen and methane which leads to diarrhea, flatulence, and abdominal pain [322]. The refractive index of lactose solution at room temperature can

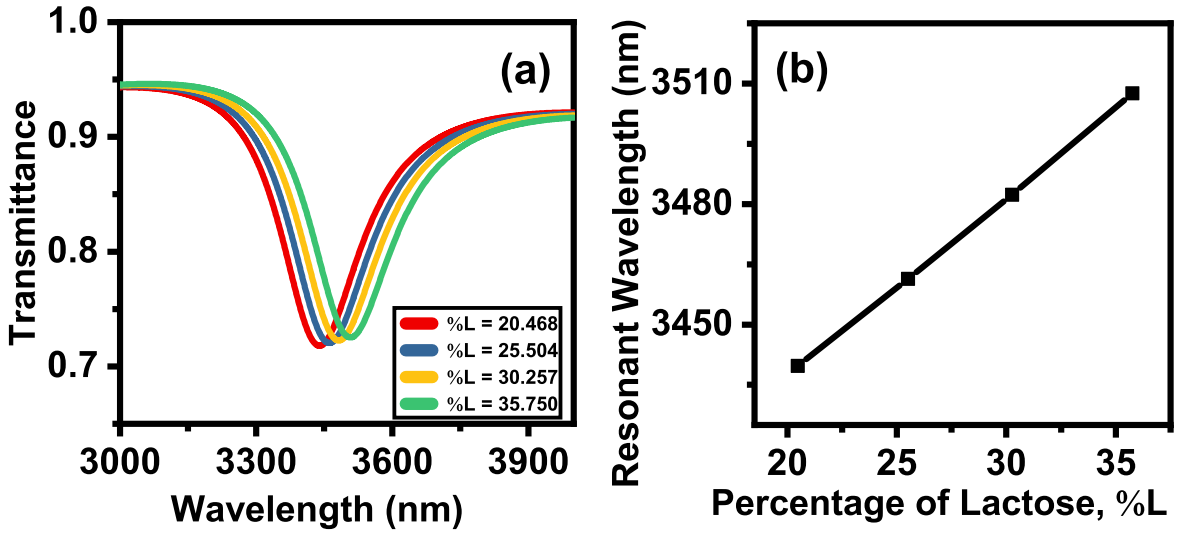

Figure 4.54: (a) Transmittance characteristics for different percentages of Lactose, (b) Relationship between resonant wavelength and different percentages of water.

be calculated from the equation as follows, [323],

$$n = 1.3325 + 0.001384 \times \%L + 0.00000624 \times \%L^2 \tag{4.20}$$

Here, n is the refractive index of the lactose solution and $\%L$ is the percentage of lactose present in the solution. Since the second-order coefficient is significantly small, the relationship between the refractive index and the lactose concentration is almost linear.

The refractive index for different concentrations of lactose is shown in table 4.26. This can be used to measure the lactose concentration present in a solution. Figure 4.54(a) represents

Table 4.26: Measurement of Lactose Concentration in Lactose Solution

Percentage of Lactose (%L)	**Refractive Index** [323]	**Resonant Wavelength,** λ_{res} **(nm)**
20.468	1.3634	3439.7
25.504	1.3719	3461.4
30.257	1.3800	3482.3
35.750	1.3900	3507.6

the transmittance characteristics of lactose solution consisting of different concentrations of lactose and figure 4.54(b) represents the relationship between lactose percentage and λ_{res}. By using the relationship of figure 4.54(a), lactose percentage can be measured by detecting the shift of λ_{res} using a spectral analyzer.

4.5.4.3 Measurement of Fat Percent in Milk

Fat in milk refers to the natural lipid content found in this dairy product. It plays a significant role in providing flavor, texture, and satiety. Whole milk contains a higher fat percentage,

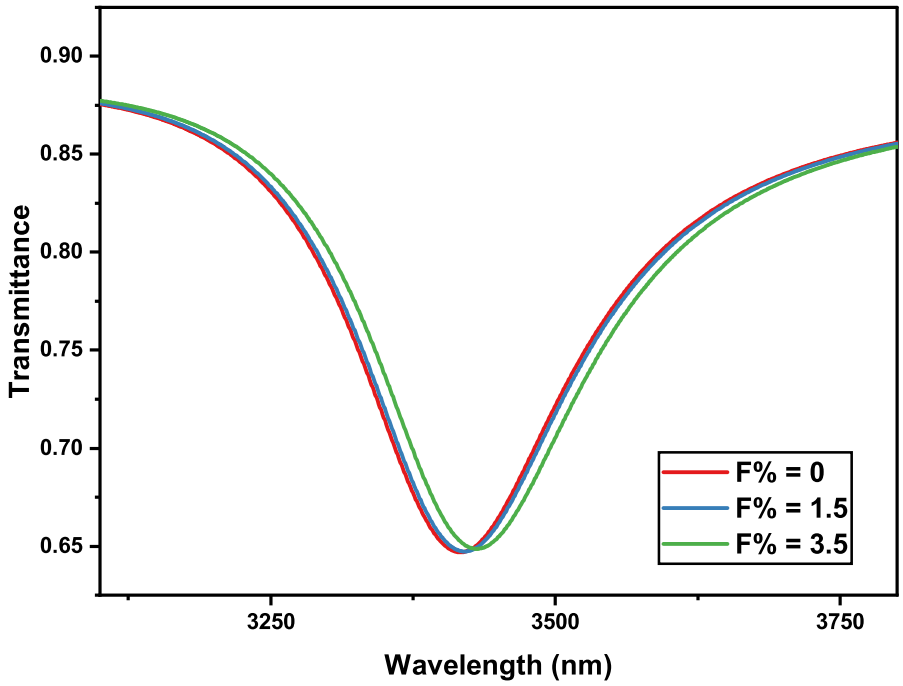

Figure 4.55: Transmittance characteristics for different percentages of fat in milk.

contributing to its creaminess and richness. However, low-fat and skim milk options are also available for those seeking reduced fat content while still benefiting from essential nutrients like calcium and vitamin D. The percentage of fat in milk can be measured by the proposed sensor. The refractive index of milk changes with the change in fat percentage in milk. Fig. 4.55 shows the transmittance characteristics of the sensor in the presence of fat of different percentages where the percentage of fat is represented as F%. The transmittance characteristics change when the percentage of fat. Table 4.27 shows the resonant wavelength corresponding to the percentage. By detecting the resonant wavelength, it is possible to measure the percentage of fat.

Table 4.27: Measurement of Fat Percentage in Milk.

Percentage of Fat (F%)	**Refractive Index** [324]	**Resonant Wavelength,** λ_{res} **(nm)**
0	1.3469	3416.41
1.5	1.3483	3419.87
3.5	1,3525	3431.00

4.5.4.4 Measurement of Sucrose Percentage in Solution

Sucrose in solution refers to the presence of the disaccharide sucrose dissolved in a liquid. Sucrose, commonly known as table sugar, is composed of glucose and fructose molecules. When dissolved in a solvent such as water, sucrose forms a sweet-tasting solution. This solution can be used in various culinary applications, as well as in laboratory settings for

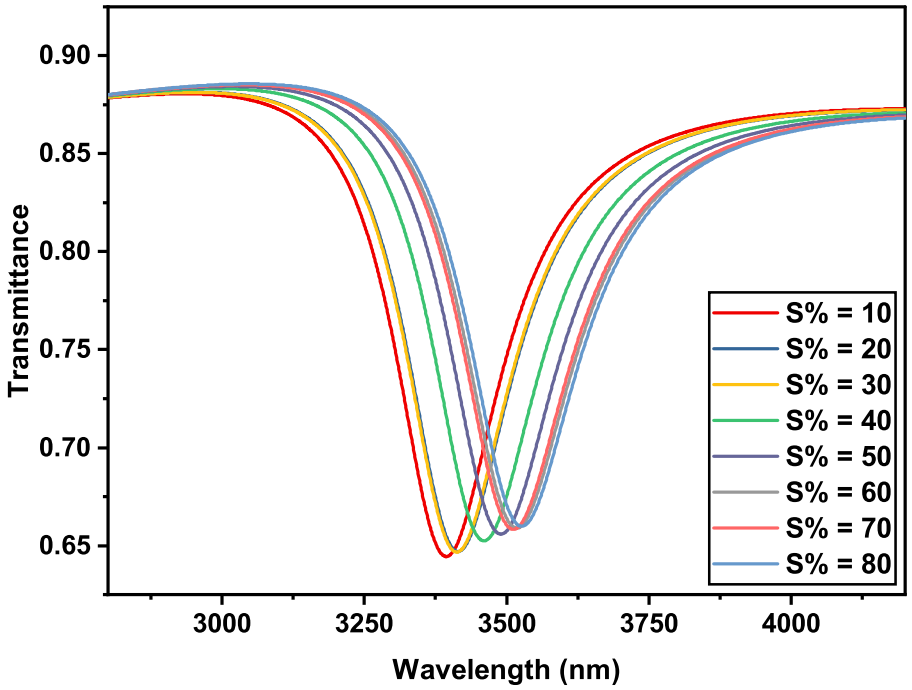

Figure 4.56: Transmittance characteristics for different percentages of sucrose.

experiments or as a reference for calibrating instruments that measure sugar concentration. The percentage of sucrose has effects on the refractive index of the solution. So the transmittance characteristics also change with respect to changes in sucrose percentage which is shown in Fig 4.56. The corresponding resonant wavelength for each sucrose percentage is shown in table 4.28 which can be detected by the spectral analyzer to measure the percentage of sucrose.

Table 4.28: Measurement of Sucrose Percentage in Solution.

Percentage of Sucrose (S%)	**Refractive Index** [325]	**Resonant Wavelength,** λ_{res} **(nm)**
10	1.33826	3393.94
20	1.34624	3414.56
30	1.34537	3412.07
40	1.36399	3459.94
50	1.37565	3490.00
60	1.38638	3517.96
70	1.38407	3511.80
80	1.38973	3526.78

4.5.4.5 Measurement of Glucose Concentration in Solution

Glucose is a vital energy source for the human body and is commonly found in fruits, honey, and certain carbohydrates. When glucose is dissolved in a solvent such as water, it forms a clear and sweet-tasting solution. Glucose solutions are commonly used in medical settings

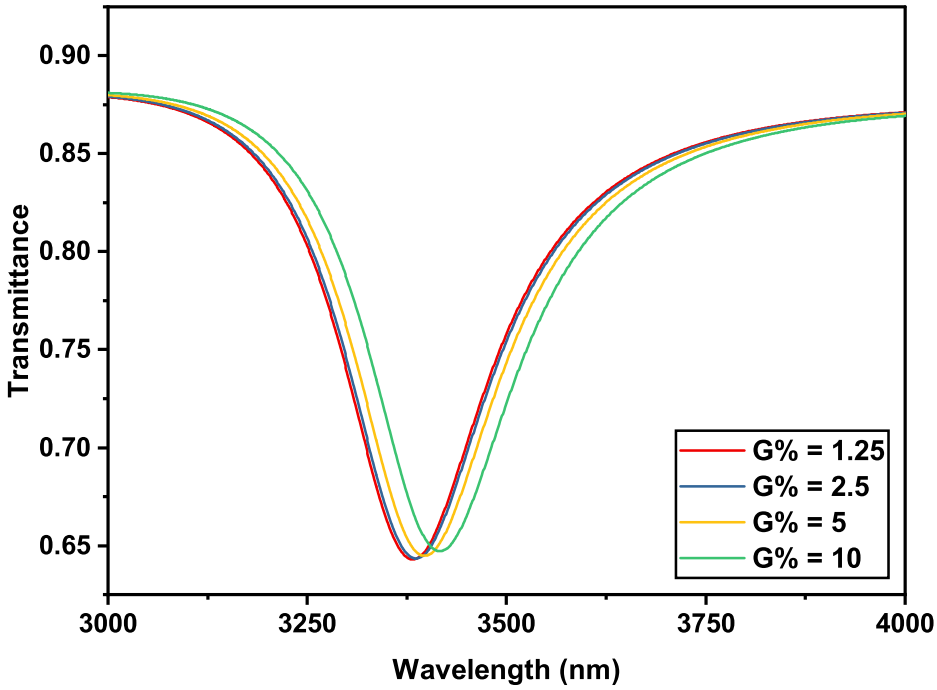

Figure 4.57: Transmittance characteristics for different percentages of Glucose.

for intravenous administration to provide a rapid source of energy in situations where oral intake is not possible or sufficient. In Fig. 4.57 the effect on transmission characteristics by the concentration of glucose is shown where G% is the concentration of glucose in percentage. The resonant wavelength corresponding to the percentage of glucose is shown in Table 4.29 and it can be detected by spectral analyzers.

Table 4.29: Measurement of Glucose Percentage in Solution.

Percentage of Sucrose (S%)	**Refractive Index** [326]	**Resonant Wavelength,** λ_{res} **(nm)**
1.25	1.333685	3382.51
2.50	1.335185	3386.59
5.00	1.339386	3397.23
10.0	1.346831	3416.21

Chapter 5

Conclusions

5.1 Thesis Summary

In this paper, numerical investigation of plasmonic refractive index nanosensors was carried out. The theoretical background of plasmonic devices is also elaborately discussed The effectiveness and performance of the nanosensors were examined and verified using electromagnetic wave equations and they were evaluated using 2-D FEM of COMSOL Multiphysics software. Three sensor designs are proposed in this paper and they were optimized and tuned for maximum performance. The potential application of the sensors in real-life scenarios was numerically investigated and it is verified that RI sensors are capable of measuring minuscule changes in refractive index to measure other physical quantities. Plasmonic nanosensors paved the path for new research and innovations. The sensors are low-cost, selective, and can be used for label-free rapid detection. These unique features of nanosensors give them an edge over traditional sensors.

5.2 Future Prospects of Our Work

This work presents the design and optimization of three distinct refractive index (RI) sensors for silver (Ag) using the Lorentz-Drude model. The goal of this study was to investigate the plasmonic properties of Ag-based refractive index sensors and verify their abilities and applications in different fields. For this purpose, we have numerically investigated the sensor properties and tuned the sensors rigorously and iteratively to achieve optimal performance. We have maximized the sensitivity and FOM of the proposed designs of the sensors. In the future, some steps can be taken to improve the performance of RI sensors and expand the research scopes of MIM waveguide-based plasmonic nanosensors:

- To fully understand and improve MIM-based plasmonic devices, it's important to do more than just simulations. We need to create and test these devices in real-life situations. While simulations can provide helpful insights, they can't capture all the com-

plexities and limitations of the fabrication process. It's crucial to thoroughly examine the practical challenges that arise during fabrication, such as errors in manufacturing, flaws in materials, and the influence of the substrate on device performance. By conducting real-world testing, researchers can gain a better understanding of how these devices behave and perform in practical scenarios. This hands-on approach allows them to validate simulation results and identify any unexpected issues that may arise during fabrication. Real-world testing provides concrete data and observations that can be used to optimize device design and fabrication techniques. It helps bridge the gap between theoretical predictions and actual device performance, ensuring that the devices are reliable, efficient, and meet the necessary requirements.

- Exploring different materials and investigating their optical properties can be a possible way of designing new MIM waveguide-based RI sensors. While traditional designs extensively incorporate silver and gold in the designs, they have certain drawbacks of being noble metals. They lack tunable optical properties and they have a comparatively lower melting point. On the other hand, transition metal nitrides (TMN) have emerged as a potential solution to these problems. Their optical properties resemble to that of metals in the visible and near-infrared spectrum. They are CMOS compatible, tunable, and have high-temperature stability. Investigation of such material-based refractive index sensors may pave the way for more advanced and practical RI sensor solutions.

- It is possible to achieve a transmission profile similar to the Fano resonance by adjusting the structural parameters of the MIM-based sensor. This profile has a specific asymmetric shape, which can have a substantial impact on the sensor's spectral properties and overall performance. Researchers can improve the sensor's sensitivity and figure of merit by carefully fine-tuning certain structural properties. Researchers can improve the sensor's ability to discriminate between different signal components or closely spaced spectral characteristics by generating a Fano-like transmission profile through parameter modification. This enhancement in spectrum properties helps to the sensor's overall accuracy and dependability, making it more suitable for demanding applications requiring accurate detection.

- The performance and efficiency of MIM waveguide-based sensors can be improved by fine-tuning them with the aid of machine learning. As of now, the optimization process requires an iterative approach which is unpredictable and time-consuming at the same time. The pattern of change in performance parameters is very difficult for humans to comprehend without rigorous investigation. In order to mitigate this problem, machine learning can be incorporated into the optimization and tuning process. The process of optimization using machine learning is shown in Figure 5.1. For example, the published and proposed sensor designs and their geometric dimensions along

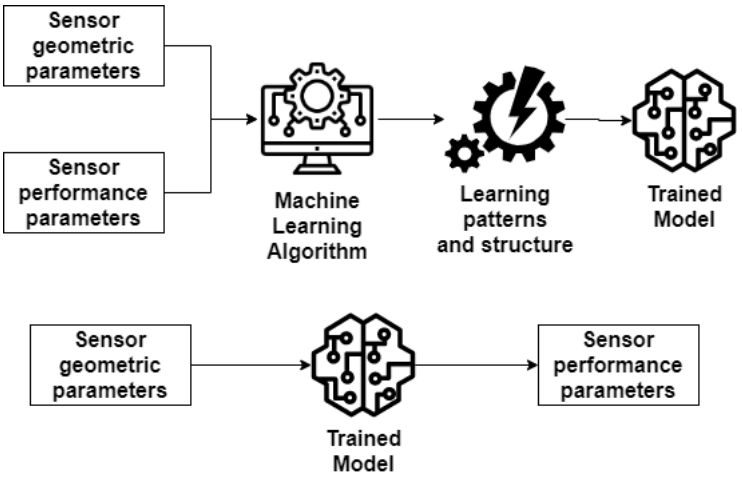

Figure 5.1: Optimization of RI sensor using machine learning.

with performance parameters can be fed into the machine learning model and a large dataset can be generated. A machine learning algorithm can be used to predict the performance parameters by assessing the geometric dimensions directly. For this purpose, unsupervised machine learning has to be used. It will allow the computer to predict performance without undergoing huge calculations. The machine learning model will learn the hidden patterns and intrinsic structure of the data of the sensor parameters. Afterwards, the machine learning model may be able to predict the performance of a newly proposed sensor upon taking the geometric parameters and structure as input.

- Additionally, investigating the potential of MIM-based plasmonic structures in various fields can provide valuable insights into their full capabilities. Fields such as biosensing, pressure sensing, and chemical sensing offer different challenges and requirements, allowing for a comprehensive evaluation of the sensors' functionality and efficiency. By testing the structures in different environments and with different stimuli, researchers can assess their response, sensitivity, selectivity, and overall performance in real-world applications. This holistic approach will enable a thorough understanding of the sensors' potential and limitations, as well as their suitability for specific sensing applications. It will also provide valuable data for comparison with existing sensing technologies, further establishing the competitiveness and advantages of the proposed plasmonic devices.

References

[1] S. A. Maier, M. L. Brongersma, P. G. Kik, S. Meltzer, A. A. Requicha, and H. A. Atwater, "Plasmonics—a route to nanoscale optical devices," *Advanced materials*, vol. 13, no. 19, pp. 1501–1505, 2001.

[2] A. Gabudean, D. Biro, and S. Astilean, "Localized surface plasmon resonance (lspr) and surface-enhanced raman scattering (sers) studies of 4-aminothiophenol adsorption on gold nanorods," *Journal of Molecular Structure*, vol. 993, no. 1-3, pp. 420–424, 2011.

[3] R. H. Ritchie, "Plasma losses by fast electrons in thin films," *Physical review*, vol. 106, no. 5, p. 874, 1957.

[4] G. Kumar and P. K. Sarswat, "Interaction of surface plasmon polaritons with nanomaterials," *Reviews in Plasmonics 2015*, pp. 103–129, 2016.

[5] Y. Wang, B. Zhao, C. Min, Y. Zhang, J. Yang, C. Guo, and X. Yuan, "Research progress of femtosecond surface plasmon polariton," *Chinese Physics B*, vol. 29, no. 2, p. 027302, 2020.

[6] A. V. Zayats, I. I. Smolyaninov, and A. A. Maradudin, "Nano-optics of surface plasmon polaritons," *Physics reports*, vol. 408, no. 3-4, pp. 131–314, 2005.

[7] D. Sarid, "Long-range surface-plasma waves on very thin metal films," *Physical Review Letters*, vol. 47, no. 26, p. 1927, 1981.

[8] P. Berini, "Long-range surface plasmon polaritons," *Advances in optics and photonics*, vol. 1, no. 3, pp. 484–588, 2009.

[9] A. V. Zayats and I. I. Smolyaninov, "Near-field photonics: surface plasmon polaritons and localized surface plasmons," *Journal of Optics A: Pure and Applied Optics*, vol. 5, no. 4, p. S16, 2003.

[10] J. Homola, S. S. Yee, and G. Gauglitz, "Surface plasmon resonance sensors," *Sensors and actuators B: Chemical*, vol. 54, no. 1-2, pp. 3–15, 1999.

[11] I. Abdulhalim, M. Zourob, and A. Lakhtakia, "Surface plasmon resonance for biosensing: a mini-review," *Electromagnetics*, vol. 28, no. 3, pp. 214–242, 2008.

[12] R. Kashyap and G. Nemova, "Surface plasmon resonance-based fiber and planar waveguide sensors," *Journal of Sensors*, vol. 2009, 2009.

[13] S. Sharmin, T. Z. Adry, M. F. Hassan, E. Surid, and R. H. Sagor, "Numerical investigation of nanodots implanted high-performance plasmonic refractive index sensor," *Plasmonics*, vol. 17, no. 4, pp. 1717–1729, 2022.

[14] H. A. Atwater, "The promise of plasmonics," *Scientific American*, vol. 296, no. 4, pp. 56–63, 2007.

[15] Z. I. Khan, M. M. Salleh, and G. Prigent, "Achievable bandwidth of a quarter wavelength side-coupled ring resonator," in *2009 IEEE Symposium on Industrial Electronics & Applications*, vol. 1. IEEE, 2009, pp. 358–361.

[16] D. K. Gramotnev and S. I. Bozhevolnyi, "Plasmonics beyond the diffraction limit," *Nature photonics*, vol. 4, no. 2, pp. 83–91, 2010.

[17] W. L. Barnes, A. Dereux, and T. W. Ebbesen, "Surface plasmon subwavelength optics," *nature*, vol. 424, no. 6950, pp. 824–830, 2003.

[18] N. Kazanskiy, S. Khonina, and M. Butt, "Plasmonic sensors based on metal-insulator-metal waveguides for refractive index sensing applications: A brief review," *Physica E: Low-dimensional systems and nanostructures*, vol. 117, p. 113798, 2020.

[19] E. D. Onal and K. Guven, "Scattering suppression and absorption enhancement in contour nanoantennas," *arXiv preprint arXiv:1511.01312*, 2015.

[20] H. N. Daghestani and B. W. Day, "Theory and applications of surface plasmon resonance, resonant mirror, resonant waveguide grating, and dual polarization interferometry biosensors," *Sensors*, vol. 10, no. 11, pp. 9630–9646, 2010.

[21] H. Raether, "Surface plasmons on smooth surfaces," *Surface plasmons on smooth and rough surfaces and on gratings*, pp. 4–39, 2006.

[22] A. Archambault, T. V. Teperik, F. Marquier, and J.-J. Greffet, "Surface plasmon fourier optics," *Physical Review B*, vol. 79, no. 19, p. 195414, 2009.

[23] M. Born, E. Wolf, A. B. Bhatia *et al.*, *Principles of optics: electromagnetic theory of propagation, interference and diffraction of light*. Cambridge university press Cambridge, 1999, vol. 7.

[24] C. U. Greven, F. Lionetti, C. Booth, E. N. Aron, E. Fox, H. E. Schendan, M. Pluess, H. Bruining, B. Acevedo, P. Bijttebier *et al.*, "Sensory processing sensitivity in the context of environmental sensitivity: A critical review and development of research agenda," *Neuroscience & Biobehavioral Reviews*, vol. 98, pp. 287–305, 2019.

[25] M. Quinten, A. Leitner, J. R. Krenn, and F. R. Aussenegg, "Electromagnetic energy transport via linear chains of silver nanoparticles," *Optics letters*, vol. 23, no. 17, pp. 1331–1333, 1998.

[26] S. A. Maier, P. G. Kik, H. A. Atwater, S. Meltzer, E. Harel, B. E. Koel, and A. A. Requicha, "Local detection of electromagnetic energy transport below the diffraction limit in metal nanoparticle plasmon waveguides," *Nature materials*, vol. 2, no. 4, pp. 229–232, 2003.

[27] J.-C. Weeber, A. Dereux, C. Girard, J. R. Krenn, and J.-P. Goudonnet, "Plasmon polaritons of metallic nanowires for controlling submicron propagation of light," *Physical Review B*, vol. 60, no. 12, p. 9061, 1999.

[28] S. I. Bozhevolnyi, J. Erland, K. Leosson, P. M. Skovgaard, and J. M. Hvam, "Waveguiding in surface plasmon polariton band gap structures," *Physical review letters*, vol. 86, no. 14, p. 3008, 2001.

[29] R. F. Oulton, V. J. Sorger, D. Genov, D. Pile, and X. Zhang, "A hybrid plasmonic waveguide for subwavelength confinement and long-range propagation," *nature photonics*, vol. 2, no. 8, pp. 496–500, 2008.

[30] A. L. Pyayt, B. Wiley, Y. Xia, A. Chen, and L. Dalton, "Integration of photonic and silver nanowire plasmonic waveguides," *Nature nanotechnology*, vol. 3, no. 11, pp. 660–665, 2008.

[31] S. I. Bozhevolnyi, V. S. Volkov, E. Devaux, and T. W. Ebbesen, "Channel plasmon-polariton guiding by subwavelength metal grooves," *Physical review letters*, vol. 95, no. 4, p. 046802, 2005.

[32] H. J. Lezec, A. Degiron, E. Devaux, R. Linke, L. Martin-Moreno, F. Garcia-Vidal, and T. Ebbesen, "Beaming light from a subwavelength aperture," *science*, vol. 297, no. 5582, pp. 820–822, 2002.

[33] G. Lerosey, D. Pile, P. Matheu, G. Bartal, and X. Zhang, "Controlling the phase and amplitude of plasmon sources at a subwavelength scale," *Nano letters*, vol. 9, no. 1, pp. 327–331, 2009.

[34] A. F. Koenderink, "Plasmon nanoparticle array waveguides for single photon and single plasmon sources," *Nano letters*, vol. 9, no. 12, pp. 4228–4233, 2009.

[35] Z. Fang, Q. Peng, W. Song, F. Hao, J. Wang, P. Nordlander, and X. Zhu, "Plasmonic focusing in symmetry broken nanocorrals," *Nano letters*, vol. 11, no. 2, pp. 893–897, 2011.

[36] K. Kneipp, Y. Wang, H. Kneipp, L. T. Perelman, I. Itzkan, R. R. Dasari, and M. S. Feld, "Single molecule detection using surface-enhanced raman scattering (sers)," *Physical review letters*, vol. 78, no. 9, p. 1667, 1997.

[37] A. M. Michaels, M. Nirmal, and L. Brus, "Surface enhanced raman spectroscopy of individual rhodamine 6g molecules on large ag nanocrystals," *Journal of the American Chemical Society*, vol. 121, no. 43, pp. 9932–9939, 1999.

[38] K. Kneipp, M. Moskovits, and H. Kneipp, *Surface-enhanced Raman scattering: physics and applications*. Springer Science & Business Media, 2006, vol. 103.

[39] E. Hao and G. C. Schatz, "Electromagnetic fields around silver nanoparticles and dimers," *The Journal of chemical physics*, vol. 120, no. 1, pp. 357–366, 2004.

[40] Y. Fang, N.-H. Seong, and D. D. Dlott, "Measurement of the distribution of site enhancements in surface-enhanced raman scattering," *Science*, vol. 321, no. 5887, pp. 388–392, 2008.

[41] W. Xu, J. Zhang, L. Zhang, X. Hu, and X. Cao, "Ultrasensitive detection using surface enhanced raman scattering from silver nanowire arrays in anodic alumina membranes," *Journal of nanoscience and nanotechnology*, vol. 9, no. 8, pp. 4812–4816, 2009.

[42] W. Xu, L. Zhang, J. Zhang, X. Hu, and L. Sun, "A comparison of surface enhanced raman scattering property between silver electrodes and periodical silver nanowire arrays," *Applied surface science*, vol. 255, no. 13-14, pp. 6612–6614, 2009.

[43] Y. Fang, H. Wei, F. Hao, P. Nordlander, and H. Xu, "Remote-excitation surface-enhanced raman scattering using propagating ag nanowire plasmons," *Nano letters*, vol. 9, no. 5, pp. 2049–2053, 2009.

[44] A. Gopinath, S. V. Boriskina, W. R. Premasiri, L. Ziegler, B. M. Reinhard, and L. Dal Negro, "Plasmonic nanogalaxies: multiscale aperiodic arrays for surface-enhanced raman sensing," *Nano letters*, vol. 9, no. 11, pp. 3922–3929, 2009.

[45] Y.-K. Kim, P. Lundquist, J. Helfrich, J. Mikrut, G. Wong, P. Auvil, and J. Ketterson, "Scanning plasmon optical microscope," *Applied physics letters*, vol. 66, no. 25, pp. 3407–3409, 1995.

[46] A. Kryukov, Y.-K. Kim, and J. B. Ketterson, "Surface plasmon scanning near-field optical microscopy," *Journal of applied physics*, vol. 82, no. 11, pp. 5411–5415, 1997.

[47] D. O. Melville, R. J. Blaikie, and C. R. Wolf, "Submicron imaging with a planar silver lens," *Applied Physics Letters*, vol. 84, no. 22, pp. 4403–4405, 2004.

[48] J. B. Pendry, "Negative refraction makes a perfect lens," *Physical review letters*, vol. 85, no. 18, p. 3966, 2000.

[49] S. Kawata, Y. Inouye, and P. Verma, "Plasmonics for near-field nano-imaging and superlensing," *Nature photonics*, vol. 3, no. 7, pp. 388–394, 2009.

[50] N. Fang, H. Lee, C. Sun, and X. Zhang, "Sub-diffraction-limited optical imaging with a silver superlens," *science*, vol. 308, no. 5721, pp. 534–537, 2005.

[51] H. Lee, Y. Xiong, N. Fang, W. Srituravanich, S. Durant, M. Ambati, C. Sun, and X. Zhang, "Realization of optical superlens imaging below the diffraction limit," *New Journal of Physics*, vol. 7, no. 1, p. 255, 2005.

[52] M. Achermann, K. L. Shuford, G. C. Schatz, D. Dahanayaka, L. A. Bumm, and V. I. Klimov, "Near-field spectroscopy of surface plasmons in flat gold nanoparticles," *Optics letters*, vol. 32, no. 15, pp. 2254–2256, 2007.

[53] P. Zijlstra, J. W. Chon, and M. Gu, "Five-dimensional optical recording mediated by surface plasmons in gold nanorods," *nature*, vol. 459, no. 7245, pp. 410–413, 2009.

[54] C. Hermann, V. Kosobukin, G. Lampel, J. Peretti, V. Safarov, and P. Bertrand, "Surface-enhanced magneto-optics in metallic multilayer films," *Physical Review B*, vol. 64, no. 23, p. 235422, 2001.

[55] M. Mansuripur, A. R. Zakharian, A. Lesuffleur, S.-H. Oh, R. Jones, N. Lindquist, H. Im, A. Kobyakov, and J. Moloney, "Plasmonic nano-structures for optical data storage," *Optics Express*, vol. 17, no. 16, pp. 14 001–14 014, 2009.

[56] D. O'Connor and A. V. Zayats, "The third plasmonic revolution," *Nature nanotechnology*, vol. 5, no. 7, pp. 482–483, 2010.

[57] O. Stenzel, A. Stendal, K. Voigtsberger, and C. Von Borczyskowski, "Enhancement of the photovoltaic conversion efficiency of copper phthalocyanine thin film devices by incorporation of metal clusters," *Solar energy materials and solar cells*, vol. 37, no. 3-4, pp. 337–348, 1995.

[58] M. Westphalen, U. Kreibig, J. Rostalski, H. Lüth, and D. Meissner, "Metal cluster enhanced organic solar cells," *Solar energy materials and solar cells*, vol. 61, no. 1, pp. 97–105, 2000.

[59] V. E. Ferry, L. A. Sweatlock, D. Pacifici, and H. A. Atwater, "Plasmonic nanostructure design for efficient light coupling into solar cells," *Nano letters*, vol. 8, no. 12, pp. 4391–4397, 2008.

[60] M. D. Brown, T. Suteewong, R. S. S. Kumar, V. D'Innocenzo, A. Petrozza, M. M. Lee, U. Wiesner, and H. J. Snaith, "Plasmonic dye-sensitized solar cells using core-shell metal- insulator nanoparticles," *Nano letters*, vol. 11, no. 2, pp. 438–445, 2011.

[61] G. Nemova and R. Kashyap, "Fiber-bragg-grating-assisted surface plasmon-polariton sensor," *Optics letters*, vol. 31, no. 14, pp. 2118–2120, 2006.

[62] S. M. Tripathi, A. Kumar, E. Marin, and J.-P. Meunier, "Side-polished optical fiber grating-based refractive index sensors utilizing the pure surface plasmon polariton," *Journal of lightwave technology*, vol. 26, no. 13, pp. 1980–1985, 2008.

[63] K. Usbeck, W. Ecke, A. T. Andreev, V. Hagemann, R. Mueller, and R. Willsch, "Distributed optochemical sensor network using evanescent field interaction in fibre bragg gratings," in *European Workshop on Optical Fibre Sensors*, vol. 3483. SPIE, 1998, pp. 90–94.

[64] J. ČtyrokÝ, F. Abdelmalek, W. Ecke, and K. Usbeck, "Modelling of the surface plasmon resonance waveguide sensor with bragg grating," *Optical and Quantum Electronics*, vol. 31, pp. 927–941, 1999.

[65] G. Nemova and R. Kashyap, "Theoretical model of a planar integrated refractive index sensor based on surface plasmon-polariton excitation," *Optics Communications*, vol. 275, no. 1, pp. 76–82, 2007.

[66] ——, "Theoretical model of a planar waveguide refractive index sensor assisted by a corrugated long period metal grating," *Optics communications*, vol. 281, no. 6, pp. 1522–1528, 2008.

[67] C. Holmes, K. Daly, I. Sparrow, J. Gates, G. D'Alessandro, and P. Smith, "Excitation of surface plasmons using tilted planar-waveguide bragg gratings," *IEEE Photonics Journal*, vol. 3, no. 5, pp. 777–788, 2011.

[68] J. N. Anker, W. P. Hall, O. Lyandres, N. C. Shah, J. Zhao, and R. P. Van Duyne, "Biosensing with plasmonic nanosensors," *Nature materials*, vol. 7, no. 6, pp. 442–453, 2008.

[69] D. G. Georganopoulou, L. Chang, J.-M. Nam, C. S. Thaxton, E. J. Mufson, W. L. Klein, and C. A. Mirkin, "Nanoparticle-based detection in cerebral spinal fluid of a soluble pathogenic biomarker for alzheimer's disease," *Proceedings of the National Academy of Sciences*, vol. 102, no. 7, pp. 2273–2276, 2005.

[70] A. V. Kabashin, P. Evans, S. Pastkovsky, W. Hendren, G. A. Wurtz, R. Atkinson, R. Pollard, V. A. Podolskiy, and A. V. Zayats, "Plasmonic nanorod metamaterials for biosensing," *Nature materials*, vol. 8, no. 11, pp. 867–871, 2009.

[71] N. L. Rosi and C. A. Mirkin, "Nanostructures in biodiagnostics," *Chemical reviews*, vol. 105, no. 4, pp. 1547–1562, 2005.

[72] M. S. Han, A. K. Lytton-Jean, and C. A. Mirkin, "A gold nanoparticle based approach for screening triplex dna binders," *Journal of the American Chemical Society*, vol. 128, no. 15, pp. 4954–4955, 2006.

[73] M. S. Han, A. K. Lytton-Jean, B.-K. Oh, J. Heo, and C. A. Mirkin, "Colorimetric screening of dna-binding molecules with gold nanoparticle probes," *Angewandte Chemie International Edition*, vol. 45, no. 11, pp. 1807–1810, 2006.

[74] Q. Lu, D. Chen, and G. Wu, "Low-loss hybrid plasmonic waveguide based on metal ridge and semiconductor nanowire," *Optics Communications*, vol. 289, pp. 64–68, 2013.

[75] C. Y. Jeong, M. Kim, and S. Kim, "Circular hybrid plasmonic waveguide with ultra-long propagation distance," *Optics express*, vol. 21, no. 14, pp. 17 404–17 412, 2013.

[76] Y. Bian, Z. Zheng, Y. Liu, J. Liu, J. Zhu, and T. Zhou, "Hybrid wedge plasmon polariton waveguide with good fabrication-error-tolerance for ultra-deep-subwavelength mode confinement," *Optics Express*, vol. 19, no. 23, pp. 22 417–22 422, 2011.

[77] P. Berini, R. Charbonneau, N. Lahoud, and G. Mattiussi, "Characterization of long-range surface-plasmon-polariton waveguides," *Journal of Applied Physics*, vol. 98, no. 4, p. 043109, 2005.

[78] B. Steinberger, A. Hohenau, H. Ditlbacher, A. Stepanov, A. Drezet, F. Aussenegg, A. Leitner, and J. Krenn, "Dielectric stripes on gold as surface plasmon waveguides," *Applied Physics Letters*, vol. 88, no. 9, p. 094104, 2006.

[79] J. Grandidier, S. Massenot, G. C. Des Francs, A. Bouhelier, J.-C. Weeber, L. Markey, A. Dereux, J. Renger, M. González, and R. Quidant, "Dielectric-loaded surface plasmon polariton waveguides: figures of merit and mode characterization by image and fourier plane leakage microscopy," *Physical Review B*, vol. 78, no. 24, p. 245419, 2008.

[80] T. Holmgaard and S. I. Bozhevolnyi, "Theoretical analysis of dielectric-loaded surface plasmon-polariton waveguides," *Physical Review B*, vol. 75, no. 24, p. 245405, 2007.

[81] A. Krasavin and A. Zayats, "Three-dimensional numerical modeling of photonic integration with dielectric-loaded spp waveguides," *Physical Review B*, vol. 78, no. 4, p. 045425, 2008.

[82] B. Steinberger, A. Hohenau, H. Ditlbacher, F. Aussenegg, A. Leitner, and J. Krenn, "Dielectric stripes on gold as surface plasmon waveguides: Bends and directional couplers," *Applied Physics Letters*, vol. 91, no. 8, p. 081111, 2007.

[83] T. Holmgaard, Z. Chen, S. I. Bozhevolnyi, L. Markey, A. Dereux, A. V. Krasavin, and A. V. Zayats, "Bend-and splitting loss of dielectric-loaded surface plasmon-polariton waveguides," *Optics Express*, vol. 16, no. 18, pp. 13 585–13 592, 2008.

[84] G. Veronis and S. Fan, "Modes of subwavelength plasmonic slot waveguides," *Journal of Lightwave Technology*, vol. 25, no. 9, pp. 2511–2521, 2007.

[85] S. Kim and R. Yan, "Recent developments in photonic, plasmonic and hybrid nanowire waveguides," *Journal of Materials Chemistry C*, vol. 6, no. 44, pp. 11 795–11 816, 2018.

[86] J. Wang, M. S. Gudiksen, X. Duan, Y. Cui, and C. M. Lieber, "Highly polarized photoluminescence and photodetection from single indium phosphide nanowires," *Science*, vol. 293, no. 5534, pp. 1455–1457, 2001.

[87] H. Kind, H. Yan, B. Messer, M. Law, and P. Yang, "Nanowire ultraviolet photodetectors and optical switches," *Advanced materials*, vol. 14, no. 2, pp. 158–160, 2002.

[88] S. M. Maričić and B. D. Lazić, "Abacus computing tool: From history to application in mathematical education," *Inovacije u nastavi-časopis za savremenu nastavu*, vol. 33, no. 1, pp. 57–71, 2020.

[89] S. Köppel, B. Ulmann, L. Heimann, and D. Killat, "Using analog computers in today's largest computational challenges," *Advances in Radio Science*, vol. 19, pp. 105–116, 2021.

[90] M. Riordan, L. Hoddeson, and C. Herring, "The invention of the transistor," *Reviews of Modern Physics*, vol. 71, no. 2, p. S336, 1999.

[91] T. N. Theis and H.-S. P. Wong, "The end of moore's law: A new beginning for information technology," *Computing in Science & Engineering*, vol. 19, no. 2, pp. 41–50, 2017.

[92] M. Horowitz, C.-K. K. Yang, and S. Sidiropoulos, "High-speed electrical signaling: Overview and limitations," *IEEE Micro*, vol. 18, no. 1, pp. 12–24, 1998.

[93] S. C. Esener, "Implementation and prospects for chip-to-chip free-space optical interconnects," in *International Electron Devices Meeting. Technical Digest (Cat. No. 01CH37224)*. IEEE, 2001, pp. 23–5.

[94] B. Hecht, H. Bielefeldt, L. Novotny, Y. Inouye, and D. Pohl, "Local excitation, scattering, and interference of surface plasmons," *Physical review letters*, vol. 77, no. 9, p. 1889, 1996.

[95] M. Butt, N. Kazanskiy, and S. Khonina, "Nanodots decorated asymmetric metal–insulator–metal waveguide resonator structure based on fano resonances for refractive index sensing application," *Laser Physics*, vol. 30, no. 7, p. 076204, 2020.

[96] M. A. Butt, "Metal-insulator-metal waveguide based plasmonic sensors: Fantasy or truth-a critical review," *Authorea Preprints*, 2022.

[97] M. Butt, S. Khonina, and N. Kazanskiy, "Plasmonic refractive index sensor based on mim square ring resonator," in *2018 International Conference on Computing, Electronic and Electrical Engineering (ICE Cube)*. IEEE, 2018, pp. 1–4.

[98] Y. Tang, Z. Zhang, R. Wang, Z. Hai, C. Xue, W. Zhang, and S. Yan, "Refractive index sensor based on fano resonances in metal-insulator-metal waveguides coupled with resonators," *Sensors*, vol. 17, no. 4, p. 784, 2017.

[99] M. R. Rakhshani, A. Tavousi, and M. A. Mansouri-Birjandi, "Design of a plasmonic sensor based on a square array of nanorods and two slot cavities with a high figure of merit for glucose concentration monitoring," *Applied optics*, vol. 57, no. 27, pp. 7798–7804, 2018.

[100] M. R. Rakhshani and M. A. Mansouri-Birjandi, "High sensitivity plasmonic refractive index sensing and its application for human blood group identification," *Sensors and Actuators B: Chemical*, vol. 249, pp. 168–176, 2017.

[101] Y.-Y. Xie, Y.-X. Huang, W.-L. Zhao, W.-H. Xu, and C. He, "A novel plasmonic sensor based on metal–insulator–metal waveguide with side-coupled hexagonal cavity," *IEEE Photonics Journal*, vol. 7, no. 2, pp. 1–12, 2015.

[102] S. Ghorbani, M. A. Dashti, and M. Jabbari, "Plasmonic nano-sensor based on metal-dielectric-metal waveguide with the octagonal cavity ring," *Laser Physics*, vol. 28, no. 6, p. 066208, 2018.

[103] Z. Zhang, J. Yang, X. He, J. Zhang, J. Huang, D. Chen, and Y. Han, "Plasmonic refractive index sensor with high figure of merit based on concentric-rings resonator," *Sensors*, vol. 18, no. 1, p. 116, 2018.

[104] S. Yan, M. Zhang, X. Zhao, Y. Zhang, J. Wang, and W. Jin, "Refractive index sensor based on a metal–insulator–metal waveguide coupled with a symmetric structure," *Sensors*, vol. 17, no. 12, p. 2879, 2017.

[105] M. Rahmatiyar, M. Afsahi, and M. Danaie, "Design of a refractive index plasmonic sensor based on a ring resonator coupled to a mim waveguide containing tapered defects," *Plasmonics*, vol. 15, pp. 2169–2176, 2020.

[106] L. Wang, Y.-P. Zeng, Z.-Y. Wang, X.-P. Xia, and Q.-Q. Liang, "A refractive index sensor based on an analogy t shaped metal–insulator–metal waveguide," *Optik*, vol. 172, pp. 1199–1204, 2018.

[107] S. Zou, F. Wang, R. Liang, L. Xiao, and M. Hu, "A nanoscale refractive index sensor based on asymmetric plasmonic waveguide with a ring resonator: A review," *IEEE Sensors Journal*, vol. 15, no. 2, pp. 646–650, 2014.

[108] Y.-X. Huang, Y.-Y. Xie, W.-L. Zhao, H.-J. Che, W.-H. Xu, X. Li, and J.-C. Li, "A plasmonic refractive index sensor based on a mim waveguide with a side-coupled nanodisk resonator," in *2014 IEEE 20th International Conference on Embedded and Real-Time Computing Systems and Applications*. IEEE, 2014, pp. 1–5.

[109] T. Wu, Y. Liu, Z. Yu, Y. Peng, C. Shu, and H. Ye, "The sensing characteristics of plasmonic waveguide with a ring resonator," *Optics express*, vol. 22, no. 7, pp. 7669–7677, 2014.

[110] Y. Binfeng, H. Guohua, Z. Ruohu, and C. Yiping, "Design of a compact and high sensitive refractive index sensor base on metal-insulator-metal plasmonic bragg grating," *Optics Express*, vol. 22, no. 23, pp. 28 662–28 670, 2014.

[111] B. Ni, X. Chen, D. Xiong, H. Liu, G. Hua, J. Chang, J. Zhang, and H. Zhou, "Infrared plasmonic refractive index-sensitive nanosensor based on electromagnetically induced transparency of waveguide resonator systems," *Optical and Quantum Electronics*, vol. 47, pp. 1339–1346, 2015.

[112] R. Zafar and M. Salim, "Enhanced figure of merit in fano resonance-based plasmonic refractive index sensor," *IEEE Sensors Journal*, vol. 15, no. 11, pp. 6313–6317, 2015.

[113] S.-B. Yan, L. Luo, C.-Y. Xue, and Z.-D. Zhang, "A refractive index sensor based on a metal-insulator-metal waveguide-coupled ring resonator," *Sensors*, vol. 15, no. 11, pp. 29 183–29 191, 2015.

[114] Z. Chen, L. Yu, L. Wang, G. Duan, Y. Zhao, and J. Xiao, "A refractive index nanosensor based on fano resonance in the plasmonic waveguide system," *IEEE Photonics Technology Letters*, vol. 27, no. 16, pp. 1695–1698, 2015.

[115] B. Li, H. Li, L. Zeng, S. Zhan, Z. He, Z. Chen, and H. Xu, "High-sensitivity sensing based on plasmon-induced transparency," *IEEE Photonics Journal*, vol. 7, no. 5, pp. 1–7, 2015.

[116] Z. Chen, H. Li, S. Zhan, Z. He, B. Li, and H. Xu, "Sensing characteristics based on fano resonance in rectangular ring waveguide," *Optics Communications*, vol. 356, pp. 373–377, 2015.

[117] T. Wu, Y. Liu, Z. Yu, H. Ye, C. Shu, Y. Peng, J. Wang, and H. He, "Tuning the fano resonances in a single defect nanocavity coupled with a plasmonic waveguide for sensing applications," *Modern Physics Letters B*, vol. 29, no. 33, p. 1550218, 2015.

[118] K. Wen, Y. Hu, L. Chen, J. Zhou, L. Lei, and Z. Guo, "Fano resonance with ultra-high figure of merits based on plasmonic metal-insulator-metal waveguide," *Plasmonics*, vol. 10, pp. 27–32, 2015.

[119] A. Ahmadivand, M. Karabiyik, and N. Pala, "Inducing multiple fano resonant modes in split concentric nanoring resonator dimers for ultraprecise sensing," *Journal of Optics*, vol. 17, no. 8, p. 085104, 2015.

[120] Z. Chen, X. Song, G. Duan, L. Wang, and L. Yu, "Multiple fano resonances control in mim side-coupled cavities systems," *IEEE Photonics Journal*, vol. 7, no. 3, pp. 1–10, 2015.

[121] X. Zhang, M. Shao, and X. Zeng, "High quality plasmonic sensors based on fano resonances created through cascading double asymmetric cavities," *Sensors*, vol. 16, no. 10, p. 1730, 2016.

[122] Y. Wang, S. Li, Y. Zhang, and L. Yu, "Independently formed multiple fano resonances for ultra-high sensitivity plasmonic nanosensor," 2016.

[123] S. Pang, Y. Huo, Y. Xie, and L. Hao, "Fano resonance in mim waveguide structure with oblique rectangular cavity and its application in sensor," *Optics Communications*, vol. 381, pp. 409–413, 2016.

[124] Z. Zhang, L. Luo, C. Xue, W. Zhang, and S. Yan, "Fano resonance based on metal-insulator-metal waveguide-coupled double rectangular cavities for plasmonic nanosensors," *Sensors*, vol. 16, no. 5, p. 642, 2016.

[125] F. Chen and D. Yao, "Realizing of plasmon fano resonance with a metal nanowall moving along mim waveguide," *Optics Communications*, vol. 369, pp. 72–78, 2016.

[126] S. Gaur, R. Zafar, and D. Somwanshi, "Plasmonic refractive index sensor based on metal insulator metal waveguide," in *2016 International Conference on Recent Advances and Innovations in Engineering (ICRAIE)*. IEEE, 2016, pp. 1–4.

[127] Y. Wang, S. Li, Y. Zhang, and L. Yu, "Ultrasharp fano resonances based on the circular cavity optimized by a metallic nanodisk," *IEEE Photonics Journal*, vol. 8, no. 6, pp. 1–8, 2016.

[128] L. Chen, Y. Liu, Z. Yu, D. Wu, R. Ma, Y. Zhang, and H. Ye, "Numerical analysis of a near-infrared plasmonic refractive index sensor with high figure of merit based on a fillet cavity," *Optics express*, vol. 24, no. 9, pp. 9975–9983, 2016.

[129] M. R. Rakhshani and M. A. Mansouri-Birjandi, "High-sensitivity plasmonic sensor based on metal–insulator–metal waveguide and hexagonal-ring cavity," *IEEE Sensors Journal*, vol. 16, no. 9, pp. 3041–3046, 2016.

[130] Y. Binfeng, Z. Ruohu, H. Guohua, and C. Yiping, "Ultra sharp fano resonances induced by coupling between plasmonic stub and circular cavity resonators," *Plasmonics*, vol. 11, pp. 1157–1162, 2016.

[131] Y. Binfeng, G. Hu, R. Zhang, and C. Yiping, "Fano resonances in a plasmonic waveguide system composed of stub coupled with a square cavity resonator," *Journal of Optics*, vol. 18, no. 5, p. 055002, 2016.

[132] B.-X. Li, H.-J. Li, L.-L. Zeng, S.-P. Zhan, Z.-H. He, Z.-Q. Chen, and H. Xu, "Sensing application in fano resonance with t-shape structure," *Journal of Lightwave Technology*, vol. 34, no. 14, pp. 3342–3347, 2016.

[133] Z. Chen, X. Cao, X. Song, L. Wang, and L. Yu, "Side-coupled cavity-induced fano resonance and its application in nanosensor," *Plasmonics*, vol. 11, pp. 307–313, 2016.

[134] B.-H. Zhang, L.-L. Wang, H.-J. Li, X. Zhai, and S.-X. Xia, "Two kinds of double fano resonances induced by an asymmetric mim waveguide structure," *Journal of Optics*, vol. 18, no. 6, p. 065001, 2016.

[135] K. Wen, Y. Hu, L. Chen, J. Zhou, L. Lei, and Z. Meng, "Single/dual fano resonance based on plasmonic metal-dielectric-metal waveguide," *Plasmonics*, vol. 11, pp. 315–321, 2016.

[136] S. Sherif, L. Shahada, D. Zografopoulos, R. Beccherelli, and M. Swillam, "Near infrared plasmonic sensor based on fano resonance," in *Integrated Optics: Devices, Materials, and Technologies XX*, vol. 9750. SPIE, 2016, pp. 55–60.

[137] Y. Chen, P. Luo, Z.-y. Zhao, L. He, and X.-n. Cui, "Study on fano resonance regulating mechanism of si contained metal–dielectric–metal waveguide coupled rectangular cavity," *Physics Letters A*, vol. 381, no. 40, pp. 3472–3476, 2017.

[138] W. Lin, H. Zhang, S.-C. Chen, B. Liu, and Y.-G. Liu, "Microstructured optical fiber for multichannel sensing based on fano resonance of the whispering gallery modes," *Optics Express*, vol. 25, no. 2, pp. 994–1004, 2017.

[139] W.-J. Mai, Y.-L. Wang, Y.-Y. Zhang, L.-N. Cui, and L. Yu, "Refractive plasmonic sensor based on fano resonances in an optical system," *Chinese physics letters*, vol. 34, no. 2, p. 024204, 2017.

[140] J. Yang, X. Song, Z. Chen, L. Cui, S. Yang, and L. Yu, "Tunable multi-fano resonances in mdm-based side-coupled resonator system and its application in nanosensor," *Plasmonics*, vol. 12, pp. 1665–1672, 2017.

[141] W.-X. Huang, J.-J. Guo, M.-S. Wang, and G.-R. Zhao, "Sensor based on fano resonances of plane metamaterial with narrow slits," *Physics Letters A*, vol. 381, no. 10, pp. 909–912, 2017.

[142] J. Yang, X. Song, S. Yang, L. Cui, and L. Yu, "Independently controllable multiple fano resonances in side-coupled mdm structure and its applications for sensing and wavelength demultiplexing," *Journal of Physics D: Applied Physics*, vol. 50, no. 32, p. 325107, 2017.

[143] Y. Zhang, S. Li, Z. Chen, P. Jiang, R. Jiao, Y. Zhang, L. Wang, and L. Yu, "Ultra-high sensitivity plasmonic nanosensor based on multiple fano resonance in the mdm side-coupled cavities," *Plasmonics*, vol. 12, pp. 1099–1105, 2017.

[144] C. Wu, H. Ding, T. Huang, X. Wu, B. Chen, K. Ren, and S. Fu, "Plasmon-induced transparency and refractive index sensing in side-coupled stub-hexagon resonators," *Plasmonics*, vol. 13, pp. 251–257, 2018.

[145] J. Zhou, H. Chen, Z. Zhang, J. Tang, J. Cui, C. Xue, and S. Yan, "Transmission and refractive index sensing based on fano resonance in mim waveguide-coupled trapezoid cavity," *AIP Advances*, vol. 7, no. 1, p. 015020, 2017.

[146] X. Zhao, Z. Zhang, and S. Yan, "Tunable fano resonance in asymmetric mim waveguide structure," *Sensors*, vol. 17, no. 7, p. 1494, 2017.

[147] A. Akhavan, H. Ghafoorifard, S. Abdolhosseini, and H. Habibiyan, "Plasmon-induced transparency based on a triangle cavity coupled with an ellipse-ring resonator," *Applied optics*, vol. 56, no. 34, pp. 9556–9563, 2017.

[148] M. R. Rakhshani and M. A. Mansouri-Birjandi, "Utilizing the metallic nano-rods in hexagonal configuration to enhance sensitivity of the plasmonic racetrack resonator in sensing application," *Plasmonics*, vol. 12, pp. 999–1006, 2017.

[149] R. Zafar, S. Nawaz, G. Singh, A. d'Alessandro, and M. Salim, "Plasmonics-based refractive index sensor for detection of hemoglobin concentration," *IEEE Sensors Journal*, vol. 18, no. 11, pp. 4372–4377, 2018.

[150] N. Jankovic and N. Cselyuszka, "Multiple fano-like mim plasmonic structure based on triangular resonator for refractive index sensing," *Sensors*, vol. 18, no. 1, p. 287, 2018.

[151] X. Zhang, Y. Qi, P. Zhou, H. Gong, B. Hu, and C. Yan, "Refractive index sensor based on fano resonances in plasmonic waveguide with dual side-coupled ring resonators," *Photonic Sensors*, vol. 8, pp. 367–374, 2018.

[152] X. Yi, J. Tian, and R. Yang, "Tunable fano resonance in mdm stub waveguide coupled with a u-shaped cavity," *The European Physical Journal D*, vol. 72, pp. 1–9, 2018.

[153] K. Wen, L. Chen, J. Zhou, L. Lei, and Y. Fang, "A plasmonic chip-scale refractive index sensor design based on multiple fano resonances," *Sensors*, vol. 18, no. 10, p. 3181, 2018.

[154] X. Shi, L. Ma, Z. Zhang, Y. Tang, Y. Zhang, J. Han, and Y. Sun, "Dual fano resonance control and refractive index sensors based on a plasmonic waveguide-coupled resonator system," *Optics Communications*, vol. 427, pp. 326–330, 2018.

[155] A. D. Khan, "Refractive index sensing with fano resonant l-shaped metasurface," *Optical Materials*, vol. 82, pp. 168–174, 2018.

[156] Z. Guo, K. Wen, Q. Hu, W. Lai, J. Lin, and Y. Fang, "Plasmonic multichannel refractive index sensor based on subwavelength tangent-ring metal–insulator–metal waveguide," *Sensors*, vol. 18, no. 5, p. 1348, 2018.

[157] Y. Chen, P. Luo, X. Liu, Y. Di, S. Han, X. Cui, and L. He, "Sensing performance analysis on fano resonance of metallic double-baffle contained mdm waveguide coupled ring resonator," *Optics & Laser Technology*, vol. 101, pp. 273–278, 2018.

[158] Z.-h. Liu, L.-z. Ding, J.-p. Yi, Z.-c. Wei, and J.-p. Guo, "Plasmonics refractive index sensor based on tunable ultra-sharp fano resonance," *Optoelectronics letters*, vol. 14, no. 6, pp. 421–424, 2018.

[159] T. Zhao and S. Yu, "Ultra-high sensitivity nanosensor based on multiple fano resonance in the mim coupled plasmonic resonator," *Plasmonics*, vol. 13, no. 4, pp. 1115–1120, 2018.

[160] Y. Wang, S. Li, Y. Zhang, and L. Yu, "Independently formed multiple fano resonances for ultra-high sensitivity plasmonic nanosensor," *Plasmonics*, vol. 13, no. 1, pp. 107–113, 2018.

[161] X. Ren, K. Ren, and C. Ming, "Self-reference refractive index sensor based on independently controlled double resonances in side-coupled u-shaped resonators," *Sensors*, vol. 18, no. 5, p. 1376, 2018.

[162] O. Mahboub, R. El Haffar, and A. Farkhsi, "Optical fano resonance in mim waveguides with a double splits ring resonator," *J. New Front. Spatial Concepts*, vol. 13, pp. 181–187, 2018.

[163] L. Dong, X. Xu, K. Sun, Y. Ding, P. Ouyang, and P. Wang, "Sensing analysis based on fano resonance in arch bridge structure," *Journal of Physics Communications*, vol. 2, no. 10, p. 105010, 2018.

[164] M. Butt, S. Khonina, and N. Kazanskiy, "An array of nano-dots loaded mim square ring resonator with enhanced sensitivity at nir wavelength range," *Optik*, vol. 202, p. 163655, 2020.

[165] A. Hocini, M. Temmar, D. Khedrouche *et al.*, "Design of mid infrared high sensitive metal-insulator-metal plasmonic sensor," *Chinese Journal of Physics*, vol. 61, pp. 86–97, 2019.

[166] M. Wang, M. Zhang, Y. Wang, R. Zhao, and S. Yan, "Fano resonance in an asymmetric mim waveguide structure and its application in a refractive index nanosensor," *Sensors*, vol. 19, no. 4, p. 791, 2019.

[167] Y. Lu, J. Xu, M. Xu, J. Xu, J. Wang, and J. Zheng, "High sensitivity plasmonic metal-dielectric-metal device with two side-coupled fano cavities," *Photonic Sensors*, vol. 9, pp. 205–212, 2019.

[168] Y. Zhang, Y. Kuang, Z. Zhang, Y. Tang, J. Han, R. Wang, J. Cui, Y. Hou, and W. Liu, "High-sensitivity refractive index sensors based on fano resonance in the plasmonic system of splitting ring cavity-coupled mim waveguide with tooth cavity," *Applied Physics A*, vol. 125, pp. 1–5, 2019.

[169] M. Butt, S. Khonina, and N. Kazanskiy, "Plasmonic refractive index sensor based on metal–insulator-metal waveguides with high sensitivity," *Journal of Modern Optics*, vol. 66, no. 9, pp. 1038–1043, 2019.

[170] Y. Zhang and M. Cui, "Refractive index sensor based on the symmetric mim waveguide structure," *Journal of Electronic Materials*, vol. 48, pp. 1005–1010, 2019.

[171] Y.-F. Chou Chau, C.-T. Chou Chao, H. J. Huang, N. Kumara, C. M. Lim, and H.-P. Chiang, "Ultra-high refractive index sensing structure based on a metal-insulator-metal waveguide-coupled t-shape cavity with metal nanorod defects," *Nanomaterials*, vol. 9, no. 10, p. 1433, 2019.

[172] Z. Li, K. Wen, L. Chen, L. Lei, J. Zhou, D. Zhou, Y. Fang, and B. Wu, "Refractive index sensor based on multiple fano resonances in a plasmonic mim structure," *Applied optics*, vol. 58, no. 18, pp. 4878–4883, 2019.

[173] Y. Chen, Y. Xu, and J. Cao, "Fano resonance sensing characteristics of mim waveguide coupled square convex ring resonator with metallic baffle," *Results in physics*, vol. 14, p. 102420, 2019.

[174] S. Yu, T. Zhao, J. Yu, and D. Pan, "Tuning multiple fano resonances for on-chip sensors in a plasmonic system," *Sensors*, vol. 19, no. 7, p. 1559, 2019.

[175] M. R. Rakhshani, "Fano resonances based on plasmonic square resonator with high figure of merits and its application in glucose concentrations sensing," *Optical and Quantum Electronics*, vol. 51, no. 9, p. 287, 2019.

[176] X. Yang, E. Hua, M. Wang, Y. Wang, F. Wen, and S. Yan, "Fano resonance in a mim waveguide with two triangle stubs coupled with a split-ring nanocavity for sensing application," *Sensors*, vol. 19, no. 22, p. 4972, 2019.

[177] Y. Fang, K. Wen, Z. Li, B. Wu, L. Chen, J. Zhou, and D. Zhou, "Multiple fano resonances based on end-coupled semi-ring rectangular resonator," *IEEE photonics journal*, vol. 11, no. 4, pp. 1–8, 2019.

[178] Y. Chen, L. Chen, K. Wen, Y. Hu, and W. Lin, "Multiple fano resonances in a coupled plasmonic resonator system," *Journal of Applied Physics*, vol. 126, no. 8, p. 083102, 2019.

[179] L. Cheng, Z. Wang, X. He, and P. Cao, "Plasmonic nanosensor based on multiple independently tunable fano resonances," *Beilstein journal of nanotechnology*, vol. 10, no. 1, pp. 2527–2537, 2019.

[180] F. Chen and J. Li, "Refractive index and temperature sensing based on defect resonator coupled with a mim waveguide," *Modern Physics Letters B*, vol. 33, no. 03, p. 1950017, 2019.

[181] M. A. A. Butt and N. Kazanskiy, "Enhancing the sensitivity of a standard plasmonic mim square ring resonator by incorporating the nano-dots in the cavity," *Photonics Letters of Poland*, vol. 12, no. 1, pp. 1–3, 2020.

[182] M. A. Butt, N. L. Kazanskiy, and S. N. Khonina, "Highly sensitive refractive index sensor based on plasmonic bow tie configuration," *Photonic sensors*, vol. 10, pp. 223–232, 2020.

[183] Y.-P. Qi, L.-Y. Wang, Y. Zhang, T. Zhang, B.-H. Zhang, X.-Y. Deng, and X.-X. Wang, "Multiple fano resonances in metal–insulator–metal waveguide with umbrella resonator coupled with metal baffle for refractive index sensing," *Chinese Physics B*, vol. 29, no. 6, p. 067303, 2020.

[184] S. Asgari, S. Pooretemad, and N. Granpayeh, "Plasmonic refractive index sensor based on a double concentric square ring resonator and stubs," *Photonics and Nanostructures-Fundamentals and Applications*, vol. 42, p. 100857, 2020.

[185] S. E. Achi, A. Hocini, H. B. Salah, and A. Harhouz, "Refractive index sensor mim based waveguide coupled with a slotted side resonator," *Progress In Electromagnetics Research M*, vol. 96, pp. 147–156, 2020.

[186] J. Guo, X. Yang, Y. Wang, M. Wang, E. Hua, and S. Yan, "Refractive index nanosensor with simple structure based on fano resonance," *IEEE Photonics Journal*, vol. 12, no. 4, pp. 1–10, 2020.

[187] X. Yang, E. Hua, H. Su, J. Guo, and S. Yan, "A nanostructure with defect based on fano resonance for application on refractive-index and temperature sensing," *Sensors*, vol. 20, no. 15, p. 4125, 2020.

[188] X. Liu, J. Li, J. Chen, S. Rohimah, H. Tian, and J. Wang, "Fano resonance based on d-shaped waveguide structure and its application for human hemoglobin detection," *Applied Optics*, vol. 59, no. 21, pp. 6424–6430, 2020.

[189] Z. Li, K. Wen, L. Chen, L. Lei, J. Zhou, D. Zhou, Y. Fang, and Y. Qin, "Manipulation of multiple fano resonances based on a novel chip-scale mdm structure," *IEEE Access*, vol. 8, pp. 32 914–32 921, 2020.

[190] Y. Sharma, R. Zafar, S. K. Metya, and V. Kanungo, "Split ring resonators-based plasmonics sensor with dual fano resonances," *IEEE Sensors Journal*, vol. 21, no. 5, pp. 6050–6055, 2020.

[191] S. Wang, S. Yu, T. Zhao, Y. Wang, and X. Shi, "A nanosensor with ultra-high fom based on tunable malleable multiple fano resonances in a waveguide coupled isosceles triangular resonator," *Optics communications*, vol. 465, p. 125614, 2020.

[192] Q. Yang, X. Liu, F. Guo, H. Bai, B. Zhang, X. Li, Y. Tan, and Z. Zhang, "Multiple fano resonance in mim waveguide system with cross-shaped cavity," *Optik*, vol. 220, p. 165163, 2020.

[193] D. Chauhan, R. Adhikari, R. K. Saini, S. H. Chang, and R. P. Dwivedi, "Subwavelength plasmonic liquid sensor using fano resonance in a ring resonator structure," *Optik*, vol. 223, p. 165545, 2020.

[194] R. H. Sagor, M. F. Hassan, S. Sharmin, T. Z. Adry, and M. A. R. Emon, "Numerical investigation of an optimized plasmonic on-chip refractive index sensor for temperature and blood group detection," *Results in Physics*, vol. 19, p. 103611, 2020.

[195] Y. Wang, S. Yu, T. Zhao, Z. Hu, and S. Wang, "High figure of merit refractive index nanosensor based on fano resonances in waveguide," *Journal of Nanophotonics*, vol. 14, no. 2, pp. 026 021–026 021, 2020.

[196] Z. Chen, Y. Yu, Y. Wang, N. Guo, and L. Xiao, "Compact plasmonic structure induced mode excitation and fano resonance," *Plasmonics*, vol. 15, pp. 2177–2183, 2020.

[197] M. R. Rakhshani, "Optical refractive index sensor with two plasmonic double-square resonators for simultaneous sensing of human blood groups," *Photonics and Nanostructures-Fundamentals and Applications*, vol. 39, p. 100768, 2020.

[198] J. Chen, J. Li, X. Liu, S. Rohimah, H. Tian, and D. Qi, "Fano resonance in a mim waveguide with double symmetric rectangular stubs and its sensing characteristics," *Optics communications*, vol. 482, p. 126563, 2021.

[199] N. Amoosoltani, K. Mehrabi, A. Zarifkar, A. Farmani, and N. Yasrebi, "Double-ring resonator plasmonic refractive index sensor utilizing dual-band unidirectional reflectionless propagation effect," *Plasmonics*, vol. 16, pp. 1277–1285, 2021.

[200] M. Butt and N. Kazanskiy, "Nanoblocks embedded in l-shaped nanocavity of a plasmonic sensor for best sensor performance," *Optica Applicata*, vol. 51, no. 1, pp. 109–120, 2021.

[201] J. Zhu and C. Wu, "Optical refractive index sensor with fano resonance based on original mim waveguide structure," *Results in Physics*, vol. 21, p. 103858, 2021.

[202] F. Hu, F. Chen, H. Zhang, L. Sun, and C. Yu, "Sensor based on multiple fano resonances in mim waveguide resonator system with silver nanorod-defect," *Optik*, vol. 229, p. 166237, 2021.

[203] R. H. Sagor, M. F. Hassan, A. A. Yaseer, E. Surid, and M. I. Ahmed, "Highly sensitive refractive index sensor optimized for blood group sensing utilizing the fano resonance," *Applied Nanoscience*, vol. 11, pp. 521–534, 2021.

[204] Y.-F. C. Chau, C.-T. Chou Chao, S. Z. B. H. Jumat, M. R. R. Kooh, R. Thotagamuge, C. M. Lim, and H.-P. Chiang, "Improved refractive index-sensing performance of multimode fano-resonance-based metal-insulator-metal nanostructures," *Nanomaterials*, vol. 11, no. 8, p. 2097, 2021.

[205] S. She, S. Shen, Z. Wang, Q. Tan, J. Xiong, and W. Zhang, "Fano-resonance-based refractive index sensor with ultra-high sensitivity," *Results in Physics*, vol. 25, p. 104327, 2021.

[206] J. Chen, H. Yang, Z. Fang, M. Zhao, and C. Xie, "Refractive index sensing based on multiple fano resonances in a split-ring cavity-coupled mim waveguide," in *Photonics*, vol. 8, no. 11. MDPI, 2021, p. 472.

[207] X. Zhang, S. Yan, T. Li, P. Liu, Y. Zhang, L. Shen, Y. Ren, and E. Hua, "Refractive index sensor based on fano resonance in a ring with a rectangular cavity structure," *Results in Physics*, vol. 31, p. 104997, 2021.

[208] C. Wu, Z. Guo, S. Chen, J. Yang, and K. Wen, "Refractive index sensing based on multiple fano resonances in a plasmonic defective ring-cavity system," *Results in Physics*, vol. 27, p. 104508, 2021.

[209] X. Liu, J. Li, J. Chen, S. Rohimah, H. Tian, and J. Wang, "Independently tunable triple fano resonances based on mim waveguide structure with a semi-ring cavity and its sensing characteristics," *Optics Express*, vol. 29, no. 13, pp. 20 829–20 838, 2021.

[210] H. Bahri, S. Mouetsi, A. Hocini, and H. Ben Salah, "A high sensitive sensor using mim waveguide coupled with a rectangular cavity with fano resonance," *Optical and Quantum Electronics*, vol. 53, no. 6, p. 332, 2021.

[211] G. Xiao, Y. Xu, H. Yang, Z. Ou, J. Chen, H. Li, X. Liu, L. Zeng, and J. Li, "High sensitivity plasmonic sensor based on fano resonance with inverted u-shaped resonator," *Sensors*, vol. 21, no. 4, p. 1164, 2021.

[212] M. R. Rakhshani, "Refractive index sensor based on dual side-coupled rectangular resonators and nanorods array for medical applications," *Optical and Quantum Electronics*, vol. 53, no. 5, p. 232, 2021.

[213] P. Liu, S. Yan, Y. Ren, X. Zhang, T. Li, X. Wu, L. Shen, and E. Hua, "A mim waveguide structure of a high-performance refractive index and temperature sensor based on fano resonance," *Applied Sciences*, vol. 11, no. 22, p. 10629, 2021.

[214] Y. Yu, J. Cui, G. Liu, R. Zhao, M. Zhu, G. Zhang, and W. Zhang, "Research on fano resonance sensing characteristics based on racetrack resonant cavity," *Micromachines*, vol. 12, no. 11, p. 1359, 2021.

[215] S. Yu, Y. Su, Z. Sun, T. Zhao, and J. Yu, "Multi-fano resonances in mim waveguides coupled with split annular cavity connected with rectangular resonator and application for multichannel refractive index sensor," *Journal of Nanophotonics*, vol. 15, no. 1, pp. 016 004–016 004, 2021.

[216] C.-T. C. Chao, Y.-F. C. Chau, and H.-P. Chiang, "Multiple fano resonance modes in an ultra-compact plasmonic waveguide-cavity system for sensing applications," *Results in Physics*, vol. 27, p. 104527, 2021.

[217] C. Zhou, Y. Huo, Y. Guo, and Q. Niu, "Tunable multiple fano resonances and stable plasmonic band-stop filter based on a metal-insulator-metal waveguide," *Plasmonics*, vol. 16, no. 5, pp. 1735–1743, 2021.

[218] Z. Shao, S. Yan, F. Wen, X. Wu, and E. Hua, "Double ring nanostructure with an internal cavity and a multiple fano resonances system for refractive index sensing," *Applied Optics*, vol. 60, no. 22, pp. 6623–6631, 2021.

[219] H. Shi, S. Yan, X. Yang, H. Su, X. Wu, and E. Hua, "Nanosensor based on fano resonance in a metal-insulator-metal waveguide structure coupled with a half-ring," *Results in Physics*, vol. 21, p. 103842, 2021.

[220] A. Harhouz and A. Hocini, "Highly sensitive plasmonic temperature sensor based on fano resonances in mim waveguide coupled with defective oval resonator," *Optical and Quantum Electronics*, vol. 53, no. 8, p. 439, 2021.

[221] C.-T. C. Chao, Y.-F. C. Chau, A. H. Mahadi, M. R. R. Kooh, N. Kumara, H.-P. Chiang *et al.*, "Plasmonic refractive index sensor based on the combination of rectangular and circular resonators including baffles," *Chinese Journal of Physics*, vol. 71, pp. 286–299, 2021.

[222] H. Su, S. Yan, X. Yang, J. Guo, J. Wang, and E. Hua, "Sensing features of the fano resonance in an mim waveguide coupled with an elliptical ring resonant cavity," *Applied Sciences*, vol. 10, no. 15, p. 5096, 2020.

[223] J. Li, J. Chen, X. Liu, H. Tian, J. Wang, J. Cui, and S. Rohimah, "Optical sensing based on multimode fano resonances in metal-insulator-metal waveguide systems with x-shaped resonant cavities," *Applied Optics*, vol. 60, no. 18, pp. 5312–5319, 2021.

[224] S. Rohimah, H. Tian, J. Wang, J. Chen, J. Li, X. Liu, J. Cui, Q. Xu, and Y. Hao, "Fano resonance in the plasmonic structure of mim waveguide with r-shaped resonator for refractive index sensor," *Plasmonics*, vol. 17, no. 4, pp. 1681–1689, 2022.

[225] M. Wang, H. Tian, X. Liu, J. Li, and Y. Liu, "Multiparameter sensing based on tunable fano resonances in mim waveguide structure with square-ring and triangular cavities," in *Photonics*, vol. 9, no. 5. MDPI, 2022, p. 291.

[226] B. Li, H. Sun, H. Zhang, Y. Li, J. Zang, X. Cao, X. Zhu, X. Zhao, and Z. Zhang, "Refractive index sensor based on the fano resonance in metal–insulator–metal waveg-

uides coupled with a whistle-shaped cavity," *Micromachines*, vol. 13, no. 10, p. 1592, 2022.

[227] X. Zhang, S. Yan, J. Liu, Y. Ren, Y. Zhang, and L. Shen, "Refractive index sensor based on a metal-insulator-metal bus waveguide coupled with a u-shaped ring resonator," *Micromachines*, vol. 13, no. 5, p. 750, 2022.

[228] H. Bensalah, A. Hocini, H. Bahri, D. Khedrouche, S. Ingebrandt, and V. Pachauri, "A plasmonic refractive index sensor with high sensitivity and its application for temperature and detection of biomolecules," *Journal of Optics*, pp. 1–12, 2022.

[229] H. Fan, H. Fan, and H. Fan, "Multiple fano resonance refractive index sensor based on a plasmonic metal-insulator-metal based taiji resonator," *JOSA B*, vol. 39, no. 1, pp. 32–39, 2022.

[230] Z. Guo, K. Wen, Y. Qin, Y. Fang, Z. Li, and L. Chen, "A plasmonic refractive-index sensor based multiple fano resonance multiplexing in slot-cavity resonant system," *Photonic Sensors*, pp. 1–10, 2022.

[231] S. Yan, Q. Wang, L. Shen, F. Liu, Y. Su, Y. Zhang, Y. Cui, G. Zhou, J. Liu, and Y. Ren, "Novel nanoscale refractive index sensor based on fano resonance," in *Photonics*, vol. 9, no. 11. MDPI, 2022, p. 795.

[232] Y. Ren, Q. Wang, L. Shen, F. Liu, Y. Cui, C. Zhu, Z. Chen, B. Huang, and S. Yan, "Nanoscale refractive index sensors based on fano resonance phenomena," in *Photonics*, vol. 9, no. 12. MDPI, 2022, p. 982.

[233] V. Najjari, S. Mirzanejhad, and A. Ghadi, "Plasmonic refractive index sensor and plasmonic bandpass filter including graded 4-step waveguide based on fano resonances," *Plasmonics*, vol. 17, no. 4, pp. 1809–1817, 2022.

[234] S. Tavana and S. Bahadori-Haghighi, "Visible-range double fano resonance metal–insulator-metal plasmonic waveguide for optical refractive index sensing," *Plasmonics*, pp. 1–9, 2022.

[235] S. Rohimah, H. Tian, J. Wang, J. Chen, J. Li, X. Liu, J. Cui, and Y. Hao, "Tunable multiple fano resonances based on a plasmonic metal-insulator-metal structure for nano-sensing and plasma blood sensing applications," *Applied Optics*, vol. 61, no. 6, pp. 1275–1283, 2022.

[236] G. Zhou, S. Yan, L. Chen, X. Zhang, L. Shen, P. Liu, Y. Cui, J. Liu, T. Li, and Y. Ren, "A nano refractive index sensing structure for monitoring hemoglobin concentration in human body," *Nanomaterials*, vol. 12, no. 21, p. 3784, 2022.

[237] A. Harhouz, A. Hocini, and H. Tayoub, "Refractive index sensing and label-free detection employing oval resonator structured plasmonic sensor," 2022.

[238] Q. Wang, S. Yan, J. Liu, X. Zhang, L. Shen, P. Liu, Y. Cui, T. Li, and Y. Ren, "Refractive index and alcohol-concentration sensor based on fano phenomenon," *Sensors*, vol. 22, no. 21, p. 8197, 2022.

[239] S. Dong, H. Liu, Y. Zheng, J. Zhang, S. Xia, C. Dong, K. Shen, C. Deng, W. Luo, M. Su *et al.*, "Numerical study on the biosensing in mid-infrared based on multiple fano-resonance plasmonic waveguide," *Optik*, vol. 270, p. 170042, 2022.

[240] L. Shen, S. Yan, P. Liu, J. Cui, J. Liu, and Z. Chen, "Tunable nano refractive-index sensor structure base on fano resonance," in *2022 4th International Conference on Intelligent Control, Measurement and Signal Processing (ICMSP)*. IEEE, 2022, pp. 247–250.

[241] G. Zhou, S. Yan, L. Shen, Y. Zhang, and Y. Ren, "A high-performance nano-refractive index sensor structure based on fano resonance," in *2022 9th International Forum on Electrical Engineering and Automation (IFEEA)*. IEEE, 2022, pp. 30–33.

[242] Q. Wang, S. Yan, C. Zhu, L. Shen, and Y. Ren, "Petal-type refractive index sensor based on fano resonance," in *2022 9th International Forum on Electrical Engineering and Automation (IFEEA)*. IEEE, 2022, pp. 34–37.

[243] Y. Liu, H. Tian, X. Zhang, M. Wang, and Y. Hao, "Quadruple fano resonances in mim waveguide structure with ring cavities for multisolution concentration sensing," *Applied Optics*, vol. 61, no. 35, pp. 10 548–10 555, 2022.

[244] W. Wu, X. Zhang, Z. Chen, Y. Zhang, F. Wen, and S. Yan, "Refractive index sensor based on fano resonance in a ring with a stub cavity structure," in *2022 4th International Conference on Intelligent Control, Measurement and Signal Processing (ICMSP)*. IEEE, 2022, pp. 415–418.

[245] I. Tathfif, M. F. Hassan, K. S. Rashid, A. A. Yaseer, and R. H. Sagor, "A highly sensitive plasmonic refractive index sensor based on concentric triple ring resonator for cancer biomarker and chemical concentration detection," *Optics Communications*, vol. 519, p. 128429, 2022.

[246] Q. Wu, Y. Zhang, D. Qu, and C. Li, "Independently tunable triple fano resonances in plasmonic waveguide structure and its applications for sensing," *Journal of Nanophotonics*, vol. 16, no. 3, p. 036008, 2022.

[247] Y. Pan, Q. Meng, and F. Chen, "Realizing multiple fano resonance in an end-coupled semi-ring resonator-coupled waveguide structure," *Journal of Optics*, pp. 1–9, 2022.

[248] "Ap physics c: E&m – 5.3 maxwell's equations — fiveable," https://library.fiveable.me/ap-physics-e-m/unit-5/maxwells-equations/study-guide/YsKXHFylQLUCBDwyS3kR, (Accessed on 05/13/2023).

[249] J. Pérez-Coll Jiménez, P. Tenfjord, M. Hesse, C. Norgren, N. Kwagala, H. M. Kolstø, and S. F. Spinnangr, "The role of resistivity on the efficiency of magnetic reconnection in mhd," *Journal of Geophysical Research: Space Physics*, vol. 127, no. 6, p. e2021JA030134, 2022.

[250] D. J. Hagan, "Ose5312–light-matter interaction," 2013.

[251] G. Wang, C. Wang, R. Yang, W. Liu, and S. Sun, "A sensitive and stable surface plasmon resonance sensor based on monolayer protected silver film," *Sensors*, vol. 17, no. 12, p. 2777, 2017.

[252] C. S. Desai and J. F. Abel, *Introduction to the finite element method; a numerical method for engineering analysis*. Van Nostrand Reinhold, 1971.

[253] M. N. Sadiku, *Numerical techniques in electromagnetics with MATLAB*. CRC press, 2018.

[254] "University physics with modern physics - pdf free download," https://epdf.tips/university-physics-with-modern-physics-5ea812696fe3f.html, (Accessed on 05/13/2023).

[255] S. BEA and M. Teich, "Fundamentals of photonics," *Wiley*, p. 313, 1991.

[256] F. Pisano, M. F. Kashif, A. Balena, M. Pisanello, F. De Angelis, L. M. de la Prida, M. Valiente, A. D'Orazio, M. De Vittorio, M. Grande *et al.*, "Plasmonics on a neural implant: Engineering light–matter interactions on the nonplanar surface of tapered optical fibers," *Advanced Optical Materials*, vol. 10, no. 2, p. 2101649, 2022.

[257] G. Wang, C. Wang, R. Yang, W. Liu, and S. Sun, "A sensitive and stable surface plasmon resonance sensor based on monolayer protected silver film," *Sensors*, vol. 17, no. 12, p. 2777, 2017.

[258] M. Danaie and A. Shahzadi, "Design of a high-resolution metal–insulator–metal plasmonic refractive index sensor based on a ring-shaped si resonator," *Plasmonics*, vol. 14, no. 6, pp. 1453–1465, 2019.

[259] M. F. Hassan, R. H. Sagor, M. R. Amin, M. R. Islam, and M. S. Alam, "Point of care detection of blood electrolytes and glucose utilizing nano-dot enhanced plasmonic biosensor," *IEEE Sensors Journal*, vol. 21, no. 16, pp. 17 749–17 757, 2021.

[260] K. S. Rashid, I. Tathfif, A. A. Yaseer, M. F. Hassan, and R. H. Sagor, "Cog-shaped refractive index sensor embedded with gold nanorods for temperature sensing of multiple analytes," *Optics Express*, vol. 29, no. 23, pp. 37 541–37 554, 2021.

[261] M. Yan and M. Qiu, "Analysis of surface plasmon polariton using anisotropic finite elements," *IEEE Photonics Technology Letters*, vol. 19, no. 22, pp. 1804–1806, 2007.

[262] A. D. Rakić, A. B. Djurišić, J. M. Elazar, and M. L. Majewski, "Optical properties of metallic films for vertical-cavity optoelectronic devices," *Applied optics*, vol. 37, no. 22, pp. 5271–5283, 1998.

[263] M. Butt, S. Khonina, and N. Kazanskiy, "A multichannel metallic dual nano-wall square split-ring resonator: design analysis and applications," *Laser Physics Letters*, vol. 16, no. 12, p. 126201, 2019.

[264] X.-P. Jin, X.-G. Huang, J. Tao, X.-S. Lin, and Q. Zhang, "A novel nanometeric plasmonic refractive index sensor," *IEEE transactions on nanotechnology*, vol. 9, no. 2, pp. 134–137, 2010.

[265] S. A. Maier *et al.*, *Plasmonics: fundamentals and applications*. Springer, 2007, vol. 1.

[266] Q. Zhang, X.-G. Huang, X.-S. Lin, J. Tao, and X.-P. Jin, "A subwavelength coupler-type mim optical filter," *Optics express*, vol. 17, no. 9, pp. 7549–7554, 2009.

[267] C. Yang, B. Yan, Q. Wang, J. Zhao, H. Zhang, H. Yu, H. Fan, and D. Jia, "Sensitivity improvement of an optical fiber sensor based on surface plasmon resonance with pure higher-order modes," *Applied Sciences*, vol. 13, no. 6, p. 4020, 2023.

[268] Y. Zhang, B. Lin, S. C. Tjin, H. Zhang, G. Wang, P. Shum, and X. Zhang, "Refractive index sensing based on higher-order mode reflection of a microfiber bragg grating," *Optics express*, vol. 18, no. 25, pp. 26 345–26 350, 2010.

[269] M. Butt, S. Khonina, and N. Kazanskiy, "Hybrid plasmonic waveguide-assisted metal–insulator–metal ring resonator for refractive index sensing," *Journal of Modern Optics*, vol. 65, no. 9, pp. 1135–1140, 2018.

[270] M. Bazgir, M. Jalalpour, F. B. Zarrabi, and A. S. Arezoomand, "Design of an optical switch and sensor based on a mim coupled waveguide using a dna composite," *Journal of Electronic Materials*, vol. 49, pp. 2173–2178, 2020.

[271] C.-T. Chou Chao, Y.-F. Chou Chau, H. J. Huang, N. Kumara, M. R. R. Kooh, C. M. Lim, and H.-P. Chiang, "Highly sensitive and tunable plasmonic sensor based on a nanoring resonator with silver nanorods," *Nanomaterials*, vol. 10, no. 7, p. 1399, 2020.

[272] M. A. Butt, A. Kaźmierczak, N. L. Kazanskiy, and S. N. Khonina, "Metal-insulator-metal waveguide-based racetrack integrated circular cavity for refractive index sensing application," *Electronics*, vol. 10, no. 12, p. 1419, 2021.

[273] N. L. Kazanskiy, S. N. Khonina, M. A. Butt, A. Kaźmierczak, and R. Piramidowicz, "A numerical investigation of a plasmonic sensor based on a metal-insulator-metal waveguide for simultaneous detection of biological analytes and ambient temperature," *Nanomaterials*, vol. 11, no. 10, p. 2551, 2021.

[274] M. A. Butt, S. N. Khonina, and N. L. Kazanskiy, "Simple and improved plasmonic sensor configuration established on mim waveguide for enhanced sensing performance," *Plasmonics*, vol. 17, no. 3, pp. 1305–1314, 2022.

[275] W. K. Jung and K. M. Byun, "Fabrication of nanoscale plasmonic structures and their applications to photonic devices and biosensors," *Biomedical Engineering Letters*, vol. 1, pp. 153–162, 2011.

[276] S.-W. Lee, K.-S. Lee, J. Ahn, J.-J. Lee, M.-G. Kim, and Y.-B. Shin, "Highly sensitive biosensing using arrays of plasmonic au nanodisks realized by nanoimprint lithography," *ACS nano*, vol. 5, no. 2, pp. 897–904, 2011.

[277] M. F. Hassan, I. Tathfif, M. Radoan, and R. H. Sagor, "A concentric double-ring resonator based plasmonic refractive index sensor with glucose sensing capability," in *2020 IEEE REGION 10 CONFERENCE (TENCON)*. IEEE, 2020, pp. 91–96.

[278] H. Nugroho, L. Hasanah, C. Wulandari, R. Pawinanto, M. H. Haron, A. R. Zain, D. Berhanuddin, B. Mulyanti, P. Singh, and P. S. Menon, "Silicon on insulator-based microring resonator and au nanofilm krestchmann-based surface plasmon resonance glucose sensors for lab-on-a-chip applications," *International Journal of Nanotechnology*, vol. 17, no. 1, pp. 29–41, 2020.

[279] S. Ghorbani, M. Sadeghi, and Z. Adelpour, "A highly sensitive and compact plasmonic ring nano-biosensor for monitoring glucose concentration," *Laser Physics*, vol. 30, no. 2, p. 026204, 2019.

[280] K. E. You, N. Uddin, T. H. Kim, Q. H. Fan, and H. J. Yoon, "Highly sensitive detection of biological substances using microfluidic enhanced fabry-perot etalon-based optical biosensors," *Sensors and Actuators B: Chemical*, vol. 277, pp. 62–68, 2018.

[281] M. Amasia and M. Madou, "Large-volume centrifugal microfluidic device for blood plasma separation," *Bioanalysis*, vol. 2, no. 10, pp. 1701–1710, 2010.

[282] A. W. Mohammad, R. K. Basha, and C. P. Leo, "Nanofiltration of glucose solution containing salts: Effects of membrane characteristics, organic component and salts on retention," *Journal of Food Engineering*, vol. 97, no. 4, pp. 510–518, 2010.

[283] M. Xu, D. P. Papageorgiou, S. Z. Abidi, M. Dao, H. Zhao, and G. E. Karniadakis, "A deep convolutional neural network for classification of red blood cells in sickle cell anemia," *PLoS computational biology*, vol. 13, no. 10, p. e1005746, 2017.

[284] S. Mostufa, A. K. Paul, and K. Chakrabarti, "Detection of hemoglobin in blood and urine glucose level samples using a graphene-coated spr based biosensor," *OSA Continuum*, vol. 4, no. 8, pp. 2164–2176, 2021.

[285] R. Kumar, "Iron deficiency anemia (ida), their prevalence, and awareness among girls of reproductive age of distt mandi himachal pradesh, india," *International Letters of Natural Sciences*, 2014.

[286] A. J. Erslev, J. Caro, E. Kansu, O. Miller, and E. Cobbs, "Plasma erythropoietin in polycythemia," *The American Journal of Medicine*, vol. 66, no. 2, pp. 243–247, 1979.

[287] M. A. Jabin, K. Ahmed, M. J. Rana, B. K. Paul, M. Islam, D. Vigneswaran, and M. S. Uddin, "Surface plasmon resonance based titanium coated biosensor for cancer cell detection," *IEEE Photonics Journal*, vol. 11, no. 4, pp. 1–10, 2019.

[288] P. Sharma, P. Sharan, and P. Deshmukh, "A photonic crystal sensor for analysis and detection of cancer cells," in *2015 International conference on pervasive computing (ICPC)*. IEEE, 2015, pp. 1–5.

[289] P. Kumar, V. Kumar, J. S. Roy *et al.*, "Dodecagonal photonic crystal fibers with negative dispersion and low confinement loss," *Optik*, vol. 144, pp. 363–369, 2017.

[290] V. Dhinakaran, M. Chellappan Thangappan, A. Natesan, and K. Krishnan, "High amplitude sensitivity gold-coated trichannel photonic crystal fibre for refractive index sensor," *IET Optoelectronics*, vol. 15, no. 4, pp. 185–193, 2021.

[291] M. Kumar, V. Muniswamy, K. Guha, J. Iannacci, and N. Krishnaswamy, "Analysis of integrated silicon nitride lab-on-a-chip optofluidic sensor at visible wavelength for absorbance based biosensing applications," *Microsystem Technologies*, pp. 1–8, 2021.

[292] R. Bacallao, K. Kiai, and L. Jesaitis, "Guiding principles of specimen preservation for confocal fluorescence microscopy," *Handbook of biological confocal microscopy*, pp. 311–325, 1995.

[293] I. J. Bigio and S. G. Bown, "Spectrroscopic sensing of cancer and cancer therapy: Current status of translational research," *Cancer biology & therapy*, vol. 3, no. 3, pp. 259–267, 2004.

[294] R. J. Simpson, "Homogenization of mammalian tissue," *Cold Spring Harbor Protocols*, vol. 2010, no. 7, pp. pdb–prot5455, 2010.

[295] A. Boyde and C. Wood, "Preparation of animal tissues for surface-scanning electron microscopy," *Journal of Microscopy*, vol. 90, no. 3, pp. 221–249, 1969.

[296] J.-C. Lai, Y.-Y. Zhang, Z.-H. Li, H.-J. Jiang, and A.-Z. He, "Complex refractive index measurement of biological tissues by attenuated total reflection ellipsometry," *Applied optics*, vol. 49, no. 16, pp. 3235–3238, 2010.

[297] Z. Zhang, L. Luo, C. Xue, W. Zhang, and S. Yan, "Fano resonance based on metal-insulator-metal waveguide-coupled double rectangular cavities for plasmonic nanosensors," *Sensors*, vol. 16, no. 5, p. 642, 2016.

[298] X.-P. Jin, X.-G. Huang, J. Tao, X.-S. Lin, and Q. Zhang, "A novel nanometeric plasmonic refractive index sensor," *IEEE transactions on nanotechnology*, vol. 9, no. 2, pp. 134–137, 2010.

[299] Y.-F. C. Chau, C.-T. Chou Chao, S. Z. B. H. Jumat, M. R. R. Kooh, R. Thotagamuge, C. M. Lim, and H.-P. Chiang, "Improved refractive index-sensing performance of multimode fano-resonance-based metal-insulator-metal nanostructures," *Nanomaterials*, vol. 11, no. 8, p. 2097, 2021.

[300] S. Yan, M. Zhang, X. Zhao, Y. Zhang, J. Wang, and W. Jin, "Refractive index sensor based on a metal–insulator–metal waveguide coupled with a symmetric structure," *Sensors*, vol. 17, no. 12, p. 2879, 2017.

[301] X. Zhang, Y. Qi, P. Zhou, H. Gong, B. Hu, and C. Yan, "Refractive index sensor based on fano resonances in plasmonic waveguide with dual side-coupled ring resonators," *Photonic Sensors*, vol. 8, pp. 367–374, 2018.

[302] M. Wang, M. Zhang, Y. Wang, R. Zhao, and S. Yan, "Fano resonance in an asymmetric mim waveguide structure and its application in a refractive index nanosensor," *Sensors*, vol. 19, no. 4, p. 791, 2019.

[303] M. A. Butt, N. L. Kazanskiy, and S. N. Khonina, "Highly sensitive refractive index sensor based on plasmonic bow tie configuration," *Photonic sensors*, vol. 10, pp. 223–232, 2020.

[304] Y.-F. Chou Chau, T. Y. Ming, C.-T. Chou Chao, R. Thotagamuge, M. R. R. Kooh, H. J. Huang, C. M. Lim, and H.-P. Chiang, "Significantly enhanced coupling effect and gap plasmon resonance in a mim-cavity based sensing structure," *Scientific Reports*, vol. 11, no. 1, p. 18515, 2021.

[305] M. Irigoyen, J. A. Sánchez-Martin, E. Bernabeu, and A. Zamora, "Tapered optical fiber sensor for chemical pollutants detection in seawater," *Measurement Science and Technology*, vol. 28, no. 4, p. 045802, 2017.

[306] Y. W. Fen, W. M. M. Yunus *et al.*, "Characterization of the optical properties of heavy metal ions using surface plasmon resonance technique," *Opt. Photonics J*, vol. 1, no. 03, pp. 116–123, 2011.

[307] P. Sun, Y. Chen, C. Gao, X. Liu, X. Yang, and M. Xu, "Heavy metal ion detection on a surface plasmatic resonance based on the change of refractive index," in *9th international symposium on advanced optical manufacturing and testing technologies: optoelectronic materials and devices for sensing and imaging*, vol. 10843. SPIE, 2019, pp. 365–373.

[308] P. Arasu, Y. Al-Qazwini, B. I. Onn, and A. Noor, "Fiber bragg grating based surface plasmon resonance sensor utilizing fdtd for alcohol detection applications," in *2012 IEEE 3rd International Conference on Photonics*. IEEE, 2012, pp. 93–97.

[309] J. Zhu and G. Wang, "Measurement of water content in heavy oil with cavity resonator," *Results in Physics*, vol. 18, p. 103192, 2020.

[310] K. Ahmed, M. J. Haque, M. A. Jabin, B. K. Paul, I. S. Amiri, and P. Yupapin, "Tetra-core surface plasmon resonance based biosensor for alcohol sensing," *Physica B: Condensed Matter*, vol. 570, pp. 48–52, 2019.

[311] K. S. Rashid, M. F. Hassan, A. A. Yaseer, I. Tathfif, and R. H. Sagor, "Gas-sensing and label-free detection of biomaterials employing multiple rings structured plasmonic nanosensor," *Sensing and Bio-Sensing Research*, vol. 33, p. 100440, 2021.

[312] Z. Jun, W. Xu, Z. Xu, D. Fu, S. Song, and D. Wei, "Surface plasmon polariton mode in the metal-insulator-metal waveguide," *Optik*, vol. 134, pp. 187–193, 2017.

[313] Y. Fang, K. Wen, Z. Li, B. Wu, and Z. Guo, "Plasmonic refractive index sensor with multi-channel fano resonances based on mim waveguides," *Modern Physics Letters B*, vol. 34, no. 16, p. 2050173, 2020.

[314] R. Al Mahmud, M. O. Faruque, and R. H. Sagor, "Plasmonic refractive index sensor based on ring-type pentagonal resonator with high sensitivity," *Plasmonics*, vol. 16, pp. 873–880, 2021.

[315] W. Guo, X. Zhu, Y. Liu, and H. Zhuang, "Sugar and water contents of honey with dielectric property sensing," *Journal of Food Engineering*, vol. 97, no. 2, pp. 275–281, 2010.

[316] E. Diacu and E. F. Tantaveanu, "Determination of moisture content and its correlation with other parameters in honey quality control," *REVISTA DE CHIMIE-BUCHAREST-ORIGINAL EDITION-*, vol. 58, no. 12, p. 1310, 2007.

[317] O. James, M. Mesubi, L. Usman, S. Yeye, K. Ajanaku, K. Ogunniran, O. O. Ajani, and T. Siyanbola, "Physical characterisation of some honey samples from north-central nigeria," *International Journal of Physical Sciences*, vol. 4, no. 9, pp. 464–470, 2009.

[318] M. Paques and C. Lindner, *Lactose: Evolutionary role, health effects, and applications*. academic press, 2019.

[319] S. A. Abrams, I. J. Griffin, and P. M. Davila, "Calcium and zinc absorption from lactose-containing and lactose-free infant formulas," *The American journal of clinical nutrition*, vol. 76, no. 2, pp. 442–446, 2002.

[320] E. Romero-Velarde, D. Delgado-Franco, M. García-Gutiérrez, C. Gurrola-Díaz, A. Larrosa-Haro, E. Montijo-Barrios, F. A. Muskiet, B. Vargas-Guerrero, and J. Geurts, "The importance of lactose in the human diet: Outcomes of a mexican consensus meeting," *Nutrients*, vol. 11, no. 11, p. 2737, 2019.

[321] S. B. Matthews, J. Waud, A. G. Roberts, and A. K. Campbell, "Systemic lactose intolerance: a new perspective on an old problem," *Postgraduate medical journal*, vol. 81, no. 953, pp. 167–173, 2005.

[322] R. Mattar, D. F. de Campos Mazo, and F. J. Carrilho, "Lactose intolerance: diagnosis, genetic, and clinical factors," *Clinical and experimental gastroenterology*, pp. 113–121, 2012.

[323] E. J. McDonald and A. L. Turcotte, "Density and refractive indices of lactose solutions," *Journal of research of the National Bureau of Standards*, vol. 41, no. 63, p. e68, 1948.

[324] A. Jääskeläinen, K.-E. Peiponen, and J. Räty, "On reflectometric measurement of a refractive index of milk," *Journal of dairy science*, vol. 84, no. 1, pp. 38–43, 2001.

[325] N. Wagholikar and S. Jagtap, "Optical characterization of sucrose (c12h21o11) at different temperatures," *IJIRSET*, vol. 6, pp. 2625–2630, 2017.

[326] N. Kinrot, *Investigation of Bulk Material Sensing Using Periodically Segmented Waveguide Mach-Zehnder Interferometer for Chemical/biosensing*. Tel Aviv University, 2005.